Master Thesis

by

J.S. van Dokkum

to obtain the degree of Master of Science
at the Delft University of Technology,
to be defended publicly on Tuesday July 11th, 2017 at 10:00 AM.

Student number:	4008693	
Project duration:	July 1, 2016 – July 1, 2017	
Thesis committee:	Prof. dr. ir. L. Nicola,	TU Delft, supervisor
	Dr. ir. M. Janssen,	TU Delft
	Dr. ir. A.M. Aragón,	TU Delft
	MSc. S.P. Venugopalan,	TU Delft, daily supervisor

Abstract

It is well known that most of the natural or man-made metal surfaces have self-affine roughness [1, 2]. Green's function molecular dynamics (GFMD) is a simulation technique to study the contact response of elastic bodies by modeling explicitly only the surface [3], and making use of damped dynamic energy minimization to solve the boundary-value problem. However, GFMD was limited to problems where a rough rigid substrate is pressed against a flat incompressible elastic solid assuming frictionless contact and only considering normal displacement to study continuum bodies [4, 5, 6]. Recently, the formulation was extended by Venugopalan *et al.* [3] to account for shear and compressible finite bodies.

The GFMD method is used to determine the real contact area fraction a_r of linear-elastic bodies in contact as a function of the nominal contact pressure $\bar{p}$. It is well known from experiments [7] and simulations [8, 9, 4, 5] that for a small nominal pressures $\bar{p}$, a linear dependence of the real contact area fraction a_r on the nominal contact pressure $\bar{p}$ is observed. Currently, no consensus is reached about the value of the proportionality coefficient κ between a_r and $\bar{p}$. Here, we perform GFMD simulations for the indentation of bodies with a rough rigid indenter with self-affine roughness, and make use of an extrapolation method to determine the value of the proportionality coefficient κ. Moreover, we comment on the earlier predicted values of κ by statistical models [10, 11, 12, 13, 14] and numerical simulations [9, 4, 5]. It is found that GFMD reproduces the value of κ in good agreement with Persson's theory [12].

We extend GFMD to study the contact mechanics of deformable self-affine metal bodies. To date, only mapping [15] is used, limiting the choice of material properties and contact conditions. In the extended GFMD method, we impose displacement to an initially flat surface to form simple surface topographies. The strain required for the deformation corresponding to the simple surface topography is numerically calculated. When the desired topography is reached, a GFMD simulation is performed whereby the calculated strain inside the deformable body, due to the imposed loading, is corrected with the strain calculated in the previous step. The two-step GFMD approach is validated by comparing its results to calculations based on the finite-element method (FEM). However, one of the limitations of the new method is the restriction in maximum allowable root mean square gradient $\bar{g}$ (RMSG), of the type observed in classical GFMD simulations. Therefore, the range of different self-affine surface topographies that can be studied is limited.

In order to capture the correct linear-elastic response of a solid with rough surface the surface discretization is several decades smaller than the smallest roughness [4, 5]. This is computationally very costly [3]. To limit the computational time, the critical damping coefficient is calculated prior to the simulation. To this end, for the first time, the critical damping coefficient is here derived analytically for the numerical integration scheme used by GFMD, the position (Störmer-)Verlet algorithm [16]. The critical damping coefficient depends on the material properties, substrate geometry and discrete time-step. It is found, that the displacement coming to equilibrium slowest is the center-of-mass displacement in tangential direction, therefore this displacement determines the critical damping coefficient.

Contents

Chapter 1

Introduction

According to Gillingham *et al.* [17] the total world consumption of marketed energy is expected to expand from 549 quadrillion British thermal units (Btu) in 2012 to 629 quadrillion Btu in 2020 and to 815 quadrillion Btu in 2040 - a 48% increase from 2012 to 2040. 1 Btu is equivalent to 1060 joules. With increasing global energy consumption, sustainability becomes more and more important. One of the main reasons for energy dissipation is friction. Friction is a phenomenon that consists of various physical mechanisms that act on different length scales [18, 19]. Tribology is the study of friction, wear and lubrication. An important quantity to study in tribology is the real contact area fraction a_{r}. It is well known that experiments [7] and theory show that this real area of contact A is much smaller than the projected area A_0 of the contacting surfaces. It is also well know that for a small nominal pressures $\bar{p}$, a linear dependence of a_{r} on the nominal contact pressure $\bar{p}$ is observed. However, so far, the value of the proportionality coefficient κ between a_{r} and $\bar{p}$ is disputed.

When two macroscopic bodies with microscopic roughness come in contact, the contact occurs at multiple asperities of arbitrary shape. To study the effect of elastic deformation on contact behavior, models using continuum mechanics theories have been developed. According to Hertz [20] $a_{\mathrm{r}} \propto \bar{p}^{2/3}$ for elastic contact where friction and adhesion are ignored. The pioneering model introduced by Greenwood and Williamson (GW) [10] represented rough surface contact, at low nominal pressure $\bar{p}$, as non-interacting uniform Hertzian spherical asperities with their maximum heights exponentially distributed over the contact area. GW reported $a_{\mathrm{r}} \propto \bar{p}$ for a large number of asperities of different heights [21]. This formed the start for a body of literature studying contact response of elastic bodies with deterministic surfaces, also known as bearing area models. Bush *et al.* [11] included both distribution of radii and a-spherical asperities in the GW theory. Figure 1.1 shows three models of the rough surface by Hertz, GW and Bush *et al.* [11].

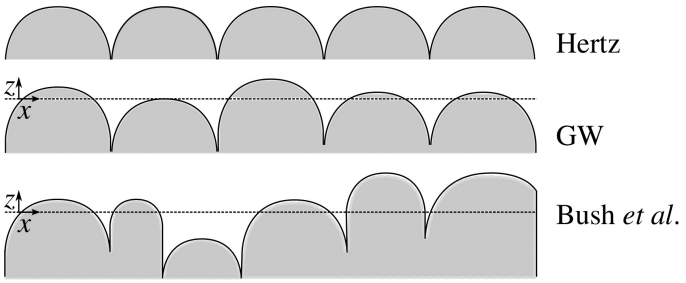

Figure 1.1: Three different models of a rough surface by Hertz [20], Greenwood and Williamson (GW) [10], and Bush *et al.* [11].

These theories consider explicit probability distributions for asperity peaks and sum the Hertzian contact areas calculated for each peak without including correlations between peaks. Also, the original theories by GW and Bush *et al.* ignore the interaction between asperities. Nevertheless, both theories reproduce the expected linear dependence of a_{r} on $\bar{p}$.

Following Bush *et al.* [11], the linear scaling of a_{r} with $\bar{p}$ for an elastic semi-infinite body and non-adhesive contacts is:

$$a_{\mathrm{r}} = \frac{\kappa \bar{p}}{\bar{g} E^*}, \tag{1.1}$$

where $\bar{g}$ is the root mean square gradient (RMSG) and E^* is the effective modulus:

$$E^* = \frac{E}{1-\nu^2}, \tag{1.2}$$

where E is the elastic modulus and ν is the Poisson's ratio. According to Bush *et al.* [11] the value of $\sqrt{\pi/8} \leq \kappa \leq \sqrt{2\pi}$. GW theory has been extended over recent years. Ciaverella [22] used GW theory and applied it to real fractured surfaces of elastic solids, for which he found that $a_r \propto \bar{p}$. This model, like GW, still lacked interaction between adjacent asperities and uniform compression of the elastic solid. Subsequently, Ciavarella [13] formulated an extended version of the GW theory with the inclusion of interaction between Hertzian asperities, obtaining results comparable to those reported in [22]. Carbone [14] extended GW to allow for varying curvature of the spheres depending on the asperity height and reported the same value of κ for small nominal loads as Bush *et al.* [11]. Another load bearing area model uses Archard's theory [23]. Archard [23] models surface roughness as a set of stacked hemispheres whose radii reduced as the height of the stack increased. This model considered multiple scales of roughness, therefore it was new, but scarcely used until fractal characterization of surface roughness became popular.
The pioneering work by Mandelbrot *et al.* [1] used fractal scaling to characterize fractured steel surfaces and reported that the microscopic roughness of metal surfaces displays self-affine characteristics. Subsequent research showed that metal surfaces are self-affine at small length scales [1, 24, 2, 25]. The independent variable for self-affinity is the Hurst's exponent H, this exponent determines the auto-correlation function (ACF) of the rough surface topography. Figure 1.2 is a numerically generated rough surface topography with Hurst's exponent $H = 0.9$.

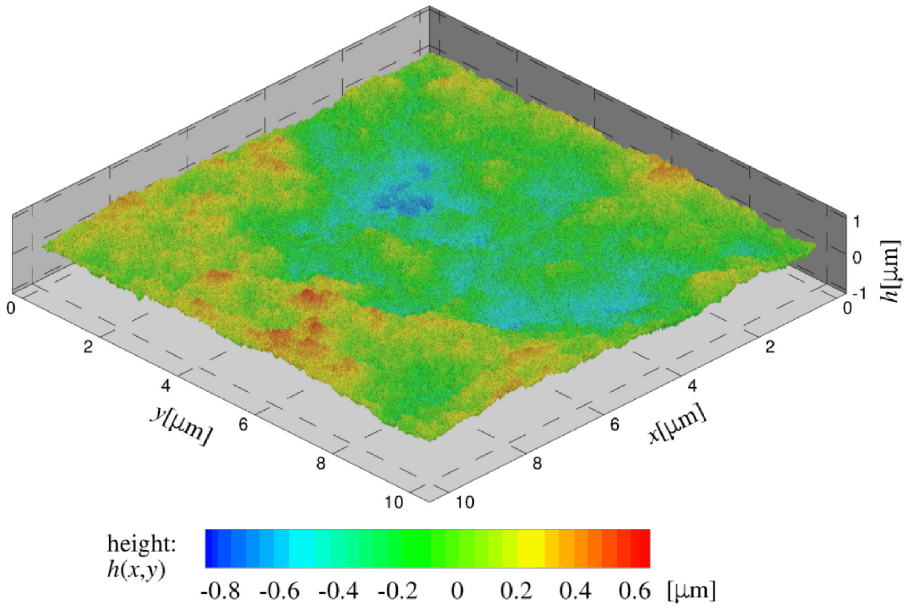

Figure 1.2: Numerically generated surface topography height $h(x, y)$ for $H = 0.9$.

The assumptions of smooth Hertzian asperities and no uniform compression made by GW and Bush *et al.* break down for self-affine surfaces and for moderate and high nominal pressure $\bar{p}$ [13]. Jackson *et al.* [26] described a non-statistical multi-scale model of the normal contact between rough

surfaces. In this method, the theory proposed by Archard [23] is used. The net load carried by the asperities at each length scale does not change with magnification. According to Jackson *et al.* [26] $a_r \propto \bar{p}$ for small nominal loads. This model approximated the self-affine roughness characteristics by a multi-scale deterministic surface. Therefore, the model still has the approximation of stacked Hertzian asperities at different length scales to model the self-affine surface roughness. Persson [12] developed a renormalization-group approach to contact mechanics for frictionless contact, where a diffusion-like equation is solved using the boundary conditions for full contact and detachment. Persson's theory models a contact problem as indicated in Fig. 1.3.

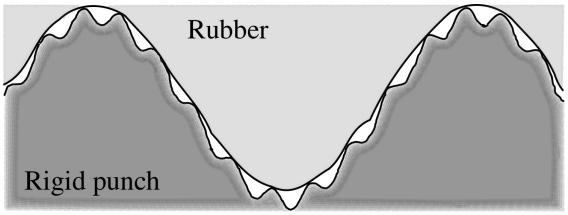

Figure 1.3: A rubber block pressed against a rigid substrate with roughness on two length scales.

Persson's theory predicts a value of $\kappa = \sqrt{8/\pi}$ independent of the Hurst's exponent H, it includes the effect of the asperity height correlation and is exact in the limit $a_r \to 1$. Therefore, the theory works well for incompressible materials like rubber. When detachment occurs, local effects are treated in an average way. Two important assumptions in Persson's theory are: (1) Non-contact regions are prohibited from diffusing back into contact; (2) The diffusion of pressure is independent of the magnitude of the local pressure. However, by treating local effects in an average way, quite a few interfacial properties are predicted very accurately by Persson's theory [6]. Contrary to rubber-like materials, full contact is almost never reached for metallic bodies. All of the above mentioned theories neglect one or multiple important phenomena in contact mechanics of metal surfaces. According to Müser [27] the comparisons between the aforementioned statistical asperity models [23, 10, 11, 12] and simulations are weak tests, since theories merely need to reproduce a single proportionality coefficient while they usually depend on more than one adjustable parameter, which may not even be well defined from experiment or the model definition. Therefore, the adjustable parameter becomes effectively a fitting parameter. This reasoning leads to the conclusion that adjusting continuum asperity theories to model predictions is not a suitable representation of contact mechanics problem. We agree with this notion, because using a fitting parameter based upon empirical results is nothing more than a phenomenological description of a subset of contact mechanical properties, and we can not rigorously apply it to a generic contact problem without the risk of large over- and/or under prediction of any contact mechanical property. Therefore, we do not pursue such a heuristic approach, but in this work we use a numerical model to determine contact mechanical properties.

With the advent of computer technology, numerical contact models of 3-D rough surfaces have been developed. These models can simulate digitized rough surfaces with no assumptions concerning the roughness distribution [28]. At the end of the twenty-first century, Williamson [29], Gupta and Cook [30] and Bhushan and Cook [31] digitized topographies of contacting surfaces and studied elastic deformation at individual contacts for which the contact pressure and contact area were approximated as Hertzian contacts. Among the first brute-force methods was Hyun *et al.* [9], they used FEM to study non-adhesive, frictionless contact between elastic solids with a periodic self-affine surfaces and an aspect ratio $a = 1$. The aspect ratio a is defined as the periodic cell height z_m over the periodic cell width L_x, and represents the periodic cells slab geometry. According to

Hyun *et al.* [9] the value of κ is close to Persson's theory for surfaces with a Gaussian ACF ($H = 1$), while κ for surfaces with an exponential ACF ($H = 0.5$) $\kappa \approx \sqrt{2\pi}$. According to Hyun *et al.* [9] the value of κ rises nearly linearly with the Poisson's ratio ν and saturates as ν approaches the limiting value of 0.5. The increase in κ with ν is attributed to the increased interactions between nearby asperities. Figure 1.4 displays the ratio of $\kappa(\nu)/\kappa(0)$ as a function of the Poisson's ratio ν for different Hurst's exponents H by Hyun *et al.* [9], where $\kappa(0)$ is the value for κ with Poisson's ratio $\nu = 0$.

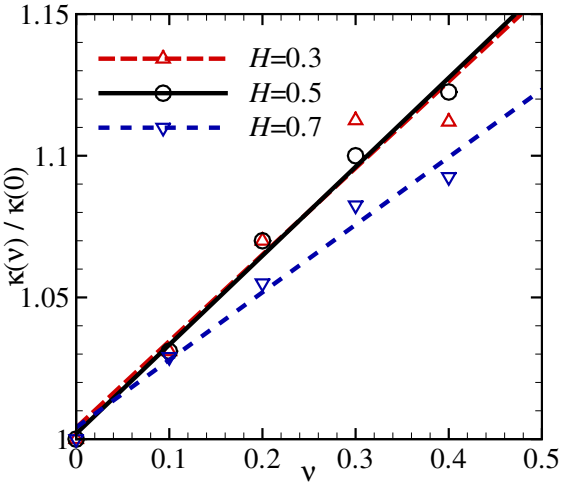

Figure 1.4: Plot of the ratio $\kappa(\nu)/\kappa(0)$ as a function of the Poisson's ratio ν for different Hurst's exponents $H = 0.3$, $H = 0.5$ and $H = 0.7$ by Hyun *et al.* [9]. Lines are linear fits to the data respectively.

The linear fits in Fig. 1.4 represent a linear dependency of $\kappa(\nu)$ on the Poisson's ratio ν. According to Eq. (1.1), the value of κ is inversely quadratically depended on the Poisson's ratio ν. This can be interpreted as a higher order dependency of κ on ν that is not correctly captured by the effective modulus E^*. The numerical model of Hyun *et al.* includes only one node per asperity, and according to Yestrabov *et al.* [32] the contact area was overestimated.
Komvopoulos *et al.* [33] developed a comprehensive analysis of layered elastic solids in contact with a rough surface with self-affine topography. They obtained by means of linear fitting the relationships for the contact pressure and the half-contact width in terms of the asperity radius, layer thickness and elastic properties for a single asperity contact by means of plane-strain FEM calculations, and these relationships were used in the contact stress analysis. In this analysis the local slope of the asperity within the interference is approximated by a smooth Hertzian contact, therefore neglecting features at smaller wavelengths than the interference width. Also, the stress fields inside the substrate are approximated by superposition of triangular stress distributions for individual Hertzian contacts. According to Komvopoulos *et al.* [33], $a_r \propto \bar{p}$ and the value of κ is highly dependent on the fractal characteristic and elastic modulus and less on the layer thickness. The effect of layer thickness is reported to be negligible for a small nominal pressure $\bar{p}$. This model gives a good macroscopic representation of the stresses inside the body, but it can not correctly represent the local deformation of the surface of the substrate.
Other brute force methods have been developed over the years, namely: The fast-Fourier-transform boundary-element method (FFT-BEM) [34, 35], the biconjugate-gradient stabilized method (BICG–STAB) [36], Boundary-element and the B-spline algorithm (BEM+B) [37], Fast-Fourier-transform integrated adhesion (FFT-IA) [38] and Green's function molecular dynamics (GFMD) [4, 6, 5, 3].

According to Müser *et al.* [27] FFT-BVM and GFMD are fastest and comparable in computational time for a given discretization nx. Both methods can capture contact down to the scale of the inter-atomic spacing a, and both are FFT based methods. However, so far, only GFMD is incorporated in multi-scale models with Molecular Dynamics (MD) [39] and discrete dislocation dynamics (DDD), and GFMD has the proven potential to do so with other methods in the future. Therefore, we consider only GFMD methods in this work.

GFMD is a boundary-value method allowing one to simulate the linear-elastic response of a solid to an external load by modeling explicitly only the surface, making use of damped dynamic energy minimization to solve the boundary-value problem. GFMD was first implemented to study open questions evolving around the contact mechanics of elastic solids with self-affine surface roughness under the action of external loads by Campañá *et al.* [4]. The model assumed near full-contact of infinite solids with both Lamé constants set to unity and non-adhesive interfacial interaction, and it only considered normal displacement of the surface. However, the Poisson's ratio $\nu = 0.25$ acts as a scaling factor for the effective modulus used in the elastic energy formulation of the semi-infinite solid and the displacement of the surface is equivalent to that of an incompressible solid with a reduced effective strength. According to Campañá *et al.* [4] there is no difference in the value of κ for real or virtual surface topographies with the same roughness characteristics. The value of κ lays between the predictions by Bush *et al.* [11] and Persson's theory and κ is only weakly dependent on H. Figure 1.5 shows the value of κ as a function of the Hurst's exponent H.

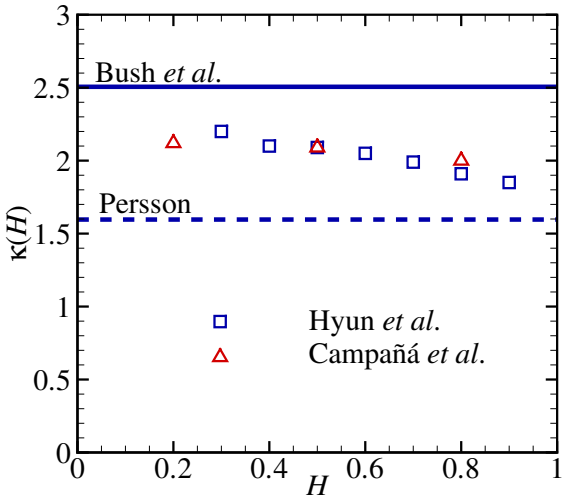

Figure 1.5: Plot of κ as a function of the Hurst's exponent H for Bush *et al.* [11], Persson [12], Hyun *et al.* [9] and Campañá et al. [4]

A more recent numerical study by Prodanov *et al.* [5] utilized the model by Campañá *et al.* [4] and presented an in-depth study of the value of κ and extrapolated results to the thermal, fractal and continuum (TFC) limit. The proportionality coefficient κ in the TFC-limit can be thought of as the continuum mechanical value of κ obtained through extrapolation of its numerically calculated values. According to Prodanov *et al.* [5] and Dapp *et al.* [6] the value of κ in the TFC limit differs no more than 10% for H close to 0 and to 1 and a_r scales linearly with $\bar{p}$ for low nominal pressure $\bar{p}$. Table 1.1 summarizes the values of κ obtained by different authors.

Year	Authors	κ [−]
1976	Bush *et al.* [11]	$\sqrt{2\pi} \approx 2.5 ... \sqrt{\pi/8} \approx 1.6$
2001	Persson [12]	$\sqrt{8/\pi} \approx 1.6$
2004	Hyun *et al.* [40]	1.8...2.2
2007	Campañá *et al.* [4]	1.98...2.09
2014	Prodanov *et al.* [5]	1.93...2.16

Table 1.1: The values of κ at low nominal pressure $\bar{p}$ obtained by different authors.

So far, GFMD was limited to problems where a rough rigid substrate is pressed against a flat incompressible elastic solid assuming frictionless contact and only considering normal displacement. These contact problems would give the same response if the roughness is on the rigid or deformable body, *i.e.*, the principle of mapping [15]. If the contact conditions are frictional, and the deformable body is compressible this is no longer the case. Venugopalan *et al.* [3] extended GFMD method for the simulation of incompressible solids under normal loading in several ways: shear is added; And, Poisson ratio ν as well as the heights of the deformed body z_m can now be chosen at will. This recent development by Venugopalan *et al.* [3] allows us to relax some of the assumptions made in prior GFMD studies of continuum models [4, 6, 5].

In this work, for the first time, the proportionality coefficient κ is rigorously determined for the elastic solid over a range of aspect ratios a and Poisson's ratios ν with a single method. Here, we perform GFMD simulations for the indentation of bodies with a rough rigid indenter with self-affine roughness, and make use of an extrapolation method to determine the value of the proportionality coefficient κ in the TFC limit. Moreover, we comment on the earlier predicted values of κ by statistical models [10, 11, 12, 13, 14] and numerical simulations [9, 4, 5]. It is found that GFMD reproduces the value of κ in good agreement with Persson's theory [12].

The aforementioned GFMD simulations are all under the assumption that the nominally flat surface of an elastic body is indented with a rough rigid punch. The traction in tangential direction is implicitly taken to be zero, *i.e.*, frictionless contact. In this work, the GFMD method is extended to study the contact mechanics of deformable bodies with simple surface topographies. This extended method is called 'two-step GFMD'. This work is done by us, in order to simulate metal contacts where commonly only small relative contact fractions a_r are observed, the Poisson's ratio ranges for common engineering metals between $\nu \approx 0.2$ for cast iron and $\nu \approx 0.44$ for gold [41], frictionless contact is a poor assumption and the effect of local slope is expected to be of major influence on the contact behavior.

First, common rough surface characteristics are summarized and methods to numerically generate rough surface topographies are presented. There are several real and reciprocal space methods to numerically generate self-affine surface topographies [42]. The most suitable method is selected and its pseudo-code is given. The reciprocal space method called power spectral density method (PSDM) [42, 43] is selected for all GFMD simulations in this work.

Then, the value of the proportionality coefficient κ is determined for an arbitrary body geometry and Poisson's ratio ν. The TFC-limit is numerically calculated by independently varying the ratio between the characteristic wavelengths of the self-affine roughness, and extrapolating the value of κ towards its limit respectively. The values of the proportionality coefficient κ are numerically determined for both a finite slab approaching an infinite solid and aspect ratios $a = 1, 0.5$, and for compressible and incompressible solids. In order to numerically calculate the TFC-limit for the value of κ, thousands of numerical simulations are run. Individual simulations can take between an one and twenty four hours. Note that an over-damped dynamic energy minimization will result in an asymptotic approach of the equilibrium position. To this end, we ensure that the energy

minimum is reached and the computational time is minimized by critically damping the damped dynamic energy minimization in GFMD simulations.
Subsequently, we extend the GFMD method by Venugopalan *et al.* [3] to simulate deformable compressible substrates with simple surface topographies. In two-step GFMD, we impose displacement to an initially flat surface to form the desired surface topography. We perform a GFMD simulation whereby the calculated strain inside the body due to the imposed loading is corrected with the strain calculated in the previous step. The formulation by Venugopalan *et al.* [3] for the full stress tensor inside the deformed body is corrected for the finite surface topography. This two-step GFMD approach is validated by comparing its body fields to calculations based on FEM, and a maximum allowable RMSG $\bar{g} = 0.030$ is observed.
Finally, an analytical expression for the critical damping coefficient and the equilibrium time are derived to minimize the computational time of GFMD simulations. To determine the critical damping coefficient in GFMD simulations the following steps are taken. The critical damping coefficient is derived for the numerical integration scheme used by GFMD to describe the motion of an harmonic oscillator. This critical damping coefficient is linked to the analytical critical damping coefficient in the limit of an infinitesimally small discrete time-step $\mathrm{d}t$. A scalar damping coefficient is assumed and the critical damping coefficient in GFMD simulations is derived in the same manner. The equilibrium time is approximated, we adapt the method as presented by Ogata [44] for this approximation. The critical damping coefficient and equilibrium time are numerically determined without prior knowledge of the analytical expression of the critical damping coefficient. As to be expected, there is good agreement between the numerical and the analytical expression of the critical damping coefficient. The critical damping coefficient depends on the material properties, substrate geometry, interfacial properties and the discrete time-step $\mathrm{d}t$. The equilibrium time is independent of the discrete time-step $\mathrm{d}t$.
The remainder of this work is organized as follows: In Chapter 2, an in depth introduction to the GFMD method is given. Common rough surface characteristics of metals are summarized and a method to numerically generate rough surface topographies is selected in Chapter 3. Subsequently, in Chapter 4, we determine the proportionality between area and load. Then, we present the two-step GFMD approach in Chapter 5. The critical damping coefficient and equilibrium time in GFMD dynamics are derived in Chapter 6. Finally, we give a conclusion of this work and an outlook in Chapter 7.

Chapter 2

Green's function molecular dynamics

"*The name of a man is a numbing blow form which he never recovers.*"

Marshall McLuhan

2.1 Introduction

Green's function molecular dynamics (GFMD) is a boundary-value method allowing one to simulate the linear-elastic response of a solid to an external load by modeling only the surface. The surface is discretized using nx equi-spaced grid-points. These grid-points interact with each other through an effective stiffness. Recently, GFMD was extended to include the shear component of the displacement in a slab of finite height z_{m} and generic Poisson's ratio ν [3]. Figure 2.1 is the schematic representation of a mixed boundary-value problem (BVP) in GFMD simulations, for the case of an array of flat rigid punches indenting an elastic layer.

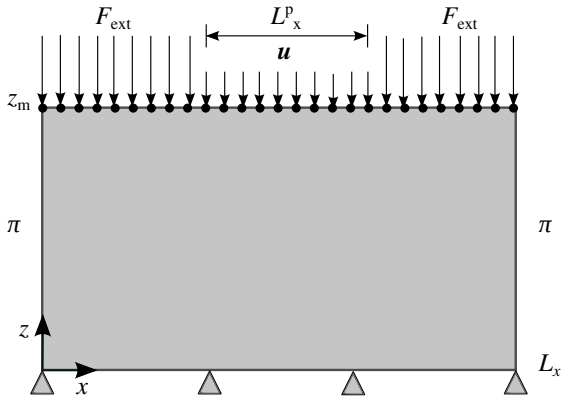

Figure 2.1: Schematic representation of a mixed boundary-value problem in GFMD simulations: A flat rigid punch indentation.

A rigid punch, with width L^{p}_x, indents an elastic substrate with aspect ratio $a = z_{\mathrm{m}}/L_x$, where z_{m} is the height of the substrate and L_x the width of the substrate. The rigid motion of the punch causes an increase in elastic energy density v_{el}, which causes the grid-points that represent the surface of the substrate to move to their new equilibrium position. This is because we can treat all modes corresponding to a single wave vector $\boldsymbol{q}$ independent of all modes corresponding to higher and/or lower wavevectors. The displacement of the surface with periodicity L_x is calculated in Fourier space. The surface displacement $\tilde{\boldsymbol{u}}(\boldsymbol{q}) = (\tilde{u}_1(\boldsymbol{q}), \tilde{u}_2(\boldsymbol{q}), \tilde{u}_3(\boldsymbol{q}))$ for each mode with wave vector $\boldsymbol{q}$ is obtained numerically. In this work, we only consider plane strain cases. Therefore, for the (1+1)-dimensional substrate, the in-plane wave vectors become scalars and can be written as:

$$q = \frac{2\pi}{L_x} k, \tag{2.1}$$

where k is the wave number index. In order to derive the areal elastic energy v_{el}, we first determine the displacement field $\boldsymbol{u}(x, z)$ by solving the differential equation of the equilibrium condition of a linear-elastic slab with finite-height z_{m} and generic Poisson's ratio ν for a fully displacement prescribed BVP, namely, a fixed bottom $\boldsymbol{u}(x, 0) = 0$ and a generic displacement at the surface $\boldsymbol{u}(x, z_{\mathrm{m}})$. We make use of the fact the solutions of the in-plane cosine transform of the lateral u_1 displacement couples to the in-plane sine transform of the normal u_3 displacement, and vice versa [3]. Once the displacement fields $\boldsymbol{u}(x, z)$ inside the body is known, we analytically calculate the Cauchy's strain tensors $\epsilon_{\alpha\beta}(x, z)$. Hence, with the well-known stress-strain relation, the stress field $\boldsymbol{\sigma}(x, z)$ and the tractions $\boldsymbol{\tau}(x)$ can be analytically calculated. When the strain and stress fields are known, we can calculate the areal elastic energy $v_{\mathrm{el}}(q)$ for a given sinusoidal displacement $\boldsymbol{u}(q)$ assuming a small-slope at the surface. Note that by taking advantage of the independence of modes

in Fourier space and the superposition principle of linear-elastic materials, we can also decompose an arbitrary surface displacement $\boldsymbol{u}(x, z_\mathrm{m})$ into its Fourier coefficients $\tilde{\boldsymbol{u}}(q)$, and subsequently sum over each individual wave number q to determine the total areal elastic energy v_el. With these analytical expressions for the displacement, strain and stress fields, we can determine the displacement at the surface $\boldsymbol{u}(q)$ for generic tractions $\boldsymbol{\tau}(q)$, and vice versa.
In this work, however, we are interested in mixed BVP, allowing us to determine contact between rough bodies for which the contact area is not known *a priori*. In order to solve the mixed BVP, we make use of dynamic energy minimization. A finite displacement at the surface causes an increase in the areal elastic energy v_el. The surface is allowed to oscillate, and to come to its new equilibrium position through Newton's equation of motion. This work only treats static loading, therefore the exact trajectory of the surface nodes is not a sought after result, and hence we can use damped dynamics to obtain the static solution [5]. Note that the surface displacement is numerically calculated in Fourier space for each set of modes corresponding to a single wave number q, *i.e.*, mode in normal direction and mode in tangential direction, using the equation of motion of a harmonic oscillator with two degrees of freedom (DOF) in Fourier space. Moreover, we can derive an analytical expression for the critical damping, *i.e.*, critical damping coefficient $\boldsymbol{c}_\mathrm{cr}$, ensuring correct and fast convergence of the surface displacement to its new equilibrium position.
The remainder of this work is organized as follows: First, we give the derivation of the displacement fields $\boldsymbol{u}\,(x, z)$ inside and on the linear-elastic, finite-height slab in Sec. 2.2. Then, we present the derivation by Venugopalan *et al.* [3] of the total areal elastic energy v_el for the aforementioned displacement field in Sec. 2.3. Next, we discuss the damped dynamic energy minimization in GFMD method in Sec. 2.4. Finally, we discuss the advantages and limitations of the GFMD method in Sec. 2.5. In the appendix, we give the pseudo-code of the GFMD method.

2.2 Displacement field of finite-height slab with generic Poisson's ratio

Following Venugopalan *et al.* [3], we consider the linearly elastic body of cubic symmetry in the slab geometry with the fixed bottom, *i.e.*, the displacement is $\boldsymbol{u}(x, z = 0) = 0$. The equilibrium condition is $\partial_\alpha \sigma_{\alpha\beta}(r) = 0$, where $\sigma_{\alpha\beta}(r)$ is the stress at the point r inside the body and $\partial_\alpha \equiv \partial/\partial r_\alpha$. We write the equilibrium condition as:

$$\begin{aligned}[C_{11}\partial_1^2 + C_{44}\partial_3^2]u_1 + (C_{44} + C_{12})\partial_1\partial_3 u_3 = 0;\\ [C_{11}\partial_3^2 + C_{44}\partial_1^2]u_3 + (C_{44} + C_{12})\partial_3\partial_1 u_1 = 0,\end{aligned} \tag{2.2}$$

where C_ij denotes coefficient of the elastic tensor in Voigt notation. The solutions of the in-plane cosine transform of the lateral u_1 displacement couples to the in-plane sine transform of the normal u_3 displacement, and vice versa [3]. The displacement inside the body is:

$$\begin{aligned}u_1^{\mathrm{c}}(x, z) = \cos(qx)\tilde{u}_1^{\mathrm{c}}(q, z);\\ u_3^{\mathrm{s}}(x, z) = \sin(qx)\tilde{u}_3^{\mathrm{s}}(q, z).\end{aligned} \tag{2.3}$$

Solution satisfying the boundary condition $\boldsymbol{u}(x, 0) = 0$ and the equilibrium condition then reduces to:

$$\begin{bmatrix}\tilde{u}_1^{\mathrm{c}}(q, z)\\ \tilde{u}_3^{\mathrm{s}}(q, z)\end{bmatrix} = \begin{bmatrix}f_1(qz) & -f_2(qz)\\ f_2(qz) & f_3(qz)\end{bmatrix}\begin{bmatrix}A_1\\ A_2\end{bmatrix}, \tag{2.4}$$

with

$$\begin{aligned}f_1(qz) &= \sinh(qz) + \frac{1-s}{1+s}qz\cosh(qz);\\ f_2(qz) &= \frac{1-s}{1+s}qz\sinh(qz);\\ f_3(qz) &= \sinh(qz) - \frac{1-s}{1+s}qz\cosh(qz),\end{aligned} \tag{2.5}$$

where $s \equiv C_{44}/C_{11}$, and s ranges from 0 to 1 [45]. The pertinent coefficients $A_{1,2}$ are evaluated at $z = z_{\mathrm{m}}$. The pertinent coefficients $B_{1,2}$ for the in-plane sine transform of u_1 and the cosine transform of u_3 are determined similarly to Eqs. (2.3), (2.4) and (2.5). Moreover, the pertinent coefficients $A_{1,2}, B_{1,2}$ allow us to evaluate the displacement inside the linear-elastic body for a generic normal and tangential displacement at the surface $\boldsymbol{u}(x, z_{\mathrm{m}})$. In Fig. 2.2, we show the displacement fields inside a body with aspect ratio $a = 1/4$ using the analytical expression in [3] for $u_1(x, z_{\mathrm{m}}) = 0$ and $u_3(x, z_{\mathrm{m}}) = u_3^0 \sin\left(\dfrac{2\pi}{L_x}x\right)$ at the surface with $u_3^0/L_x = 5 \times 10^{-5}$.

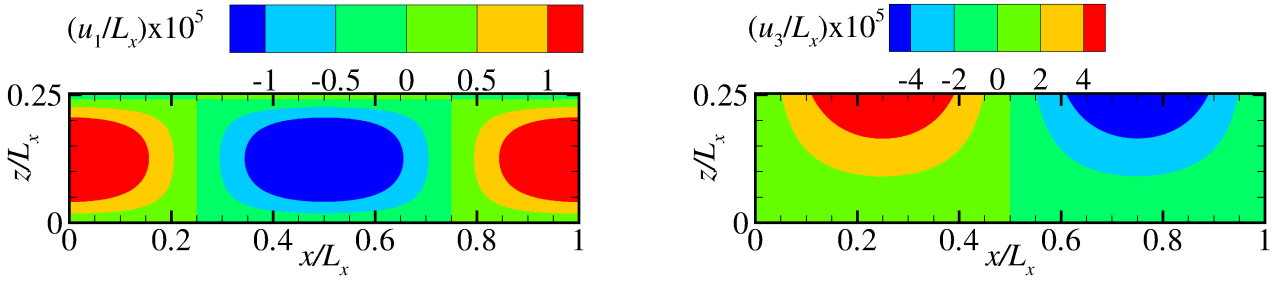

(a) (b)

Figure 2.2: Displacement fields of (a) the normalized displacement u_1/L_x in x-direction and (b) the normalized displacement u_3/L_x in z-direction.

2.3 Areal elastic energy of finite-height slab

Following [3], we write of the infinitesimal Cauchy's strain field $\boldsymbol{\epsilon}(x,z)$ as:

$$\begin{aligned}
\epsilon_1(x,z) &\equiv \partial_1 u_1^{\mathrm{c}}(x,z);\\
&= -q\sin(qx)\tilde{u}_1^{\mathrm{c}}(q,z);\\
\epsilon_3(x,z) &\equiv \partial_3 u_3^{\mathrm{s}}(x,z);\\
&= \sin(qx\partial_3\tilde{u}_3^{\mathrm{s}}(q,z);\\
\epsilon_5(x,z) &\equiv (\partial_3 u_1^{\mathrm{c}}(x,z) + \partial_1 u_3^{\mathrm{s}}(x,z));\\
&= \cos(qx)(qu_3^{\mathrm{s}}(q,z) + \partial_3 u_1^{\mathrm{c}}(q,z)).
\end{aligned} \tag{2.6}$$

This allows us also to determine the stress field $\boldsymbol{\sigma}(x,z)$ in the linear-elastic body using the well-known stress-strain relation, *i.e.*, $\sigma_{\alpha\beta} = C_{\alpha\beta\gamma\delta}\epsilon_{\gamma\delta}$. Following Venugopalan *et al.* [3], we can determine the work per unit area to deform the body with slab height z_{m}– assuming small-slope approximation, *i.e.*, $\tau_\alpha = \sigma_{\alpha\beta}n_\beta$, with the tangential component of the surface normal $n_\alpha = 0$ – as:

$$v_{\mathrm{el}} = \frac{1}{w}\int_0^w \mathrm{d}x \left[\int_0^{u_1(x,z_{\mathrm{m}})} \sigma_{13}(x,z_{\mathrm{m}})\mathrm{d}w_1(x,z_{\mathrm{m}}) + \int_0^{u_3(x,z_{\mathrm{m}})} \sigma_{33}(x,z_{\mathrm{m}})\mathrm{d}w_3(x,z_{\mathrm{m}})\right]. \tag{2.7}$$

For a given wavenumber q, the areal elastic energy $v_{\mathrm{el}}(q)$ is:

$$v_{\mathrm{el}}(q) = \frac{C_{44}}{2}\tilde{\epsilon}_5^{\mathrm{c}}(q,z_{\mathrm{m}})\tilde{u}_1^{\mathrm{c}}(q,z_{\mathrm{m}}) + \left\{\frac{C_{11}}{2}\tilde{\epsilon}_3^{\mathrm{s}}(q,z_{\mathrm{m}}) + \frac{C_{12}}{2}\tilde{\epsilon}_1^{\mathrm{s}}(q,z_{\mathrm{m}})\right\}\tilde{u}_3^{\mathrm{s}}(q,z_{\mathrm{m}}), \tag{2.8}$$

with

$$\begin{aligned}
\tilde{\epsilon}_1^{\mathrm{s}}(q,z_{\mathrm{m}}) &= -q\tilde{u}_1^{\mathrm{c}}(q,z_{\mathrm{m}});\\
\tilde{\epsilon}_3^{\mathrm{s}}(q,z_{\mathrm{m}}) &= \partial_3\tilde{u}_3^{\mathrm{s}}(q,z_{\mathrm{m}});\\
&= r\frac{\cosh^2(qz_{\mathrm{m}}) - r(qz_{\mathrm{m}})^2 - 1}{\parallel f(z_{\mathrm{m}})\parallel}q\tilde{u}_1^{\mathrm{c}}(q,z_{\mathrm{m}})\\
&\quad + (1-r)\frac{\cosh(qz_{\mathrm{m}})\sinh(qz_{\mathrm{m}}) + r(qz_{\mathrm{m}})}{\parallel f(z_{\mathrm{m}})\parallel}q\tilde{u}_3^{\mathrm{s}}(q,z_{\mathrm{m}});\\
\tilde{\epsilon}_5^{\mathrm{c}}(q,z_{\mathrm{m}}) &= qu_3^{\mathrm{s}}(q,z_{\mathrm{m}}) + \partial_3 u_1^{\mathrm{c}}(q,z_{\mathrm{m}});\\
&= (1+r)\frac{\cosh(qz_{\mathrm{m}})\sinh(qz_{\mathrm{m}}) - r(qz_{\mathrm{m}})}{\parallel f(z_{\mathrm{m}})\parallel}q\tilde{u}_1^{\mathrm{c}}(q,z_{\mathrm{m}})\\
&\quad + \frac{(1-r)\sinh^2(qz_{\mathrm{m}}) - 2r^2(qz_{\mathrm{m}})^2}{\parallel f(z_{\mathrm{m}})\parallel}q\tilde{u}_3^{\mathrm{s}}(q,z_{\mathrm{m}}),
\end{aligned} \tag{2.9}$$

where

$$r = \frac{1-s}{1+s}, \tag{2.10}$$

and

$$\begin{aligned}
\parallel f(z_{\mathrm{m}})\parallel &= f_1(z_{\mathrm{m}})f_3(z_{\mathrm{m}}) + f_2(z_{\mathrm{m}})^2;\\
&= \cosh^2(qz_{\mathrm{m}}) - (rqz_{\mathrm{m}})^2 - 1.
\end{aligned}$$

Following Venugopalan *et al.* [3], we rewrite the total areal elastic energy v_{el} as the sum over all wave numbers q:

$$v_{\mathrm{el}} = \sum_q \frac{C_{11} q}{2} \left[\tilde{u}_1^*(q), \tilde{u}_3^*(q)\right] \begin{bmatrix} M_{11}(q) & -\mathrm{i}M_{13}(q) \\ \mathrm{i}M_{13}(q) & M_{33}(q) \end{bmatrix} \begin{bmatrix} \tilde{u}_1(q) \\ \tilde{u}_3(q) \end{bmatrix}, \tag{2.11}$$

with

$$\begin{aligned} M_{11}(q) &= (1-r)\frac{\cosh(qz_{\mathrm{m}})\sinh(qz_{\mathrm{m}}) - r(qz_{\mathrm{m}})C_{11}}{\parallel f(z_{\mathrm{m}}) \parallel}; \\ M_{13}(q) &= \left(\frac{1-r}{1+r}\right)\frac{(1-r)\sinh^2(qz_{\mathrm{m}}) + 2r^2(qz_{\mathrm{m}})^2 C_{11}}{\parallel f(z_{\mathrm{m}}) \parallel}; \\ M_{33}(q) &= (1-r)\frac{\cosh(qz_{\mathrm{m}})\sinh(qz_{\mathrm{m}}) + r(qz_{\mathrm{m}})C_{11}}{\parallel f(z_{\mathrm{m}}) \parallel}. \end{aligned} \tag{2.12}$$

Note that from the total elastic energy density v_{el}, we can determine the Fourier transform of the elastic restoring force $\boldsymbol{F}_{\mathrm{el}}(q)$ at the surface as a function of the Fourier transform of a generic displacement at the surface $\tilde{\boldsymbol{u}}(q)$, and vice versa. The elastic restoring force $\tilde{\boldsymbol{F}}_{\mathrm{el}}(q)$ is determined as:

$$\frac{\tilde{\boldsymbol{F}}_{\mathrm{el}}(q)}{A_0} = \tilde{\boldsymbol{G}}^{-1}(q)\,\tilde{\boldsymbol{u}}(q) = \nabla_{\tilde{\boldsymbol{u}}} v_{\mathrm{el}}, \tag{2.13}$$

where A_0 is the total surface area, $\tilde{\boldsymbol{G}}^{-1}(q)$ the inverse Green's function, determined by the evaluation of the areal elastic energy density v_{el} in Eq. (2.11). Moreover, the inverse Green's function is the linear spring constant in Fourier space in the damped dynamic energy minimization that is explained in the following section.

2.4 Damped dynamic energy minimization

In static equilibrium, the equilibrium condition can be written as:

$$\tilde{\boldsymbol{F}}_{\mathrm{el}}(q) + \tilde{\boldsymbol{F}}_{\mathrm{ext}}(q) + \tilde{\boldsymbol{F}}_{\mathrm{if}}(q) = 0, \tag{2.14}$$

where $\tilde{\boldsymbol{F}}_{\mathrm{ext}}(q)$ the external force and $\tilde{\boldsymbol{F}}_{\mathrm{if}}(q)$ the interfacial force. When tractions are prescribed on a section of the surface, equilibrium is reached when the elastic restoring force $\tilde{\boldsymbol{F}}_{\mathrm{el}}(q)$ and the external force $\tilde{\boldsymbol{F}}_{\mathrm{ext}}(q)$ are balanced with $\tilde{\boldsymbol{F}}_{\mathrm{if}}(q) = 0$. If displacement is prescribed on a section of the surface, equilibrium is reached when the elastic restoring force $\tilde{\boldsymbol{F}}_{\mathrm{el}}(q)$ and the interfacial force $\tilde{\boldsymbol{F}}_{\mathrm{if}}(q)$ are balanced $\tilde{\boldsymbol{F}}_{\mathrm{ext}}(q) = 0$. At a given dimensionless time t, before equilibrium is attained, the equation of motion at the interface can be written as:

$$\tilde{\boldsymbol{F}}_{\mathrm{el}}(q,t) + \tilde{\boldsymbol{F}}_{\mathrm{ext}}(q,t) + \tilde{\boldsymbol{F}}_{\mathrm{if}}(q,t) + \boldsymbol{c}\frac{\mathrm{d}\tilde{\boldsymbol{u}}(q,t)}{\mathrm{d}t} = m\frac{\mathrm{d}^2\tilde{\boldsymbol{u}}(q,t)}{\mathrm{d}t^2}, \tag{2.15}$$

where $\boldsymbol{c} = (c_1, c_3)$ is the positive real valued directionally dependent linear damping coefficient and m is the real valued mass. The mass m is taken to be unity. The equation of motion of a damped mode in Fourier space is solved numerically by the position (Störmer-)Verlet (pSV) method [16] over dimensionless time-step Δt. Note that in this work, the force at the interface $\tilde{\boldsymbol{F}}_{\mathrm{if}}(q)$ is not explicitly known, but only implicitly through the interfacial boundary condition (b.c.). A hard-wall interaction b.c. is employed at the end of each iteration to ensure there is no inter penetration at the surface, *i.e.*,

$$z_{\mathrm{punch}}(x) \geq z_{\text{grid-point}}(x), \tag{2.16}$$

where z_{punch} and $z_{\text{grid-point}}$ are the z-coordinates of the punch surface and substrate respectively. Figure 2.3 is the schematic representation of the hard-wall interaction b.c. for an indentation with a flat rigid punch.

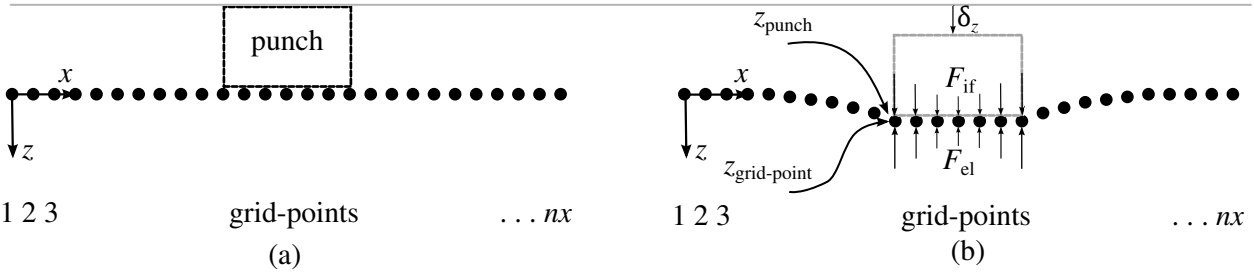

Figure 2.3: Schematic representation of a mixed boundary-value problem in GFMD simulations: A flat rigid punch indentation. Step (a) is the initial configuration, and step (b) shows the constant displacement δ_{z} of the rigid punch at time $t > 0$.

At the end of the each iteration, the grid-points that violate the hard-wall interaction b.c. are displaced back to the z-location of the surface of the rigid punch, *i.e.* $z_{\mathrm{punch}}(x)$. Note that the GFMD method is not limited to hard-wall interaction, but we use the hard-wall b.c. for its convenience and its possibility to non-arbitrarily determine the contact area fraction a_{r}. In this work, the contact area fraction a_{r} is determined as the number of grid-points violating the hard-wall b.c. over the final dimensionless time-step Δt as a fraction of the total number of grid-points nx.

2.5 Advantages and limitations

With the GFMD approach, we are able to numerically calculate the linear-elastic response of a solid to an external load by modeling only the surface. This allows us to study more complicated surface geometries by adding more degrees of freedom at the surface. For example, if one wants to study self-affine rough surfaces that has roughness spanning length scales 100 μm to 50 nm, the number of grid-points $nx \geq 2^{14}$. The computational gain offered by GFMD is appreciable in such cases. Although, in this work, we only consider plane strain cases, the GFMD method can be extended to plane stress cases [46] and also a (2+1)-dimensional substrate.
According to Venugopalan *et al.* [3], the GFMD method provides the relevant information to determine the relative contact area a_{r}, but with a signification gain in simulation time. Moreover, GFMD method employs an interfacial potential between contacting bodies that the user can chose at will. GFMD is also suitable for mixed BVP, therefore applicable to contact mechanical problems where the contact area is not known *a priori*. It is known that FEM typically needs several iterations and updating of the b.c. in order to converge to a final contact area [47]. Moreover, according to Venugopalan *et al.* [47], GFMD is very suitable to be built as a multi-scale model following the work of Pastewka *et al.* [48]. In such a multi-scale model [48], we give the surface an atomistic description, and the linear-elastic substrate we treat with the GFMD approach.
In GFMD simulations, we consider linear-elastic material and loading conditions satisfying the infinitesimal strain theory. Therefore, for large nominal pressure $\bar{p}$ between contacting metallic bodies, both these assumptions break down. However Venugopalan *et al.* [47] has made a first step relaxed this assumption by including plasticity.
Note that the areal elastic energy v_{el} is calculated assuming a small surface slope $g(x)$. In the regions of contact between nominally flat surfaces at low nominal pressure $\bar{p}$, we have observed that the local gradient $g(x)$ is of such magnitude that it already violates the small-slop approximation. Therefore, future work should focus on relaxing the small-slope assumption.

Appendix 2.A Pseudo-code

a. Setup rigid punch with surface topography $h(x)$;

b. Determine damping factor vector $\boldsymbol{\eta}_{\mathrm{cr}}$ such that all modes are critically and/or under-damped, and calculate the dimensionless equilibrium time t_{equil};

c. Give the rigid punch initial displacement in normal direction, *i.e.*, $z_{\mathrm{punch}} = h(x) - \delta_{\mathrm{z}}$, where δ_{z} is the finite indentation depth;

d. Loop over dimensionless time-step Δt till the equilibrium time t_{equil} is reached.

   – Discrete fast Fourier transform (DFFT) surface displacement $\boldsymbol{u}(x)$ using the FFTW3 library [49].

   – Calculate elastic restoring force, $\tilde{\boldsymbol{F}}_{\mathrm{el}}(q) = \tilde{\boldsymbol{G}}^{-1}(q)\,\tilde{\boldsymbol{u}}(q)$;

   – Add external force, $\tilde{\boldsymbol{F}}(q) \leftarrow \tilde{\boldsymbol{F}}(q) + \tilde{\boldsymbol{F}}_{\mathrm{ext}}(q)$

   – Add damping forces, $\tilde{\boldsymbol{F}}_{\mathrm{d}}(q) \leftarrow \tilde{\boldsymbol{F}}(q) + \boldsymbol{\eta}\{\tilde{u}_{\mathrm{old}}(q) - \tilde{u}_{\mathrm{new}}(q)\}$

   – Use pSV to solve equation of motion, $\tilde{\boldsymbol{u}}_{\mathrm{new}}(q) = 2\tilde{\boldsymbol{u}}_{\mathrm{now}}(q) - \tilde{\boldsymbol{u}}_{\mathrm{old}}(q) + \tilde{\boldsymbol{F}}_{\mathrm{d}}(q)\Delta t^2$

   – Reverse DFFT displacement $\tilde{\boldsymbol{u}}_{\mathrm{new}}(x)$ into real space;

   – Implement the hard-wall b.c., $\tilde{u}_{\mathrm{new}}(x) \leftarrow \min\{\tilde{u}_{\mathrm{new}}(x), h(x) - \delta_{\mathrm{z}}\}$;

   – Assign $\tilde{\boldsymbol{u}}_{\mathrm{old}}(x) \leftarrow \tilde{\boldsymbol{u}}_{\mathrm{now}}(x)$ & $\tilde{\boldsymbol{u}}_{\mathrm{now}}(x) \leftarrow \tilde{\boldsymbol{u}}_{\mathrm{new}}(x)$.

Chapter 3

Rough surfaces: Numerical methods to generate fractal roughness

"*These must be splendid clothes indeed!" thought the Emperor.*"

Hans Christian Andersen, The Emperor's new clothes

3.1 Introduction

Surface roughness is the local deviation of a surface from a perfectly flat plane, and is also known as surface texture or surface finish. To obtain properties of rough surfaces, different experimental techniques are used [50]. These techniques yield surface statistics, which are instrumental to classifying real rough surfaces and modeling artificial surface topographies. A wide variety of surfaces are experimentally found to have fractal roughness [1, 2, 24], either mounded or self-affine roughness depending on surface processing [51]. The surface roughness is self-affine if it looks statistically the same under dilatation with different factors in different directions. This dilatation factor is called the Hurst's exponent H. The mounded surface has a dominant wavelength λ, larger than the scale where it is self-affine. To date, most in-depth brute-force simulations [40, 33, 4, 5] and statistical theories [12, 25, 22, 13] have focused on self-affine surface roughness. Brute-force simulations approximate mounded surfaces as nominally flat at length scales larger than the correlation length ξ, regardless of the characteristic wavelength λ. This approximation reduces the size of the computational repetitive cell by decades, but is correct only for certain mounded surfaces. Here, we define for which parameters λ, ξ the assumed size of repetitive cell for any mounded surface breaks down. In this way we are now also capable of correctly determining the minimum surface discretization prior to the simulation.

Statistical models of surface roughness are widely used in tribology [10, 11, 12]. Most models are based upon the assumption that a Gaussian surface height distributions best mimics experimentally measured surface roughness as a random process [52, 53, 25, 54]. Despite, Borodich *et al.* [54] disputed the assumption of a Gaussian height distribution for nano-scale surfaces, Yastrebov *et al.* [32] showed that the averaged mechanical response of non-Gaussian surfaces is not equivalent to the mechanical response of the averaged surface, whose distribution is Gaussian. In this work, we adhere to the common Gaussian assumption.

At present, the four most commonly used methods for numerically generating self-affine surface topographies for brute-force methods are: The random midpoint displacement method (RMD) [42]; The successive random addition method (SRA) [42]; The Fourier filtering method (FFM); And the power spectral density method (PSDM) [43]. RMD and SRA originally generated topographies with a non-Gaussian height distribution, and show spectral remnants for $H \neq 0.5$. However, it is well known that RMD and SRA are the most suitable methods to produce a topography with specific statistics at a given position on the surface, and both easily incorporate, alter or remove small wavelengths for a given topography. These two methods are very suitable for slid island analysis [43]. It is known that PSDM and FFM lack the spectral remnants shown by RMD and SRA, and PSDM even allows for the scaling of individual Fourier coefficients of the power spectral density function (PDSF) of the surface.

In this chapter, we select out of these four the method most suitable to numerically generate surface topographies for Green's function molecular dynamics (GFMD) simulations [5, 3]. To this end, RMD and SRA are extended to generate periodic surfaces with Gaussian height distribution. It is necessary to extend RMD and SRA to generate periodic surfaces, because the surface statistics must be stationary over the periodic boundary of the GFMD method. The extended RMD and SRA can then be compared with PSDM and FFM. In this work we determine the proportionality coefficient κ. Therefore, the numerical method that generates the surface topography with statistics as close as possible to the required surface statistics is selected. PSDM is selected as the most suitable method for future research. Finally, a real rough surface topography and the surface topography numerically generated by PSDM are compared.

The remainder of this chapter is organized as follows: We summarize relevant statistical surface properties used throughout this work in Sec. 3.2. Then, in Sec. 3.3, we summarize four rough-

ness measurement techniques and put forth the current and past discussions on rough surface topographies of metals. Subsequently, we give the analytical models of fractals as basis for numerical methods, and we define the parameters λ, ξ for which the assumed size of repetitive cell for mounded surfaces breaks down in Sec. 3.4. RMD and SRA are extended to numerically generate Gaussian height distributions, all four aforementioned method are discussed and the most suitable numerical method for this work is chosen in Sec. 3.5. Then, we compare a surface topography generated by PSDM to experimental results in Sec. 3.6. This work ends with the conclusion and the discussion in Sec. 3.7. In the appendix, we give the derivation of the discrete Fourier transform of a purely real Gaussian signal. Then, we give the pseudo-code of PSDM. Subsequently, we derive the analytical expression of the height distribution for discrete convolution of a Gaussian with the self-affine auto-correlation function. Finally, we attempt to give a ratio between repetitive cell size L_x and correlation length ξ as a function of the Hurst's exponent H for which the numerically generated surface topography has the Gaussian height distribution.

3.2 Mathematical description of surface roughness

Roughness can be described by a single-valued function $h(\boldsymbol{r})$, where $h(\boldsymbol{r})$ is the height of the surface above position vector $\boldsymbol{r}$ on the d-dimensional reference plane. Dong *et al.* [55] give a comprehensive overview of choice of reference plane for surface roughness measurements. Figure 3.1 is a schematic representation of an height profile $h(r)$, with its height distribution function $p(h)$. The height distribution function $p(h)$ is the probability of a surface height to fall between h and $h + \mathrm{d}h$. The distribution $p(h)$ is a real, positive and normalized function of h. The height distribution function provides a complete specification of the random variable $h(\boldsymbol{r})$ at position $\boldsymbol{r}$.

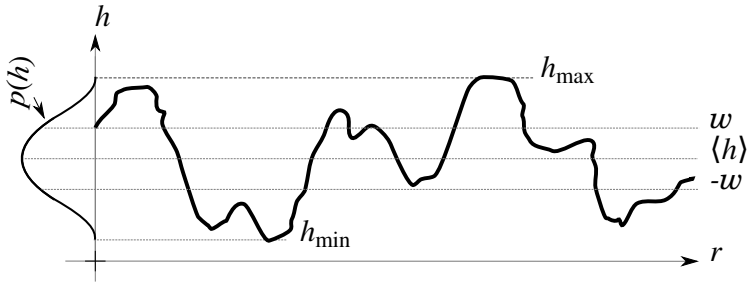

Figure 3.1: Schematic representation of the height profile $h(r)$, with the associated height distribution function $p(h)$, maximum height, $h_{\max}$, minimum height, $h_{\min}$ and root mean square height w.

Rough surfaces can be classified in three ways, according to their statistical properties, their continuity properties and rational symmetries. The associated parameters can be divided in three categories, namely amplitude, spacing and hybrid parameters.
Amplitude parameters quantify the vertical characteristics of a surface, like the average height $\langle h(\boldsymbol{r})\rangle$ and root mean square height (RMSH) $w = \sqrt{\langle h(\boldsymbol{r})^2\rangle}$. Spacing parameters quantify the distribution of horizontal or lateral features of a surface, like the smallest wavelength λ_{s} and the largest wavelength λ_{l}. Hybrid parameters are a combination of amplitude and spacing features of a surface, as the root mean square gradient (RMSG) $\bar{g} = \sqrt{\langle (\nabla h(\boldsymbol{r}))^2\rangle}$, and Hurst's exponent H.
When we consider statistical properties, surface roughness is divided into two categories: Deterministic rough surfaces and random rough surfaces. A deterministic surface is defined by a deterministic

function of the surface height profile. The form of this function defines all properties of the surface roughness. From a statistical point of view, surface heights between two points on a deterministic surface are fully correlated.
The surface height of a random surface profile cannot be expressed as a deterministic function of the position on the surface, but through a random field (random process for $d = 1$) [50]. In this work, we focuses on random rough surfaces, because random surfaces give the most realistic representation of experimentally measured rough surfaces without any prior assumptions on the individual asperity shape.
For the complete description of a random field one needs to know the n-dimensional joint distribution function $p_n(h_1, h_2, ..., h_n; \boldsymbol{r}_1, \boldsymbol{r}_1, ..., \boldsymbol{r}_n)$, where $\boldsymbol{r}_1, \boldsymbol{r}_2, ..., \boldsymbol{r}_n$ are a set of different positions on the surface and $h_1, h_2, ..., h_n$ are the corresponding random variables.
A random field is called homogeneous (*i.e.*, stationary in an one-dimensional random process) if all the probability distribution functions are defined by the relative location and not the absolute location in parameter space. A random field is ergodic if all of the information about its joint distribution is derivable from a single realization of the random field.
This work is on random surfaces described by homogeneous, isotropic and ergodic fields. In many brute-force methods [33, 40, 4, 5], higher-order correlation functions are omitted because statistical continuum models omit higher-order correlation [10, 11, 12] correctly predict experimental observations. Therefore, the surface roughness is determined by the first-order and second-order statistics of a random field, because higher-order correlation functions are commonly not considered relevant for contact mechanics [4]. We agree with this notion, and we also limit the description of surface roughness to the first- and second-order statistics of the random field.
The first-order statistics described in this section are the surface height distribution function, RMSH and the characteristic function. The most used height distribution is the Gaussian height distribution:

$$p_{\mathrm{G}}(h) = \frac{1}{\sqrt{2\pi}w} e^{\left(-\frac{h^2}{2w^2}\right)}. \tag{3.1}$$

The n^{th} moment of a variable h is defined as $m_n = \langle h^n \rangle$. The second moment of h, describes the surface roughness, represented by w^2. The skewness of the surface m_3/w^3 is a measure of the symmetry of a distribution about the means surface level. Kurtosis of the surface m_4/w^4 is a measure of the sharpness of the height distribution function. A Gaussian height distribution has the kurtosis $\gamma_4 = 3$. The characteristic function $\phi(q)$ is the Fourier transform of the height distribution function. Here q is the wave number.
First-order statistics only describe the statistical properties of random variables of the random field at individual positions. In order to differentiate the spatial difference of the surface topography, one needs to know the correlation of a random field $h(\boldsymbol{r})$ at two different positions $\boldsymbol{r}_1$ and $\boldsymbol{r}_2$. The three second-order statistical properties discussed and used in this section are:

a. The auto-correlation function (ACF) $R(\boldsymbol{\rho})$, with the correlation length ξ and the translation vector $\boldsymbol{\rho}$, see Fig. 3.2a;

b. The height-height correlation function (HHCF) $H(\boldsymbol{\rho}) = \langle (h(\boldsymbol{r}) - h(\boldsymbol{r} + \boldsymbol{\rho}))^2 \rangle$, as shown in Fig. 3.2b;

c. The power spectral height function (PSHF), $C_{\mathrm{h}}(\boldsymbol{q}) = \langle |\tilde{h}(\boldsymbol{q})|^2 \rangle$, where $\tilde{h}(\boldsymbol{q})$ is the Fourier transform of $h(\boldsymbol{r})$ and $\boldsymbol{q}$ is the wave vector. The PSHF is the expectancy of the power spectral density function (PSDF) $C(\boldsymbol{q}) = |\tilde{h}(\boldsymbol{q})|^2$, see Fig. 3.2c.

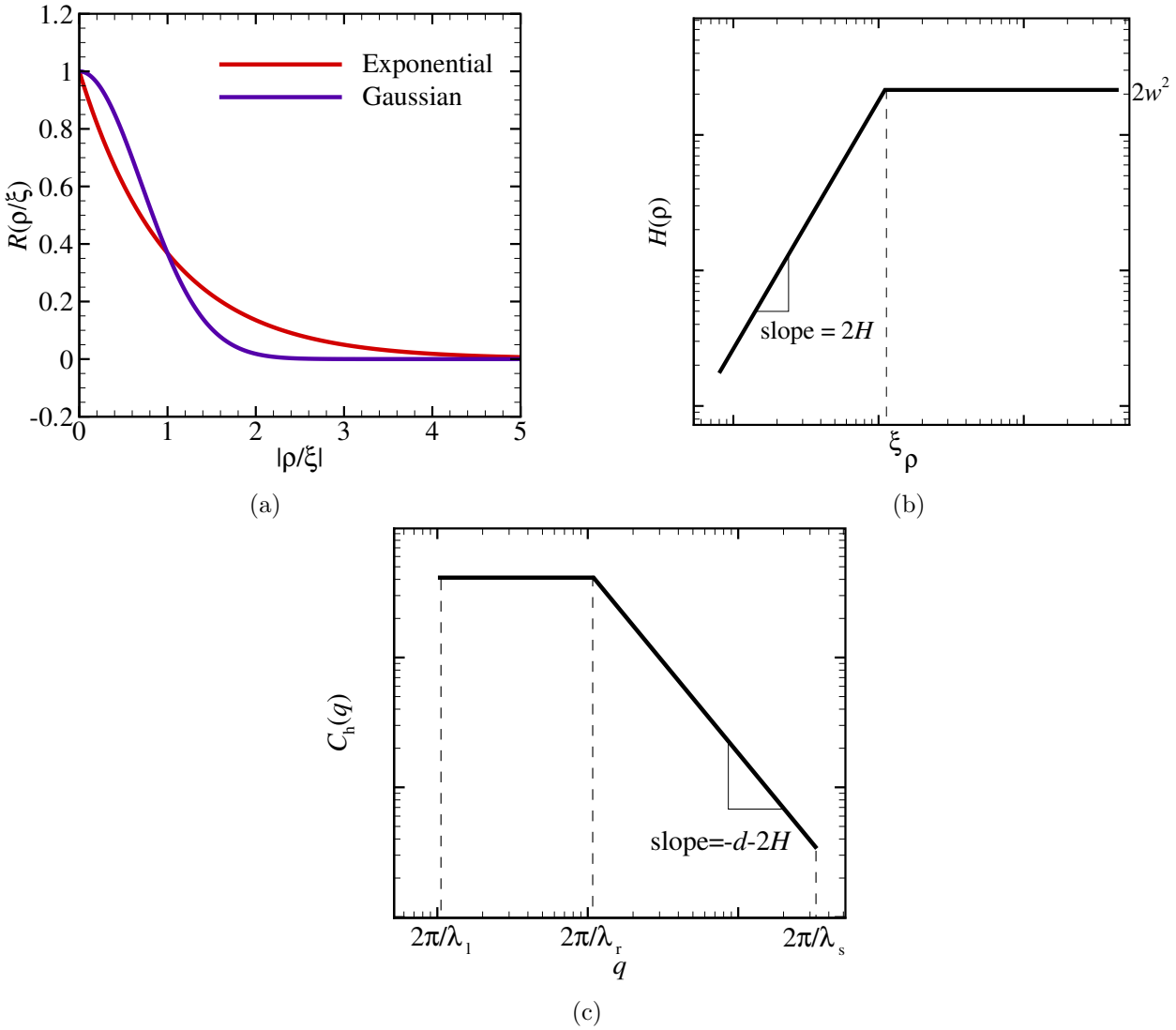

Figure 3.2: Three second-order statistics of a self-affine surface topography, on a d-dimensional reference plane: (a) Plot of the exponential and Gaussian auto-correlation functions $R(\rho/\xi)$ as a function of the absolute normalized translation scalar $|\rho/\xi|$; (b) Log-log plot of the height-height correlation function $H(\rho)$ of a self-affine surface as a function of the translation scalar ρ, with correlation length ξ and RMSH w; (c) Log-log plot of the power spectra height function $C_h(q)$ as a function of the wave number q, largest wavelength λ_l, cut-off wavelength λ_r and smallest wavelength λ_s.

The two parameters w and ξ are not enough to give a full description of the ACF. An additional parameter is needed, the Hurst exponent H. A surface with exponential ACF corresponds to $H = \frac{1}{2}$, with Gaussian ACF to $H = 1$ and white noise to $H = 0$.

Rough surfaces are classified by their continuity properties depending on the resolution (*i.e.*, smallest wavelength λ_s). If the smallest wavelength is much larger than the atomic distance a, the surface is described as continuous. If this condition is not met, the surface is described as a discrete surface. In this work we consider only continuum descriptions of the surface roughness.
A rough surface is classified by its rational symmetry: if the surface fluctuation is independent of direction on the reference plane, the surface is isotropic; otherwise, anisotropic. Thus, a rough surface classified as anisotropic has second-order statistics depending both on relative location on and their direction in the d-dimensional reference plane [50]. In this work, we report on both rational symmetries.
With this knowledge of the mathematical descriptions of surface roughness, we discuss here the experimental roughness measuring methods and experimentally observed surface roughness.

3.3 Characterization of rough surface topographies

The smallest observable wavelengths of the fractal roughness are dominant in determining the measured root mean square gradient (RMSG) $\bar{g}$ [5]. The RMSG has a major effect on contact mechanics (see chapter 1). The commonly reported cut-on wavelength $\lambda_{s,H} \approx 50$ nm, because this value corresponds to the minimum lateral resolution of AFM [50]. Lower cut-on lengths have been reported for scanning tunneling microscopy (STM) measurements [50], but in smaller number of publications than AFM experiments. STM has a large error for metallic surfaces due to their large root mean square height w (RMSH) [50]. The effect of processing techniques on small length scales is disputed [2, 24]. This value of $\lambda_{s,H} \approx 50$ is often reported as the smallest wavelength of the fractal region regardless of material and/or processing technique [24, 2, 50]. The measurement range of AFM makes it attractive to measure surface statistics, while other experimental techniques have a lower resolution. The prevalent use of AFM, with its relative larger resolution, to measure surface statistics is one of the reasons no consensus has been reached on the value of cut-on wavelength $\lambda_{s,H}$.
Two experimental techniques are used to measure real surface topographies: Real-space scanning techniques; And, scattering techniques (ST). Real-space techniques are used in static experiments and are capable of direct real space imaging. Scattering techniques, which measure statistical surface properties in reciprocal space, are most suitable for dynamic experiments, but their results need interpretation in real-space.
Stylus profilometry (SP), scanning tunneling microscopy (STM) and AFM are real-space scanning techniques. SP scans the surface topography by measuring the vertical movement of a stylus laterally moving, in contact, across the surface of a sample. STM scans the surface topography by measuring the tunneling current between probe and surface and is suitable only for metals and semi-conductors. AFM scans the surface topology by measuring different kinds of intermolecular forces. Table 3.1 gives an overview of the measurement range and resolution of the afore-mentioned real-space scanning techniques.

	Measurement range		Resolution	
Technique	Lateral	Vertical	Lateral	Vertical
SP	300 mm	6 mm	0.05 - 0.15 μm	>0.05 nm
STM	500 μm	2 μm	0.1 nm	0.2 nm
AFM	500 μm	2 μm	5 nm	$\leq$ 0.1 nm

Table 3.1: Maximum lateral and vertical measurement range and lateral and vertical resolution [50].

Scattering techniques, X-ray diffraction and white light interferometry, show lateral resolutions of 40 nm [56], but have a measurement range decades smaller than AFM and STM. Also spectral artifact at discontinuities are more severe in scattering techniques than in real-space techniques. Figure 3.3 depicts the measurement ranges of SP, STM, AFM and ST on the schematic representation of the PSHF of a self-affine random rough surface.

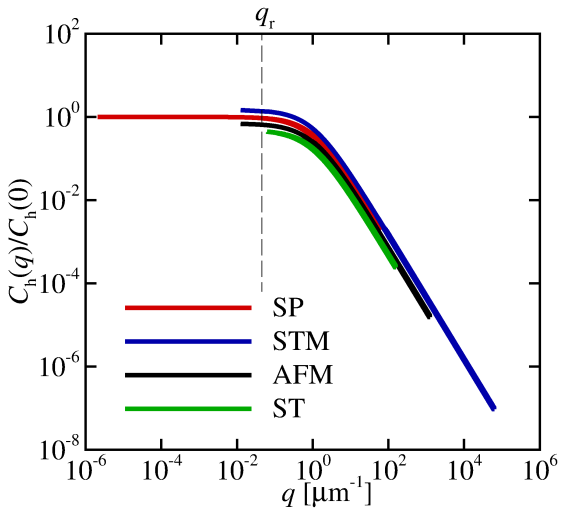

Figure 3.3: Comparison of the lateral measurement ranges of SP, AFM, STM and ST through the schematic representation of the PSHF of a self-affine random rough surface with $H = \frac{1}{2}$ and $\lambda_r = 100$ μm [50, 56].

STM seems to be the most suitable method to measure surface topographies up to the nm scale. Although its resolution goes up to the atomic scale and its vertical measurement range is equal to AFM, the error for large RMSH makes it unsuitable for most real rough surfaces [50]. AFM is the most suitable and versatile method at present and limits the lateral resolution to between 5 and 50 nm.

According to Plouraboué *et al.* [2] also the processing technique influences the small scale roughness, and the measured surface slopes remain small in all directions, but increase with a decrease in lateral and vertical measurement resolution. This trend suggests a continuation of self-affine region below the minimum measurement resolution. For cold rolled aluminum the typical slope was $0.03 \leq \sigma(\theta) \leq 0.28$ in longitudinal direction and $0.09 \leq \sigma(\theta) \leq 0.64$ in transverse direction. Self-affinity ranges from $\mathcal{O}^0$ nm to $\mathcal{O}^1$ μm for highly polished surface and even further for regular surfaces, as stated by Persson *et al.* [25] and B. Bhushan [28]. The cut-on wavelength for self-affinity, suggested by Pelliccione [51], is the wavelength corresponding to the inter-atomic distance a. This is disputed though, because measurement with AFM and STM have only displayed self-affinity up to the order of $\mathcal{O}^1$ nanometer [50]. In this work, we chose the cut-on wavelengths $\lambda_{s,H}$ to be between 5 and 50 nm corresponding to AFM measurements.

3.3.1 Rough surface topographies of metals

FCC metals have Hurst's exponents ranging between 0.3 and 1, which depends on the processing technique and material's properties [1, 24, 2]. At small length scales, metals exhibit self-affine isotropic roughness, which is associated to the material property independent of the processing technique. At large length scale, self-affinity breaks down and/or has an anisotropic rational symmetry. Whether a surface topography has a characteristic length scale depends on the processing technique and changes over processing time [51]. Further more, experimental surface topographies of FCC metal show a cut-off wavelength of the self-affine region, which depends on the surface processing technique. We agree with the notion that the cut-off wavelength solely depends on the processing conditions. According to Plouraboué *et al.* [2], roughness transfer takes place over all length scales, *i.e.*, micro to nano scale, for cold-rolling of aluminum.
However, note that fractal surfaces are extensively studied, dating back to a pioneering work by Mandelbrot *et al.* [1]. According to Mandelbrot *et al.* [1] the value of Hurst's exponents H of metallic surfaces ranged form 0.7 to 0.85. Moreover, an extensive body of experimental work, that followed Mandelbrot *et al.* [1], showed Hurst's exponents $H \approx 0.8$ for fractured metals. From these observations one could conclude that there is one universal Hurst's exponent $H \approx 0.8$ for any given metallic rough surface. However, recently, small scale analysis using STM and AFM showed departure from $H \approx 0.8$ [51, 57, 58]. At small scale, an exponent of $H \approx 0.5$ with correlating lengths up to 1 μm for TiAl alloys [50] were measured. Therefore, in this work, we chose to vary the value of the Hurst's exponent H.
Note that it was commonly assumed that the PSHF of machined metals follow a typical pattern. For example, at small wavelengths stainless steel surface processing does not affect the surface structure. At such scales the PSHF of all surfaces coincide, determining a unique fractal dimension of $D_f = 1.5$, as shown by Majumdar *et al.* [24]. The influence of surface processing is felt only for roughness features of wavelength larger than a certain cut-off wavelength λ_{r} [24]. In this large wavelength region, each processing technique produces a different type of spectral profile. The common self-affine roughness at small scales is a material property [24]. However, more recent, Plouraboué *et al.* [2] showed with AFM that cold rolled aluminum alloy (Al 5182) has self-affinity up to the order of 50 nm. The cold rolled specimens have high anisotropy of scaling with $H \approx 0.9$ in transverse direction and $0.3 \leq H \leq 0.7$ in longitudinal direction. The cut-off wavelength can be of the order of 100 μm. The RMSH ranged from 0.3 μm to 2.5 μm. Roughness transfer, due to rolling, can take place from the macroscopic to the nano scale. Nonetheless, all experimentally studied surfaces display, at a small scale, a common self-affine isotropic roughness. Fig. 3.4 is an AFM image of cold rolled aluminum, by Plouraboué *et al.* [2].

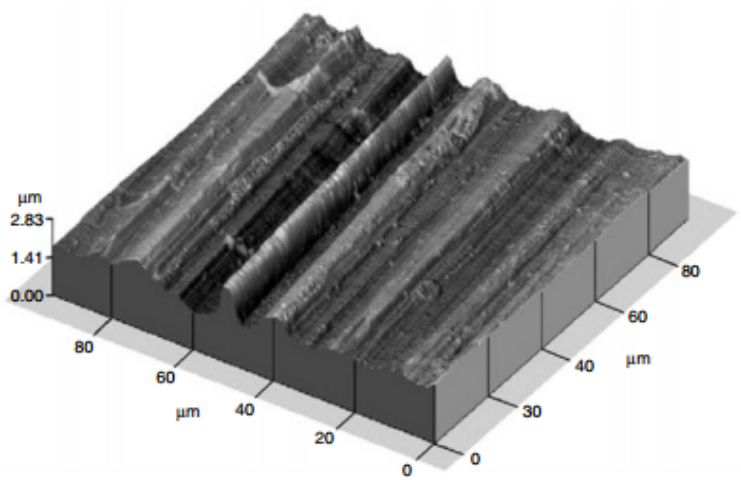

Figure 3.4: A 512×512 points AFM image of cold-rolled aluminum alloy sheet, showing non-isotropic self-affine scaling over three orders of magnitude from 50 nm to 50 μm [2].

Note that the surface roughness depends on the processing conditions, although to what small length scales the influence of the processing conditions extends is still controversial. We conclude that, in this work, we need to numerically generate fractal surfaces with generic Hurst's exponents H, roll-off λ_{r} and roll-on wavelengths $\lambda_{\mathrm{s},H}$. We chose the Hurst's exponent $0.3 \leq H \leq 0.8$. Moreover, we chose the higher limit $H = 0.8$, because for larger values of H the ratio $L_x/\xi \approx 400$, *i.e.* $nx \geq 2^{18}$, where nx is the number of grid-points in GFMD. In order to numerically generate these surface topographies, we here present mathematical description of fractal surfaces.

3.4 Mathematical description of fractal surface roughness

In this work, we present the mathematical descriptions of fractal surfaces for two reasons. First, in this section, we use them to determine the maximum ratio ξ/λ for which the mounded structure can be modeled as self-affine. Secondly, the HHCF and the PSHF are the inputs to the reciprocal space methods presented in Sec. 3.5.

3.4.1 Self-affine surfaces

Self-affine surfaces can be described by the function:

$$h(r_1, r_2) = \epsilon_1^{-H_1} \epsilon_2^{-H_2} h(\epsilon_1 r_1, \epsilon_2 r_2), \tag{3.2}$$

where h is the single-valued height, ϵ is the dilatation factor and r_1 and r_2 are the positions on the reference plane. Real rough surfaces only exhibit self-affine behavior over a certain range of length scales. They display a cut-off wavelength λ_r (also called roll-off wavelength), corresponding to the correlation length ξ, above which length scale the surface topography is no longer self-affine, *i.e.*, commonly referred to as the asymptotic behavior of fractal roughness. In this work we consider the continuous description of surface roughness. To this end, the smallest length scale l_s is much smaller than the correlation length ξ and the surface is treated as if $l_\mathrm{s} \to 0$. Then the HHCF for an isotropic self-affine surface is:

$$H(\boldsymbol{\rho}) = 2w^2 f\,(\tfrac{\boldsymbol{\rho}}{\xi}), \tag{3.3}$$

where $f\left(\frac{\boldsymbol{\rho}}{\boldsymbol{\xi}}\right)$ is a scaling function [50] (see Fig. 3.2b), with the following properties:

$$f\left(\frac{\boldsymbol{\rho}}{\xi}\right) = \begin{cases} \left(\frac{\boldsymbol{\rho}}{\xi}\right)^{2H}, & \text{for } \left(\frac{\boldsymbol{\rho}}{\xi}\right) << 1; \\ 1, & \text{for } \left(\frac{\boldsymbol{\rho}}{\xi}\right) >> 1. \end{cases} \tag{3.4}$$

The asymptotic behavior of the HHCF can be expressed as:

$$H(\boldsymbol{\rho}) = \begin{cases} (m\boldsymbol{\rho})^{2H}, & \text{for } \boldsymbol{\rho} << \xi; \\ 2w^2, & \text{for } \boldsymbol{\rho} >> \xi, \end{cases} \tag{3.5}$$

with,

$$m = \frac{w^{1/H}}{\xi}, \tag{3.6}$$

where m is the local slope. The Hurst's exponent is directly related to the local surface fractal dimension D_f by $H = d + 1 - D_\mathrm{f}$. The fractal dimension D_f is an index for characterizing fractal patterns or sets by quantifying their complexity as a ratio of the change in detail to the change in scale [1]. Within the lateral correlation length ξ the surface heights of any two points are correlated. Following [51], the asymptotic behavior of the PSHF can be expressed as :

$$C_\mathrm{h}(\boldsymbol{q}) = w^2 \xi^d g\,(\boldsymbol{q}\xi)\,, \tag{3.7}$$

where $g(\boldsymbol{q}\xi)$ is a scaling function, with the following properties:

$$g\,(\boldsymbol{q}\xi) \propto \begin{cases} 1, & \text{for } \boldsymbol{q}\xi << 1; \\ (\boldsymbol{q}\xi)^{-2H-d}, & \text{for } \boldsymbol{q}\xi >> 1. \end{cases} \tag{3.8}$$

Eqs. (3.5) and (3.8) only give the asymptotic behavior of the characteristic functions, the exact forms of these characteristic functions may vary.
Functional forms of the HHCF try to capture the stochastic process associated with isotropic self-affine surface topographies and its asymptotic form (*i.e.*, Eq. (3.5)). Any model that satisfies the asymptotic form of the HHCF may be considered a model of self-affine surface topography [59, 60]. The rough surface topographies measured in experiments are also fitted with these models to determine the fractal properties of the surface roughness [50]. Two models, discussed in this work, are called the exponential correlation model (ECM) [61] and the K-correlation model (KCM) [62], also known as fractal characterization models. Fractal characterization models are models that provide the capability to model surface that are not purely self-affine – they do not continue at the same log-log slope across all wavelengths (see Fig. 3.2c). Following [61], the HHCF according to the ECM for an isotropic self-affine surface is:

$$H(\boldsymbol{\rho}) = 2w^2 \left(1 - e^{-\left(\frac{\boldsymbol{\rho}}{\boldsymbol{\xi}}\right)^{(2H)}} \right). \tag{3.9}$$

Note that HHCF according to the ECM cannot represent $H = 0$. Following [61], the ACF according to the ECM for an isotropic self-affine surface reads:

$$R(\boldsymbol{\rho}) = \exp\left(-\frac{|\boldsymbol{\rho}|^{2H}}{\xi} \right). \tag{3.10}$$

Following [51], we can write the PSHF:

$$C(\boldsymbol{q}) = \begin{cases} \dfrac{w^2\xi}{2\pi H} \sum_{j=0}^{\infty} \dfrac{\Gamma\left(\dfrac{j+\frac{1}{2}}{H}\right)}{2j!} \left(-q^2\xi^2\right)^j, & \text{for } d = 1; \\ \dfrac{w^2\xi^2}{4\pi H} \sum_{j=0}^{\infty} \dfrac{\Gamma\left(\dfrac{j+1}{H}\right)}{(j!)^2} \left(-\dfrac{\boldsymbol{q}^2\xi^2}{4}\right)^j, & \text{for } d = 2, \end{cases} \tag{3.11}$$

where $\Gamma(x)$ is the Gamma function. The HHCF according to the KCM reads:

$$H(\boldsymbol{\rho}) = 2w^2 \left(1 - \frac{H}{2^{H-1}\Gamma(H+1)} \left(\frac{\boldsymbol{\rho}}{\xi}\sqrt{2H}\right)^H K_H \left(\frac{\boldsymbol{\rho}}{\xi}\sqrt{2H}\right) \right), \tag{3.12}$$

where $K_H(x)$ is the H^{th}-order modified Bessel function. Then, for the ACF we can write:

$$R(\boldsymbol{\rho}) = \frac{H}{2^{H-1}\Gamma(H+1)} \left(\frac{\boldsymbol{\rho}}{\xi}\sqrt{2H}\right)^H K_H \left(\frac{\boldsymbol{\rho}}{\xi}\sqrt{2H}\right). \tag{3.13}$$

The PSHF according to the KCM reads:

$$C_{\text{h}}(\boldsymbol{q}) = \begin{cases} \dfrac{w^2\xi}{\sqrt{2\pi}} \dfrac{\sqrt{H}\Gamma\left(H+\frac{1}{2}\right)}{\Gamma(H+1)} \left(1 + \dfrac{q^2\xi^2}{2H}\right)^{-H-\frac{1}{2}}, & \text{for } d = 1; \\ \dfrac{w^2\xi^2}{2\pi\left(1 + \dfrac{\boldsymbol{q}^2\xi^2}{2H}\right)^{H+1}}, & \text{for } d = 2. \end{cases} \tag{3.14}$$

The ACF according to both ECM and KCM are compared in Fig. 3.5.

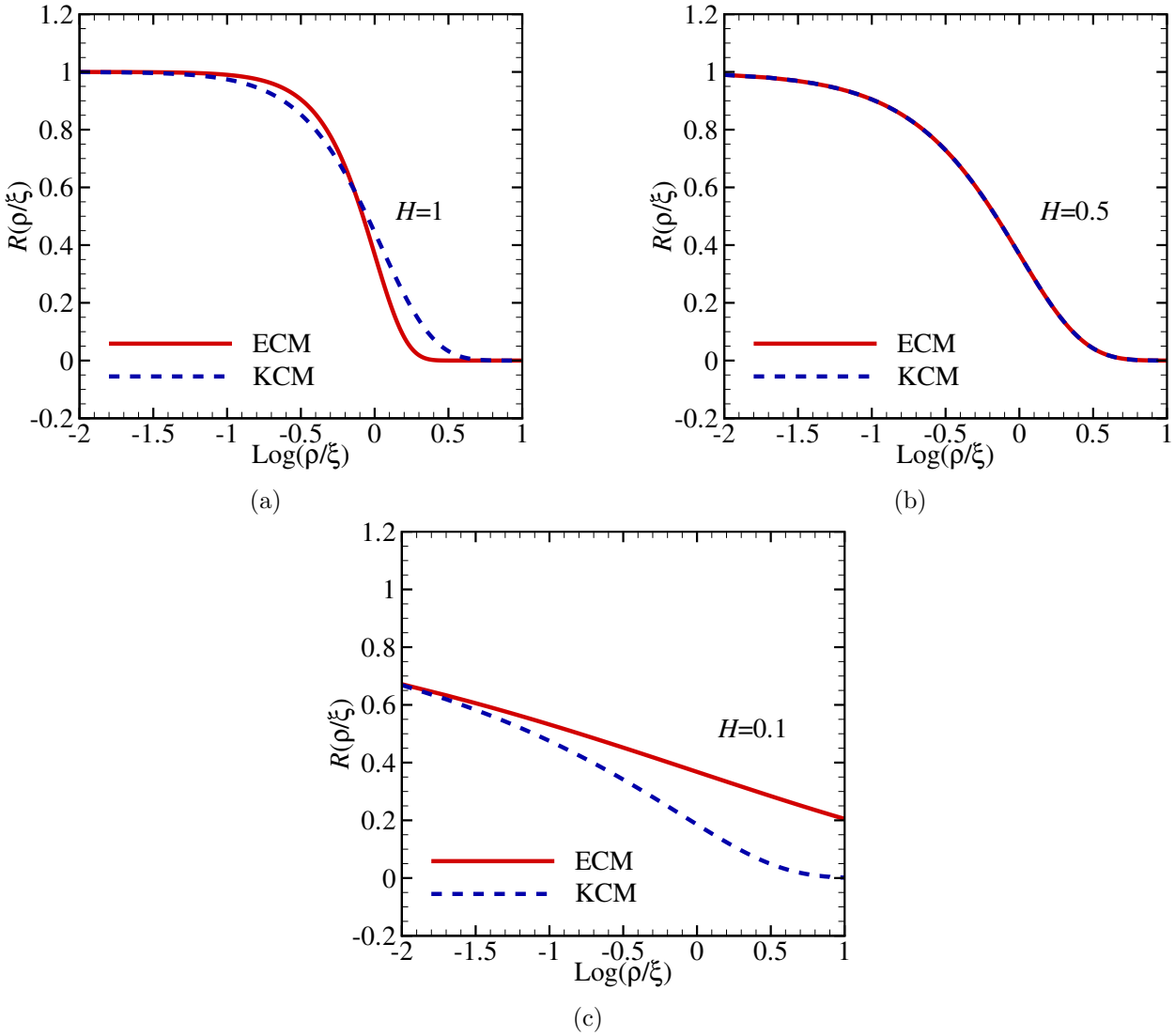

Figure 3.5: Log-linear plots of the auto-correlation function $R(\rho/\xi)$ as a function of the ratio ρ/ξ for the ECM and the KCM, for a given Hurst exponent: (a) $H = 1.0$; (b) $H = 0.50$; (c) $H = 0.1$.

For $H > \frac{1}{2}$, the KCM approaches zero more gradually than the ECM. For $H < \frac{1}{2}$, the KCM approaches zero more rapidly than the ECM. For $H = \frac{1}{2}$ the KCM and ECM coincide. A major advantage of the KCM over the ECM is that the PSHF (Eq. 3.14) can be expressed in closed form. In this work, we limit the study into rational symmetry to anisotropy of correlation length and anisotropy of scaling for $(2+1)$-dimensional self-affine surfaces. These two rational symmetries are most frequently experimentally observed [50]. Moreover, these anisotropic models for the PSHF of random rough surfaces are presented, because of their use measuring surface topographies and future work on $(2+1)$-dimensional deformable substrates. Following [63], the PSHF of the KCM for a topology with correlation-length anisotropy reads:

$$C_{\mathrm{h}}(\boldsymbol{q}) = \frac{2H\xi_1\xi_2 w^2}{(1+q_1^2\xi_1^2+q_2^2\xi_2^2)^{(1+H)}}. \tag{3.15}$$

Following [50], the PSHF of the KCM for a topography with anisotropy of scaling we can write:

$$C_{\mathrm{h}}(\boldsymbol{q}) = \frac{2\xi_1\xi_2 w^2 \Gamma\left(\frac{1}{2}+H_1\right)\Gamma\left(\frac{1}{2}+H_2\right)}{\Gamma(H_1)\,\Gamma(H_2)\left(1+q_1^2\xi_1^2\right)^{\left(\frac{1}{2}+H_1\right)}\left(1+q_2^2\xi_2^2\right)^{\left(\frac{1}{2}+H_2\right)}}. \tag{3.16}$$

Note that the aforementioned description was for a rough surface that was nominally flat for length scales larger than the cut-off wavelength λ_{r}. However, it is known that many rough surfaces have a characteristic wavelength λ larger than the auto-correlation length ξ. Therefore, here, we present the ECM and KCM of mounded surfaces.

3.4.2 Mounded surfaces

Up to date, not known is for what lengths of λ and ξ the mounded structures influence the self-affine part of the PSHF. It is expected that for $\lambda >> \xi$ the mounded structure does not influence the self-affine PSHF. Neglecting the mounded structure corresponds to the practice of removing waviness from a topography measurement before studying its properties. This characteristic length scale for mounded surfaces, is also called the average mound separation λ. Figure 3.6 is a schematic representation a mounded surface profile $h(r)$ and the PSHF $C_{\mathrm{h}}(q)$ of a mounded surface.

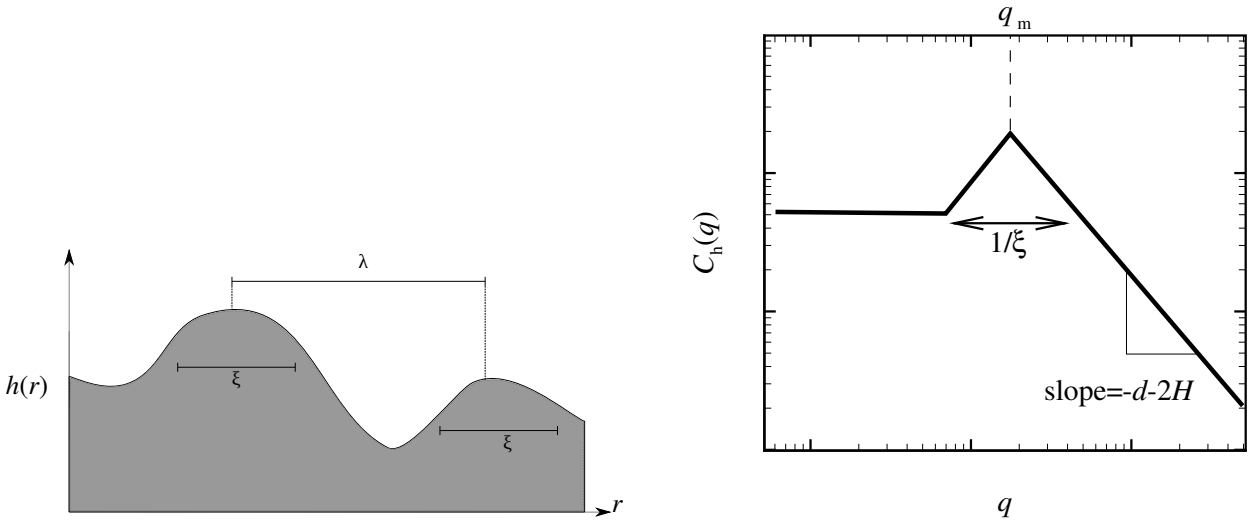

Figure 3.6: Schematic representation of a mounded surface topography: (a) Height profile $h(r)$ as a function of scalar r, with correlation length ξ and average mound separation λ; (b) Log-log plot of the PSHF $C_h(q)$ as a function of the wave number q, with a peak at wave number $q_{\mathrm{m}} = 2\pi/\lambda$.

The correlation length is still well defined, and is a measure of the size of the mounds, as depicted in Fig. 3.6a. Average mound separation and correlation length always satisfies $\lambda \geq \xi$. Following

[51], the HHCF according to the ECM of mounded surfaces reads:

$$H(\boldsymbol{\rho})=\begin{cases}2w^2\left(1-e^{\left(\frac{\rho}{\xi}\right)^{2a}}\cos\left(\frac{2\pi\rho}{\lambda}\right)\right), & \text{for } d=1;\\ 2w^2\left(1-e^{\left(\frac{\boldsymbol{\rho}}{\xi}\right)^{2a}}J_0\left(\frac{2\pi\boldsymbol{\rho}}{\lambda}\right)\right), & \text{for } d=2,\end{cases} \tag{3.17}$$

where $J_0(x)$ is the 0^{th}-order Bessel function. The PSHF according to ECM of mounded surfaces is:

$$C_{\text{h}}(\boldsymbol{q})=\begin{cases}\frac{w^2\xi}{4\pi H}\sum_{j=0}^{\infty}\frac{\Gamma\left(\frac{j+\frac{1}{2}}{H}\right)}{(2j)!}\left(-\xi^2\right)^j\left[\left(q-\frac{2\pi}{\lambda}\right)^{2j}+\left(q+\frac{2\pi}{\lambda}\right)^{2j}\right], & \text{for } d=1;\\ \frac{w^2\xi^2}{8\pi^2 H}\sum_{j=0}^{\infty}\frac{\Gamma\left(\frac{j+1}{H}\right)}{(j!)^2}\left[-\frac{\pi\boldsymbol{q}\xi^2}{b\lambda}\right]^j\int_0^{2\pi}\left[1-b\cos\theta\right]^j\mathrm{d}\theta, & \text{for } d=2,\end{cases} \tag{3.18}$$

where

$$b=\frac{4\pi\lambda\boldsymbol{q}}{\boldsymbol{q}^2\lambda^2+4\pi^2}. \tag{3.19}$$

We can write the PSHF according to KCM as:

$$C_{\text{h}}(\boldsymbol{q})=\begin{cases}\frac{w^2\xi}{2\sqrt{2\pi}}\frac{\sqrt{H}\Gamma\left(H+\frac{1}{2}\right)}{\Gamma(H+1)}\left[\left(1+\frac{\left(q-\frac{2\pi}{\lambda}\right)^2\xi^2}{2H}\right)^{-H-\frac{1}{2}}+\left(1+\frac{\left(q+\frac{2\pi}{\lambda}\right)\xi^2}{2H}\right)^{-H-\frac{1}{2}}\right], & \text{for } d=1;\\ \frac{w^2\xi^2}{2\pi\Gamma(H+1)\left[1+\frac{\boldsymbol{q}^2\xi^2}{2H}+\frac{2\pi^2\xi^2}{H\lambda^2}\right]^{1+H}}\sum_{j=0}^{\infty}\frac{\Gamma(2j+H+1)}{(j!)^2}\left(\frac{b^2}{4}\right)^j, & \text{for } d=2,\end{cases} \tag{3.20}$$

where

$$b=\frac{4\pi\xi^2\lambda\boldsymbol{q}}{2H\lambda^2+\boldsymbol{q}^2\xi^2\lambda^2+4\pi^2\xi^2}. \tag{3.21}$$

For a mounded surface it is known that the local surface is quite smooth and $H\approx 1$ [50]. Following [61], the PSHF according to ECM for mounded surfaces with $H=1$ is:

$$C_{\text{h}}(\boldsymbol{q})=\begin{cases}\frac{w^2\xi}{2\sqrt{\pi}}\exp\left[-\frac{\left(4\pi^2+q^2\lambda^2\right)\xi^2}{4\lambda^2}\right]\cosh\left(\frac{\pi q\xi^2}{\lambda}\right), & \text{for } d=1;\\ \frac{w^2\xi^2}{4\pi}\exp\left[-\frac{\left(4\pi^2+\boldsymbol{q}^2\lambda^2\right)\xi^2}{4\lambda^2}\right]K_0\left(\frac{\pi\boldsymbol{q}\xi^2}{\lambda}\right), & \text{for } d=2.\end{cases} \tag{3.22}$$

A comparison of the ECM given in Eqs. (3.14) and (3.22) and the KCM in Eqs. (3.11) and (3.20), for the Hurst exponent $H = 1$ and correlation length $\xi = 1$ μm is presented in Fig. 3.7. This is done to determine the range of values of ξ and λ for which the effect of mounds has to be incorporated in numerically generating a surface topography.

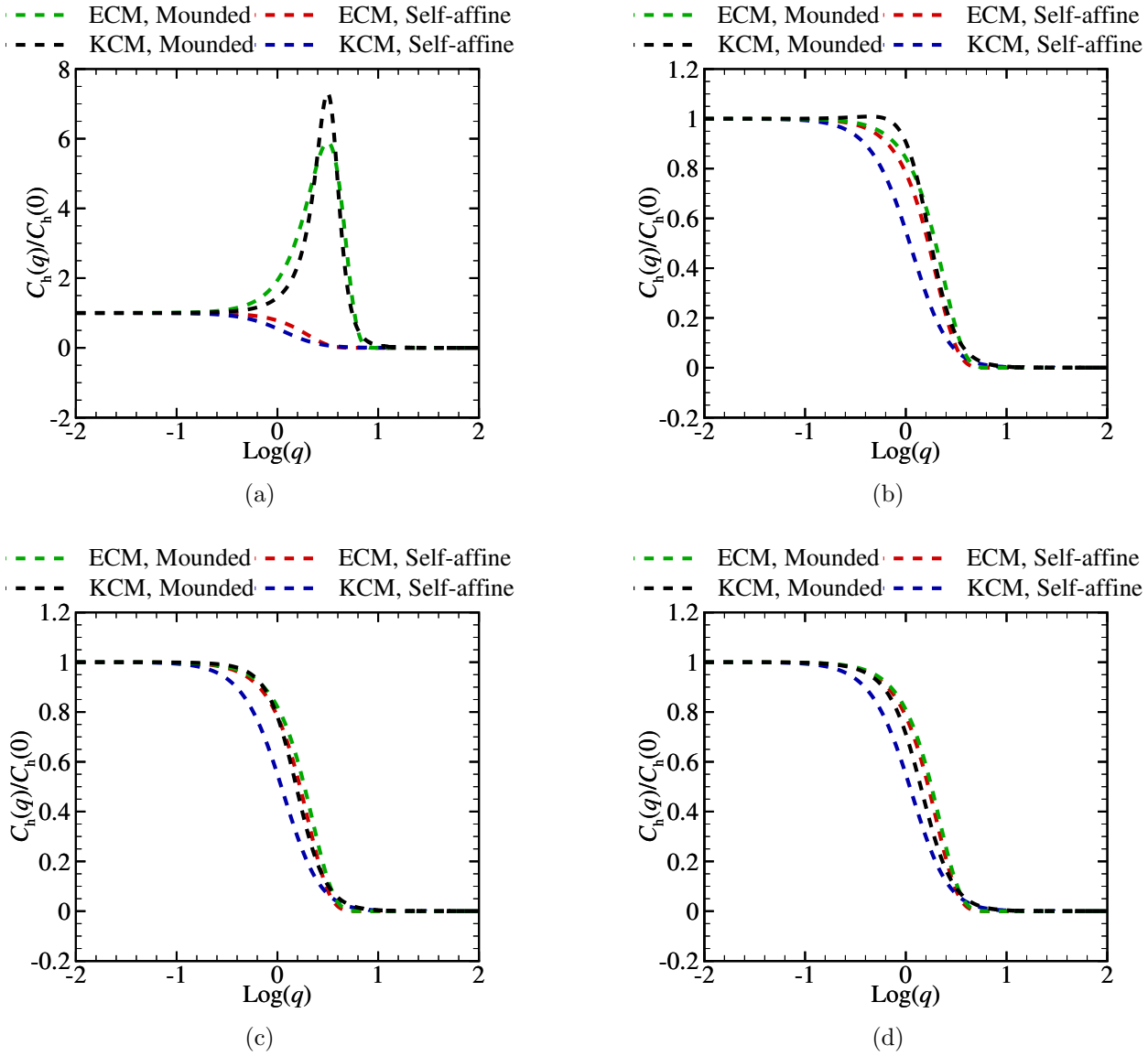

Figure 3.7: Log-linear plots of the power spectral height function $C_{\rm h}(q)$ as a function of the wave number q for the ECM and the KCM of mounded and self-affine random rough surfaces, with correlation length $\xi = 1$ μm and Hurst exponent $H = 1$ and characteristic length: (a) $\lambda = 2$ μm; (b) $\lambda = 8$ μm; (c) $\lambda = 10$ μm; (d) $\lambda = 12$ μm.

Measuring and numerically generating random rough mounded surfaces by a self-affine correlation model only approximates the surface roughness when the correlation length $\frac{\xi}{\lambda} \leq 0.1$ and wave vectors $q << \xi^{-1}$ are omitted. This corresponds to subtracting waviness from the measured height profile before analysis of the surface roughness (Sec. 3.2) and is as expected. When the ratio $\xi/\lambda > 0.1$ the characteristic wavelength λ severely influences the self-affine region of the

PSHF. Numerical generation of surface topographies with $\xi/\lambda > 0.1$ will need scaling of the PSHF $C_h(q < q_r)$. For the remainder of this work, we assume the surface topography to be self-affine, but the periodic reciprocal space methods in Sec. 3.5 can be easily modified to generate mounded surfaces.

3.5 Generating virtual surface roughness

In this section, a method is selected to numerically generate virtual surface topographies. We will consider four commonly used methods in tribological research. Two methods are recursive real space methods: The random midpoint displacement (RMD) method, used by Ramisetti *et al.* [43]; And, the successive random addition (SRA) method, used by Hyun *et al.* [40], Campagñá *et al.* [39], Yastrebov *et al.* [32] and Dapp *et al.* [6]. The other two methods are periodic reciprocal space methods: The Fourier filtering method (FFM); And, the power spectral density method (PSDM), used by Campañá *et al.* [64] and Prodanov *et al.* [5]. The applicability of a certain method depends on the numerical simulation method one uses and the quantity that one wishes to determine. However, often the limitations and drawbacks of various methods are not taken into consideration. Well known is that current recursive real space methods can not generate a stationary process [42], to what extent the ACF generated with RMD or SRA varies from the required ACF is currently unknown. Moreover, according to Voss [42], recursive real space methods do not generate a topography with the Gaussian height distribution $p(h)$. Note that, up to date, these methods were only discussed in the context of personal computer texture visualization [42]. Due to the differences in methods and their specific advantages and drawbacks, we can not select the most suitable method *a priori*. Therefore, we give here a rigorous analysis, in the light of tribological research, of all four methods. In this work, we also extend all four methods so they are capable of numerically generating, (1) a periodic surface L_x with (2) its height distribution $p(h)$ approaching a Gaussian. We also want to be able to (3) vary the value of each coefficient of the PSDF corresponding to a single wave number $C_h(q)$ independently scalable. The RMD method forms the basis for the SRA method. Therefore, we extend the RMD method here first.

3.5.1 Recursive real space methods

Two algorithms for generating statistical self-affine surfaces are formulated by Voss [42], the random midpoint displacement and the successive random addition method. In RMD, an isotropic self-affine rough surface is generated by a recursive technique which adds roughness in incremental steps n. Figure 3.8 is a schematic representation of the evolution of the point grid in real space, using a recursive method.

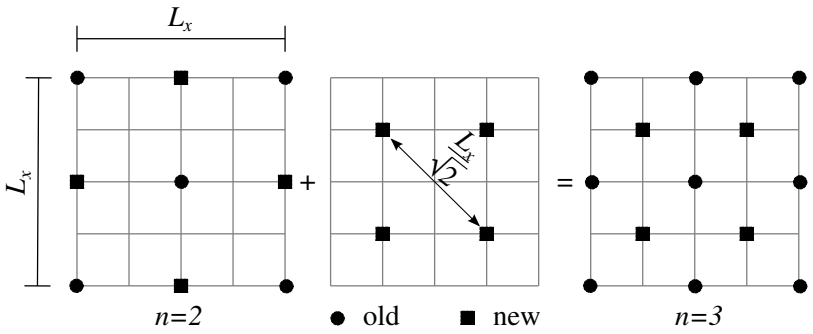

Figure 3.8: Schematic representations of 2-dimensional point grid of the n^{th} step. The midpoints of the n^{th} step are determined from the grid points present in the $(n-1)^{\text{th}}$ step.

Initially (*i.e.*, at $n = 0$), the equally spaced d-dimensional point grid has a height equal to the required average height $\langle h(\boldsymbol{r})\rangle$ with the addition of a Gaussian variable with $\mu = 0$ and variance $\frac{w^2}{4}$. Each following step, the midpoints of the points present in the previous step are determined as the average height of the first neighboring points with the addition of a Gaussian random variable. The first step ($n = 1$) for a self-affine rough surface, with $d = 1$, is:

$$h\left(\phi_n^n \cdot L_x\right) = 0.5\left(h\left(0\right) + h\left(L_x \cdot \phi_n^{n-1}\right)\right) + \Delta_n, \tag{3.23}$$

where $\phi_n = \frac{1}{2}$ is the constant scaling ratio and Δ_n is a Gaussian variable of the n^{th}-step with zero mean and variance Δ_n^2. Derived from the ACF of an isotropic self-affine rough surface (Eq. 3.10), the variance of the Gaussian random variable of the n^{th}-step Δ_n in RMD is:

$$\Delta_n^2 = \frac{w^2}{\left(2^n\right)^{2H}}\left(1 - 2^{2H-2}\right). \tag{3.24}$$

The height $h(\boldsymbol{r})$ at point $\boldsymbol{r}$ is determined only once. Although RMD generates a fractal, the points generated across successive steps lack the correlation needed to become a stationary process. All additional stages change $h(r < r_i)$ independent from $h(r > r_i)$. For a stationary process, the HHCF should be constant for all translations ρ. The absence of correlation across an earlier stage requires that $R(\rho) = 2R(\rho/2)$, this is true when $H = 1/2$. Hence, RMD generated isotropic self-affine surface topography, with $H \neq \frac{1}{2}$, has spectral artifacts (*i.e.*, lack of correlation) and its characteristic function is not Gaussian.
We modify the original RMD method so that the isotropic surface topography at large length scales, wavelengths larger than the cut-off wavelength of the self-affine region, are generated with a constant variance (Δ_n^2). We observe that the height distribution $p(h)$ becomes Gaussian for a constant cut-off wavelength λ_{r} and an increase in periodic width L_x. Moreover, we modified the original method so that the isotropic surface topography at small length scales, wavelengths smaller than the cut-on wavelength of the self affine region, are generated by taking the Fourier transform of $h(\boldsymbol{r})$ and adding scaled Fourier coefficients up to the smallest virtual wavelength λ_s or by using a standard spline interpolation algorithm [9].

3.5.1.1 Successive random addition

SRA uses the RMD-algorithm and a Gaussian random variable is added to all points at each step of the recursive subdivision process. This allows for a varying scaling ratio at each step (*i.e.*, $0 < \phi_n < 1$). According to the Nyquist sampling theorem, nx grid points need $nx/2$ sinusoidal components, to capture all the information from a continuous-time process of finite bandwidth. When the topography is magnified to $2nx$ grid points, the additional $nx/2$ sinusoidal components alter the height at all the current $2nx$ grid-points. SRA adds sinusoidal components to nx points at every n^{th} step instead of only adding the additional sinusoidal components to $\frac{nx}{2}$ points per n^{th}-step as RMD does. This reduces the spectral artifacts in SRA, compared to RMD.
Hence, SRA can be viewed as magnifying a real isotropic self-affine rough Gaussian surface, where the spatial resolution increases over all present points during magnification. The variance of the Gaussian added to all nx grid points of the n^{th}-step in SRA is:

$$\Delta_n^2 \propto \left((\phi_n)^n\right)^{2H} . \tag{3.25}$$

We make the same modifications to the SRM method as we mention in Sec. 3.5.1. The isotropic Gaussian surface topography at large length scales ($\lambda > \lambda_{\text{r}}$) are generated with a constant variance (Δ_n^2). The isotropic Gaussian surface topography at small length scales ($\lambda < \lambda_{\text{s}}$) are generated by taking the Fourier transform of $h(\boldsymbol{r})$ and adding scaled Fourier coefficients up to the smallest virtual wavelength or by a standard spline interpolation algorithm. We also ensure that the second-order statistics are independent of location $\boldsymbol{r}$ on the d-dimensional reference plane for the periodic surface. The original SRM method fails to comply with this requirement, and that failure results in edge-effects, *i.e.*, a non-homogeneous random field. The midpoint determined at grid points $(r_1, 0)$, (r_1, L_x), $(0, r_2)$ and (L_x, r_2) are constrained every n^{th}-step by:

a. $h(r_1, 0) = h(r_1, L_x)$ and $h(0, r_2) = h(L_x, r_2)$;

b. $\langle \left(h\left((L_x, L_x) - \frac{1}{2}\boldsymbol{\rho}\right) - h\left(\frac{1}{2}\boldsymbol{\rho}\right)\right)^2 \rangle = H(\boldsymbol{\rho})$.

Figure 3.9 displays the contour plot of the heights $h(\boldsymbol{r})$ and surface profiles of the two modified recursive real space methods for a given set of roughness parameters.

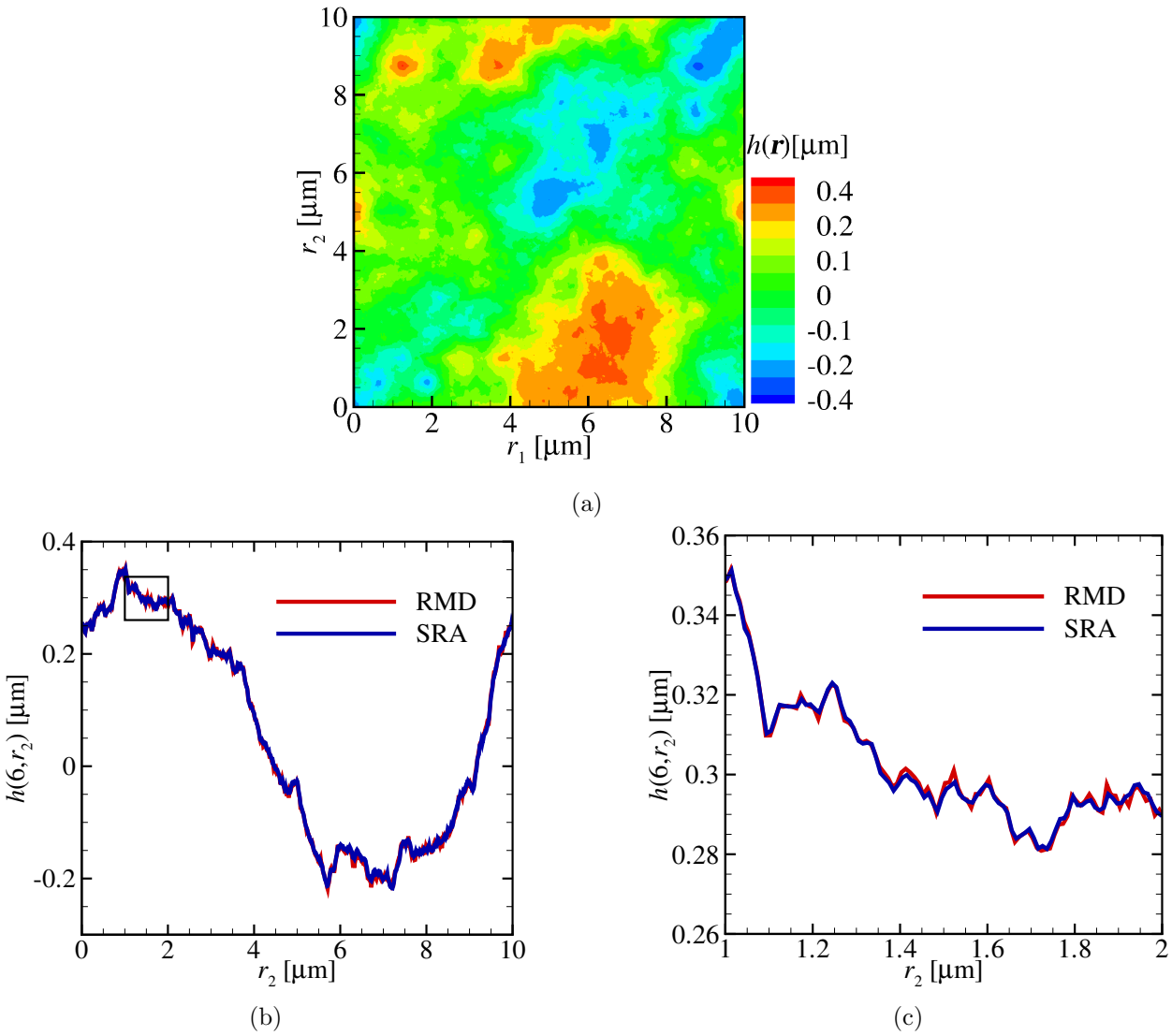

Figure 3.9: (a) Countour plot of the height $h(\boldsymbol{r})$ as a function of $\boldsymbol{r}$ numerically generated by RMD and SRA, with L_x=10 μm, $nx = 2^{20}$, RMSH= 0.15 μm and $H = 0.9$. (b) Surface profiles $h(6, r_2)$ as a function of r_2 by both RMD and SRA, and the solid square indicates the area in Fig. 3.9c. (c) Local surface profiles $h(6, r_2)$ as a function of r_2 by both RMD and SRA.

RMD and SRA numerically generate macroscopically the same surface as is displayed in Fig. 3.9a. Both the modified RMD and SRA are now capable of generating periodic rough surface topographies. Their second-order statistics are independent of $\boldsymbol{r}$. Although the contour plots of SRA and RMD appear similar, the surface profile generated by RMD in Fig. 3.9c shows higher local gradients.

Both RMD and SRA are most commonly used in brute-force models when there is the need

to change local properties on a small length scale, while one preserves the overall topography. Ramisetti *et al.* [43] use RMD for the slid-island method to determine the effect of smaller length scales on the auto-correlation between islands. Moreover, According to Dapp *et al.* [6], SRA is highly applicable when studying re-entry of local asperity tops into the contact area when studying contact mechanics over smaller and smaller length scales. It is common to test the second-order statistical properties post numerical-generation of an individual surface realization by calculating the PSHF [9]. However, in this work, we argue that this trail-and-error method is not suitable for studying contact mechanical properties of thousandths of individual surface realizations with different periodicities L_x, cut-off wavelengths λ_r and smallest wavelengths λ_s.

3.5.2 Periodic reciprocal space methods

The Fourier filtering method (FFM) generates a self-affine periodic surface topography by the convolution of a Gaussian profile $G(\boldsymbol{r})$ with the ACF of the desired self-affine surface topography. The resulting surface has again a Gaussian height distribution. This is reported by Maystrenko [65] only for the convolution of a discrete periodic random surface with a height distribution with finite variance w and a generic ACF $R[n]$. The Fourier transform of the surface $\tilde{G}_\mathrm{p}(\boldsymbol{q})$ and the ACF $\tilde{R}(\boldsymbol{q})$ are generated with a fast Fourier transform (FFT) algorithm and multiplied in Fourier space:

$$\tilde{h}_\mathrm{p}(\boldsymbol{q}) = \tilde{G}_\mathrm{p}(\boldsymbol{q})\tilde{R}(\boldsymbol{q}). \tag{3.26}$$

The Fourier transform $\tilde{h}(\boldsymbol{q})$ is transformed with an inverse FFT back to real space, resulting in the self-affine periodic surface topography $h_\mathrm{p}(\boldsymbol{r})$.
The periodic surface at large and small length scales can be generated by scaling the corresponding Fourier coefficients. The PSHF of wave numbers smaller than the region of self-affine length scales have to be modeled with care, because a discontinuity of the PSHF leads to spectral artifacts in real-space due to the discrete FFT. A major drawback, in comparison with recursive real space methods (*i.e.*, RMD and SRA), is the need to do multiple FFTs for studying the effect of incorporating smaller and smaller wavelengths for given roughness parameters w, ξ and H.

3.5.2.1 The power spectral density method

The power spectral density method generates periodic self-affine surface topographies. Initially the Fourier transform of the height profile is constructed as:

$$\tilde{h}_\mathrm{p}(\boldsymbol{q}) = h_0\tilde{\Delta}_\mathrm{G}(\boldsymbol{q})\sqrt{C_\mathrm{h}(\boldsymbol{q})}, \tag{3.27}$$

where h_0 is a real valued constant and $\tilde{\Delta}_\mathrm{G}(\boldsymbol{q})$ a Gaussian with random phase and $\langle\tilde{\Delta}_\mathrm{G}(\boldsymbol{q})\rangle = 0$. In Appx. 3.A, a well known method is given to numerically generate the Gaussian in Fourier space. The constant h_0 is chosen to adjust the RMSH of the self-affine periodic Gaussian surface topography. The Fourier transform $\tilde{h}_\mathrm{p}(\boldsymbol{q})$ is then transformed back into real space, resulting in the periodic self-affine rough surface $h_\mathrm{p}(\boldsymbol{r})$. The Fourier transforms of an isotropic fully self-affine surface profile can be determined as:

$$\tilde{h}_\mathrm{p}(q) = h_0\frac{\tilde{\Delta}_\mathrm{G}(q)}{q^{\left(\frac{d}{2}+H\right)}}. \tag{3.28}$$

The periodic surface topography at large and small length scales is simply determined by its PSHF. In Figure 3.10, we show the ACF $R(\rho)$ as a function of the translation scalar ρ plotted for RMD, SRA, FFM, PSDM and its analytical expressions.

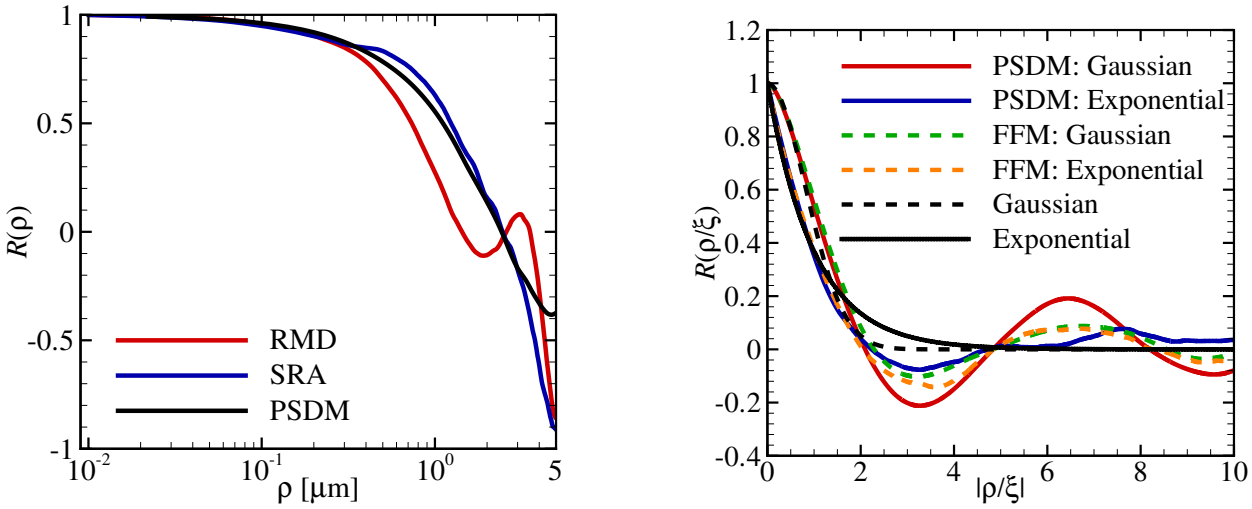

(a) (b)

Figure 3.10: Plots of (a) the auto-correlation $R(\rho)$ as a function of translation scalar ρ by both RMD, SRA and PSDM for the height profile in fig. 3.9c and (b) the ACF $R(\rho/\xi)$ as a function of the absolute normalized translation scalar $|\rho/\xi|$ is plotted for PSDM, FFM and its analytical expression, with $nx = 2^{19}$ and $H = 0.5$ (*i.e.*, exponential) or $H = 1$ (*i.e.*, Gaussian).

In Fig. 3.10a, we observe between RMD and SRA a shift in correlation length of $\Delta\xi \approx 1$ μm. RMD and PSDM display the biggest difference in ACF. SRA approximates the ACF of PSDM up till $\rho \approx 2.5$ μm. This spectral artifacts for SRA are suppressed compared with RMD. The spectral artifacts result in a shift of the correlation length ξ, which corresponds to a lack of long range correlation. This is as expected for a Hurst exponent $H \neq 0.5$ (Sec. 3.5.1). Note that a disadvantage of SRA is that there are still spectral artifacts in the surface topography, and these are not easily defined in a visual inspection. Moreover, note that only checking the scaling post numerical generation, *i.e.*, the Hurst's exponent H, is a non-rigorous way of verifying the second-order statistics of the surface. As we show in Fig. 3.10a, for example the gradients on the log-linear scale for SRA and PSDM for $0.9 < \rho < 0.5$ are comparable, but there is a significant shift in correlation length ξ between both methods.
In Fig. 3.10b, we observe that the ACF for both PSDM and FFM are in good correspondence with their analytical expression for $\rho/\xi \leq 2$. This is comparable to the correspondence between analytical ACF and experimental results [50, 51]. Both display similar oscillations at translation lengths that are several times the auto-correlation length.
Note that the extended SRA shows considerably more spectral artifacts than PSDM at length scales larger than 10^{-1} μm. As to be expected, this non-stationarity is more pronounced over larger lengths scales, because the non-stationarity is more sever over the first few n steps. We conclude that this is due to the still non-stationary process of SRA. Moreover, we conclude that PSDM numerically generates topographies with comparable ACF as experimentally observed. Finally, we conclude that PSDM is the most suitable method to numerically generate rough surfaces in this work. However, in this work, we observe that for a large Hurst's exponent $0.7 < H$ the height distribution $p(h)$ of the numerically generated topography was not strictly Gaussian. This observed difference between generated and required height distribution $p(h)$ violates the prior assumption of a Gaussian height distribution $p(h)$. Therefore, we discuss this observation here.

3.5.3 Numerically generated height distribution

All extended methods are capable of generating the surface topography with a Gaussian height distribution. It is observed that for an increase in Hurst's exponent H the ratio L_x/ξ has to increase to generate the Gaussian height distribution. However, the ensemble averaged height distribution will be Gaussian. This is shown in Fig. 3.11 for a given Hurst's exponent H the height distribution becomes Gaussian for an increase in ratio L_x/ξ.

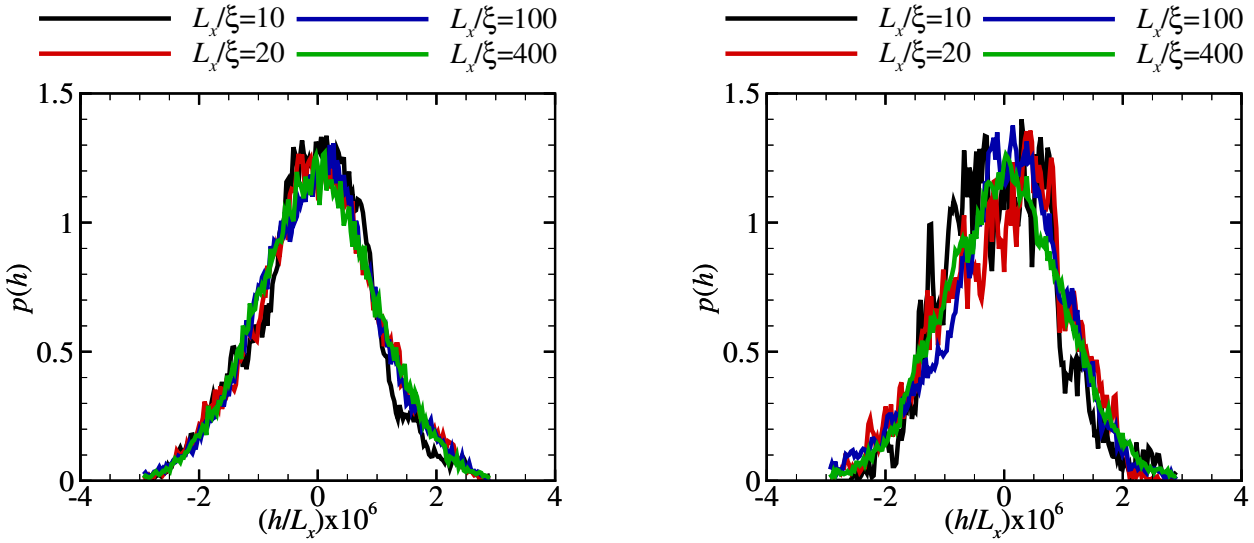

Figure 3.11: Line representation of the histogram of the height distribution function $p(h)$ as a function of the normalized height of the surface h/L_x for (a) H=0.4 and (b) $H = 0.8$ with $L_x/\xi = 10$, $L_x/\xi = 20$, $L_x/\xi = 100$, $L_x/\xi = 400$ and $q_{s,H}/L_x = 5 \times 10^{-5}$.

For a given ratio L_x/ξ the height distribution function deviates less from the Gaussian distribution for a lower Hurst's exponent H. The increase of ratio L_x/ξ corresponds to multiple realizations over length scale ξ converge in the mean square to the Gaussian height distribution. This is also observed by Persson [25] for fracture-produced surfaces, whose behavior appears fractal like up to the longest length scale studied. The RMSH of fracture-produced surfaces is determined mainly by the large lengths scales. If the surface studied over a range with the substrate width $L_x >> \xi$, ensemble averaging and averaging over the surface will give identical results for $p(h)$. This ratio for the periodic reciprocal space method for $0 \leq H \leq 0.8$ we observe to be $L_x/\xi \geq 400$ for $d = 1$. A possible reason for the increase in minimal ratio L_x/ξ for an increase in Hurst's exponent H is the increase in magnitude of the PSHF for large wavelengths. This increase results in an increase of difference in variance w^2 over successive wavelengths and a slower convergence in the mean square to the Gaussian height distribution. No proportionality between the Hurst's exponent H, substrate with L_x and correlation length ξ is reported to date. In Appx. 3.C and 3.D, we elaborate further on this expected proportionality.

3.6 Comparison between numerically generated and a real surface topography

The experimental surface profiles in longitudinal direction of cold rolled aluminum by Plouraboué [2] are compared to the numerically generated height profiles using PSDM. We only consider PSDM as the numerical method to generate surface topographies, because we only use PSDM in the remainder of this work. Moreover, the surface roughness properties of a random rough surface are taken to be fully defined by the ACF $R(\rho)$ and the height distribution function $p(h)$. The parameters determining both properties are the Hurst's exponent H, correlation length ξ and RMSH w. According to the Nyquist criterion [67], the substrate width L_x and smallest wavelength λ_s are related by the number of grid-points nx:

$$nx \geq 2\left(\frac{L_x}{\lambda_\mathrm{s}}\right). \tag{3.29}$$

Following [68], the maximum number of grid-points depends on the dimensionless FFT error ϵ:

$$\mathrm{Max}(nx) = \epsilon^{-1}. \tag{3.30}$$

The measured parameters by Plouraboué are: $H = 0.65$, $\lambda_\mathrm{r} = 50$ μm, $w = 0.3$ μm and the height distribution assumed to be Gaussian. The PSDF as depicted in Fig. 3.2c is assumed, to satisfy the asymptotic behavior of the self-affine surface topography. Figure 3.12 shows the numerically generated surface profile $h(r)$ in the longitudinal direction r, generated with the known parameters of the 512×512 point AFM measurement of cold-rolled aluminum alloy sheet by Plouraboué [2].

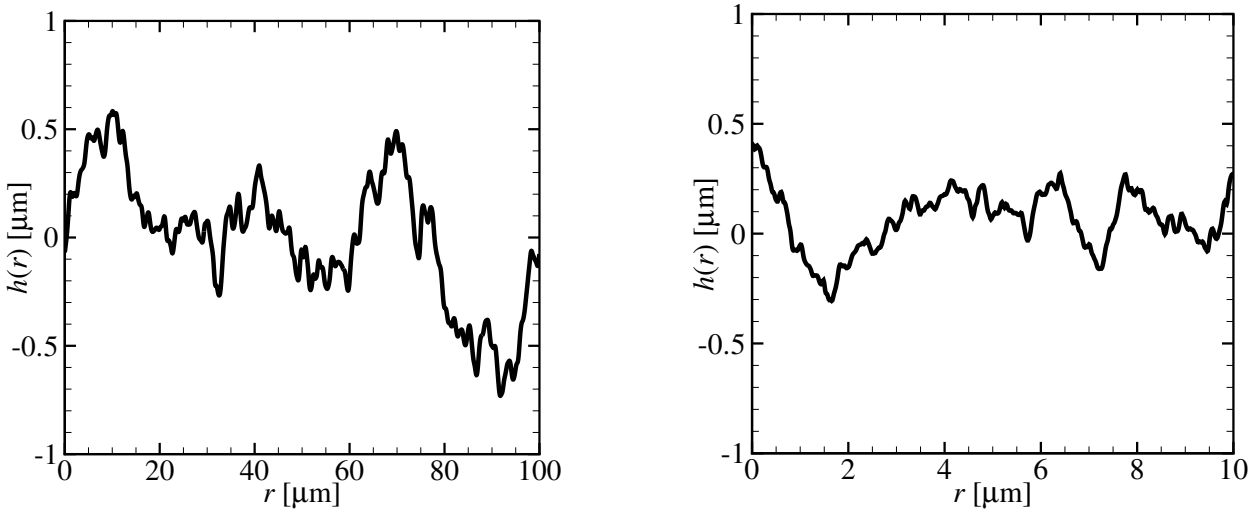

(a) (b)

Figure 3.12: Plots of numerically generated surface profiles $h(r)$ in longitudinal direction r of cold rolled aluminum, interpolated with 512 points and $\lambda_\mathrm{s} = \lambda_{\mathrm{s},H} = 50$ nm: (a) $L_x = 100$ μm and $nx = 4096$; (b) $L_x = 10$ μm and $nx = 8192$.

The numerically generated height profile in longitudinal direction with a given set of parameters is comparable to those of the aluminum surface profile in Fig. 3.4. Table 3.2 displays the measured and numerically generated Hurst's exponents, RMSH and typical slope $\sigma(\theta)$, by Plouraboué [2]

and calculated values from the height profiles as shown in Fig. 3.12. The typical slope $\sigma(\theta)$ is the square root of the slope variance, where θ is the slope.

	Measured	Calculated	
		$L_x = 100$ μm	$L_x = 10$ μm
H	0.700	0.699 - 0.701	0.689 - 0.712
w	0.300	0.300	0.300
$\sigma(\theta)$	$0.300 - 0.5000$	0.497	0.877

Table 3.2: Measured an numerically generated Hurst's exponents H, RMSHs and typical slopes $\sigma(\theta)$, by Plouraboué [2] and calculated from the height profiles as shown Fig. 3.12.

The measured and calculated values of the Hurst's exponent H and RMSG w are in good agreement. Note that unlike RMD and SRA, we do not need to check the scaling after each numerical generation of a new topography. The average slope for $L_x = 10$ μm is higher than the measured values, because the numerically generated surfaces have a smallest wavelength of $\lambda_s \approx 10$ nm in comparison to $\lambda_s \approx 50$ nm measured using the AFM imaging. This difference in typical slope, between the two simulations, is in agreement with the observation by Plouraboué *et al.* (Sec. 3.2) that the typical slope increases with the decreasing observation length scale. We conclude that PSDM is capable of numerically generating surface topographies highly comparable to experimentally measured topographies for a given Hurst's exponent H, roll-off wavelength λ_r and RMSG $\bar{g}$.

3.7 Conclusions and discussion

We find PSDM to be the most suitable method to numerically generate surface topographies for future GFMD simulations in this work. The value of the Hurst's exponent is chosen as $0.3 \leq H \leq 0.8$ for FCC metals, and the cut-on wavelength is chosen as $50 \geq \lambda_{s,H} \geq 5$ nm. The roll-off wavelength λ_r depends on the surface processing technique. We make use of the analytical descriptions of self-affine and mounded surfaces to define the maximum ratio $\xi/\lambda \leq 0.1$ for which the mounded structure can be modeled as self-affine.

We present for the first time the extended RMD and SRA to generate periodic rough surfaces. We observe that the differences in periodic ACF between both real space methods and their required ACF is too large to be used in this work. We are of the opinion that verifying only the Hurst's exponent H of a topography generated with one of the recursive real-space method is a non-rigorous way of verifying the surfaces second-order statistics. Moreover, we observe that for a given ratio L_x/ξ the height distribution function $p(h)$ deviates less from the Gaussian distribution for a lower Hurst's exponent H. The minimum ratio L_x/ξ of a numerically generated topography with a Gaussian height distribution $p(h)$ increases for an increase in Hurst's exponent. We conclude that the rate of convergence in the mean-square to the Gaussian distribution depends on the Hurst's exponent H. An attempt is made in Appxs. 3.C and 3.D to give an analytical expression for the minimum ratio L_x/ξ as a function of the Hurst's exponent H. This analytical expression would allow us to determine the characteristic wavelengths and the minimum discretization of the surface prior to numerically generating the surface topography. Future work should focus on determining this expression, to ensure a Gaussian height distribution for all numerically generated topographies for a generic Hurst's exponent H.

Finally, we conclude that PSDM is capable of numerically generating surface topographies highly comparable to experimentally measured topographies for a given Hurst's exponent H, roll-off wavelength λ_r and RMSG w.

Appendix 3.A Gaussian random variable in Fourier space

The method to directly numerically generate the Fourier transform of the Gaussian variable Δ_{G} is given in this appendix. The Gaussian $\tilde{\Delta}_{\mathrm{G}}(q)$ in Fourier space is written as:

$$\tilde{\Delta}_{\mathrm{G}}(q) = \mathcal{R}\{\tilde{\Delta}_{\mathrm{G}}\}(q) + i\mathcal{I}\{\tilde{\Delta}_{\mathrm{G}}\}(q), \tag{3.31}$$

where $\mathcal{R}$ and $\mathcal{I}$ stand for the real an the imaginary part of a complex number. The real and imaginary part of a real-valued Gaussian sequence $G[n]$ of finite length nx are:

$$\mathcal{R}\{\tilde{\Delta}_{\mathrm{G}}\}(q) = \frac{1}{nx}\sum_{n=0}^{nx-1} G[n]\cos qn,\ \mathcal{I}\{\tilde{\Delta}_{\mathrm{G}}\}(q) = \frac{1}{nx}\sum_{n=0}^{nx-1} G[n]\sin qn. \tag{3.32}$$

The variance w^2 of the Gaussian $G[n]$ is determined as:

$$w^2 = \frac{1}{nx}\sum_{n=0}^{nx-1} G^2[n]. \tag{3.33}$$

Using the formulas $\sum_{n=0}^{nx-1}\sin^2 qn = (1-\delta_{q,0})\dfrac{nx}{2}$ and $\sum_{n=0}^{nx-1}\cos^2 qn = (1+\delta_{q,0})\dfrac{nx}{2}$, where $\delta_{q,0}$ is the Kronecker delta symbol, it is derived that $\mathcal{R}\{\tilde{\Delta}_{\mathrm{G}}\}$ and $\mathcal{I}\{\tilde{\Delta}_{\mathrm{G}}\}$ are Gaussian distributed with variances:

$$w^2_{\mathcal{R}\{\tilde{\Delta}_{\mathrm{G}}\}} = \frac{(1+\delta_{q,0})}{2nx},\ w^2_{\mathcal{I}\{\tilde{\Delta}_{\mathrm{G}}\}} = \frac{(1-\delta_{q,0})}{2nx}. \tag{3.34}$$

Using the Box-Muller transform [69], $\mathcal{R}\{\tilde{\Delta}_{\mathrm{G}}\}$ and $\mathcal{I}\{\tilde{\Delta}_{\mathrm{G}}\}$ are numerically generated by the Box-Muller transform:

$$\begin{aligned}\mathcal{R}\{\tilde{\Delta}_{\mathrm{G}}\}(q) &= w_{\mathcal{R}\{\tilde{\Delta}_{\mathrm{G}}\}}\sqrt{-2\ln(U_1)}\cos(2\pi U_2);\\ \mathcal{I}\{\tilde{\Delta}_{\mathrm{G}}\}(q) &= w_{\mathcal{I}\{\tilde{\Delta}_{\mathrm{G}}\}}\sqrt{-2\ln(U_1)}\sin(2\pi U_2),\end{aligned} \tag{3.35}$$

where U_1 and U_2 are independent random variables uniformly distributed on the interval $[0,1]$.

Appendix 3.B Pseudo-code for the power spectral density method

The pseudocode for numerically generating a surface topography using PSDM, is as follows:

- Determine the minimal and maximum number of grid points, using $nx \geq 2\left(\dfrac{L_x}{\lambda_s}\right)$ (Eq. (3.29));
- Calculate smallest integer i to satisfy: $2^i \geq nx$ and set $nx = 2^i$;
- Calculate the minimum wave number $q_{\mathrm{l}} = \frac{2\pi}{L_x}$ and maximum wave number $q_{\mathrm{s}} = q_{\mathrm{l}}\frac{nx}{2}$;
- Seed the random Gaussian generator, generate Gaussian field $\tilde{\Delta}_{\mathrm{G}}(\boldsymbol{q}_{\mathrm{l}} \leq \boldsymbol{q} \leq \boldsymbol{q}_{\mathrm{s}})$ with random phase and $\langle\tilde{\Delta}_{\mathrm{G}}\rangle = 0$;
- Calculate $\sqrt{C_{\mathrm{h}}(\boldsymbol{q}_{\mathrm{l}} \leq \boldsymbol{q} \leq \boldsymbol{q}_{\mathrm{s},H})}$ from a suitable PSHF from Sec. 3.4, with w, ξ, H and λ. Determine the roll-off, for $C_{\mathrm{h}}(\boldsymbol{q} > \boldsymbol{q}_{\mathrm{s},H})$;
- Calculate Fourier transform $\tilde{h}_{\mathrm{p}}(\boldsymbol{q}) = h_0\tilde{\Delta}_{\mathrm{G}}\sqrt{C_{\mathrm{h}}(\boldsymbol{q})}$ (Eq. 3.27). Verify the Hurst exponent by a linear fit on the log-log plot of $C(\boldsymbol{q}_{\mathrm{l},H} \leq \boldsymbol{q} \leq \boldsymbol{q}_{\mathrm{s},H}) = |\tilde{h}(\boldsymbol{q})|^2$;

– Calculate the reverse Fourier transform by FFT of $\tilde{h}(\boldsymbol{q})$. Add aspired average height to all grid points to generate the surface topography $h(\boldsymbol{r})$;

– Calculate the height distribution $p(h)$. Compare the distribution to the expected Gaussian height distribution $p_{\mathrm{G}}(h) = \frac{1}{\sqrt{2\pi}w} e^{\left(-\frac{h^2}{2w^2}\right)}$ (Eq. (3.1)). If $p(h) \approx p_{\mathrm{G}}(h)$, the height distribution is correct, else, increase the substrate length L_x and recalculate $h(\boldsymbol{r})$ as presented above.

Appendix 3.C Height distribution function for discrete convolution

The height distribution function $p(h)$ of the convolution of a Gaussian variable with the self-affine auto-correlation function (ACF) is expected to be Gaussian, with a different root mean square height (RMSH). The dependency of the RMSH w on the correlation length ξ and substrate width L_x for $\xi \leq L_x$ and whether the $p(h)$ remains Gaussian is derived in this appendix. The periodic discrete surface height $h[n]$ $(n = 0, ..., nx-1)$ is the convolution of a discrete and periodic Gaussian $G[n]$ $(n = 0, ..., nx-1)$ with the periodic discrete self-affine ACF $R[n]$ and is written as:

$$h[n] = G[n] * R[n] = \sum_{n'=0}^{nx-1} G[n']R[n-n'] = \sum_{n'=0}^{nx-1} G[n-n']R[n'] \tag{3.36}$$

where,

$$R[\rho] = e^{-\left(\frac{|\rho|}{\xi}\right)^{2H}}, \ 0 \leq H \leq 1, \tag{3.37}$$

and

$$\rho = n - n'. \tag{3.38}$$

The characteristic function $\phi(q)$ is the Fourier transform of the height distribution function $p(h)$:

$$\tilde{\phi}(q) = \langle e^{iqh[n]} \rangle = \int_{-\infty}^{\infty} \mathrm{d}h p(h) e^{iqh}, \tag{3.39}$$

with,

$$q = \frac{2\pi}{nx} k, \tag{3.40}$$

where q is the wave number and k is the wave index. Substituting the explicit expression for $h[n]$ (Eq. (3.36)) into Eq. (3.39), the characteristic function $\phi(q)$ is written as:

$$\tilde{\phi}(q) = \langle e^{iq \sum_{n'=0}^{nx-1} G[n']R[n-n']} \rangle. \tag{3.41}$$

Following [65], $c^{|\sum_{n'=s}^{t} f[n']|} = \prod_{n'=s}^{t} c^{f[n']}$, the statistical independence of $G[n]$ and Eq. (3.39), equation (3.41) is written as:

$$\begin{aligned} \tilde{\phi}(q) &= \prod_{n'=0}^{nx-1} \langle e^{iqR[n']G[n-n']} \rangle; \\ &= \prod_{n'=0}^{nx-1} \int_{-\infty}^{\infty} \mathrm{d}G p_{\mathrm{G}}(G) e^{iqR[n']G}. \end{aligned} \tag{3.42}$$

The Gaussian height distribution with zero mean μ and variance w^2 is written as:

$$p_{\mathrm{G}}(h) = \frac{1}{\sqrt{2\pi}w} e^{\left(-\frac{h^2}{2w^2}\right)}. \tag{3.43}$$

The characteristic function of the Gaussian height distribution is written as:

$$\tilde{\phi}_{\mathrm{G}}(q) = \tilde{p}_{\mathrm{G}}(q) = e^{-\frac{w^2q^2}{2}}. \tag{3.44}$$

Using Eqs. (3.43), (3.44) and $c^{|\sum_{n'=s}^{t} f[n']|} = \prod_{n'=s}^{t} c^{f[n']}$, equation (3.42) is written as:

$$\begin{aligned} \tilde{\phi}_{\mathrm{h}}(q) &= \prod_{n'=0}^{nx-1} e^{-\frac{R[n']^2w^2q^2}{2}}; \\ &= e^{\left(-\frac{|\sum_{n'=0}^{nx-1} q^2w^2R^2[n']|}{2}\right)}. \end{aligned} \tag{3.45}$$

The sum in Eq. (3.45) is evaluated over two limits: $H = 0$ (white noise), $H = 1$ (Gaussian ACF) and the exponential ACF $H = 0.5$. In the first limit, i.e., $H = 0$:

$$\sum_{n'=0}^{nx-1} q^2w^2R^2[n'] = \frac{q^2w^2nx}{e^2}. \tag{3.46}$$

In the second limit, i.e., $H = 1$:

$$\sum_{n'=0}^{nx-1} q^2w^2R^2[n'] = \sum_{n'=0}^{nx-1} e^{-2\left(\frac{|n'|}{\xi}\right)^2}; \tag{3.47}$$

For an exponential ACF, i.e., $H = \dfrac{1}{2}$:

$$\sum_{n'=0}^{nx-1} q^2w^2R^2[n'] = q^2w^2e^{\frac{1-nx}{\xi}} \operatorname{csch}\left(\frac{1}{\xi}\right) \sinh\left(\frac{nx}{\xi}\right). \tag{3.48}$$

The second limit, i.e., $H = 1$ (Eq. (3.47)), is evaluated in two limits: $nx \to \infty$ and $L_x = \xi$. The Jacobi theta function ϑ_α is written as:

$$\theta_3(c_1, c_2) = 2\sum_{n'=1}^{\infty} c_2^{n^2} \cos(2nc_1) + 1, \tag{3.49}$$

Where c_1 and c_2 are constants. In the first limit, i.e., $nx \to \infty$. When $\xi << L_x$, Eq. (3.47) is written as:

$$\begin{aligned} \sum_{n'=0}^{\infty} q^2w^2R^2[n'] &= \frac{1}{2}q^2w^2 \left(1 + \sum_{n'=1}^{\infty} e^{-2\left(\frac{|n'|}{\xi}\right)^2}\right); \\ &= \frac{1}{2}q^2w^2 \left(1 + \theta_3(0, e^{-\frac{2}{\xi^2}})\right). \end{aligned} \tag{3.50}$$

Figure 3.13 is a plot of the Jacobi theta function $\theta_3(0, e^{-\frac{2}{\xi^2}})$ as a function of the correlation length ξ.

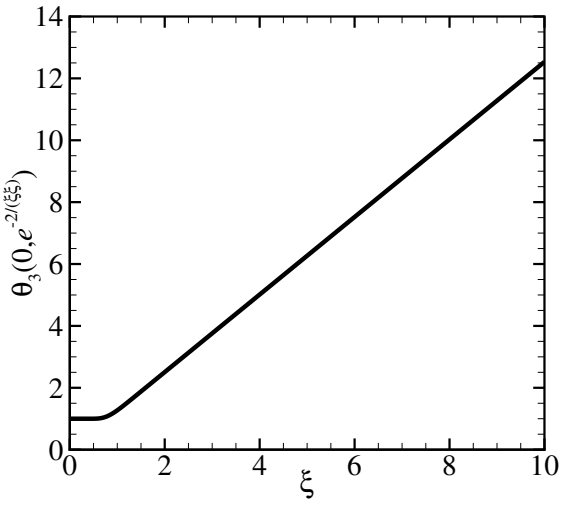

Figure 3.13: Plot of the Jacobi theta function $\theta_3(0, e^{-\frac{2}{\xi^2}})$ as a function of the correlation length ξ.

In the second limit i.e., $\xi = L_x$. The sum in Eq. (3.45) is written as:

$$\sum_{n'=0}^{nx-1} q^2 w^2 R^2[n'] = \sum_{n'=0}^{nx-1} q^2 w^2 e^{-2\left(\frac{|n'|}{nx}\right)^{2H}} \quad ; \tag{3.51}$$

For $nx = 1$, Equation (3.51) is $q^2 w^2$. For $nx >> 1$, Equation (3.51) is approximated by an integral written as:

$$\sum_{n'=0}^{nx-1} q^2 w^2 R^2[n'] \approx \int_0^{nx-1} q^2 w^2 \exp\left(-2\left(\frac{n}{nx}\right)^2\right) \mathrm{d}n = \frac{1}{4}\sqrt{\frac{\pi}{2}} nx q^2 w^2 \mathrm{erf}\left(\frac{\sqrt{2}(nx-1)}{nx}\right) \approx \frac{2}{3} q^2 w^2 nx, \tag{3.52}$$

where erf() is the error function.
Hence, for $L_x \geq \xi$ and $0 \leq H \leq 1$, the inverse Fourier transform of Eq. (3.45) is the height distribution function $p_{\mathrm{h}}(h)$ and is Gaussian, with the variance $(w')^2$ written as:

$$(w')^2 = w^2 \sum_{n'=0}^{nx-1} R^2[n'], \tag{3.53}$$

It is concluded that the height distribution function of the convolution of a Gaussian surface with the self-affine auto-correlation function (ACF) is Gaussian, with a different RMSH depending on the correlation length ξ and number of grid points nx, for $\xi \leq L_x$. This corresponds to the conclusion by A. Maystrenko [65].

Appendix 3.D Height distribution function for the power spectral density method

It is observed that the height distribution function $p(h)$ of a periodic surface profile $h[n]$ ($n = 0, ..., nx-1$) numerically generated by the PSDM for a self-affine surface is Gaussian for a sufficiently

large ratio L_x/ξ. In this appendix the height distribution function $p(h)$ is referred to as probability density function (PDF). PDF is the term used in literature on random fields [70, 71]. An attempt is made to derive the analytical expression for the proportionality between the substrate width L_x, correlation length ξ and the Hurst's exponent H when the PDF $p(h)$ is Gaussian. The PSHF of a self-affine Gaussian surface topography with a given cut-off wave number $q_\mathrm{r} = \frac{2\pi}{nx}k_\mathrm{r}$, cut-on wave number $q_\mathrm{s} = \frac{2\pi}{nx}k_\mathrm{s}$ and $d = 1$ is written as:

$$\tilde{h}_\mathrm{p}(q) = \Theta(q_\mathrm{s} - q)\Theta(q - q_\mathrm{r})h_0 \frac{\tilde{\Delta}_\mathrm{G}(q)}{q^{\left(\frac{d}{2}+H\right)}}, \tag{3.54}$$

where $\Theta(q)$ is the Heaviside step function and $\tilde{\Delta}_\mathrm{G}(q)$ is a Gaussian with zero mean and random phase. PSDM uses the superposition of scaled sinusoids with different wave numbers q. The discrete periodic height profile $h[n]$ is written as:

$$h[n] = \sum_{k=k_\mathrm{r}}^{k_\mathrm{s}} 2\mathcal{R}\{\tilde{h}_\mathrm{p}(k)\}\cos(\frac{2\pi}{nx}kn) + 2\mathcal{I}\{\tilde{h}_\mathrm{p}(k)\}\sin(\frac{2\pi}{nx}kn) \tag{3.55}$$

This is a cosine random process. Following [72], the cosine random process in real space is defined as:

$$f(t) \stackrel{\Delta}{=} \zeta\cos\lambda t + \zeta'\sin\lambda t, \tag{3.56}$$

where ζ and ζ' are uncorrelated, distributed, random variables and λ is a positive constant. The cosine process can also be written as:

$$f(t) = R\cos\left(\lambda t - \Theta\right), \tag{3.57}$$

where $R^2 = \zeta^2 + (\zeta')^2$ and $\Theta = \arctan(\frac{\zeta'}{\zeta}) \in [-\pi, \pi]$. The discrete periodic height profile $h[n]$ can be rewritten as:

$$h[n] = \sum_{k=k_\mathrm{r}}^{k_\mathrm{s}} R(k)\cos\left(\frac{2\pi}{nx}kn - \Theta(k)\right), \tag{3.58}$$

where,

$$\begin{aligned} R(k) &= |2\mathcal{R}\{h_0\frac{\tilde{\Delta}_\mathrm{G}}{\left(\frac{2\pi}{nx}k\right)^{\left(\frac{1}{2}+H\right)}}\}| + |2\mathcal{I}\{h_0\frac{\tilde{\Delta}_\mathrm{G}}{\left(\frac{2\pi}{nx}k\right)^{\left(\frac{1}{2}+H\right)}}\}| \\ &= \frac{2h_0}{\left(\frac{2\pi}{nx}k\right)^{\left(\frac{1}{2}+H\right)}}\left(|\mathcal{R}\{\tilde{\Delta}_\mathrm{G}\}| + |\mathcal{I}\{\tilde{\Delta}_\mathrm{G}\}|\right) \end{aligned} \tag{3.59}$$

Following [70], the PDF of the absolute value of the Gaussian distribution $|\Delta_\mathrm{G}|$ is equal to the half normal distribution written as:

$$p(x) = \frac{\sqrt{2}}{w\sqrt{\pi}}e^{-\frac{x^2}{2w^2}}, \text{ for } x \geq 0. \tag{3.60}$$

$\mu_\mathrm{f} = w\sqrt{\frac{2}{\pi}}$ is the mean of the half normal Gaussian distribution and $w_\mathrm{f}^2 = \mu^2 + w^2 - \mu_\mathrm{f}^2$ is the variance of the half normal Gaussian distribution. The PDF of the addition of two independent

variables is the convolution of their PDFs. The PDF of $\left(||\mathcal{R}\{\tilde{\Delta}_{\mathrm{G}}\}|| + ||\mathcal{I}\{\tilde{\Delta}_{\mathrm{G}}\}||\right)$ is:

$$p(x) = \frac{1}{\sqrt{2\pi}w} e^{-\frac{x^2}{8w^2}}, \text{ for } x \geq 0. \tag{3.61}$$

Now the PDF of the sinusoidal term in Eq. (3.58) is derived. The sinusoidal height profile $h_{\mathrm{s}}[n]$ is written as:

$$h_{\mathrm{s}}[n] = A_{\mathrm{h}} \cos(qn), \tag{3.62}$$

Following [71], in the limit: $nx \to \infty$ the continuous PDF of the sinusoidal height profile $p(h)$ is written as:

$$p_{\mathrm{s}}(h) = \frac{1}{\pi A_h \sqrt{1 - \left(\frac{h_s}{A_h}\right)^2}}. \tag{3.63}$$

This is called the ArcSin-distribution A. Figure (3.14) is the plot of the PDF $p_s(h_{\mathrm{s}})$ (Eq. (3.63)) of the sinusoid $h_{\mathrm{s}}[n]$ as a function of the normalize amplitude $\frac{h_{\mathrm{s}}}{A_{\mathrm{h}}}$.

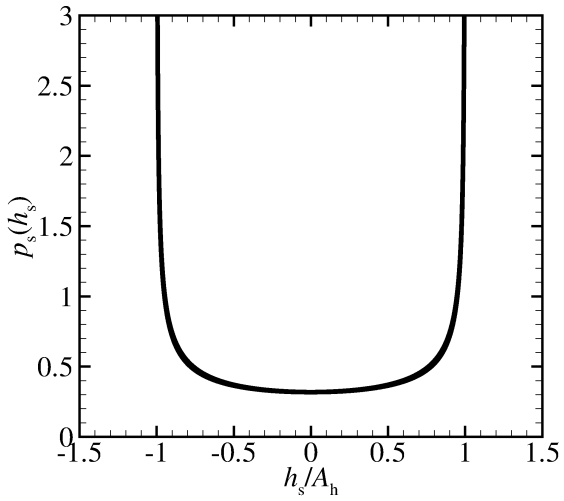

Figure 3.14: Plot of the PDF $p_{\mathrm{s}}(h_{\mathrm{s}})$ of the sinusoidal height profile $h_{\mathrm{s}}[n]$ in the limit: $nx \to \infty$ as a function of the normalize amplitude $h_{\mathrm{s}}/A_{\mathrm{h}}$.

In the limit $nx \to \infty$, the continuous PDF of the mode corresponding to k is written as:

$$p(h_k(n)) = \frac{1}{\pi R(k) \sqrt{1 - \left(\frac{h_k(n)}{R(k)}\right)^2}}. \tag{3.64}$$

Its characteristic function is written as:

$$\tilde{\phi}_{h_k}(q') = \langle e^{iqh_k[n]} \rangle = \mathcal{J}_0(q'R(k)), \tag{3.65}$$

$\mathcal{J}_0()$ is the Bessel function of the first kind. Then the characteristic function of the height profile is written as:

$$\phi_h(q') = \prod_{k_{\mathrm{r}}}^{k_{\mathrm{s}}} \phi_{h_k}(q'). \tag{3.66}$$

This approach results in the undefined product in Eq. 3.66, except for $H = -\frac{1}{2}$. Assuming $H = -\frac{1}{2}$, The discrete periodic height profile $h[n]$ is written as:

$$h[n] = \sum_{k=k_{\mathrm{r}}}^{k_{\mathrm{s}}} AR. \tag{3.67}$$

The continuous characteristic function is written as:

$$\phi_h(q') = \left(e^{-4h_0^2 w^2 q'^2} \mathcal{J}_0\left(4h_0^2 w^2 q'^2\right)\right)^{k_{\mathrm{s}}-k_{\mathrm{r}}} \approx e^{-\frac{w^2 q'^2}{2}}, \text{ for } k_s >> k_r. \tag{3.68}$$

The inverse Fourier Transform of this function is a bounded PDF approximating the Gaussian distribution. It can be concluded that the PSDM for $H = -1/2$ numerically generates the periodic surface with the bounded height distribution which approximates the Gaussian distribution with the $\mu = 0$ and variance w^2. It is concluded that by this approach there is no analytical expression found for the proportionality between the substrate width L_x, correlation length ξ and the Hurst's exponent H when the PDF $p(h)$ is Gaussian.

Chapter 4

Proportionality between area and load: Thermodynamic, fractal and continuum corrections to the proportionality coefficient

"*This is a game of misses. The guy who misses the best is going to win.*"

Ben Hogan

4.1 Introduction

An important quantity to study in tribology is the real contact area fraction a_r. It is well known that experiments [7] and theory show that this real area of contact A is much smaller than the projected area A_0 of the contacting nominally flat surfaces. It is also well known that for a small nominal pressure $\bar{p}$, a linear dependence of a_r on the nominal pressure $\bar{p}$ is observed. However, to this date, no consensus has been reached to the precise value of the proportionality coefficient κ between a_r and $\bar{p}$ for the small nominal pressures $\bar{p}$.
Statistical asperity models predict κ ranging from 1.6 to 2.51, and dependent on the Hurst's exponent H [10, 11]. According to Persson [12], the value of κ is independent of the Hurst's exponent H. Also, brute-force contact mechanic models predict κ independent of the Hurst's exponent H and ranging from 1.9 to 2.2. Moverover, according to Hyun *et al.* [9], the proportionality coefficient κ has a higher order-dependency on the Poisson's ratio ν. However, up to date, the aforementioned brute-force methods were only applied to incompressible semi-infinite solids [4, 5], or the value of κ was reported for a single aspect ratio $a = 1$ [9], where the aspect ratio a is the substrate height z_m over the periodic cell width L_x.
In this chapter, we determine κ for an elastic slab with various values of the Poisson's ratio ν, the aspect ratios a and the Hurst's exponent H, in the thermodynamic, fractal and continuum (TFC) limit. The proportionality coefficient κ in the TFC-limit can be thought of as the continuum mechanical value of κ obtained through extrapolation of its numerically calculated values. We numerically calculate the real contact area of a nominally flat rough rigid punch with self-affine roughness indenting the elastic slab with a flat surface. We assume hard-wall interactions between the bodies. We determine the relative contact area as the fraction of the surface where z-position of the rigid punch and the surface of the elastic solid coincide at the static equilibrium.
First, the value of κ is determined for the incompressible semi-infinite elastic solid. Unexpectedly, we observe a difference of a factor 0.5 between the value of κ reported by Prodanov *et al.* [5] and this work. Note that the work by by Prodanov *et al.* [5] also uses the GFMD approach. We find that the difference is the result of omitting the scaling of the energy in the discrete fast Fourier transform (DFFT) library [49]. Therefore, the value of κ is redetermined for the incompressible semi-infinite solid with the GFMD method described by Prodanov *et al.* [5] with correct scaling in DFFT. Subsequently, we study the effect of the Poisson's ratio ν and the aspect ratio a on the value of κ. No consensus has up to date been reached on the effect of the aspect ratio a and the higher-order dependency of the value of κ on the Poisson's ratio ν. We expect the value of κ to decrease when the effective strength of the elastic slab increases [41]. Therefore, the value of κ is expected to decrease with a decrease in aspect ratio a. Moreover, in this work, we observe no higher-order dependency on the Poisson's ratio ν.
The remainder of this chapter is organized as follows: In Sec. 4.2, we present the definition of proportionality coefficient κ in the TFC-limit. Then, we give the method used in this work. The proportionality coefficient κ is determined for the semi-infinite solid in Sec. 4.3. Subsequently, we determine the proportionality coefficient κ for the elastic slab in Sec. 4.4. This work ends with the conclusion and the discussion in Sec. 4.5. In the appendix, we briefly revisit Persson's [12] derivation of the value of the proportionality coefficient κ.

4.2 Thermodynamic, fractal and continuum limit

Following Bush *et al.* [11], the linear scaling of a_r with $\bar{p}$ for an elastic semi-infinite body and non-adhesive contacts is:

$$a_\mathrm{r} = \frac{\kappa \bar{p}}{\bar{g} E^*}, \tag{4.1}$$

where E^* is the effective modulus and $\bar{g}$ the root mean square gradient (RMSG). In Fig. 4.1, we show the normalized power spectral height function $C_h(q)/C_h(0)$ as a function of the wave number q used in PSDM.

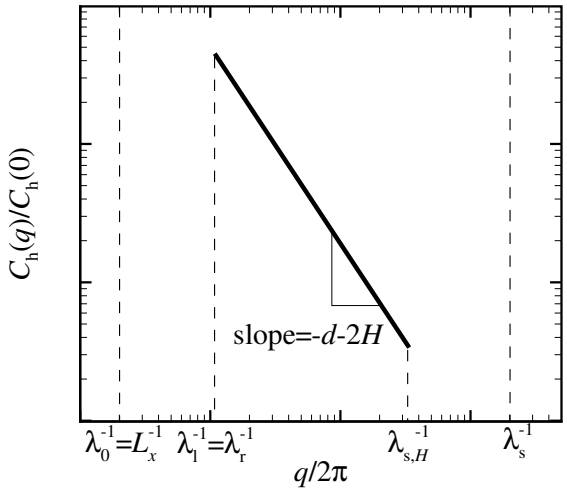

Figure 4.1: Log-log plot of the power spectral height function $C_h(q)$ as a function of the wave number q with the Hurst's exponent H, dimension of the surface d, the largest wavelength $\lambda_0 = L_x$, the cut-off wavelength $\lambda_\mathrm{r} = \lambda_\mathrm{l}$, the cut-on wavelength $\lambda_{\mathrm{s},H}$ and smallest wave length λ_s.

The RMSG $\bar{g}$ numerically calculated for discrete systems in Fourier space is:

$$\bar{g} = \sum_q = q^2 |\tilde{h}\,(q)\,|. \tag{4.2}$$

In this work, we use the GFMD method, where the finite sized system is discretized and periodic over finite width L_x. When a boundary-value problem is discretized by introducing a grid with nx grid-points, the boundary-value problem transforms from a singular to a regular perturbation problem. The singular nature of the problem resurfaces when we study the continuum mechanical proportionality coefficient κ. We can not numerically calculate a proportionality coefficient κ with $nx \to \infty$. Therefore, we use the following mathematical approach.
In order to calculate the continuum mechanical proportionality coefficient κ, we replace the discrete periodic Fourier transforms with Fourier integrals. These Fourier integral represent an infinite continuous system, *i.e.* continuum mechanical description. Therefore, we change from a periodic to an infinite representation of the surface in Fourier space, and satisfy the thermodynamic limit $L_x \to \infty$. An infinite representation excludes finite-size repetitive cell effects, and is thus called in this work the thermodynamic limit. In this work, following [5], we chose to define the thermodynamic discretization $\epsilon_\mathrm{t} = \lambda_l/\lambda_0$. We argue that the thermodynamic discretization presents the convergence to the required stochastic properties of the roughness. A large thermodynamic discretization results in a strictly non-Gaussian height distribution $p(h)$, and the rough surface has

only a few large "macro asperities", that cluster the contact zone. This clustering coupled with the periodicity L_x changes the elastic response of the surface, and consequently the topography and the value of the real contact area fraction a_r [32]. It is important to note that no consensus has yet been reached on the effect of the strictly non-Gaussian height distribution on the proportionality coefficient κ.

The continuum representation of the surface is only reached when the discrete Fourier transform becomes a continuous integral in Fourier space, and this continuous integral is reached in the fractal limit $\lambda_{s,H}/\lambda_\mathrm{l} \to 0^+$. Note that this decrease in magnitude of $\lambda_{s,H}/\lambda_\mathrm{l} \to 0^+$ can be thought as incorporating smaller and smaller roughness in to the description of the self-affine rough surface. In this work, following [5], we chose to define the fractal discretization $\epsilon_\mathrm{f} = \lambda_{\mathrm{s},H}/\lambda_l$. The fractal discretization represents the resolution of individual asperities [5, 32], not to be confused with the highest resolution of the smallest roughness. According to Prodanov *et al.* [5], the fractal discretization has to be small for large values of the Hurst's exponent H, where roughness lives more strong on large length scales. Moreover, the self-affine scaling over successive wave numbers increases with increasing Hurst's exponent H, and the scaling results in the need for a small fractal discretization to correctly represent the local topography of the individual asperity. No consensus is up to date reached on the effect of large fractal discretization. We expect that for a large fractal discretization the roughness represents a set of uncorrelated uncoupled spherical asperities, because the roughness is presented by the summation of a set of sinusoids over a small number of successive wave numbers q.

According to Prodanov *et al.* [5], the nx-grid points introduce discretization effects. These discretization effects are the result of a finite number of wave numbers describing the smallest asperities corresponding to the length scale $\lambda_{\mathrm{s},H}$. Therefore, the surface has a finite minimum deformation length scale λ_s. That is why we also study the continuum limit $nx \to \infty$. In this work, following [5], we chose to define the continuum discretization $\epsilon_\mathrm{c} = \lambda_\mathrm{s}/\lambda_{\mathrm{s},H}$. The smallest length scales of self-affine roughness determine the root mean square gradient (RMSG) $\bar{g}$ [5], and for a self-affine roughness, with a low Hurst's exponent H, the roughness is most prevalent at the smallest length scales. For a smaller continuum discretization, we expect that the resolution increases of the smallest roughness, and thus the discretization effects decrease.

It is well known that, when we assume that the value of the proportionality coefficient κ^TFC in the TFC-limit is unique, *i.e.*, a unique value of κ in the TFC-limit is independent of the order in which we extrapolate the three individual limits, we can, following to Prodanov *et al.* [5], write the proportionality coefficient in the TFC-limit κ^TFC as:

$$\kappa^\mathrm{TFC}\left(\bar{p}/E^*\bar{g}, H\right) = \kappa^\mathrm{sim}\left(\bar{p}/E^*\bar{g}, H, \epsilon_\mathrm{t}, \epsilon_\mathrm{f}, \epsilon_\mathrm{c}\right) - C_\mathrm{t}\epsilon_\mathrm{t}^{\alpha_\mathrm{t}} - C_\mathrm{f}\epsilon_\mathrm{f}^{\alpha_\mathrm{f}} - C_\mathrm{c}\epsilon_\mathrm{c}^{\alpha_\mathrm{c}}, \tag{4.3}$$

where,

$$\begin{aligned} \epsilon_\mathrm{t} &= \frac{q_0}{q_\mathrm{l}}; \\ \epsilon_\mathrm{f} &= \frac{q_\mathrm{l}}{q_{\mathrm{s},H}}; \\ \epsilon_\mathrm{c} &= \frac{q_{\mathrm{s},H}}{q_\mathrm{s}}. \end{aligned} \tag{4.4}$$

According to Prodanov, $\alpha_\mathrm{c} = \alpha_\mathrm{f} = 0.67$, $\alpha_\mathrm{t} = 1$ for $0.3 \leq H \leq 0.8$. We extrapolate the proportionality constant κ^sim to the TFC-limit κ^TFC by computing the coefficients and exponents to the independent continuum, fractal and thermodynamic discretization. We then can determine the

individual corrections e_i to the value of κ^{sim}:

$$\begin{aligned} e_{\mathrm{t}} &= C_{\mathrm{t}}\epsilon_{\mathrm{t}}^{\alpha_{\mathrm{t}}}, && \text{for the thermondynamic correction;} \\ e_{\mathrm{f}} &= C_{\mathrm{f}}\epsilon_{\mathrm{f}}^{\alpha_{\mathrm{f}}}, && \text{for the fractal correction;} \\ e_{\mathrm{c}} &= C_{\mathrm{c}}\epsilon_{\mathrm{c}}^{\alpha_{\mathrm{c}}}, && \text{for the continuum correction.} \end{aligned} \tag{4.5}$$

Moreover, we are then able to determine the ensemble error $e = e_{\mathrm{t}} + e_{\mathrm{f}} + e_{\mathrm{c}}$ for a given thermodynamic, fractal and continuum discretization. Note that a proportionality coefficient κ might have an error up to 20%, if it is not extrapolated to the TFC-limit [27]. This error makes it necessary to extrapolate an observable to the TFC-limit or make a choice of continuum, fractal and thermodynamic discretization depending on the error one choses to tolerate.
The values of κ at $\bar{p}/E^* \approx 0.1$ obtained by different authors are given in Tab. 4.1. This is an extension to the concise summary reported by Prodanov *et al.* [5].

Authors	H	κ	$\epsilon_{\mathrm{c}}^{-1}$	$\epsilon_{\mathrm{f}}^{-1}$	$\epsilon_{\mathrm{t}}^{-1}$	a	$\kappa = \mathrm{f}(x)$
Bush *et al.* [11]	0...1	$\sqrt{8/\pi}...\sqrt{2\pi}$	0	≈ 1	0	∞	H
Persson [12]	0...1	$\sqrt{8/\pi}$	0	0	0	∞	-
Hyun *et al.* [40]	0.3...0.9	2.2...1.8	2	≈ 1000	1	1	ν, H
Campañá *et al.* [4]	0.2...0.8	2.09...1.98	ext.	≈ 1000	1	∞	H
Prodanov *et al.* [5]	0...0.8	2.16...1.93	ext.	ext.	ext.	∞	-

Table 4.1: The values of κ at $\bar{p}/E^* \approx 0.1$ obtained by different authors. The term "$\kappa = \mathrm{f}(x)$" indicates the observed dependency of the value of κ, "ext." means extrapolation to the corresponding limit, *i.e.*, $\epsilon_i \to 0^+$.

Bush *et al.* [11] use, in their work, as statistical asperity model. Therefore, his value of κ is reported in the continuum- and thermodynamic limit. However, they choose to describe the individual asperities as uncorrelated uncoupled non-spherical asperities, and have but several wavelength corresponding to the radii of the spherical asperities tips, *i.e.*, $\epsilon_{\mathrm{f}}^{-1} \approx 1$ (see Fig. 1.1).
Persson [12] formulated a renormalization-group theory without any assumptions on the individual asperity shapes. Via the Fourier integral of the assumed self-affine surface topography, he satisfies all three limits. In Appx. 4.A, we give the derivation of the value of the proportionality coefficient κ for the statistical model by Persson [12], and we comment on the effect of slab height z_{m}.
Hyun *et al.* [9] use an FEM model in plane strain, and report $1.8 \leq \kappa \leq 2.2$ for the finite-height slab with $a = 1$ and Poisson's ratios $0 \leq \nu \leq 0.5$. They observe that the proportionality coefficient κ is dependent on the Hurst's exponent H. Moreover, they report that the proportionality coefficient has a higher-order dependency on the Poisson's ratio ν (see Fig. 1.4). Hyun *et al.* [40] choose $\epsilon_{\mathrm{c}}^{-1} = 2$, and vary $\epsilon_{\mathrm{f}}^{-1} \leq 1000$. Note that for a real system, it is known that there is a finite length scale for which the continuum description of the surface no longer holds true (see Chapter 3). Therefore, they gave a description of the value of the proportionality coefficient κ for a real system.
The previously mentioned method all assume a 1-dimensional surfaces. Campañá *et al.* [4] and to Prodanov *et al.* [5] both use the GFMD approach to model the contact for an (2+1)-dimensional incompressible semi-infinite linear elastic solid squeezed against a rough rigid substrate with self-affine roughness. For the 2-dimensional surface the value of the proportionality constant κ is expected to be lower [73] than for a 1-dimensional surface. The difference in method between both works is the choice of range of Hurst's exponents H and the performed extrapolations. Note that the reason for the range of values of κ according to Campañá *et al.* [4] is a dependency of κ on the

Hurst's exponent H, and according Prodanov *et al.* [5] the 10% difference between minimum and maximum value of κ is due to the choice of the TFC-discretization in his numerical calculations.

4.2.1 Methodology

4.2.1.1 Choice of parameters

In this work, we determine the individual corrections e_i to the numerically calculated proportionality coefficient κ^{sim} for the contact between a $(1+1)$-dimensional compressible linear-elastic solid and a rough rigid punch with a 1-dimensional self-affine surface topography. In order to do so, we extrapolate the numerically calculated proportionality coefficient κ^{sim} to the TFC-limit value κ^{TFC} using Eq. (4.3). The dimensionless nominal pressure $\bar{p}^* = \bar{p}/E^*\bar{g} = 0.007$ is chosen such that it is comparable to the nominal pressure used in the brute-force methods in Tab. 4.1 [9, 64, 5]. Moreover, the value of the nominal pressure $\bar{p}$ is kept below the yield strength of aluminum, the elastic modulus is taken as $E = 70$ GPa. Note that by keeping the dimensionless nominal pressure constant $\bar{p}^* = \bar{p}/E^*\bar{g} = 0.007$, the expected contact area fraction $a_{\mathrm{r}} \approx 0.014$. The method we use in this work is comparable to the method by Prodanov *et al.* [5], and we present the method in the following.
First, we chose a reference system with constant discretizations ϵ_i. These constant discretizations of the reference system are $\epsilon_{\mathrm{c}}^{-1} = 2$, $\epsilon_{\mathrm{f}}^{-1} = 1024$ and $\epsilon_{\mathrm{t}}^{-1} = 2$. We chose these values in accordance with Prodanov *et al.* [5], and the continuum and fractal discretization are comparable to those used by Hyun *et al.* [9] (see Tab. 4.1). Note that $\epsilon_{\mathrm{f}}^{-1} = 1024$ with $\epsilon_{\mathrm{f}}^{-1} = \infty$ and $\epsilon_{\mathrm{t}}^{-1} = \infty$, gives a maximum 4% error [5].
Then, we vary the continuum discretization over the values $\epsilon_{\mathrm{c}}^{-1} = 1, 2, 4, 8$ and numerically calculate κ^{sim}, all the while keeping the fractal and thermodynamic discretization constant, *i.e.*, $\epsilon_{\mathrm{f}}^{-1} = 1024$ and $\epsilon_{\mathrm{t}}^{-1} = 2$. Subsequently, we vary the thermodynamic discretization over the values $\epsilon_{\mathrm{t}}^{-1} = 1, 2, 4, 8$, all the while keeping the other two discretizations at the values of the reference system. Finally, we vary the fractal discretization over the values $\epsilon_{\mathrm{f}}^{-1} = 512, 1024, 2048, 4096$, again keeping the other two discretizations constant and numerically calculate κ^{sim}. For each individual discretization ϵ_i, we perform N numerical calculations with different surface topographies with constant second-order statistics, *i.e.*, Hurst's exponent H and auto-correlation length $\xi = \lambda_{\mathrm{r}}$, using the power spectral density method (PSDM) (see Chapter 3). The average and the variance of the proportionality coefficient κ^{sim} are calculated over the N roughness realizations. Note that we chose $N > 10$ for all performed simulations.
With the average values of $\kappa^{\mathrm{sim}}(\epsilon_i)$ as a function of the discretization ϵ_i, we perform a power-law fit using Eq. (4.3) to determine the coefficient C_i and the exponent α_i for each individual limit. We do this over various values of the Hurst's exponent H, Poisson's ratio ν and aspect ratio a, and discuss these various values in the following.
The proportionality coefficient κ is $\kappa = \mathrm{f}(\bar{p}^*, H, a_{\mathrm{r}})$. Following the GFMD approach presented by Venugopalan *et al.* [3], we are now able to study, contrary to Prodanov *et al.* [5], the influence of the tangential displacement of the substrate on the value of κ. In this work, we can rewrite the proportionality coefficient κ as $\kappa = \mathrm{f}(\bar{p}^*, \nu, z_{\mathrm{m}}, L_x, H, a_{\mathrm{r}})$. We decide to reduce the number of simulations one needs to perform by studying only the influence of the aspect ratio $a = z_{\mathrm{m}}/L_x$. We do this because the fundamental linear-elastic solution of a sinusoidal displacement at the surface is a function of the aspect ratio a, not the individual values of L_x and z_{m} (see Chapter 2). Therefore, in this work, we express the proportionality coefficient:

$$\kappa^{\mathrm{TFC}}\left(\bar{p}/E^*\bar{g}, \nu, a, H\right) = \kappa^{\mathrm{sim}}\left(\bar{p}/E^*\bar{g}, \nu, a, H, \epsilon_{\mathrm{t}}, \epsilon_{\mathrm{f}}, \epsilon_{\mathrm{c}}\right) - C_{\mathrm{t}}\epsilon_{\mathrm{t}}^{\alpha_{\mathrm{t}}} - C_{\mathrm{f}}\epsilon_{\mathrm{f}}^{\alpha_{\mathrm{f}}} - C_{\mathrm{c}}\epsilon_{\mathrm{c}}^{\alpha_{\mathrm{c}}}. \tag{4.6}$$

We chose the Hurst's exponents $H = 0.3, 0.5, 0.8$. These values of the Hurst's exponent H are chosen as such, because both statistical asperity models [11, 22] and brute-force methods [9, 64, 5] report the proportionality coefficient κ for these particular values. Moreover, it is commonly known that metallic surfaces display roughness with Hurst's exponents H in this range (see Chapter 3).
We perform the numerical calculations in this work with Poisson's ratio ν approaching the incompressible solid $\nu = 0.49$, the Poisson's ratio of aluminum $\nu = 0.33$ and the minimum Poisson's ratio $\nu = 0.20$ found in engineering metals, i.e., cast iron [41].
Moreover, the value of κ is determined for the semi-infinite slab, aspect ratio $a = 4$ approaching the semi-infinite solid, the aspect ratio $a = 1$, and the aspect ratio $a = 0.5$. We observe that the results for the compressible semi-infinite solid and the substrate approaching a semi-infinite solid are comparable. This is as to be expected, and we do this in order to verify our values of κ over successive sections. Moreover, we chose the aspect ratio $a = 1$ to compare the numerical results in this work with the results from the FEM calculations by Hyun *et al.* [40] (see Tab. 4.1).

4.2.1.2 Numerical method

We use two methods to reach the desired dimensionless nominal pressure $\bar{p}^*$. The choice of method depends on the aspect ratio a. For the semi-infinite solid, we prescribe the nominal pressure $\bar{p}$ on the surface. For the finite-height slab, the desired dimensionless nominal pressure $\bar{p}^*$ is obtained by an iterative method. In this method, we start with giving the rough rigid punch an initial average displacement, and numerically calculate displacement at the surface. Then, the nominal pressure $\bar{p}$ is calculated as the uniform traction in the normal direction $\tilde{\tau}_3(q = 0)$. Depending on the sign of the difference between the required and the numerically calculated dimensionless nominal pressure $\bar{p}^*$, we scale the average displacement of the punch by a factor 2 or 0.5. The equilibrium position is numerically calculated again, and we do this until the dimensionless nominal pressure $\bar{p}^*$ has converged within an 0.1% error.
In this work, for a constant aspect ratio a, we vary the Hurst's exponent H and the Poisson's ratio ν. Following the method by Prodanov *et al.* [5], we assume the exponents α_i in Eq. (4.6) to be independent of the Hurst's exponent H and Poisson's ratio ν. The assumption of independence from the Poisson's ratio ν is confirmed in Sec. 4.3. In this work, we use the following method to determine the correction $e_i = C_i \epsilon_i^{\alpha_i}$: First, we determine the power-law fit for a given Hurst's exponent H and Poisson's ratio ν, *i.e.* α_i and C_i. Then, we calculate the average exponent $\bar{\alpha}_i$ over all exponents α_i with $H = 0.3, 0.5, 0.8$ and $\nu = 0.2, 0.33, 0.5$ over each individual limit. Subsequently, we perform a linear-fit with the scaled discretization $\epsilon_i^{\bar{\alpha}_i}$ to determine the corresponding coefficient C_i. The numerical results we present in tables with the values of C_i and α_i of the power-law fit and values of C_i and $\bar{\alpha}_i$ of the linear-fit. Finally, we plot the linear-fit of the numerically calculated average values of κ as a function of the scaled discretization $\epsilon_i^{\bar{\alpha}_i}$ for each individual limit.
Note that, *a priori*, it is not known whether the exponents α_i have a dependency on the aspect ratio a. Therefore, we repeat the aforementioned power-law and linear-fits for each aspect ratio a.
We start in the next section with the analysis of the semi-infinite incompressible solid, because of the large difference between the value of κ we observe in this work and the value of κ observed by Prodanov *et al.* [5].

4.3 Semi-infinite solid

We determine the TFC corrections for the rough rigid punch indenting the incompressible elastic semi-infinite solid. Note that the effective strength of the incompressible semi-infinite solid is given by the effective modulus, so there is no higher-order dependency on ν. We perform $N = 30$ different rough surface realizations for each mean and variance value of κ for a given limit ϵ_i and Hurst's exponent H. In this section, we use the GFMD method described by Prodanov *et al.* [5] with correct scaling in DFFT. Note that we use G++ to compile the FFTW3. In Fig. 4.2, we show how the proportionality coefficient κ depends on the discretization ϵ_i for the reference values of ϵ_i .

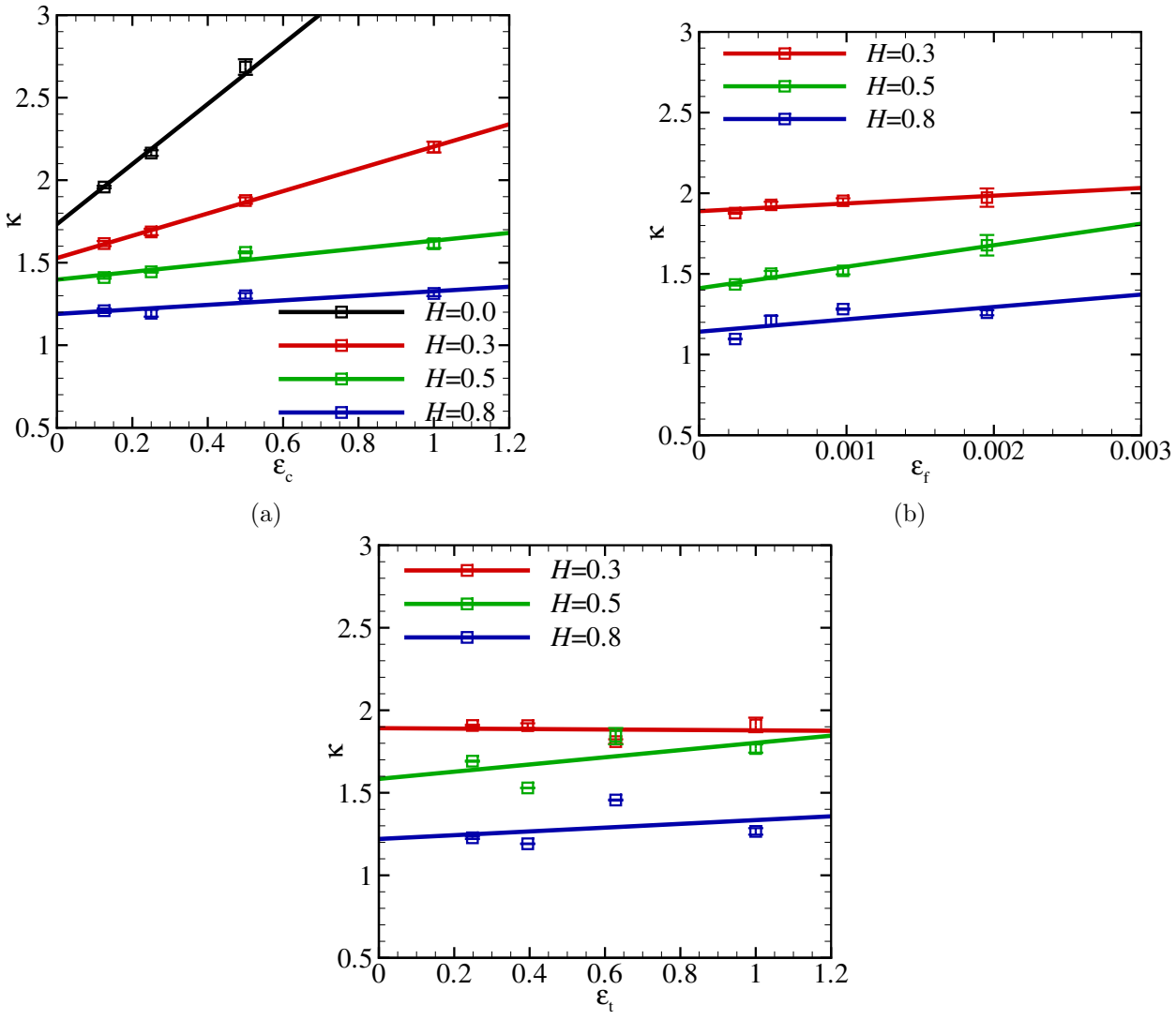

Figure 4.2: Plot of the proportionality coefficient κ as a function of (a) the continuum discretization ϵ_c (b) the fractal discretization ϵ_f and (c) the thermodynamic discretization ϵ_t with Hurst's exponents $H = 0.3, 0.5, 0.8$.

The values of the proportionality coefficient κ that we numerically calculate are between 0.75 to 0.5 times the previously reported values of the proportionality coefficient κ [10, 11, 40, 4, 5].

The smaller value of the proportionality coefficient κ is due to the result of the higher effective strength [41] of the semi-infinite solid. Especially striking is the difference between the value of the proportionality coefficient κ in this work and previous GFMD simulations by Campañá *et al.* [64] and Prodanov *et al.* [5]. Note that we only present the linear fit on the numerically calculated values of κ for $H = 0.0$ with different continuum discretizations. This is done in order to show results for a self-affine surface with a strictly Gaussian height distribution $p(h)$ (see Chapter 3).
We found that the difference in previously reported values of the proportionality coefficient κ for numerical calculations by GFMD simulations were the result of omitting the scaling of the displacement $\tilde{u}(q)$ and elastic energy density v_{el} while using the DFFT. According to Prodanov *et al.* [5], they use the FFTW library [49]. For a purely real input to the DFFT, the output satisfies the Hermitian redundancy, *i.e.* $\tilde{u}(q) = \overline{\tilde{u}(-q)}$. The output is scaled by a factor 0.5, and the output is zero-padded to prevent possible aliasing [49]. Therefore, omitting this scaling will half the areal elastic energy, and in turn the effective strength of the semi-infinite solid. This scaling holds also true for a purely real $2-$dimensional array input to the DFFT. Moreover, we conducted several numerical calculations for a 2-dimensional surface with and without the scaling of the Fourier transform of the displacement $\tilde{u}(q)$, following the method as reported by Prodanov *et al.* [5]. We find that the values of the proportionality coefficient κ, without scaling, are equal to that reported by Prodanov *et al.* [5]. For the correct scaling, we find values of the proportionality constant κ between 1.4 and 1.8 for the discretizations $\epsilon_{\mathrm{c}}^{-1} = 4$, $\epsilon_{\mathrm{f}}^{-1} = 512$ and $\epsilon_{\mathrm{f}}^{-1} = 2$. We used these discretizations only for determining the κ for a 2-dimensional surface in order to limit the computational time.
In Tab. 4.5, we summarize the coefficients C_i and α_i of the power-law fit, and the coefficients C_i of the linear-fit with the average exponent $\bar{\alpha}_i$ for the incompressible semi-infinite solid.

H	fit	C_{c}	C_{f}	C_{t}	α_{c}	α_{f}	α_{t}
0.0	pow.	0.685	-	-	0.902	-	-
	lin.	2.063	-	-	0.73	-	-
0.3	pow.	0.685	-	-	0.961	-	-
	lin.	0.765	48.002	-0.002	0.73	1	1
0.5	pow.	0.843	276.527	-	0.145	18.402	-
	lin.	0.273	133.402	0.0393	0.73	1	
0.8	pow.	0.249879	2.183	-	0.339	0.106	-
	lin.	0.158	122.47	0.062	0.73	1	1

Table 4.2: Coefficients C_i and exponents α_i for κ required to determined κ^{TFC} using Eq. (4.6). "pow." means power-law, "lin." means linear and "-" indicates that no suitable fit is found.

We observe that the continuum coefficient C_{c} of the linear fit decreases monotonically with a decrease in Hurst's exponent. This is as expected, because for a lower Hurst's exponent H roughness is more pronounced on shorter length scales than for $H = 0.8$. Moreover, we observe that the fractal coefficient C_{f} of the linear-fit increases non-monotonically with an increase in Hurst's exponent H. According to Prodanov *et al.* [5] and Yastrebov *et al.* [32], the resolution of the interacting macroscopic asperities is expected to have a major influence on the contact mechanical behavior for Hurst's exponent $H = 0.8$. Moreover, it is expected that the continuum mechanical behavior of interacting asperities is better approximated for a small fractal discretization ϵ_{f}. Therefore, it is as expected that the coefficient C_{f} increases for the increase in the Hurst's exponent. A possible explanation for the non-monotonic increase is the deviation of the height distribution $p(h)$ from

the required Gaussian distribution for high Hurst's exponent $H = 0.8$ and high thermodynamic limit $\epsilon_{\mathrm{t}}^{-1} = 2$. We find this aforementioned deviation from the expected monotonic increase in all but one numerical calculations in this work. Note that the maximum 8% error we observe is twice the 4% error reported by Prodanov *et al.* [5]. We find that the thermodynamic coefficient C_{t} is small in magnitude and scattered due to the poor linear-fit. This is as excepted and comparable to previous TFC-analysis [5].
Note that we neglected the poor fit of exponent $\alpha_c = 0.145$ for the Hurst's exponent $H = 0.5$ in determining the average exponent $\bar{\alpha}_{\mathrm{c}}$. Moreover, exponent α_{f} is very different for the Hurst's exponent $H = 0.5$ and $H = 0.8$, therefore we chose $\bar{\alpha}_{\mathrm{f}} \approx 1$. In Fig. 4.3, we depict how the proportionality coefficient κ depends on scaled discretization ϵ_{c} for the reference values of ϵ_i.

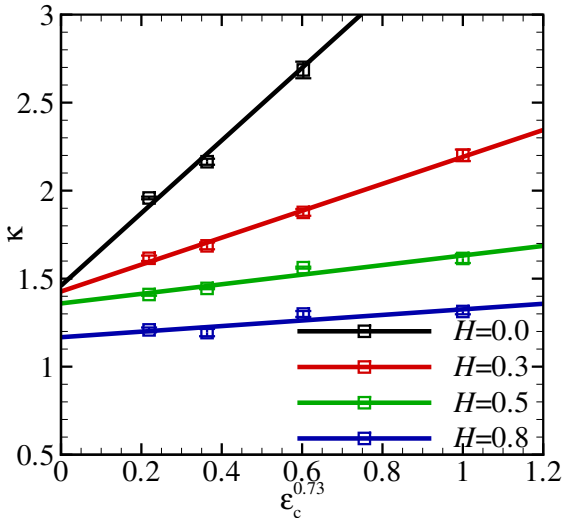

(a)

Figure 4.3: Plot of the proportionality coefficient κ as a function of the scaled continuum discretization $\epsilon_{\mathrm{c}}^{0.73}$ with $H = 0.3, 0.5, 0.8$ for the incompressible semi-infinite solid.

The value of κ decreases for all limits as the Hurst's exponent H increases. We observe that the value of the numerically calculated proportionality coefficient κ^{sim} converges to $\kappa^{\mathrm{c}} \approx 1.45$ in the continuum limit for Hurst's exponents $H = 0.0, 0.3, 0.5$. Note that, throughout this report, we find that κ^{sim} converges to $\kappa^{\mathrm{c}} \approx 1.45$ in the continuum limit with Hurst's exponents $H = 0.0, 0.3, 0.5$ for different aspect ratio's. This as to be expected from Persson's theory [12]. Persson's theory predicts that the value of $\kappa \approx 1.6$ and independent of the Hurst's exponent H. This is unexpected, because the predictions of Persson's theory commonly assumed to be more precise for high nominal pressures $\bar{p}$ than low nominal pressures $\bar{p}$. In Appx. 4.A, we give the derivation of the value of κ by Persson's theory [12]. Note that the height distribution $p(h)$ for $H = 0$ is Gaussian, independent of the ratio between the periodicity and the correlation length L_x/ξ, but for $H = 0.8$ the ratio $L_x/\xi \approx 200$ to become Gaussian (see Chapter 3).
We observe that the value of κ in the continuum limit for $H = 0.8$ is approximately 1.19. For the Hurst's exponent $H = 0.8$, we show in Chapter 3 that the height distribution $p(h)$ only approaches a Gaussian for $L_x/\xi >> 1$, *i.e.*, small thermodynamic discretization. Therefore, the reason for the difference between the value of $\kappa^{\mathrm{c}} \approx 1.45$ and $\kappa = 1.19$ for $H = 0.8$ is given by the deviation of the height distribution $p(h)$ from the Gaussian distribution for the thermodynamic discretization $\epsilon_{\mathrm{t}}^{-1} = 2$. Therefore, we conclude that the proportionality constant for the incompressible

semi-infinite solid is independent of the Hurst's exponent H and the Poisson's ratio ν, and between 0.5 and 0.75 times previously reported values of proportionality coefficient κ numerically calculated with GFMD approach [74, 5]. Note that quantifying the deviation of the numerically generated height distribution $p(h)$ from the Gaussian distribution is attempted by the author in Appx. 3.D. However, there is up to date no analytical expression for this deviation.

4.3.1 Semi-infinite compressible solid

Here, we consider various values of the Poisson's ratios $\nu = 0.20, 0.33, 0.49$. The effect of the Poisson's ratio ν was so far considered to be correctly captured by Eq. (4.1). We perform $N = 30$ different rough surface realizations, and we use the GFMD method as described by Venugopalan *et al.* [3] with his asymptotic elastic energy v_{el} for the elastic compressible semi-infinite solid. For the remainder of this work, we use Ifort to compile the F77 code and the FFTW3.

In Fig. 4.4, we show how the proportionality coefficient κ depends on the discretization ϵ_i for the reference values of ϵ_i.

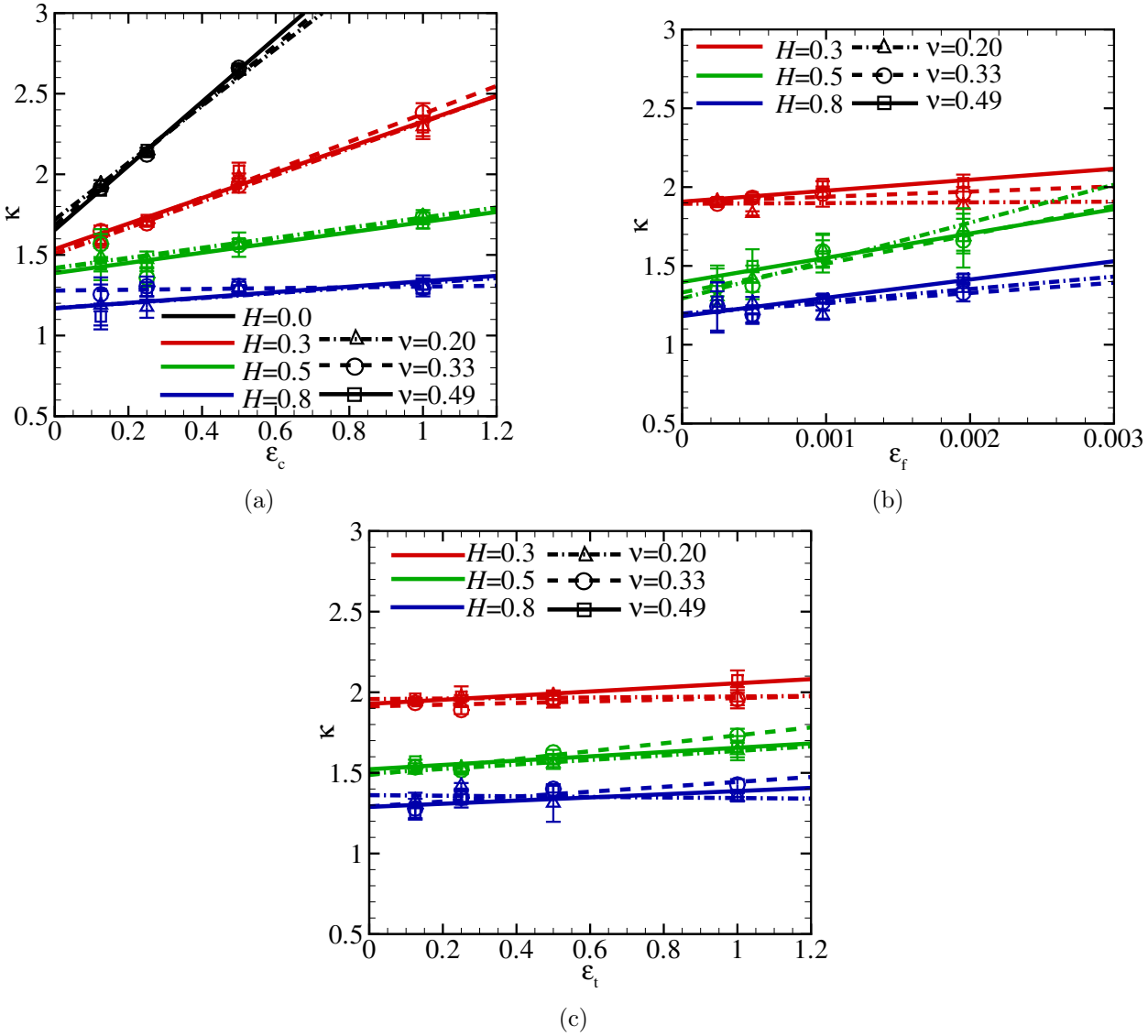

Figure 4.4: Plot of the proportionality coefficient κ as a function of (a) the continuum discretization ϵ_{c} with $H = 0.0$, (b) the fractal discretization ϵ_{f} and (c) the thermodynamic discretization ϵ_{t} with Hurst's exponents $H = 0.3, 0.5, 0.8$ and Poisson's ratios $\nu = 0.20, 0.33, 0.49$.

The value of proportionality coefficient κ in the continuum limit is between 1.20 and 1.75. The value of proportionality coefficient κ in the fractal limit is between 1.2 and 1.9. The value of proportionality coefficient κ in the thermodynamic limit is between 1.30 and 1.95. Moreover, we observe that the value of κ^{sim} tends to converge in the continuum limit. These numerically calculated values of the proportionality coefficients κ are comparable to those for the incompressible semi-infinite solid. In Fig. 4.4, we observe that the variance increases for the smallest continuum and fractal discretization with increasing Hurst's exponents H. This increase in variance is because of a numerical error. This error results in rather large error in the equilibrium displacement $\boldsymbol{u}(x)$ at the surface. Moreover, note that for the FFTW3 is compiled with G++ *i.e.*, error up to $\mathcal{O}^{-16}$, we do not observe

this increase in variance (see Fig. 4.2). After obtaining the numerical results in this work, we find that the precision could become comparable to G++ compiled code, when the array precision was increased from single to double precision in Fortran77. For the remainder of this section, we ignore the data-points with a variance much larger than observed for the incompressible semi-infinite solid. We observe no higher-order dependency of the proportionality coefficient κ on the Poisson's ratio ν in all three limits. We conclude that there is no higher-order dependence of the value of κ on the Poisson's ratio ν for a semi-infinite compressible solid. Therefore, we conclude that Eq. (4.1) is also applicable for the contact of compressible semi-infinite solids. Note that this confirms the assumption that the average exponent $\bar{\alpha}_i$ is independent of the Poisson's ratio ν.
The value of $\bar{\alpha}_c \approx 1.00$ gives the best average fit for all Hurst's exponents H and Poisson's ratio's ν. According to Prodanov *et al.* [5], the continuum and the fractal limit scale sub-linearly, *i.e.*, $\bar{\alpha}_\mathrm{c} = \bar{\alpha}_\mathrm{f} = 0.67$. α_f is very scattered, hence we chose $\bar{\alpha}_\mathrm{f} \approx 1$ for a good comparison with the CT limits. We observe that the dependence of the value of κ on ϵ_t is weak in Fig. 4.4c, therefore chose $\bar{\alpha}_\mathrm{t} = 1$. In Tab. 4.3, we summarize the coefficients C_i and α_i of the power-law fit, and the coefficients C_i of the linear-fit with the average exponent $\bar{\alpha}_i$ for the incompressible semi-infinite solid.

H	fit	C_c	C_f	C_t	α_c	α_f	α_t
0.3	pow.	1.066	-	-	0.562	-	-
	lin.	0.819	4.534	0.017	1	1	1
0.5	pow.	0.277	4.939	-	1.630	0.722	-
	lin.	0.312	240.481	0.140	1	1	1
0.8	pow.	0.358	1465.990	-	0.249	236.361	-
	lin.	0.156	78.592	-0.018	1	1	1

(a)

H	fit	C_c	C_f	C_t	α_c	α_f	α_t
0.3	pow.	0.813	-	-	1.232	-	-
	lin.	0.866	32.630	0.051	1	1	1
0.5	pow.	0.263	4.810	-	2.423	0.311	-
	lin.	0.299	182.981	0.134	1	1	1
0.8	pow.	-	442.545	-	-	62.129	-
	lin.	0.025	65.104	0.152	1	1	1

(b)

H	fit	C_c	C_f	C_t	α_c	α_f	α_t
0.3	pow.	1.233	-	0.128	0.420	-	1
	lin.	0.792	69.508	0.129	1	1	1
0.5	pow.	0.323	3.971	5	0.939	0.308	1
	lin.	0.316	154.237	0.116	1	1	1
0.8	pow.	-	1140.93	0.099	-	174.874	1
	lin.	0.168	115.985	0.0982	1	1	1

(c)

Table 4.3: Coefficients C_i and exponents α_i for κ required to determined κ^{TFC} using Eq. (4.6) with the Poisson's ratio (a) $\nu = 0.20$, (b) $\nu = 0.33$ and (c) $\nu = 0.49$.

We observe an increase in the error e_i for an increase in Poisson's ratio ν. This is as expected, when the Poisson's ratio ν increases the interaction between asperities increases. Therefore, the fractal corrections is expected to increase, which can be thought of as the importance of the exact representation of the asperity shapes. However, note that this does not effect the dependency of the value of κ on the Poisson's ratio ν in the TFC-limit.
For the given continuum limit $\epsilon_{\mathrm{c}}^{-1} = 10$ and fractal discretization $\epsilon_{\mathrm{f}}^{-1} = 0$ and thermodynamic discretization $\epsilon_{\mathrm{t}}^{-1} = 2$, the error in the value of κ^{sim} is only 5% error of the the value of κ^{TFC}. A 5% error corresponds to the continuum limit $\epsilon_{\mathrm{c}}^{-1} \to 0^{+}$ and fractal discretization $\epsilon_{\mathrm{f}}^{-1} = 512$ and thermodynamic limit $\epsilon_{\mathrm{t}}^{-1} \to 0^{+}$. Brute-force methods that employ larger fractal discretization, *i.e.*, $\epsilon_{\mathrm{f}}^{-1} = 32$, are prone to overestimate the value of κ^{TFC} by a factor two. As expected, for fractal discretization $\epsilon_{\mathrm{f}}^{-1} = 32$, Yastrebov *et al.* [32] predicted the value of κ close to the value reported by Bush *et al.* [11]. They argue that this is due to the fact that for small values of fractal discretization $\epsilon_{\mathrm{f}}^{-1}$, the contact mechanical response of a semi-infinite solid is comparable to a set of non-interacting asperities [5]. We agree with this argument.
In Fig. 4.5, we depict how the proportionality coefficient κ depends on a scaled discretization ϵ_{c} for the reference values of ϵ_i with the exponent $\bar{\alpha}_{\mathrm{c}} = 0.73$ out of Sec. 4.3.

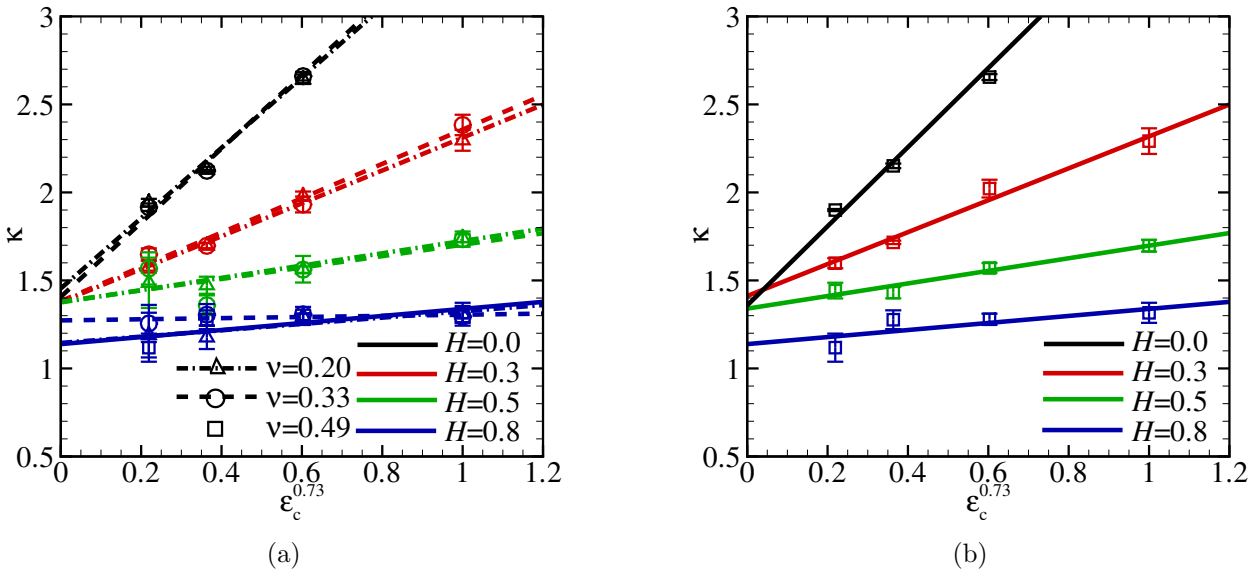

Figure 4.5: Plot of the proportionality coefficient κ as a function of the scaled continuum discretization $\epsilon_{\mathrm{c}}^{0.73}$ with $H = 0.0, 0.3, 0.5, 0.8$ for the compressible semi-infinite solid with (a) the Poisson's ratios $\nu = 0.2, 0.33, 0.49$ and (b) the Poisson's ratio $\nu = 0.49$.

In Fig. 4.5a, we observe that the value of the proportionality constant κ in the continuum limit is between 1.15 and 1.50 for the incompressible semi-infinite solid. The value of the proportionality constant κ for Hurst's exponents $H = 0, 0.3, 0.5$ converges to $\kappa^{\mathrm{c}} \approx 1.40$ in the continuum limit. We observe a large variance for $\epsilon_{\mathrm{c}}^{-1} = 8$, and chose to not consider its value here. Moreover, we observe again the behavior discussed in Sec. 4.3 for a strictly non-Gaussian height distribution $p(h)$. Therefore, we conclude that the proportionality constant κ for the compressible semi-infinite solid is independent of the Hurst's exponent H.

4.4 Finite slab

We repeat our analysis with the simulations in Sec. 4.3 considering various aspect ratios $a = 0.5, 1, 4$. Up to date, the aspect ratio a was considered of little effect on the contact area between nominally flat surfaces. We perform $N = 10$ different rough surface realizations. We want to make the link between semi-infinite solids and a finite slab. Therefore, we chose to present the aspect ratio $a \approx 4$ first. For aspect ratio $a = 10$, the contact mechanical response approaches that of the semi-infinite solid [27]. However, in order to limit the computational time, we choose $a \approx 4$. In Fig. 4.6, we depict how the proportionality coefficient κ depends on the discretizations ϵ_i for the reference values of ϵ_i with aspect ratio $a = 4$ and $a = \infty$ (Sec. 4.3).

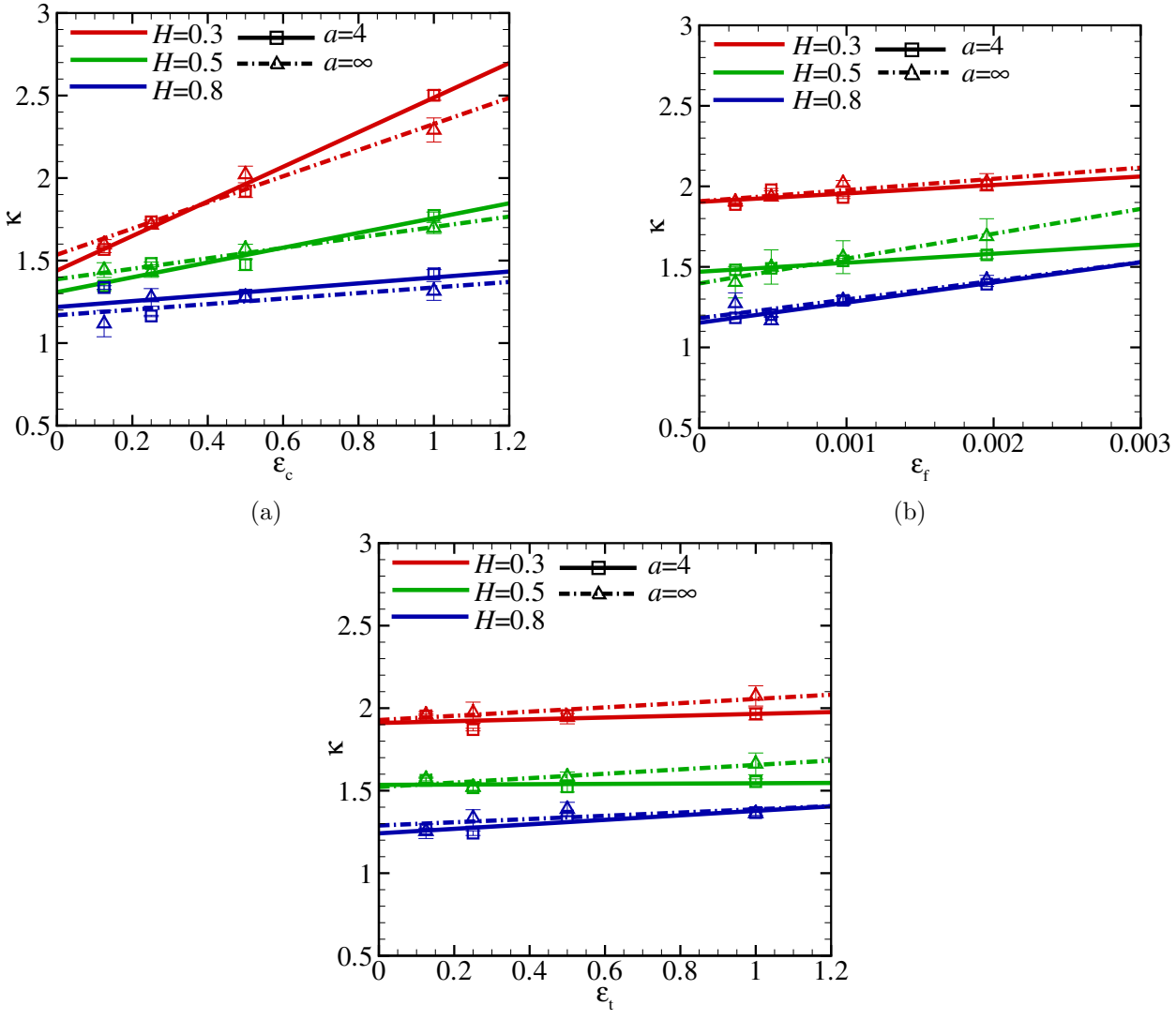

Figure 4.6: Plot of the proportionality coefficient κ as a function of (a) the continuum discretization ϵ_c, (b) the fractal discretization ϵ_f and (c) the thermodynamic discretization ϵ_t for aspect ratio $a = 4$ and $a = \infty$ with Hurst's exponent $H = 0.3, 0.5, 0.8$, and Poisson's ratio $\nu = 0.49$.

For a finite-height slab, we observe a larger variance for each data point than we calculated for a semi-infinite solid. In Tab. 4.4, we compare the coefficients C_i for $a = 4$, $a = \infty$ and Hurst's exponents $H = 0.3, 0.5, 0.8$ with the Poisson's ratio $\nu = 0.49$ and average exponent $\bar{\alpha}_i = 1$.

H	a	C_c	C_f	C_t
0.3	4	1.048	52.648	0.055
	∞	0.792	69.508	0.128
0.5	4	0.449	55.923	0.449
	∞	0.316	154.237	0.134
0.8	4	0.179	125.210	0.136
	∞	0.168	115.985	0.227

Table 4.4: Coefficients C_i for the proportionality constant κ and the average exponent $\bar{\alpha}_i = 1$ with aspect ratios $a = 4, \infty$, the Hurst's exponents $H = 0.3, 0.5, 0.8$ and Poisson's ratio $\nu = 0.49$.

As to be expected, we observe a good agreement between the error in the value of κ^sim for the finite solid in the limit of the semi-infinite solid and the semi-infinite solid in the CF-limit. However, the coefficients of the thermodynamic limit are not in agreement, and we observe again the non-monotonic increase in C_f. This difference in C_t because of the large scatter and weak dependence of the value of κ on the thermodynamic discretization ϵ_t in Fig. 4.6c. In Tab. 4.5, we summarize the coefficients C_i and α_i of the power-law fit, and the coefficients C_i of the linear-fit with the average exponent $\bar{\alpha}_i$ for the aspect ratio $a = 4$ and the Poisson's ratio $\nu = 0.49$.

H	fit	C_c	C_f	C_t	α_c	α_f	α_t
0.3	pow.	0.995	-	-	1.181	-	-
	lin.	0.879	7.591	0.055	2	0.66	1
0.5	pow.	0.401	4.503	-	1.524	0.552	-
	lin.	0.381	8.038	0.010	2	0.66	1
0.8	pow.	0.163	31.128	-	3.346	0.759	-
	lin.	0.169	17.883	0.136	2	0.66	1

Table 4.5: Coefficients C_i and exponents α_i for κ required to determined κ^TFC using Eq. (4.6) for aspect ratio $a = 4$ and Poisson's ratio $\nu = 0.49$.

Regarding the TFC-limit, we observe again that the fractal correction is substantially larger than the continuum correction and the thermodynamic correction. The average exponent $\alpha_\mathrm{c} = 2$ indicates that the error due to the continuum correction scales with the square of the continuum discretization ϵ_c. Hence, for moderate continuum discretization $\epsilon_\mathrm{c}^{-1} \approx 4$, in the fractal limit $\epsilon_\mathrm{f}^{-1} \to 0^+$ and $\epsilon_\mathrm{t}^{-1} \to 0^+$, the error is already below 5% of the value of the proportionality coefficient κ^TFC in the TFC-limit. We again observe that the fractal error e_f is doubled what was observations by Prodanov *et al.* [5]. This difference is expected to be due to the omission of the correct scaling of the DFFT by Prodanov *et al.* [5].

In Fig. 4.7, we depict how the proportionality coefficient κ depends on the scaled discretizations ϵ_i for the reference values of discretizations ϵ_i, aspect ratio $a = 4$ and Poisson's ratio $\nu = 0.49$.

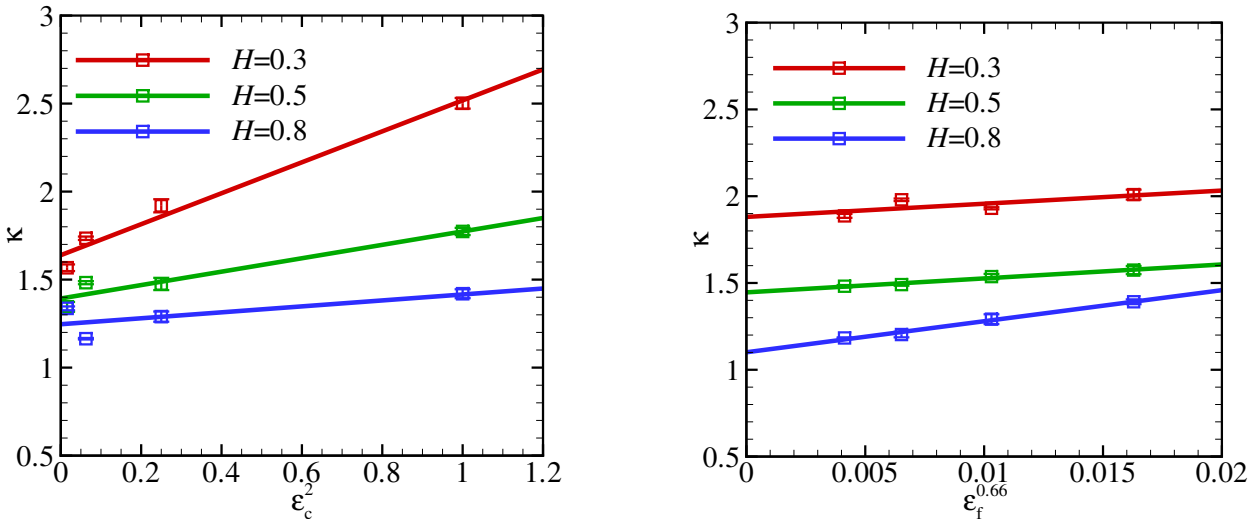

(a) (b)

Figure 4.7: Plot of the proportionality coefficient κ as a function of (a) the scaled continuum discretization ϵ_c^2 and (b) the scaled fractal discretization $\epsilon_f^{0.66}$ with Hurst's exponent $H = 0.3, 0.5, 0.8$, aspect ratio $a = 4$ and Poisson's ratio $\nu = 0.49$.

In Fig. 4.7a, we observe that the value of the proportionality coefficient κ in the continuum limit lays between 1.25 and 1.65. Considering the Hurst's exponent's $H = 0.3, 0.5$, we observe that the average expected value of the proportionality coefficient $\kappa^c \approx 1.5$. In Fig. 4.7a, we observe that the value of the proportionality coefficient κ in the fractal limit lays between 1.1 and 1.9, and are comparable to the values of κ^f for a semi-infinite solid.
The difference in κ^c for different Hurst's exponents is between 5% and 10% of the average value of κ^c. The value of the proportionality coefficient κ decreases for all limits as the Hurst's exponent H increases. We find the results non-conclusive on the dependency of the value of κ^{TFC} on the Hurst's exponent H. However, we observe that the trend between contact area and pressure is still closely approximated. Therefore, we conclude that Eq. (4.19) is applicable to an elastic finite slab with aspect ratio $a \geq 4$, and that the proportionality constant κ for $a \geq 4$ is comparable to that of the semi-infinite solid.

In Fig. 4.8, we depict how the proportionality coefficient κ depends on the scaled continuum discretizations $\epsilon_c^{0.73}$ for the reference values of discretizations ϵ_i, aspect ratio $a = 4$ and Poisson's ratio $\nu = 0.49$.

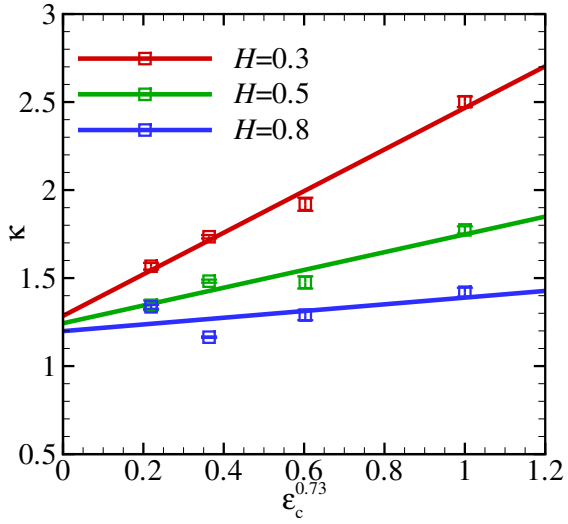

Figure 4.8: Plot of the proportionality coefficient κ as a function of the scaled continuum discretization $\epsilon_c^{0.73}$ with Hurst's exponent $H = 0.3, 0.5, 0.8$, aspect ratio $a = 4$ and Poisson's ratio $\nu = 0.49$.

Note that the exponent $\bar{\alpha}_c = 0.73$ (Sec. 4.3) does not result in the best power-law fit. However, with this power-law fit, we clearly observe the expected trend that the proportionality coefficient decreases for a decrease in aspect ratio a. We find this result non-conclusive, because of the arbitrary choice of fitting exponent $a_c = 0.73$. Moreover, this illustrates that thermodynamic, fractal and continuum corrections are case specific, *i.e.*, depending on the nominal pressure and aspect ratio, and sensitive to the choice of average exponent $\bar{\alpha}_i$. Therefore, we conclude here that the average exponent is expected to have the functional form written as $\bar{\alpha}_i = \mathrm{f}(\bar{p}^*, a)$.
The analysis of the aspect ratio a approaching the limit of the semi-infinite body is also conducted for the Poisson's ratio $\nu = 0.22, 0.30$. We find a variance up to 40% of the numerically calculated proportionality coefficient κ, and we choose not to present these results in this work. There are two reasons why we numerically calculate such a large variance: First, for a grid with $nx \geq 16384$, we find that the highest principal modes can become unstable, this is because of violating the formal Störmer-Verlet stability limit, *i.e.*, $\kappa(q)\Delta t^2 \leq 4.$, where $\kappa(q)$ is the linear force constant and Δt the discrete time-step; And, secondly, the numerical error due to precision allocation discussed in Sec. 4.3.

4.4.1 Compressible finite slab

We perform the same numerical calculations as in the previous section (Sec. 4.4) with aspect ratio $a = 1$. In Fig. 4.9, we depict how the proportionality coefficient κ depends on the limits ϵ_i for the reference values of ϵ_i with aspect ratio $a = 1$ and Poisson's ratios $\nu = 0.2, 0.33, 0.49$.

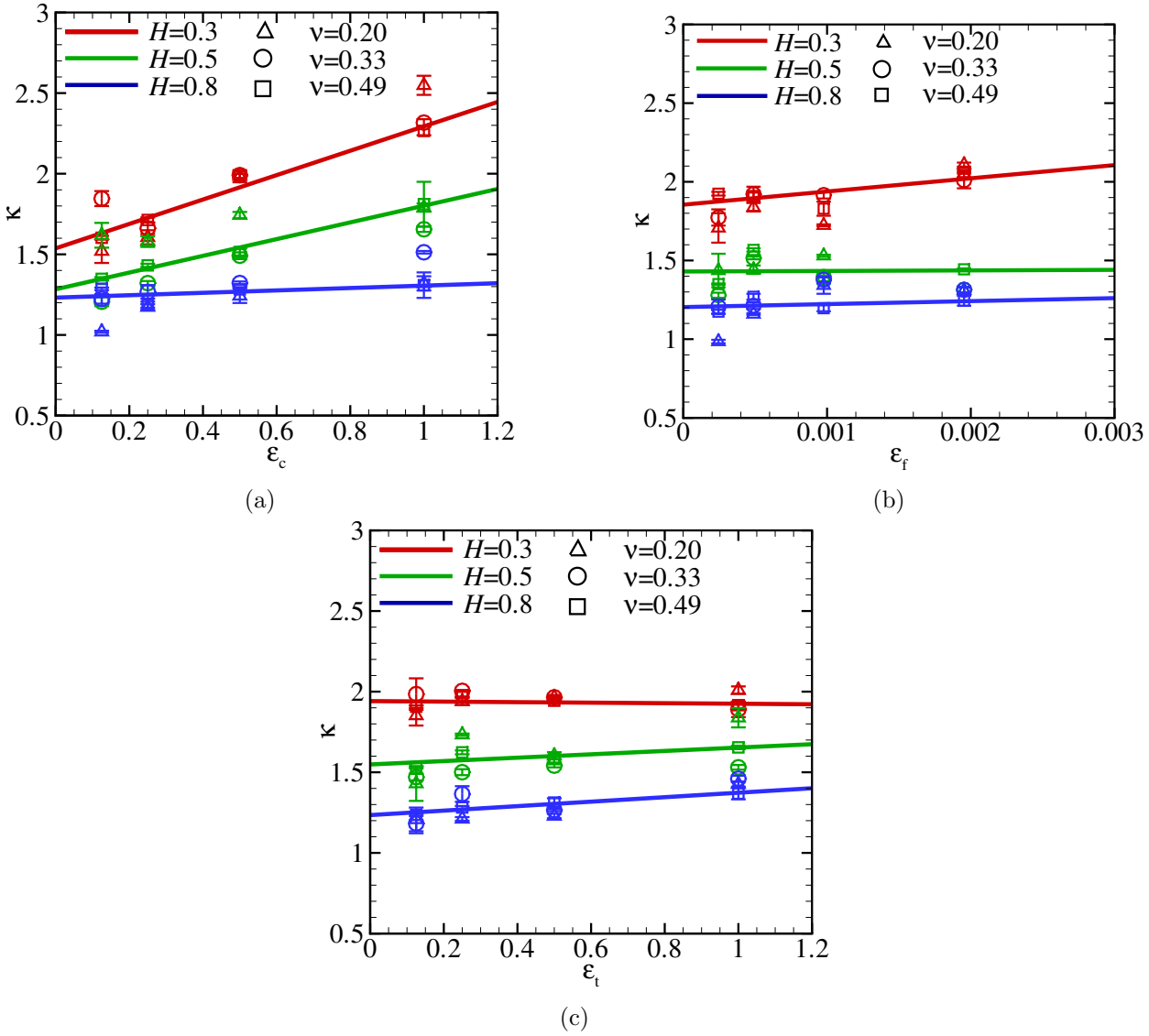

Figure 4.9: Plot of the proportionality coefficient κ as a function of (a) the continuum discretization ϵ_c, (b) the fractal discretization ϵ_f and (c) the thermodynamic discretization ϵ_t with Hurst's exponents $H = 0.3, 0.5, 0.8$, aspect ratio $a = 1$ and Poisson's ratios $\nu = 0.2, 0.3, 0.49$.

We observe a larger variance for each data point than we calculated for the compressible finite slab with aspect ratio $a = 4$ and Poisson's ratio $\nu = 0.49$. Moreover, we observe a large scatter in average value, differing for different discretizations and with no clear dependency on the Poisson's ratio ν nor the Hurst's exponent H. Due to this large variance and scatter, we omit the fits for the Poisson's ratios $\nu = 0.20, 0.33$ and the calculation of the coefficients C_i and exponents a_i.

In Tab. 4.6, we summarize the coefficients C_i and α_i of the power-law fit, and the coefficients C_i of the linear-fit with the average exponent $\bar{\alpha}_i$ for aspect ratio $a = 1$ and Poisson's ratio $\nu = 0.49$.

H	fit	C_c	C_f	C_t	α_c	α_f	α_t
0.3	pow.	1.047	-	-	0.506	-	-
	lin.	0.695	83.809	-0.0163	1.27	1	1
0.5	pow.	0.484	-	-	1.261	-	-
	lin.	0.483	3.487	0.105	1.27	1	1
0.8	pow.	0.067	-	0.377	2.043	-	0.199
	lin.	0.071	18.977	0.139	1.27	1	1

Table 4.6: Coefficients C_i and exponents α_i for κ required to determined κ^{TFC} using Eq. (4.6) for the aspect ratio $a = 1$ and Poisson's ratio $\nu = 0.49$.

Note that the linear-fit for ϵ_f is performed over three data-points. We consider these results non-conclusive. In Fig. 4.10, we depict how proportionality coefficient κ depends on scaled continuum discretization ϵ_c for the reference values of ϵ_i, aspect ratio $a = 1$ and Poisson's ratio $\nu = 0.49$.

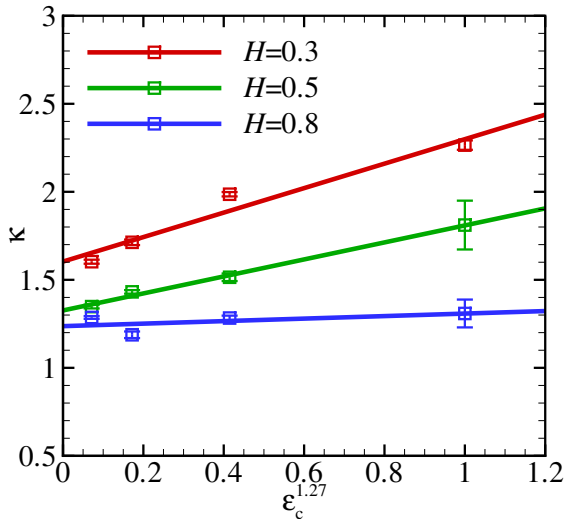

Figure 4.10

Figure 4.11: Plot of the proportionality coefficient κ as a function of the scaled continuum discretization $\epsilon_c^{1.27}$ with Hurst's exponents $H = 0.3, 0.5, 0.8$, aspect ratio $a = 1$ and Poisson's ratio $\nu = 0.49$.

In Fig. 4.10, we observe that the values of the proportionality coefficient κ in the continuum limit lay between 1.25 and 1.6. Considering the Hurst's exponent's $H = 0.3, 0.5$, we observe that the average expected value of the proportionality coefficient $\kappa^c \approx 1.4$. For the Poisson's ratio $\nu = 0.49$, we observe values of the proportionality coefficient κ in good agreement with those in Sec. 4.3. The extrapolated values of the proportionality coefficient κ with the Poisson's ratio $\nu = 0.49$ for the three corrections ϵ_i are slightly smaller than for the aspect ratio $a = 4$. This is as to be expected, because of the decrease in aspect ratio a. However, we argue that this decrease in κ is marginal, and find this observations non-conclusive.
From the calculated values of the proportionality coefficient κ with the aspect ratio $a = 1$, we

cannot determine whether there is a higher-order dependency of the proportionality constant κ on the Poisson's ratio ν. Hyun *et al.* [40] reports a higher-order dependence of κ^{TFC} on the Poisson's ratio ν for a constant continuum discretization $\epsilon_{\mathrm{c}}^{-1} = 2$, fractal discretization $\epsilon_{\mathrm{f}}^{-1} \approx 1000$ and thermodynamic discretization $\epsilon_{\mathrm{t}}^{-1} = 1$. We do not reproduce this result. The reason this difference appears can be due to the fact that, with the continuum discretization $\epsilon_{\mathrm{c}}^{-1} = 2$ and fractal discretization $\epsilon_{\mathrm{f}}^{-1} \approx 1000$, the value of κ^{obs} may not have yet converged to the continuum and fractal limit. Moreover, the small difference in the value of κ^{sim} for $\epsilon_{\mathrm{f}}^{-1} = 2048$ and $\epsilon_{\mathrm{f}}^{-1} = 4$ between different Poisson's ratios ν does not suggest so. With the current numerical calculations we find the observations non-conclusive, but they do make us expect there is no higher-order dependency of the proportionality coefficient κ on the Poisson's ratio of the magnitude reported by Hyun *et al.* [9].

We conclude that the difference between $a = 4$ and $a = 1$ is negligibly small, and Eq. (4.19) forms a good approximation for the finite slab with the aspect ratio $a \geq 1$, regardless of the chosen Poisson's ratio ν.

4.4.2 Thin periodic cell

The effective strength of the thin repetitive cell is higher than the finite slab with aspect ratio $a = 1$ [41]. Therefore, it is expected that the real contact area for the small nominal pressure $\bar{p}$ will be smaller. We chose $a = 0.5$, and determine the value of the proportionality coefficient in the TFC limit κ^{TFC}. In Fig. 4.12, we show how the proportionality coefficient κ depends on the discretizations ϵ_i for the reference values of ϵ_i with aspect ratio $a = 0.5$ and Poisson's ratios $\nu = 0.2, 0.33, 0.49$.

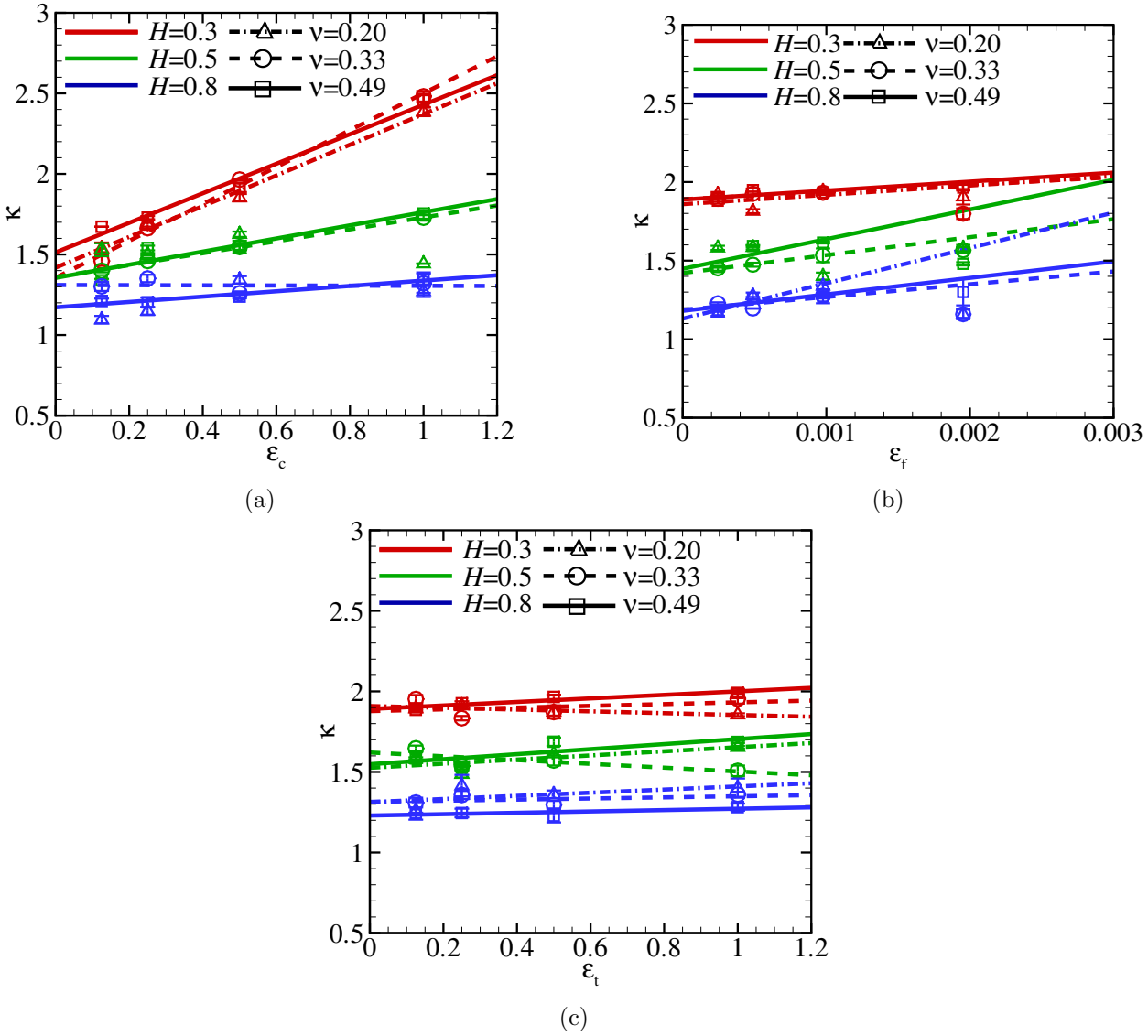

Figure 4.12: Plot of the proportionality coefficient κ as a function of (a) the continuum discretization ϵ_{c}, (b) the fractal discretization ϵ_{f} and (c) the thermodynamic discretization ϵ_{t} with Hurst's exponents $H = 0.3, 0.5, 0.8$, aspect ratio $a = 0.5$ and Poisson's ratios $\nu = 0.2, 0.3, 0.49$.

We observe a smaller variance for each data point than we calculated for the finite slab with the aspect ratio $a = 1$ and the Poisson's ratio $\nu = 0.20, 0.33, 0.49$. The proportionality coefficient κ has the dependencies on the three limits ϵ_i comparable to the semi-infinite solid (Sec. 4.3).

In the linear fit in Fig. 4.12b, we omit the proportionality constant κ for $\epsilon_{\mathrm{f}}^{-1} = 512$, because of the large variance. We observe that in the fractal limit the higher-order dependence on the Poisson's ratio ν vanishes for $H = 0.3$ and $H = 0.5$. Due to the high scatter, variance and non-Gaussian height distribution $p(h)$ for $H = 0.8$, we can not find a converging fit. We can conclude that the fractal discretization is of major importance when one wants to study the effect of the Poisson's ratio ν on the proportionality coefficient. However, we find this result non-conclusive on the expected higher-order dependency of the proportionality coefficient κ on the Poisson's ratio ν, because we omit the numerically calculated value of κ for the fractal discretization $\epsilon_{\mathrm{f}}^{-1} = 512$.
The value of $\bar{\alpha}_{\mathrm{c}} = 1.01$ gives the best average fit for all Hurst's exponents H and Poisson's ratio's ν. We chose $\bar{\alpha}_{\mathrm{c}} = \bar{\alpha}_{\mathrm{f}} = \bar{\alpha}_{\mathrm{t}} = 1$ comparable to the previous sections. In Tab. 4.7, we summarize the coefficients C_i and α_i of the power-law fit, and the coefficient C_i of the linear-fit with the average exponent $\bar{\alpha}_i$ for aspect ratio $a = 0.5$ and Poisson's ratios $\nu = 0.20, 0.33, 0.49$.

H	fit	C_{c}	C_{f}	C_{t}	α_{c}	α_{f}	α_{t}
0.3	pow.	0.900	-	-	1.208	-	-
	lin.	0.953	59.219	-0.055	1	1	1
0.5	pow.	-	-	-	-	-	-
	lin.	-	-	0.128	1	1	1
0.8	pow.	-	-	-	-	-	-
	lin.	0.199	224.765	0.098	1	1	1

(a)

H	fit	C_{c}	C_{f}	C_{t}	α_{c}	α_{f}	α_{t}
0.3	pow.	1.328	-	-	0.701	-	-
	lin.	1.145	46.411	0.054	1	1	1
0.5	pow.	0.388	-	-	0.882	-	-
	lin.	0.370	113.945	-0.118	1	1	1
0.8	pow.	-	-	-	-	-	-
	lin.	-	81.042	0.0346	1	1	1

(b)

H	fit	C_{c}	C_{f}	C_{t}	α_{c}	α_{f}	α_{t}
0.3	pow.	0.816	-	-	1.584	-	-
	lin.	0.916	57.095	0.109	1	1	1
0.5	pow.	6.21026	-	-	0.030	-	-
	lin.	0.407	188.750	0.156	1	1	1
0.8	pow.	0.143	-	-	2.174	-	-
	lin.	0.166	104.770	0.042	1	1	1

(c)

Table 4.7: Coefficients C_i and exponents α_i for κ required to determined κ^{TFC} using Eq. (4.6) for aspect ratio $a = 0.5$ with Poisson's ratio (a) $\nu = 0.20$, (b) $\nu = 0.33$ and (c) $\nu = 0.49$.

In Fig. 4.13, we depict how proportionality coefficient κ depends on scaled continuum discretization ϵ_c for the reference values of ϵ_i, aspect ratio $a = 1$ and Poisson's ratio $\nu = 0.49$.

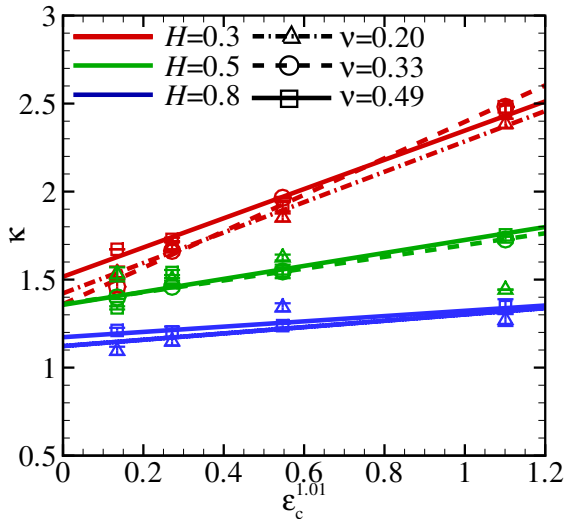

Figure 4.13

Figure 4.14: Plot of the proportionality coefficient κ as a function of the scaled continuum discretization $\epsilon_c^{1.01}$ with Hurst's exponents $H = 0.3, 0.5, 0.8$, aspect ratio $a = 0.5$ and Poisson's ratio $\nu = 0.2, 0.33, 0.49$.

In Fig. 4.13, we observe that the value of the proportionality constant κ in the continuum limit is between 1.125 and 1.51. The value of the proportionality constant κ for Hurst's exponents $H = 0.3, 0.5$ converges to $\kappa^c \approx 1.45$ in the continuum limit. We disregard the value of κ^c for $H = 0.8$ (see Sec. 4.3).
We observe that only a small number of continuum and fractal limits give the power-law fit with the error below 10 %. From here on, we consider only the trends and not the exact values of the linear fits. We observe that the trends indicate also the proportionality constant $\kappa \approx 1.45$ is independent of the Hurst's exponent H. The trends we observe for a given Poisson's ratio ν corresponds to those described in Sec. 4.3. Regarding the TFC-limit, we find no monotonic dependency of the coefficients C_i on the Poisson's ratio ν. However, we conclude that Eq. (4.19) forms a good approximation for the thin film with the aspect ratio $a \geq 0.5$ regardless of the chosen Poisson's ratio ν. Due the numerical error in the value of the proportionality coefficient κ in the TFC-limit (see Sec. 4.4), we find the results on the dependency of the proportionality coefficient κ on the aspect ratio a non-conclusive.

4.5 Conclusions and discussion

For the first time the proportionality coefficient κ is rigorously determined for the elastic solid over a range of aspect ratios a and Poisson's ratios ν with a single method. We conclude that the proportionality coefficient κ is independent of the Hurst's exponent H for a semi-infinite solid. This is in agreement with Persson [12] and Prodanov *et al.* [5]. This disagrees with the statistical asperity by Greenwood *et al.* [21], Bush *et al.* [11], Ciavarella *et al.* [22, 13], and the brute-force methods by Hyun *et al.* [9] and Campañá *et al.* [4]. The reason for this difference is the small fractal discretization used in this work.

In this work, we find that the values of the proportionality coefficient κ for the semi-infinite solid are 0.5 to 0.75 times previously reported values of κ [10, 11, 4, 5]. For statistical methods, this difference is due to the uncontrolled assumptions in the incorporation of uniform deformation and/or asperity interactions, which leads to over prediction of the relative contact area fraction a_r. For previous GFMD simulations by Campañá *et al.* [4] and Prodanov *et al.* [5], the difference is caused by the omission of the scaling of the displacement $\tilde{\boldsymbol{u}}(\boldsymbol{q})$ and elastic energy density v_el by a the factor 0.5 in DFFT [49]. Moreover, we observe that the fractal correction in this work is twice the fractal correction that was previously reported in GFMD approaches [4, 5]. We contribute this also to the incorrect scaling of the displacement in the DFFT. Therefore, future work should select a smaller fractal discretization than in this work, *i.e.*, an reference thermodynamic discretization $\epsilon_\mathrm{f}^{-1} \approx 4096$ for future work.

We observe that the proportionality coefficient κ converges in the continuum limit $\epsilon_\mathrm{c} \to 0^+$ for Hurst's exponent $H = 0.0, 0.3, 0.5$ to a value of $\kappa^\mathrm{C} \approx 1.45$, and note the value of $\kappa \approx 1.59$ predicted by Persson's theory [12]. We conclude that because the height distribution function $p(h)$ for low values of the Hurst's exponent in the limit $\epsilon_\mathrm{t}^{-1} = 2$ best approximates the Gaussian distribution, the numerically calculated value of the proportionality coefficient κ^TFC is so close to the analytically derived value of κ by Persson's theory [12]. We suggest that future work should have a smaller thermodynamic discretization ϵ_t for the reference system. This smaller ϵ_t will lead to convergence in the mean-square of the height distribution $p(h)$ to the Gaussian for higher values of the Hurst's exponent. This reduction of the thermodynamic discretization ϵ_t of the reference system was also suggested by Yastrebov *et al.* [32]. This will give a definitive answer on the applicability of Persson's theory for small nominal pressure $\bar{p}$, and the influence of the height distribution $p(h)$ on the proportionality coefficient κ.

We numerically calculate a difference in the value of the proportionality coefficient κ for the elastic slab with aspect ratio $a = 0.5, 1, 4$. We observe that the value of the proportionality coefficient κ decreases with a decrease of the aspect ratio a, although less pronounced than expected. However, this corresponds to the observation by Komvopoulos *et al.* [33], they observed a negligible small effect of aspect ratio a on the value of κ for low nominal pressures $\bar{p}$. Note that, in this work, we show that the average exponent $\bar{\alpha}_i = \mathrm{f}(a)$ for the linear-fit, omitting this dependency of the exponent on the aspect ratio a can result in under-prediction of the value of κ. We find this non-conclusive, and to give a quantitative analysis of the effect of the aspect ratio a on the proportionality coefficient κ, we will have to put forward a more rigorous analysis in the future. The discretization has to be decreased in order to correctly predict the proportionality coefficient in the TFC-limit κ^TFC and a larger range of discretizations has to be used for a better power-law fit.

We also observe that, as is commonly presumed, the expression for the relation between the contact area fraction a_r and low nominal pressure $\bar{p}$: $a_\mathrm{r} = \kappa\bar{p}/\bar{g}E^*$ with $\kappa \approx 1.5$, can be used as a good approximation for a generic Poisson's ratio $0.2 < \nu \leq 0.5$ and aspect ratio $0.5 \leq a \leq \infty$. Note that this value of κ is within a 10% error range.

We find no uniform higher-order dependency of the proportionality coefficient κ on the Poisson's

ratio ν. This lack of higher-order dependence makes us conclude that the established dependence of the proportionality coefficient κ on the material properties and surface topography, *i.e.*, $E, \nu, \bar{g}$, is a very good representation of the real contact area for the small nominal pressure $\bar{p}$ and the nominally flat surface. The absence of a the higher-order dependency on ν is unexpected. According to Hyun *et al.* [9], there is a higher-order dependency on the Poisson's ratio ν for the aspect ratio $a = 1$. We argue that this higher-order dependency is reported because the minimum continuum discretization and fractal discretization used by Hyun *et al.* [9] are too large, *i.e.*, $\epsilon_{\mathrm{c}}^{-1} = 2$ and $\epsilon_{\mathrm{f}}^{-1} \approx 1000$. We observe that for fractal discretization $\epsilon_{\mathrm{f}}^{-1} \approx 2048$ the higher-order dependence on the Poisson's ratio ν disappears. Future work should focus on a more rigorous analysis of the effect of Poisson's ratio ν on the value of the proportionality coefficient κ for aspect ratio $a = 1$.

The aforementioned results and conclusion are all under the assumption of a nominally flat elastic slab indented with a rough rigid punch. Also, we make use of the small-slope approximation, small-strain assumption and hard-wall repulsion at the interface. The traction in tangential direction is implicitly taken to be zero, *i.e.*, frictionless contact. This work allows for the relaxation of the assumption of the flat incompressible solid of infinite height and no tangential displacement at the surface. The effect of local slope is expected to be of major influence on the contact behavior for metal surfaces (see Chapter 1 and Sec. 4.4). The small-slope approximation is up to date one of the reasons why we can not yet study realistic metallic contacts (see Chapters 1 and 2). Therefore, we recommend to relax the small-slope assumption. Moreover, we make use of mapping [15] of the roughness of the contacting surfaces on to the rigid indenter. This is only valid under the assumption of frictionless contact. When the assumption of frictionless contact is relaxed, the interaction between metallic asperities can be effectively studied using an exponential potential like Xu-Needleman [75] or the cohesive zone model according to McGarry *et al.* [76], also allowing the study of interplay between adhesion and friction at the interface. To relax the assumption of frictionless contact, we have to extend the current GFMD method to allow for the elastic slab to have a rough surface topography.

Appendix 4.A Persson's theory

Persson theory in its original formulation is a renormalization-group approach to contact mechanics of self-affine surfaces for frictionless contact. It allows us to derive the analytical expression for the normal traction probability distribution $P_{\mathrm{r}}(\tau_3, q)$ in the contact area at the length scale $2\pi/q$. Persson's theory assumes the normal traction probability distribution $P_{\mathrm{r}}(\tau_3, q)$ to obey a diffusion-like equation where time is replaced by the wave number q and the spatial coordinate by the normal traction τ_3. It first assumes complete contact between the rigid punch and the substrate on all length scales with pressure distribution:

$$P_{\mathrm{r}}(\tau_3, q_0) = \delta(\tau - \bar{p}), \tag{4.7}$$

where

$$q_0 = 2\pi/L_x, \tag{4.8}$$

$\delta()$ is the Delta-Dirac function and $\bar{p}$ is the nominal pressure. When q increases to shorter length scales the normal traction distribution function broadens due to the additional undulations within the contact zone. A point on the substrate is no longer in contact with the rigid punch when the normal traction $\tau_3 = 0$. The normal traction probability distribution $P_{\mathrm{r}}(\tau_3, q)$ is written as:

$$P_{\mathrm{r}}(\tau_3, q) = \frac{1}{2\sqrt{\pi G}} \left(e^{-\frac{(\tau_3 - \bar{p})^2}{4G}} - e^{-\frac{(\tau_3 + \bar{p})^2}{4G}} \right), \tag{4.9}$$

where G, the standard deviation of the normal traction, is:

$$G = \int_{q_0}^{q} \tau_3(q)^2. \tag{4.10}$$

We can express $\tau_3(q)$ as:

$$\tau_3(q) = \frac{qE^* f(qz_{\mathrm{m}})}{2} |\tilde{h}(q)|, \tag{4.11}$$

where $f(qz_{\mathrm{m}})$ is the correction factor for an incompressible finite slab with $u_3(0, x) = 0$ and zero tangential traction:

$$f(qz_{\mathrm{m}}) = \frac{\cosh(2z_{\mathrm{m}}q) + 2(qz_{\mathrm{m}})^2 + 1}{\sinh(2qz_{\mathrm{m}}) - 2qz_{\mathrm{m}}}. \tag{4.12}$$

The standard deviation of the normal traction is a constant and independent of the wave number q. The broadening of the pressure distribution is written as:

$$P_{\mathrm{r}}(\tau_3, q^+) = \int_0^{\infty} \mathrm{d}\bar{p} K(\tau, \bar{p}, \Delta\tau) P_{\mathrm{r}}(\bar{p}, q^-), \tag{4.13}$$

where $K(\tau, \bar{p}, \Delta\tau)$ is the kernel function:

$$K(\tau, \bar{p}, G) = \frac{\left(e^{-\frac{(\tau_3 - \bar{p})^2}{4G}} - e^{-\frac{(\tau_3 + \bar{p})^2}{4G}} \right)}{4\sqrt{\pi G}}. \tag{4.14}$$

Here, $P_{\mathrm{r}}(\tau_3, q^-)$ is the normal traction distribution function for all spatial features with wave number $q' < q$ and $P_{\mathrm{r}}(\tau_3, q^+)$ is the normal traction distribution function for all spatial features

with wave number $q^+ > q'$. The scale-dependent relative contact area $a_\mathrm{r}(q')$ for all spatial features with wavenumber $q \leq q'$ is written as:

$$a_\mathrm{r}(q') = \int_0^\infty \mathrm{d}\tau' P_\mathrm{r}(\tau_3', q'). \tag{4.15}$$

Note that the integral over τ_3 of $P(\tau_3, q)$ has to be unity. To ensure this, there is a Delta-Dirac function contributing to $P(\tau_3, q)$ of the form $(1 - a_\mathrm{r}(q'))\,\delta(\tau_3)$. Substituting Eq. (4.9) into Eq. (4.15), we give after some simplification:

$$a_\mathrm{r} = \mathrm{erf}\left(\frac{\bar{p}}{2\sqrt{G}}\right). \tag{4.16}$$

For $\bar{p} << G$, Eq. (4.16) is:

$$a_\mathrm{r} \approx \frac{\bar{p}}{\pi\sqrt{G}}. \tag{4.17}$$

We assume a self-affine topography from here on. The standard deviation of the normal traction G for an elastic semi-infinite body $f(qz_\mathrm{m}) = 1$ and non-adhesive contacts is:

$$G = \int_{q_0}^{q} \left(\frac{qE^* f(qz_\mathrm{m})}{2}|\tilde{h}(q)|\right)^2 = \left(\frac{\bar{g}E^*}{2}\right)^2, \tag{4.18}$$

where $\bar{g}$ is the root mean square gradient (RMSG). The linear scaling of a_r with $\bar{p}$ is established for an elastic semi-infinite body $f(qz_\mathrm{m}) = 1$ and non-adhesive contacts as:

$$a_\mathrm{r} = \frac{\kappa\bar{p}}{\bar{g}E^*}, \tag{4.19}$$

where κ is the proportionality coefficient. Eq. (4.19) holds for $\dfrac{2\pi}{z_\mathrm{m}} \geq 10q_0$. According to Persson *et al.* [12, 77, 25] $\kappa = \sqrt{8/\pi} \approx 1.59$.

Chapter 5

Elastic deformation of rough surfaces in contact with flat rigid body: A two-step Green's function molecular dynamics approach

"*Boys we were - friendly boys although. If you don't mind me saying so.*"

Nescio, Titaantjes

5.1 Introduction

So far, Green's function molecular dynamics (GFMD) has been used to simulate the contact mechanics of solids with rough surfaces by mapping the roughness onto a rigid indenter and the substrate is modeled as an infinitesimally-flat surface, assuming frictionless contact [4, 5, 6]. Mapping is no longer valid when the surface has a large local slope $g(x)$, and frictionless contact is a poor assumption. In this work, we extend GFMD to study the contact mechanics of deformable bodies with self-affine surfaces.

In the work by Venugopalan *et al.* [3], the elastic Green's functions are derived for a finite-height slab that has an infinitesimally flat surface. In order to study slabs with a generic surface topography as a function of the x-position at the surface $z_{\mathrm{m}}(x)$, the displacement at the surface $\boldsymbol{u}(x)$ has to become a function of both the wave number q, corresponding to the displacement, and the wave number q_{surf} corresponding to the surface topography. Moreover, the solution of the displacement field $u(x, z)$ at a generic x-coordinate on the surface becomes a function of the single wavenumber q, but also of the sum of all sinusoidal components with wave number q_{surf}, corresponding to the surface height $z(x)$. Therefore, we can not solve the ordinary differential equation in Fourier space (see Chapter 2, Eq. (2.4)). An alternative is solving the boundary value problem though a differential equation in real space. This would, however, drastically increases the complexity of the areal elastic energy definition compared to the formulation by Venugopalan *et al.* [3]. We want to prevent this increase in complexity, and computational time. To this end, we analytically derive an approximation of the areal elastic energy by making use of the principal of superposition of strains. The solution is therefore bound to work only within assumption of small strain and small slope.

The first step, in this method, involves imposing displacement $\boldsymbol{u}''(x)$ to an initially flat surface to form the desired rough surface topography $h(x)$. In the second step, the strain required for the deformation is calculated. A GFMD simulation is performed in the third and final step. In this GFMD simulation, the calculated strain inside the body, due to the imposed loading, is corrected with the strain calculated in the previous step. We chose to name this extended method 'two-step GFMD'. Figure 5.1 is the schematic representation of a boundary-value problem approached by the two-step GFMD method.

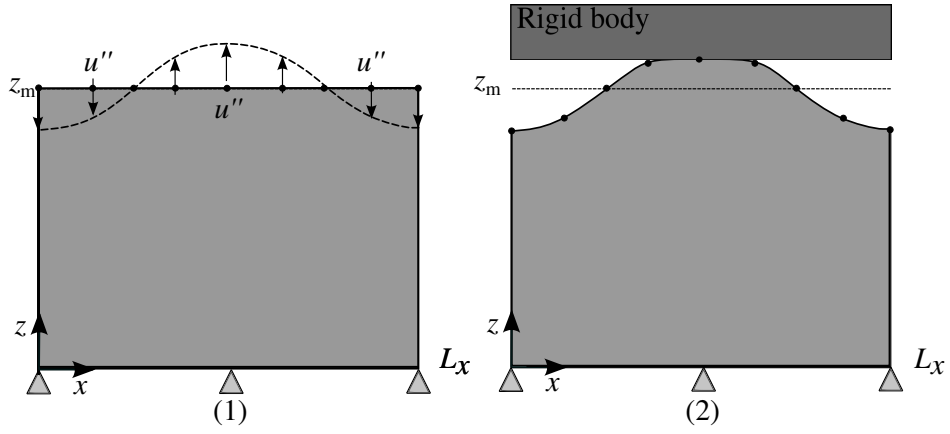

Figure 5.1: Schematic representation of the boundary-value problem approached by the two-step GFMD: (1) The initially flat surface is displaced with displacement u'' leading to a sinusoidal surface topography $h(x)$. (2) The sinusoidal asperity is flattened with a rigid punch, correcting the strain inside the body with the strain calculated in step (1).

We validate the model by comparing the body fields for the flattening of a sinusoidal surface numerically calculated with two-steps GFMD and with the finite element method (FEM), using the commercial program ABAQUS. When comparing two-step GFMD to FEM, note that, FEM starts from the traction free sinusoidal surface and does not need strain corrections. Moreover, FEM has no small-slope approximation, unlike GFMD. Here, we want to remind the reader that applying a sinusoidal loading to a flat substrate can be done in GFMD. However, the notable thing we do in this work, is using that deformed body as the starting point of a subsequent loading step, *i.e.*, step (2).

When equilibrium is reached in step (2), we observe that the surface displacement $\boldsymbol{u}(x)$ and normal traction $\tau_3(x)$ is correctly approximated over a range of aspect ratios a and rough surface topography $h(x)$. As to be expected, the maximum allowable aspect ratio a depends on the surface displacement $\boldsymbol{u}(x)$ in normal direction, root mean square height w (RMSH). Note that at the end of step (2), part of the error in the numerically calculated displacement is due to the small-slope, and an additional error due to the superposition of the strains during step (2).

After step (2), we numerically calculate the strain and stress field inside the body following [3]. *A priori*, with a simple analogy with the uniform extension of a bar, we present the analytical expression for the error in the strain $\Delta\epsilon$ due to the uniform surface displacement $u_3(q = 0)$ in normal direction, the slab height z_{m} and the RMSH w. With the analytical expression for the error $\Delta\epsilon$, we correct the analytical calculation of the strain field inside the body in [3].

We observe that the root mean square gradient $\bar{g}$ (RMSG) of the surface topography $h(x)$ that we can reach in step (1) has a maximum allowable value because of the small-slope approximation in GFMD [3]. For the limiting case $g(x) \to \infty$, on the vertical sides of a rectangular asperity, we find that the numerically calculated displacement of the surface in tangential direction $u_1(x)$ shows a large difference between two-step GFMD and FEM calculations. This difference is because the two-step GFMD does not correctly capture the vertical traction normal to the free sides of the rectangular asperity. The maximum value of the RMSG $\bar{g}$ is not known *a priori*. Therefore, we determine the maximum allowable RMSG $\bar{g}$ by comparing the numerically calculated surface displacement $\boldsymbol{u}(x)$ for the flattening of a flat-top triangular asperity with the two-step GFMD method and FEM.

The remainder of this work is organized as follows: In Sec. 5.2, we explain the two-step GFMD method. Subsequently, we give the analytical expression for the elastic energy density in two-step GFMD in Sec. 5.2.2. Further more, we derive the analytical expression for the error in the numerically calculated strain in Sec. 5.2.3. We divide the numerical results in Sec. 5.3 in four parts: In Sec. 5.3.1, we determine a tolerable error in displacements $\boldsymbol{u}(x)$ for the two-step GFMD method; In Sec. 5.3.2, we give the body fields for the flattening of the sinusoidal surface; In Sec. 5.3.3, we study the limiting case of flattening an array of rectangular asperities; And in Sec. 5.3.4, we determine the maximum allowable RMSG $\bar{g}$ from the flattening of the flat-top triangular asperity. This work ends with the conclusion and the discussion in Sec. 5.4.

5.2 Finite-height-slab with sinusoidal surface topography strain, stress and areal elastic energy

5.2.1 Methodology

In static equilibrium, the equilibrium condition is:

$$\tilde{\boldsymbol{F}}_{\mathrm{r}}\left(q\right)+\tilde{\boldsymbol{F}}_{\mathrm{ext}}\left(q\right)+\tilde{\boldsymbol{F}}_{\mathrm{if}}\left(q\right)=0. \tag{5.1}$$

where the restoring force at the surface is $\tilde{\boldsymbol{F}}_{\mathrm{r}}(q)=\nabla_{\tilde{\boldsymbol{u}}}v_{\mathrm{el}}$. For the restoring force $\tilde{\boldsymbol{F}}_{\mathrm{r}}(q)$, we rewrite:

$$\tilde{\boldsymbol{F}}_{\mathrm{r}}(q)=\tilde{\boldsymbol{F}}_{\mathrm{el}}(q)+\tilde{\boldsymbol{F}}_{\mathrm{surf}}(q), \tag{5.2}$$

where $\tilde{\boldsymbol{F}}_{\mathrm{el}}(q)$ is the elastic restoring force of an initially flat surface and $\tilde{\boldsymbol{F}}_{\mathrm{surf}}(q)$ the elastic force required to create the surface topography from the initially flat surface. The calculation of the force in Fourier space for the surface topography $\tilde{\boldsymbol{F}}_{\mathrm{surf}}\left(q\right)$ corresponding to $\boldsymbol{u}''(q)$ is step (1) of the two-step GFMD. We rewrite Eq. (5.1) as:

$$\tilde{\boldsymbol{F}}_{\mathrm{el}}\left(q\right)+\tilde{\boldsymbol{F}}_{\mathrm{ext}}\left(q\right)+\tilde{\boldsymbol{F}}_{\mathrm{if}}\left(q\right)+\tilde{\boldsymbol{F}}_{\mathrm{surf}}\left(q\right)=0, \tag{5.3}$$

where $\tilde{\boldsymbol{F}}_{\mathrm{ext}}\left(q\right)$ is the external force and $\tilde{\boldsymbol{F}}_{\mathrm{if}}\left(q\right)$ is the interfacial force.
In step (2) of the two-step GFMD, the force at the interface is not explicitly known, but only implicitly through the interfacial boundary condition. The static displacement is numerically calculated for the substrate flattened with a flat rigid punch. A hard-wall potential is employed to ensure there is no inter penetration at the surface, *i.e.*,

$$z_{\mathrm{punch}}(x)\geq z_{\mathrm{grid\text{-}point}}(x), \tag{5.4}$$

where z_{punch} and $z_{\mathrm{grid\text{-}point}}$ are the z-coordinates of the punch surface and substrate respectively. Figure 5.2 is the schematic representation of the second step of the two-step GFMD for the substrate with the sinusoidal surface topography $h(x)$ flattened by the rigid punch.

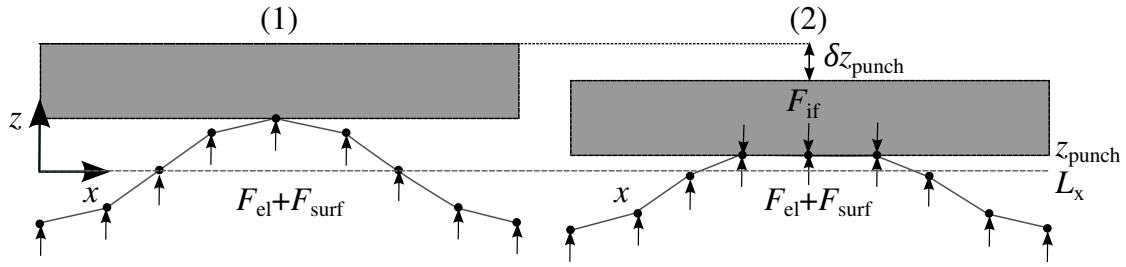

Figure 5.2: Step two: Schematic of substrate with the sinusoidal surface topography $h(x)$ flattened by the load in two-step GFMD. (1) Initial contact is in a single or multiple points of equal height. (2) The rigid punch displaced by $\delta z_{\mathrm{punch}}$.

The initial contact is made at the surface nodes of maximum height. Subsequently, the punch is displaced with the finite displacement $\delta z_{\mathrm{punch}}$. The contact remains a traction prescribed, because the hard-wall condition equals a virtual impulse J over a dimensionless discrete time-step Δt, causing an interfacial force $F_{\mathrm{if}}(x)$ [78]. After equilibrium is reached, we analytically calculate the displacement field $\boldsymbol{u}(x,z)$, strain field $\boldsymbol{\epsilon}(x,z)$ and stress field $\boldsymbol{\sigma}(x,z)$ inside the substrate following [3].

5.2.2 Superposition of strains

Following [3], we write the infinitesimal Cauchy's strain tensor (in Voigt notation) as:

$$\begin{aligned}
\epsilon_1(x,z) &\equiv \partial_1 u_1^{\mathrm{c}}(x,z) \\
&= -q\sin(qx)\tilde{u}_1^{\mathrm{c}}(q,z); \\
\epsilon_3(x,z) &\equiv \partial_3 u_3^{\mathrm{s}}(x,z) \\
&= \sin(qx\partial_3\tilde{u}_3^{\mathrm{s}}(q,z); \\
\epsilon_5(x,z) &\equiv (\partial_3 u_1^{\mathrm{c}}(x,z) + \partial_1 u_3^{\mathrm{s}}(x,z)) \\
&= \cos(qx)(qu_3^{\mathrm{s}}(q,z) + \partial_3 u_1^{\mathrm{c}}(q,z)).
\end{aligned} \tag{5.5}$$

The strain tensor $\boldsymbol{\epsilon}'(x,z)$ is determined by subtracting the strain tensor necessary to deform to the required surface topography $\boldsymbol{\epsilon}''(x,z)$ from the strain tensor of the substrate. This is written as:

$$\begin{aligned}
\epsilon_1'(x,z) &\equiv \epsilon_1(x,z) - \epsilon_1''(x,z); \\
\epsilon_3'(x,z) &\equiv \epsilon_3(x,z) - \epsilon_3''(x,z); \\
\epsilon_5'(x,z) &\equiv \epsilon_5(x,z) - \epsilon_5''(x,z).
\end{aligned} \tag{5.6}$$

Following [3], we can determine the work per unit area to deform the body – assuming small surface slopes– via:

$$v_{\mathrm{el}} = \frac{1}{w}\int_0^w \mathrm{d}x \left[\int_0^{u_1(x,z_{\mathrm{m}})} \sigma_{13}'(x,z_{\mathrm{m}})\mathrm{d}w_1(x,z_{\mathrm{m}}) + \int_0^{u_3(x,z_{\mathrm{m}})} \sigma_{33}'(x,z_{\mathrm{m}})\mathrm{d}w_3(x,z_{\mathrm{m}})\right]. \tag{5.7}$$

With the sinusoidal normal and cosine lateral displacement at the surface $(\tilde{u}_1^{\mathrm{c}}, \tilde{u}_3^{\mathrm{s}})$ corresponding to the wave number q, the elastic energy is:

$$v_{\mathrm{el}} = \frac{C_{44}}{2}\tilde{\epsilon}_5^{\mathrm{c}'}(q,z_{\mathrm{m}})\tilde{u}_1^{\mathrm{c}}(q,z_{\mathrm{m}}) + \left\{\frac{C_{11}}{2}\tilde{\epsilon}_3^{\mathrm{s}'}(q,z_{\mathrm{m}}) + \frac{C_{12}}{2}\tilde{\epsilon}_1^{\mathrm{s}'}(q,z_{\mathrm{m}})\right\}\tilde{u}_3^{\mathrm{s}}(q,z_{\mathrm{m}}), \tag{5.8}$$

with

$$\begin{aligned}
\tilde{\epsilon}_1^{\mathrm{s}'}(q,z) &\equiv -q(\tilde{u}_1^{\mathrm{c}}(q,z) + \tilde{u}_1^{\mathrm{c}''}(q,z)); \\
\tilde{\epsilon}_3^{\mathrm{s}'}(q,z) &\equiv \partial_3\tilde{u}_3^{\mathrm{s}}(q,z) - \partial_3\tilde{u}_3^{\mathrm{s}''}(q,z); \\
\tilde{\epsilon}_5^{\mathrm{c}'}(q,z) &\equiv \partial_3\tilde{u}_1^{\mathrm{c}}(q,z) - \partial_3\tilde{u}_1^{\mathrm{c}''}(q,z) + q\tilde{u}_3^{\mathrm{s}}(q,z) - q\tilde{u}_3^{\mathrm{s}''}(q,z),
\end{aligned} \tag{5.9}$$

where $\tilde{\boldsymbol{u}}''(q,z)$ is the displacement corresponding to the sinusoidal surface topography $h(x)$ (see Fig. 5.1).

We rewrite the areal elastic energy as:

$$v_{\mathrm{el}} = \frac{q}{2}\left(\left[\tilde{u}_1^{\mathrm{c}}(q,z_{\mathrm{m}}), \tilde{u}_3^{\mathrm{s}}(q,z_{\mathrm{m}})\right] \begin{bmatrix} M_{11}(qz_{\mathrm{m}}) & M_{13}(qz_{\mathrm{m}}) \\ M_{13}(qz_{\mathrm{m}}) & M_{33}(qz_{\mathrm{m}}) \end{bmatrix} \begin{bmatrix} \tilde{u}_1^{\mathrm{c}}(q,z_{\mathrm{m}}) \\ \tilde{u}_3^{\mathrm{s}}(q,z_{\mathrm{m}}) \end{bmatrix} - 2\left[\tilde{u}_1^{\mathrm{c}}(q,z_{\mathrm{m}}), \tilde{u}_3^{\mathrm{s}}(q,z_{\mathrm{m}})\right] \begin{bmatrix} N_1(qz_{\mathrm{m}}) \\ N_3(qz_{\mathrm{m}}) \end{bmatrix} \right), \tag{5.10}$$

with

$$\begin{aligned} M_{11}(qz_{\mathrm{m}}) &= (1-r)\frac{\cosh(qz_{\mathrm{m}})\sinh(qz_{\mathrm{m}}) - r(qz_{\mathrm{m}})C_{11}}{\parallel f(qz_{\mathrm{m}}) \parallel}; \\ M_{13}(qz_{\mathrm{m}}) &= \left(\frac{1-r}{1+r}\right)\frac{(1-r)\sinh^2(qz_{\mathrm{m}}) + 2r^2(qz_{\mathrm{m}})^2 C_{11}}{\parallel f(qz_{\mathrm{m}}) \parallel}; \\ M_{33}(qz_{\mathrm{m}}) &= (1-r)\frac{\cosh(qz_{\mathrm{m}})\sinh(qz_{\mathrm{m}}) + r(qz_{\mathrm{m}})C_{11}}{\parallel f(qz_{\mathrm{m}}) \parallel}; \\ \begin{bmatrix} N_1(qz_{\mathrm{m}}) \\ N_3(qz_{\mathrm{m}}) \end{bmatrix} &\equiv \begin{bmatrix} M_{11}(qz_{\mathrm{m}}) & -\mathrm{i}M_{13}(qz_{\mathrm{m}}) \\ \mathrm{i}M_{13}(qz_{\mathrm{m}}) & M_{33}(qz_{\mathrm{m}}) \end{bmatrix} \begin{bmatrix} \tilde{u}_1^{\mathrm{c}''}(q,z_{\mathrm{m}}) \\ \tilde{u}_3^{\mathrm{s}''}(q,z_{\mathrm{m}}) \end{bmatrix}, \end{aligned} \tag{5.11}$$

where

$$r = \frac{1-s}{1+s}, \tag{5.12}$$

and

$$\begin{aligned} \parallel f(qz) \parallel &\equiv f_1(qz)f_3(qz) + f_2(qz)^2 \\ &= \cosh^2(qz) - (rqz)^2 - 1. \end{aligned}$$

The elastic energy density for the general case is:

$$v_{\mathrm{el}} = \sum_{\boldsymbol{q}} \frac{q}{2}\left(\left[\tilde{u}_1^{*}(\boldsymbol{q}), \tilde{u}_3^{*}(\boldsymbol{q})\right] \begin{bmatrix} M_{11}(qz_{\mathrm{m}}) & -\mathrm{i}M_{13}(qz_{\mathrm{m}}) \\ \mathrm{i}M_{13}(qz_{\mathrm{m}}) & M_{33}(qz_{\mathrm{m}}) \end{bmatrix} \begin{bmatrix} \tilde{u}_1(\boldsymbol{q}) \\ \tilde{u}_3(\boldsymbol{q}) \end{bmatrix} - 2\left[\tilde{u}_1^{*}(\boldsymbol{q}), \tilde{u}_3^{*}(\boldsymbol{q})\right] \begin{bmatrix} N_1(qz_{\mathrm{m}}) \\ N_3(qz_{\mathrm{m}}) \end{bmatrix} \right), \tag{5.13}$$

where

$$\begin{bmatrix} N_1(qz_{\mathrm{m}}) \\ N_2(qz_{\mathrm{m}}) \end{bmatrix} = \begin{bmatrix} M_{11}(qz_{\mathrm{m}}) & -\mathrm{i}M_{13}(qz_{\mathrm{m}}) \\ \mathrm{i}M_{13}(qz_{\mathrm{m}}) & M_{33}(qz_{\mathrm{m}}) \end{bmatrix} \begin{bmatrix} \tilde{u}_1''(\boldsymbol{q}) \\ \tilde{u}_3''(\boldsymbol{q}) \end{bmatrix}, \tag{5.14}$$

and $\tilde{u}(\boldsymbol{q})$ is now the Fourier transform of the displacement of the surface $\boldsymbol{u}(x)$ corresponding to wave vector $\boldsymbol{q}$. Following Eqs. (5.2) and (5.13), we rewrite the elastic force required to create the surface topography from the initially flat surface $\tilde{\boldsymbol{F}}_{\mathrm{surf}}(q)$ as:

$$\begin{bmatrix} \tilde{F}_{1,\mathrm{surf}}(q) \\ \tilde{F}_{3,\mathrm{surf}}(q) \end{bmatrix} = -q\left[\tilde{u}_1''(q), \tilde{u}_3''(q)\right] \begin{bmatrix} M_{11}(qz_{\mathrm{m}}) & -\mathrm{i}M_{13}(qz_{\mathrm{m}}) \\ \mathrm{i}M_{13}(qz_{\mathrm{m}}) & M_{33}(qz_{\mathrm{m}}) \end{bmatrix}. \tag{5.15}$$

We use this analytical expression in the subsequent sections to determine the elastic force required to create the surface topography in step one of two-step GFMD.

5.2.3 Error in superposition of strains

The error introduced by the superposition of strains $\Delta\epsilon$ in step (3) is expected to increase with an increase in the w/z_{m} ratio (small-strain assumption), in $\bar{g}$ (small-slope assumption), or in u_3/z_{m} (small-strain). We make an analogy with a bar element in Fig. 5.3.

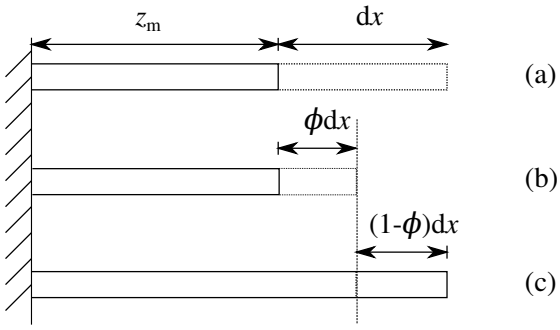

Figure 5.3: Schematic representation of the superposition of strain for a one dimensional bar. Case (a) is the elongation of a bar with length z_m to $z_\mathrm{m} + \mathrm{d}x$. Case (b) is elongation of a bar with length z_m to $z_\mathrm{m} + \phi\mathrm{d}x$. Case (c) is the compression of a bar with length $z_\mathrm{m} + \mathrm{d}x$ to $z_\mathrm{m} + \phi\mathrm{d}x$.

Considering the one dimensional case is represented by a bar with initial length $z_\mathrm{m} + \mathrm{d}x$. The bar is compressed to $z_\mathrm{m} + \phi\mathrm{d}x$, *i.e*, case (c). The strain calculated in two-step GFMD is analogous to the superposition of case (b) and (a). The error in the strain $\Delta\epsilon$ for superposition is:

$$\begin{aligned} \Delta\epsilon &= (\epsilon_\mathrm{a} - \epsilon_\mathrm{b}) - \epsilon_\mathrm{c}; \\ &= -\frac{\mathrm{d}x^2(\phi - 1)}{z_\mathrm{m}(\mathrm{d}x + z_\mathrm{m})}. \end{aligned} \tag{5.16}$$

The uniform extension dx in this case is equivalent to the RMSH w imposed in step (1) and the term $(1 - \phi)\mathrm{d}x$ is equivalent to the uniform surface displacement $u_3(q = 0)$ imposed in step (2). After step (2) is finished, we want to numerically calculate the strain fields inside the body. We find that this error scales with the slab height z_m, the RMSH w and the displacement of the surface in normal direction $u_3(x)$. The displacement in tangential direction is assumed to be small, and therefore, we assume it to be of minor influence on the error in the strain fields. In order to correct for this error, we use Eq. (5.16) for the uniform extension and subtract the error in the strain $\Delta\epsilon$ from the analytically calculated strain $\tilde{\epsilon}_3(q = 0)$. This correction to the strain field improves the solution by reducing the error from $\Delta\sigma \approx 15.0E \times 10^{-3}$ to within $\Delta\sigma \approx 0.5E \times 10^{-3}$ between two-step GFMD and FEM.

5.3 Numerical results

5.3.1 Sinusoidal surface topography

As a benchmark problem to determine the tolerable error $\Delta u_i / L_x$ in the surface displacement of a substrate with the sinusoidal surface topography, we impose no loading. This is implemented by taking $\tilde{u}_1^{\mathrm{s}''}(k = 1, z_\mathrm{m}) = 0$ and $\tilde{u}_3^{\mathrm{s}''}(k = 1, z_\mathrm{m}) = -0.01 z_\mathrm{m}$. The corresponding surface force $\boldsymbol{F}_\mathrm{surf}(x)$ is calculated in step one. We perform step two with the following parameters: $E = 70$ GPa, $\nu = 0.33$, $a = 1$, $L_x = 20$ μm, $z_\mathrm{punch}(x) = \infty$, $\Delta t = 0.01$ and $nx = 2048$, where E is the elastic modulus, ν the Poisson's ratio and nx the discretization.

The normalized displacements at the surface $\bar{u}_i/L_x$ is shown in Fig. 5.5. The over bar indicates the value of the variable at the surface.

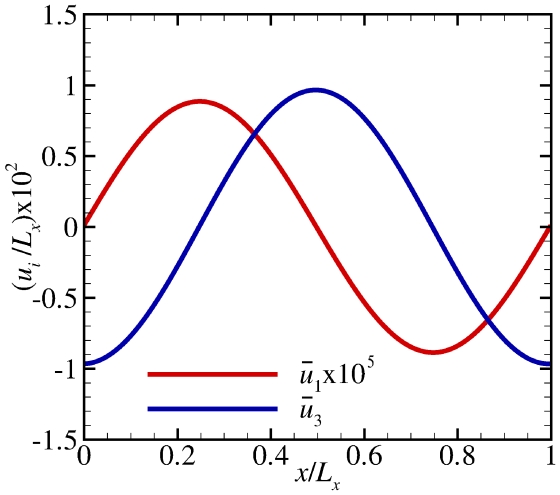

Figure 5.4

Figure 5.5: Plot of the normalized normal and tangential displacement u_i/L_x as a function of the normalized x-coordinate x/L_x.

We set the tolerable error $\Delta u_i/L_x$ to the order $\mathcal{O}^{-6}$. This corresponds to a thousandth of the typical GFMD simulation indentation depth known to satisfy the small-slope approximation. We observe that the error in surface displacement $\bar{\boldsymbol{u}}(x)$ is below the tolerable error set by us.

5.3.2 Flattening sinusoidal asperity

We flatten the substrate with sinusoidal surface in Sec. 5.3.1 with the flat rigid body and the finite displacement $\delta z_{\text{punch}} = 3.3 \times 10^{-3} z_{\text{m}}$. For the FEM calculations we use a uniform mesh of square elements, and we assume small-strain. The number of elements in x-direction nnx and the number of elements in y-direction nny are equal to nx. The normalized displacements at the surface $\bar{u}_i/L_x$ and the normalized traction in normal direction τ_3/E for two-step GFMD and FEM are shown in Fig. 5.6. The maximum difference in normalized displacement at the surface is $\bar{u}_1/L_x = 9 \times 10^{-6}$. The difference is at the maximum that we will tolerate and gives a good indication of the maximum indentation depth in two-step GFMD, *i.e.*, $\delta z_{\text{punch}} = 3.3 \times 10^{-3} z_{\text{m}}$. The difference in normalized maximum traction between two-step GFMD and FEM is $\Delta\tau_3/E = 0.2945 \times 10^{-3}$. We conclude that the results are in good agreement. We numerically calculate the displacement and stress fields inside the body for the two-step GFMD. The body fields are depicted in Figs. 5.7 and 5.8.

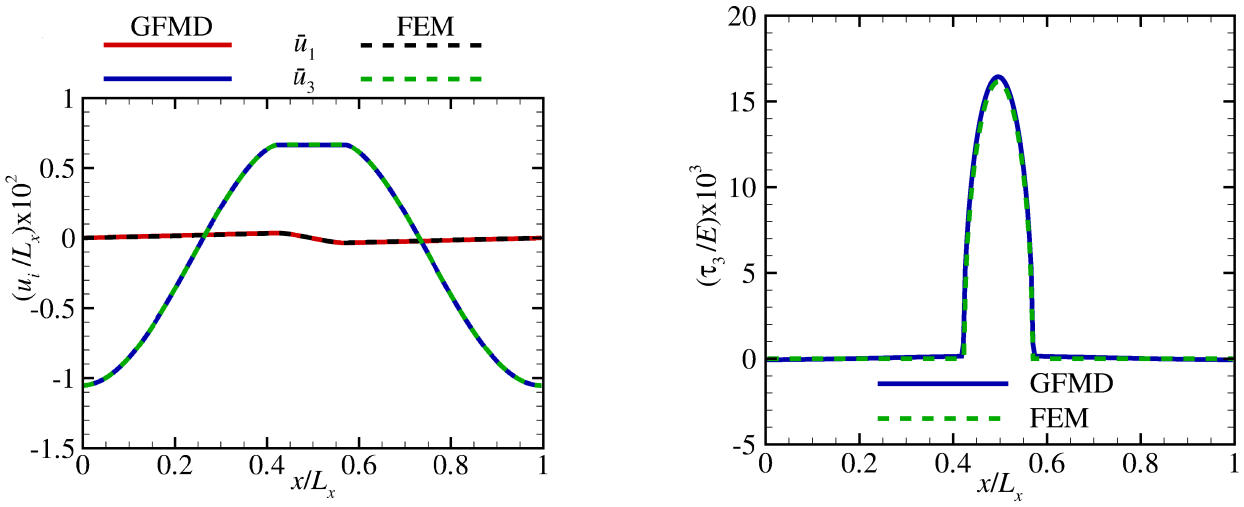

(a) (b)

Figure 5.6: (a) Plot of the normalized normal and tangential displacement u_i/L_x as a function of the normalized x-coordinate for two-step GFMD and FEM. (b) Plot of the normalized normal traction τ_3/E as a function of the normalized x-coordinate x/L_x for two-step GFMD and FEM.

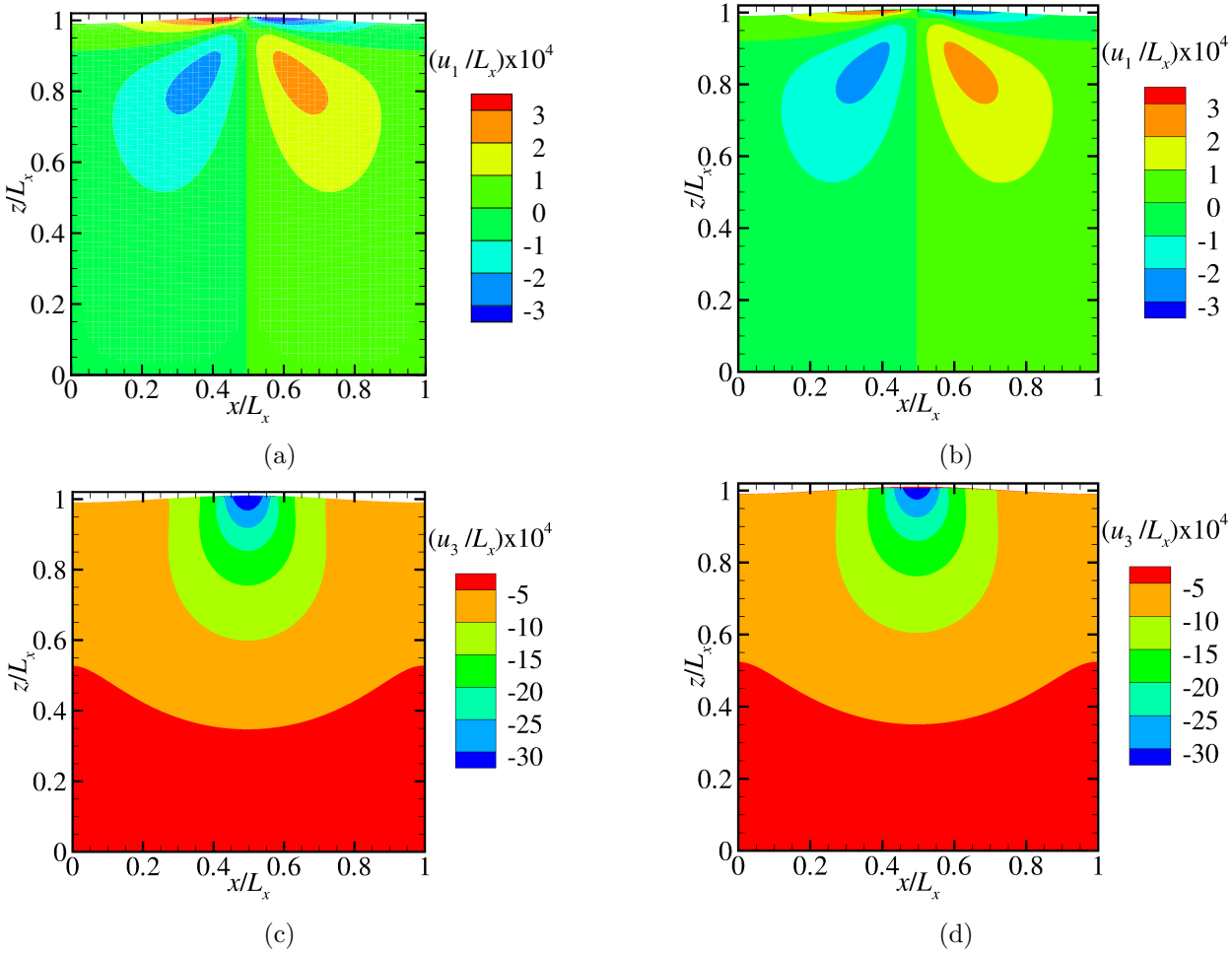

(a) (b)

(c) (d)

Figure 5.7: Displacement fields obtained using: (a), (c) two-step GFMD; (b), (d) FEM.

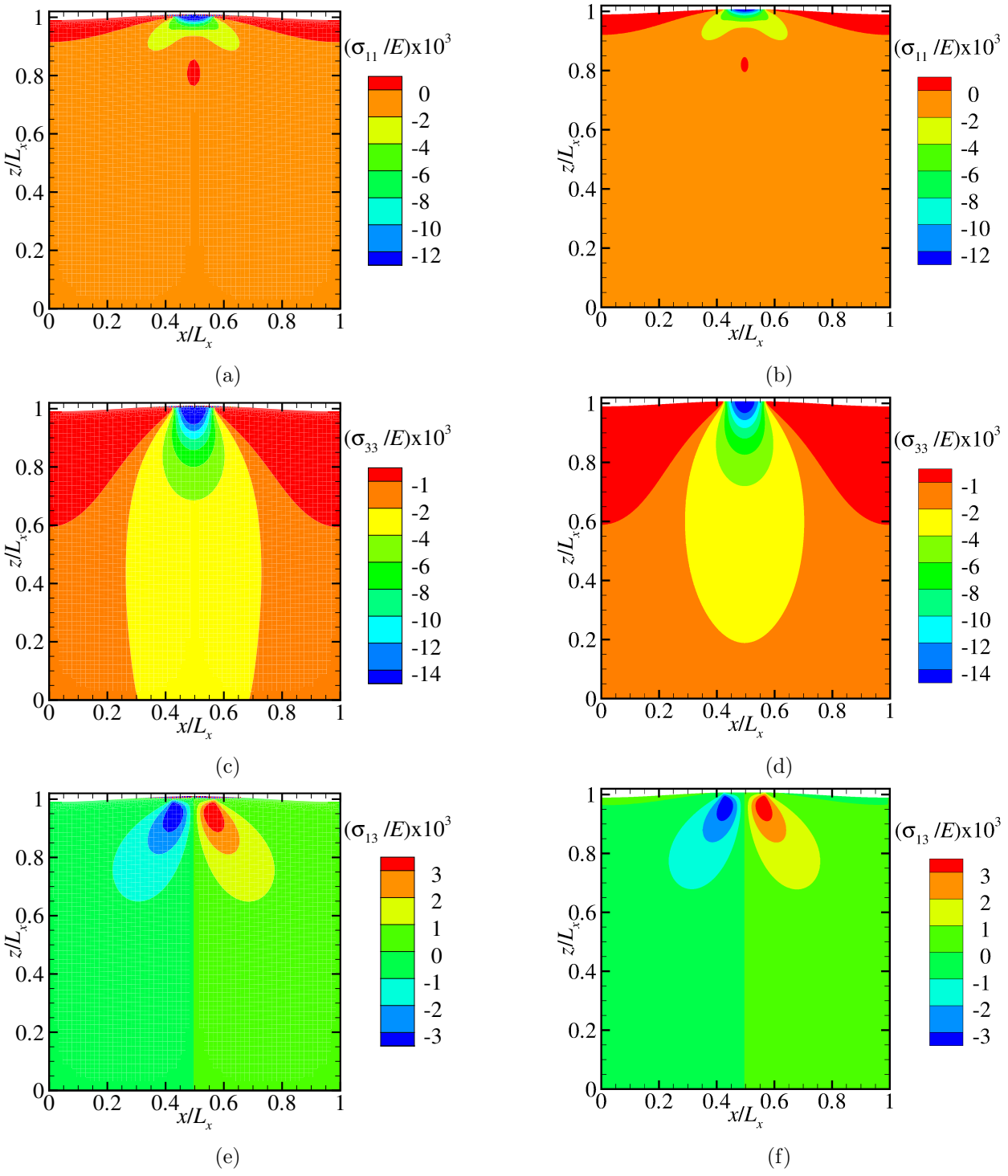

Figure 5.8: Stress fields obtained using: (a), (c), (e) two-step GFMD; (b), (d), (f) FEM.

We observe a small difference in contour plot for the normalized stress in normalized direction between the iso-lines of the zone $-2 < \sigma_{33}/E \times 10^{-}3 < -4$ between GFMD and FEM. This difference is due to the superposition of strains in step (3) (see Sec. 5.2.3). In Fig. 5.9a, the normalized normal stress σ_{33}/E is plotted as the function of the normalized z-coordinate z/L_x.

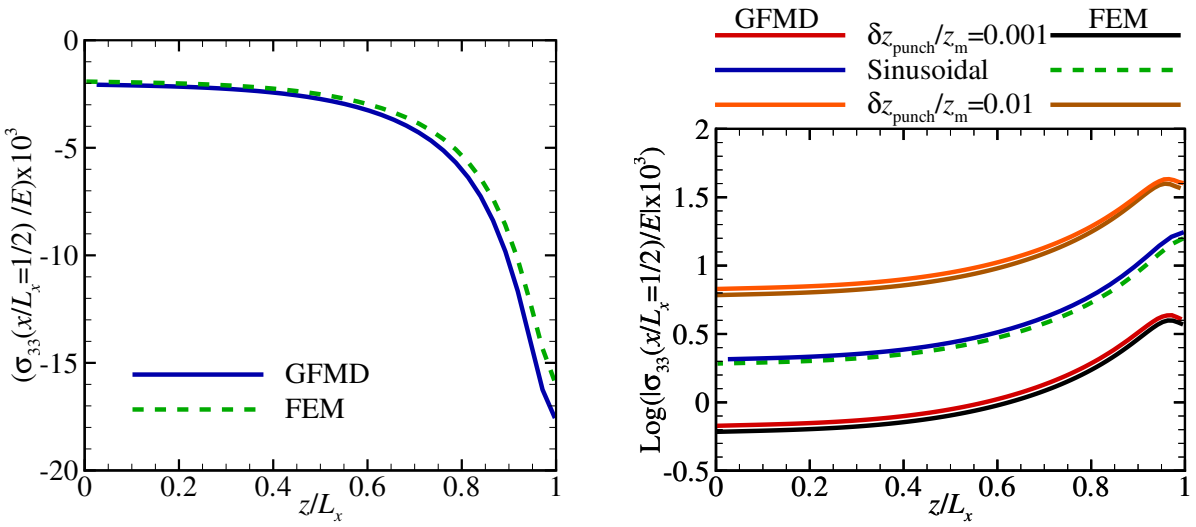

(a) (b)

Figure 5.9: Plot of the normalized stress $\sigma_{33}(x/L_x = 1/2)/E \times 10^3$ as a function of the normalized position z/L_x for (a) the sinusoidal asperity in Fig. 5.6a and (b) normalized indentation depths $\delta z_{\text{punch}}/z_{\text{m}} = 0.01$, $\delta z_{\text{punch}}/z_{\text{m}} = 0.001$ and the flattened sinusoidal asperity in Fig. 5.6a

We compare this result to indenting of a flat substrate with a flat rigid punch with width $L_x^{\text{p}} = 0.1L_x$ and normalized indentation depths $\delta z_{\text{punch}}/z_{\text{m}} = 0.01$ and $\delta z_{\text{punch}}/z_{\text{m}} = 0.001$. Figure 5.9b displays the absolute normalized stress $|\sigma_{33}(x/L_x = 1/2)/E|$ as a function of the normalized z-coordinate z/L_x. In Tab. 5.1, we summarize the minimum, the maximum and the average difference in the normalized stress $\sigma_{33}(x/L_x = 1/2)/E$ between GFMD and FEM.

	$\delta z_{\text{punch}}/z_{\text{m}} = 0.001$	flattened sinusoidal asperity	$\delta z_{\text{punch}}/z_{\text{m}} = 0.01$
$\text{Mean}(\lvert\Delta\sigma_{33}(x/L_x = 1/2)/E\rvert) \times 10^3$	0.127	0.534	1.101
$\text{Min}(\lvert\Delta\sigma_{33}(x/L_x = 1/2)/E\rvert) \times 10^3$	0.065	0.146	0.663
$\text{Max}(\lvert\Delta\sigma_{33}(x/L_x = 1/2)/E\rvert) \times 10^3$	0.365	1.696	3.149

Table 5.1: Summary of the differences in normalized stress $\sigma_{33}(x/L_x = 1/2)/E$ between GFMD and FEM for the different loading types displayed in Fig. 5.9b.

We decide to set the tolerance for maximum allowable average difference in normalized stress $\Delta\sigma/E$ equal to the mean difference in stress for the indentation of a flat substrate with a flat rigid punch, *i.e.*, $\text{Mean}(|\Delta\sigma_{33}(x/L_x = 1/2)/E|)$ for $\delta z_{\text{punch}}/z_{\text{m}} = 0.01$ in Tab. 5.1. Moreover, we set the maximum finite displacement in two-step GFMD to $\delta z_{\text{punch}}/z_{\text{m}} = 3.3 \times 10^{-3}$, in order to keep the error well below the aforementioned tolerance. However, the rough surface topography $h(x)$ is also expected to influence the numerically calculated surface displacement with two-step GFMD. We also want to study the effect of local slope on the numerically calculated surface displacement, therefore we give the limiting case of $g(x) \to \infty$ in the subsequent section.

5.3.3 Flattening rectangular asperity

Apart from the small strain, there is another assumption in GFMD: the slopes are taken to be small (see Chapter 2). Therefore, we check what is the error in the most severe limiting case of the local gradient $g(x) \to \infty$. As the second benchmark problem to compare two-step GFMD to FEM, a substrate with the surface topography $h(x)$ written as:

$$h(x) = 0.01 z_{\mathrm{m}} (\Theta(x + \tfrac{9L_x}{20}) - \Theta(x - \tfrac{11L_x}{20})), \tag{5.17}$$

is flattened with the rigid flat body with the finite displacement $\delta z_{\mathrm{punch}} = 3.0 \times 10^{-3} z_{\mathrm{m}}$. Here $\Theta(x)$ is the Heaviside step-function. In Fig. 5.10, we show the normalized normal and lateral displacement u_i/L_x as a function of the normalized x-coordinate x/L_x with $z_{\mathrm{punch}}(x) = \infty$.

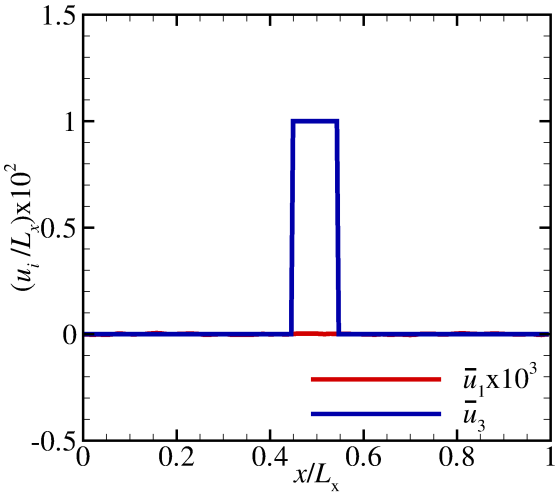

Figure 5.10: (a) Plot of the normalized normal and lateral displacement u_i/L_x as a function of the normalized x-coordinate x/L_x with $z_{\mathrm{punch}}(x) = \infty$.

The normalized displacements at the surface $\bar{u}_i/L_x$ and the normalized traction τ_3/E for two-step GFMD and FEM are shown in Fig. 5.11. The maximum absolute error in normalized displacement at the surface is $\Delta\bar{u}_1/L_x = 1.5 \times 10^{-8}$ with no flattening. The maximum difference in absolute normalized displacement at the surface is $\bar{u}_1/L_x = 1 \times 10^{-4}$ between two-step GFMD and FEM. The difference in normalized traction at $x = L_x/2$ between two-step GFMD and FEM is $\Delta\tau_3/E = 5 \times 10^{-4}$. The normal displacement at the surface and the normal traction are in very good agreement. The tangential displacement is not in agreement. Note, the observed difference in tangential displacement has an appreciable effect on the contact mechanical behavior. Even more appreciable if one intends to study frictional problems. Here, we show that two-step GFMD does not capture the effect of the free surfaces of the rectangular asperity. The body fields are compared in Figs. 5.12 and 5.13.

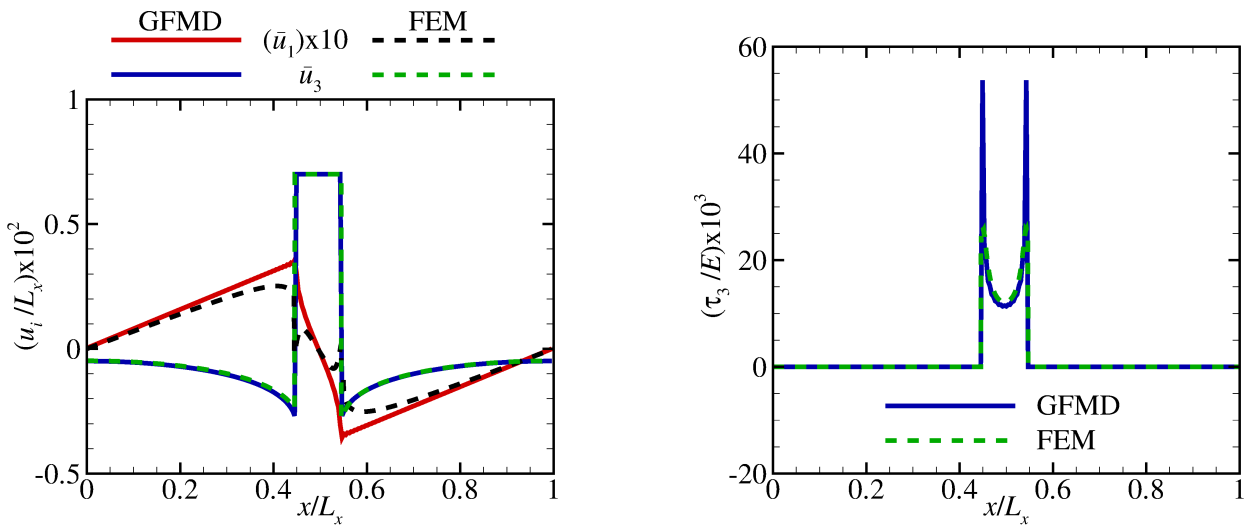

(a) (b)

Figure 5.11: (a) Plot of the normalized normal and lateral displacement u_i/L_x as a function of the normalized x-coordinate for two-step GFMD and FEM. (b) Plot of the normalized normal traction τ_3/E as a function of the normalized x-coordinate x/L_x for two-step GFMD and FEM.

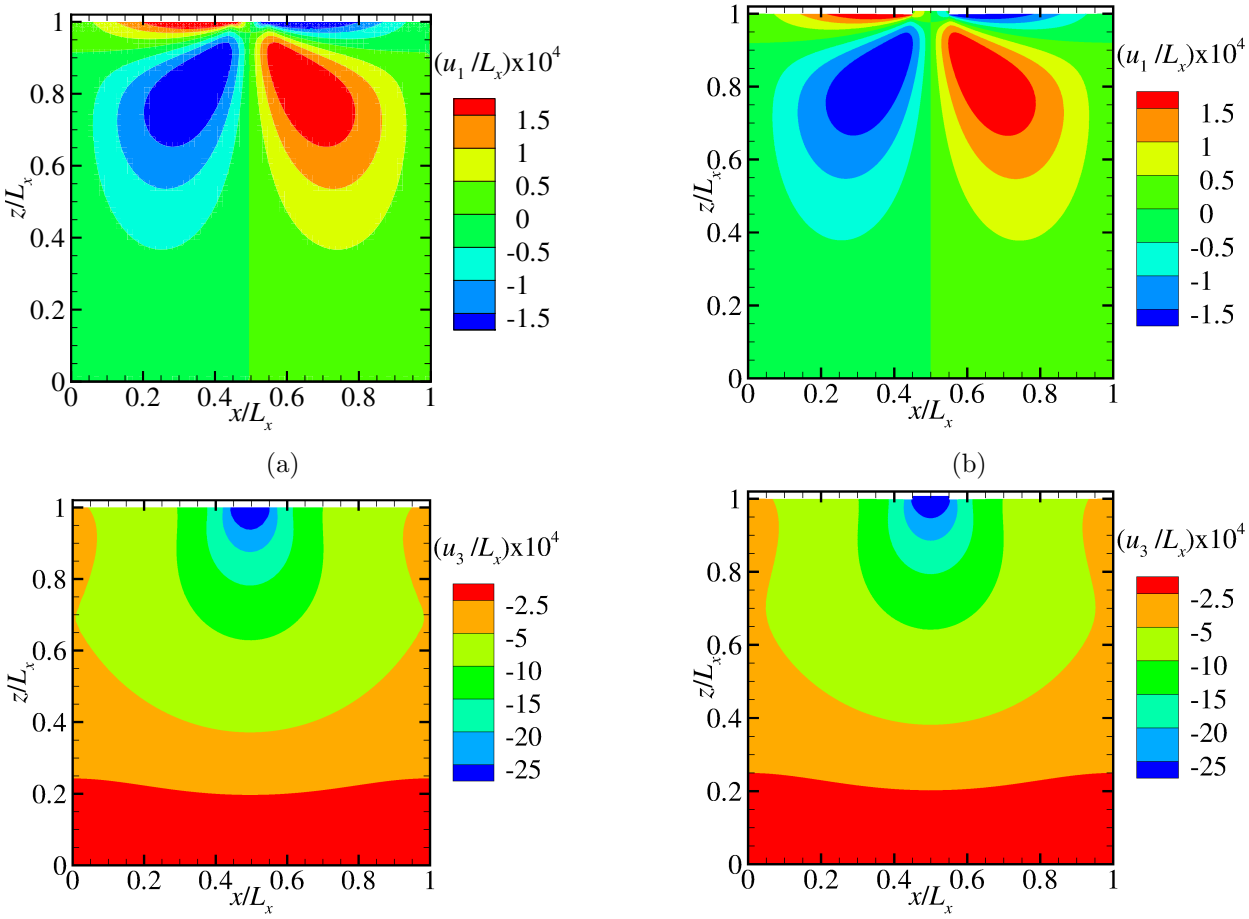

(a) (b)

(c) (d)

Figure 5.12: Displacement fields obtained using: (a), (c) two-step GFMD; (b), (d) FEM.

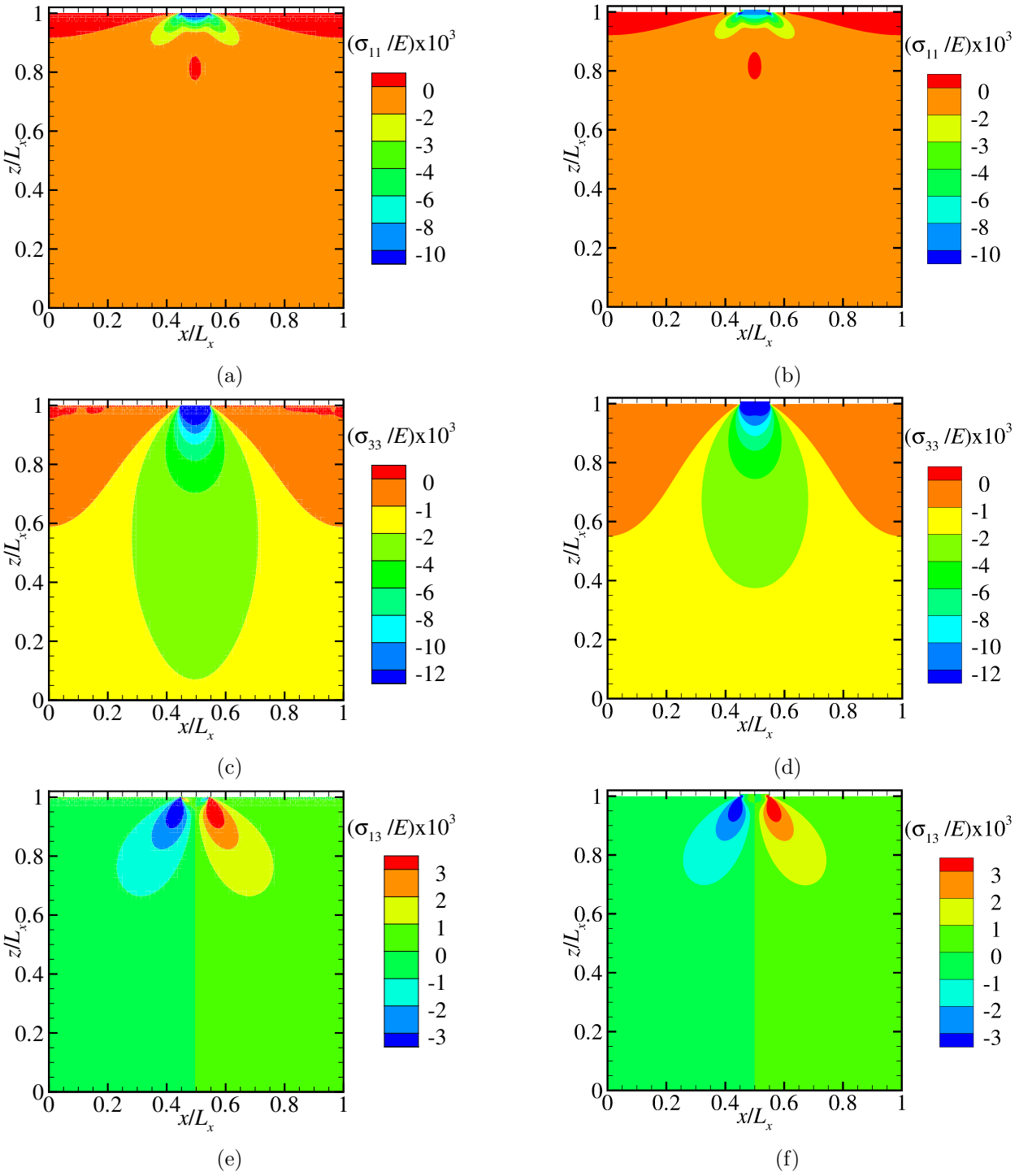

Figure 5.13: Stress fields obtained using: (a), (c), (e) two-step GFMD; (b), (d), (f) FEM.

We observe that the displacement fields inside the substrate look similar, as is observed for the stress fields. The maximum difference in stress $\Delta\sigma/E$ between two-step GFMD and FEM is smaller than the tolerable, when we disregard the regions just below the surface. As to be expected, due to the the small-slope approximation the displacement in the region around a high local slope on or just under the surface are not correctly captured by two-step GFMD. We conclude that a maximum

allowable RMSG $\bar{g}$ has to be determined for two-step GFMD. To this end, we study the flattening of flat-top triangular asperities with varying gradients in the next section.

5.3.4 Flattening flat-top triangular asperities

In order to find the maximum allowable surface gradient in two-step GFMD, we flatten a substrate with the surface topography $h(x)$ written as:

$$h(x) = 0.01 z_{\mathrm{m}} \left(1 - |gx|\right) \left(\Theta(gx + \frac{9L_x}{20}) - \Theta(gx - \frac{11L_x}{20}) \right), \tag{5.18}$$

with a rigid flat body. Here g is the slope of the triangular asperity. The triangular asperity is broadened to have the flat top. In Fig. 5.14, we depict the normalized surface profile $h(x)/L_x$ as a function of the normalized x-coordinate x/L_x with $g = 0.025$, $g = 0.028$, $g = 0.03$ and $g = 0.032$.

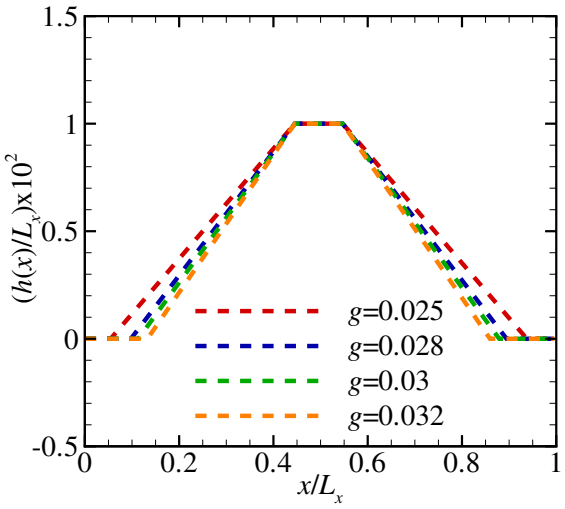

Figure 5.14: Plot of the normalized surface profile $h(x)/L_x$ as a function of the normalized x-coordinate x/L_x with $g = 0.025$, $g = 0.028$, $g = 0.03$ and $g = 0.032$.

The normalized displacements at the surface of the asperity $\bar{u}_i/L_x$ for two-step GFMD and FEM with $g = 0.025$, $g = 0.028$, $g = 0.03$ and $g = 0.032$ are shown in Fig. 5.15.

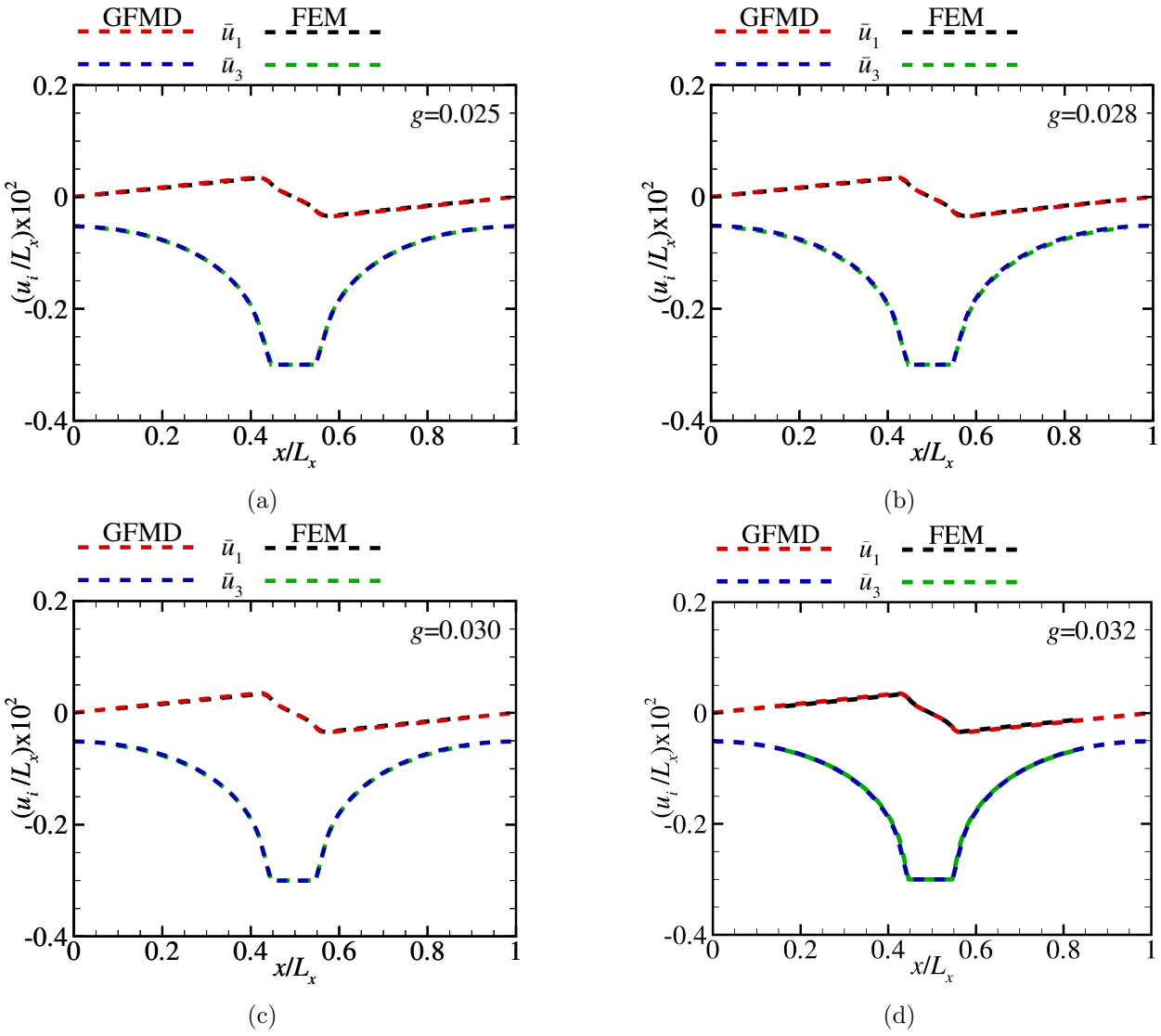

Figure 5.15: Plot of the normalized displacement u_i/L_x as a function of the normalized x-coordinate x/L_x for two-step GFMD and FEM with (a) $g = 0.025$, (b) $g = 0.028$, (c) $g = 0.030$ and (d) $g = 0.032$.

We observe that macroscopically two-step GFMD and FEM are in good agreement.

In Tab. 5.2, we give the average absolute difference in normalized tangential displacement $|\Delta\bar{u}_1/L_x|$ between two-step GFMD and FEM with gradient g.

g	$\|\Delta\bar{u}_1/L_x\| \times 10^{-6}$
0.025	0.82
0.028	1.47
0.030	2.32
0.032	3.00

Table 5.2: The average absolute difference in normalized tangential displacement $|\Delta\bar{u}_1/L_x|$ for the flattening of a flat-top triangular asperity with gradient g.

The difference in the tangential displacement at the surface increases for an increase in gradient g. For $\bar{g} \geq 0.030$, the difference in displacement is coming in to the range of maximum tolerable error of $\mathcal{O}^{-6}L_x$. However, the zone of interest to us is the region in the immediate vicinity of the contact. These regions are where we expect the largest differences between two-step GFMD and FEM. In Fig. 5.16. the normalized tangential displacement $\bar{u}_1/L_x$ at the surface of the asperity is shown as a function of the normalized x-coordinates x/L_x for two-step GFMD and FEM.

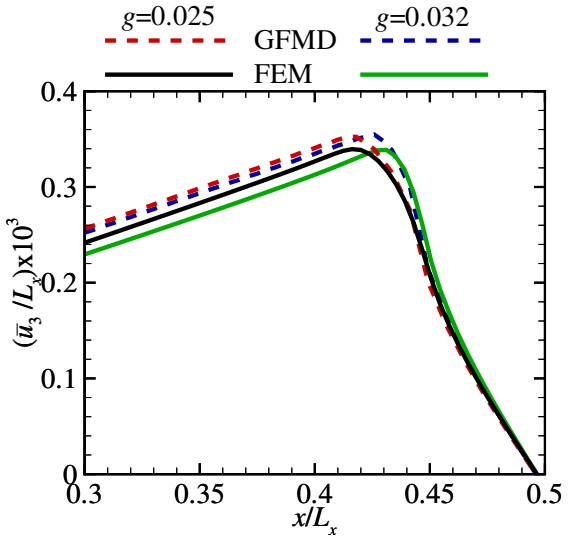

Figure 5.16: Plot of the normalized tangential displacement in the contact area $\bar{u}_1/L_x$ as a function of the normalized x-coordinate x/L_x.

Note the difference in location of the maximum displacement between two-step GFMD and FEM. For $\bar{g} = 0.032$, we observe an appreciable difference in the location of the maximum tangential displacement. This difference is expected to produce an error in the numerically calculated real contact area fraction a_r. We conclude that the tolerable RMSG of the rough surface topography $h(x)$ for two-step GFMD is $\bar{g} \leq 0.030$. Such a low RMSG does not allow us to simulate realistic metallic rough surfaces, where the RMSH w and RMSG $\bar{g}$ are several orders of magnitude larger than we use in this work. We conclude that the small-slope approximation can not capture the realistic finite slope of metallic asperities. Future work should focus on relieving the small-slope approximation.

5.4 Conclusions and discussion

For the first time GFMD is extended to apply to finite deformable solids with surface topography $h(x)$. We call this extended method two-step GFMD. In this work, the analytically calculated strain fields $\boldsymbol{\epsilon}(x, z)$ are adjusted to account for finite surface topography $h(x)$. This correction results in 95% error reduction in the calculated strain fields $\boldsymbol{\epsilon}(x, z)$ between two-step GFMD and FEM. Note this can be further reduced when correct the strain tensor over all wave numbers q (see Eqs. (5.5) and (5.6)) in future work.

In this work, we only consider the slab geometry with the aspect ratio $a = 1$. It is also important in the contact of metallic bodies to study of thin films, *i.e.*, aspect ratio $a \leq 0.5$. Therefore, we recommend to investigate two-step GFMD for thin films in future work.

We define the maximum allowable error in displacement and stresses. As to be expected, we observe that for the limiting case of flattening an array of rectangular asperities, two-step GFMD is not capable of correctly representing the local slope. We observe that the tolerable RMSG of the rough surface topography $h(x)$ for two-step GFMD is $\bar{g} \leq 0.030$. Important to note is that both GFMD and two-step GFMD have the assumption of the small-slope approximation. When this assumption is relaxed, the two-step GFMD method would be able to more correctly numerically calculate contact behavior for large RMSH w and larger local gradients $g(x)$ than currently is possible with two-steps GFMD.

Two-steps GFMD is capable of numerically calculating contact mechanical properties for a generic interaction potential at the surface, *i.e.*, finite range adhesive/repulsive potential [74]. Also, two-step GFMD can be used to numerically calculate the displacement of the surface of two deformable elastic slabs with aspect ratios a_1 and a_2, generic Poisson's ratios ν_1 and ν_2 and surface topographies $h_1(x)$ and $h_2(x)$, respectively.

Finally, we like to comment on the numerical calculations performed in this work. After gathering the presented numerical results, we found that the numerical calculations in this work have an error up to $\mathcal{O}^{-6}$, due to the allocated array precision. After increasing the precision, we are able to reach a maximum error $\Delta u_i / L_x$ in the order of $\mathcal{O}^{-16}$.

Chapter 6

Damped dynamic energy minimization: Analytical derivation of the critical damping coefficient in Green's function molecular dynamics

"*We don't really have departments of Electrical Engineering, Mechanical Engineering, Chemical Engineering, and so on, we had departments of large systems, small systems, mechanical systems, chemical systems, and so on.*"

Former dean Stanford's School of Engineering, The Fourier transform and its Applications

6.1 Introduction

Green's function molecular dynamics (GFMD) is a boundary-value method allowing one to simulate the linear-elastic response of a solid to an external load by modeling only the surface. The surface is discretized using nx equi-spaced grid-points. These grid-points interact with each other through an effective stiffness. Earlier works neglected the sideways motion of grid-points in GFMD simulations [5], only studying the normal component of the displacement on a semi-infinite solid (*i.e.*, one degree of freedom (DOF)). This did not greatly affect the solution, as long as the applied external load was normal and the substrate was incompressible. More Recently, GFMD was extended to include the shear component of the displacement in a slab of finite height z_{m} and generic Poisson's ratio ν [3]. The displacement of the surface with periodicity L_x is calculated in Fourier space. The surface displacement $\tilde{\boldsymbol{u}}(\boldsymbol{q}) = (\tilde{u}_1(\boldsymbol{q}), \tilde{u}_2(\boldsymbol{q}), \tilde{u}_3(\boldsymbol{q}))$ for each mode with wave vector $\boldsymbol{q}$ is obtained numerically. This work only treats static loading, therefore the exact trajectory of the surface nodes is not a sought after result, and damped dynamics can be used [5]. For the (1+1)-dimensional substrate, the in-plane wave vectors become scalars and can be written as:

$$q = \frac{2\pi}{L_x} k, \tag{6.1}$$

where k is the wave number index. The displacement $\tilde{\boldsymbol{u}}(q)$ in Fourier space corresponding to the single wave number q is called a displacement mode. The elastic force $\tilde{\boldsymbol{F}}_{\mathrm{el}}(q)$ is determined as: When tractions are prescribed on the surface, equilibrium is reached when the elastic restoring force $\tilde{\boldsymbol{F}}_{\mathrm{el}}(q)$ and the external force $\tilde{\boldsymbol{F}}_{\mathrm{ext}}(q)$ are balanced. At a given dimensionless instant t, before equilibrium is attained, the equation of motion at the interface can be written as:

$$\tilde{\boldsymbol{F}}_{\mathrm{el}}(q,t) + \tilde{\boldsymbol{F}}_{\mathrm{ext}}(q,t) + \tilde{\boldsymbol{F}}_{\mathrm{if}}(q,t) + \boldsymbol{c}\frac{\mathrm{d}\tilde{\boldsymbol{u}}(q,t)}{\mathrm{d}t} = m\frac{\mathrm{d}^2\tilde{\boldsymbol{u}}(q,t)}{\mathrm{d}t^2}, \tag{6.2}$$

where $\boldsymbol{c} = (c_1, c_3)$ is the positive real valued directionally dependent linear damping coefficient and m is the real valued mass. The mass m is taken to be unity. The force at the interface $\tilde{\boldsymbol{F}}_{\mathrm{if}}(q)$ is not explicitly known, but only implicitly through the interfacial b.c.. The equation of motion of a damped mode in Fourier space is solved numerically by the position (Störmer-)Verlet (pSV) method [16]. The interfacial force is damped in the following manner:

$$\tilde{\boldsymbol{F}}_{\mathrm{d}}[n] = \tilde{\boldsymbol{F}}_{\mathrm{el}}[n] + \tilde{\boldsymbol{F}}_{\mathrm{ext}} + \boldsymbol{\eta}\left(\tilde{\boldsymbol{u}}[n-1] - \tilde{\boldsymbol{u}}[n]\right), \tag{6.3}$$

where $\tilde{\boldsymbol{F}}_{\mathrm{d}}[n]$ is the damped force at $t = n(\Delta t)$ with the discrete time-step Δt and $\boldsymbol{\eta} = (\eta_1, \eta_3)$ is the real valued damping factor. This damping factor $\boldsymbol{\eta}$ is a numerical simulation parameter, and $\boldsymbol{\eta}$ is proportional to the real valued linear damping coefficient $\boldsymbol{c}$ of the solid. However, because the damping factor $\boldsymbol{\eta}$ is a simulation parameter, it has a higher-order dependency on the discrete time-step Δt, unlike the linear damping coefficient $\boldsymbol{c}$. The displacement of a single mode is:

$$\tilde{\boldsymbol{u}}[n+1] = 2\tilde{\boldsymbol{u}}[n] - \tilde{\boldsymbol{u}}[n-1] + \tilde{\boldsymbol{F}}_{\mathrm{d}}[n]\left(\Delta t\right)^2. \tag{6.4}$$

A hard-wall potential is employed at the end of each iteration to ensure there is no inter penetration at the surface, *i.e.*,

$$z_{\mathrm{punch}}(x) \geq z_{\text{grid-point}}(x), \tag{6.5}$$

where z_{punch} and $z_{\text{grid-point}}$ are the z-coordinates of the punch surface and substrate respectively. The interfacial b.c. influences the characteristic dynamic regimes of the GFMD simulation, because the conversion of kinetic into potential energy by the interfacial b.c. influences the damped

dynamics [79].
The goal of this work is to minimize the computational time when computing the displacement of the surface. For studying random rough surfaces the discretization is decades smaller than the smallest wavelength [4] (see Chapters 3 and 4) and computationally cost heavy. The minimum time to equilibrium t_{eq} is attained for a critically damped dynamic energy minimization. When the damped dynamic energy minimization is over-damped, the surface displacement never reaches equilibrium and is incorrect. To this end, the expression for the critical damping factor $\boldsymbol{\eta}_{\mathrm{cr}}$ and its associated equilibrium time t_{eq} are derived.
According to Prodanov *et al.* [5] the critical damping factor η_{cr} for a semi-infinite incompressible solid considering only normal displacement can be written as:

$$\eta_{\mathrm{cr}} \propto \left(\frac{\tilde{F}_{\mathrm{ext}}(0)}{E^* \bar{g}} \right)^{\alpha} \sqrt{\frac{\beta}{L_x}}, \tag{6.6}$$

where E^* is the effective elastic modulus, ν the Poisson's ratio, $\bar{g}$ is the root mean square gradient (RMSG) of the random rough surface profile $h(x)$, α and β are positive real valued parameters which depend on L_x and typically are found empirically. The expression in Eq. (6.6) is an empirically determined proportionality, and this expression is only suitable for the incompressible semi-infinite solid. The uniform strain in normal direction is zero for the semi-infinite solid, hence the damping factor according to Prodanov *et al.* [5] dampens the dynamics of hard-wall interaction. In this work, we consider elastic slabs with finite slab height z_{m}, therefore the damping factor of the dynamics of the hard-wall interaction in Eq. (6.6) does not necessarily critically damp the GFMD dynamics.
In GFMD simulations with 2 DOF the normal and tangential displacement of the surface are coupled via the inverse Green's function. This work shows that the coupling depends on the Poisson's ratio ν, the aspect ratio a and loading direction. The aspect ratio a is the slab height z_{m} over the periodic width L_x. Due to the coupling it is not possible to superpose the critical damping factors for the normal and tangential mode. Therefore, we can not apply the simpler solutions for the damping factor η_{cr} of damped harmonic oscillator with 1 DOF.
In this chapter, the analytical expression for the critical damping factor $\boldsymbol{\eta}_{\mathrm{cr}}$ is derived by treating the equation of motion corresponding to each wave number q in GFMD simulations as an individual forced linear damped harmonic oscillator. This is possible because the modes corresponding to a single wave number q are independent of all other modes. Also, the equation of motion for the modes corresponding to a single wave number q is the equation of motion of a damped harmonic oscillator with 2 DOF. In GFMD simulations, the computational time for the pSV is the smallest of all Verlet-type methods [80, 81, 82]. According to E. Hairer [81] the accumulated error in position r and velocity v of the pSV method over a finite integration time both scale as $\mathcal{O}(\mathrm{d}t^2)$, where $\mathrm{d}t$ is the discrete time-step. Other Verlet-type method scale as $\mathcal{O}(\mathrm{d}t^3)$ [82, 80]. The large accumulated error compared to other Verlet-type methods is the reason the analytical expression for the critical damping coefficient of the pSV applied to a damped harmonic oscillator has not received attention so far.
The analytical expression of the critical damping factor and equilibrium time can be input in future GFMD simulations. This would remove the need to check the trajectories of the first few modes post simulation, which is now common practice. The analytical expression for the critical damping factor and equilibrium time are compared to numerical results to this end.
In spite of the error from the pSV method and the coupling in displacements, the possible dependencies of the critical damping factor on the material properties and aspect ratio a can be predicted using an analogy with the damped harmonic oscillator with 1 DOF. It is well known that the effec-

tive strength of the substrate increases with increasing elastic modulus E, increasing Poisson's ratio ν and decreasing aspect ratio a [41]. An increase in effective strength corresponds to an increase of the linear constant κ of the spring of the harmonic oscillator. This results in an increase of the critical damping coefficient c_{cr} [79]. Finally, a finite-range interaction potential [83] between the surface of the punch and the surface of the substrate is comparable with a non-linear position dependent external force $f_{\mathrm{ext}}(x)$. The repulsive potential is expected to decrease the critical damping coefficient and the adhesive potential is expected to increase the critical damping coefficient. These dependencies are not known *a priori*, and they will be used to give the applicability of the analytically derived damping factor for various interaction potentials.
The remainder of this chapter is organized as follows: In Sec. 6.2, properties of the damped harmonic oscillator are revisited and the same properties are derived for the trajectory of the damped harmonic oscillator numerically solved by the pSV method. An analytical expression for the critical damping factor $\boldsymbol{\eta}_{\mathrm{cr}}$ in GFMD simulations is derived in Sec. 6.3. The analytical expression for the equilibrium time t_{eq} in GFMD simulations is derived in Sec. 6.4. The analytical expressions are compared with the numerical results from GFMD simulations in Sec. 6.5. Then, a qualitative analysis of the influence of the interfacial b.c. on the critical damping factor is given in Sec. 6.6. This chapter ends with the conclusion and discussion in Sec. 6.7.

6.2 Harmonic oscillator

The equation of motion of a linear harmonic oscillator can be written as:

$$f\left(t\right) = f_{\mathrm{ext}}\left(t\right) - \kappa\left(x\left(t\right)\right) - c\frac{\mathrm{d}x(t)}{\mathrm{d}t} = m\frac{\mathrm{d}^2x(t)}{\mathrm{d}t^2}, \tag{6.7}$$

where f_{ext} is the external force and m the mass. In Fig. 6.1 a schematic representation of a forced damped harmonic oscillator is given.

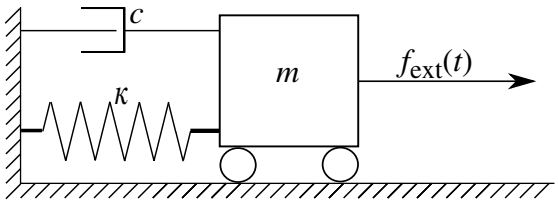

Figure 6.1: Schematic representation of a forced damped harmonic oscillator by a wagon with mass m, frictionlessly moving in the x-direction, attached to a spring with linear constant κ and a damper with linear damping coefficient c, excited by an external force $f_{\mathrm{ext}}(t)$.

The solution of this differential equation has the form $x(t) = x_{\mathrm{h}}(t) + x_{\mathrm{p}}(t)$, where x_{h} is the homogeneous solution and x_{p} the particular solution. The homogeneous solution corresponds to the impulse response and the particular solution corresponds to the steady-state response of a forced damped harmonic oscillator [79]. The linear second-order homogeneous differential equation (6.7) without the driving term $f_{\mathrm{ext}}(t)$ has the homogeneous solution $x_{\mathrm{h}}\left(t\right) = \sum_i^{2d} A_i e^{\lambda_i t}$, where A_i and λ_i are constants and d is the number of DOF. There are four forms of homogeneous solution for a

damped harmonic oscillator:

$$x_{\mathrm{h}}(t) = \begin{cases} (A_1 + A_2 t) e^{-\left(\frac{c}{2m}\right)t}, & \text{where } -\frac{c}{2m} = \lambda_i, \ i.e., \text{ critically damped;} \\ A_1 e^{\lambda_1 t} + A_2 e^{\lambda_2 t}, & \text{where } \lambda_i \text{ are complex, } i.e., \text{ under-damped;} \\ A_1 e^{\lambda_1 t} + A_2 e^{\lambda_2 t}, & \text{where } \lambda_1 \neq \lambda_2 \text{ and } \lambda_i \text{ are real, } i.e., \text{ over-damped;} \\ A_1 e^{\lambda_1 t} + A_2 e^{\lambda_2 t}, & \text{where } \lambda_i \text{ are real and positive, } i.e., \text{ unstable.} \end{cases} \tag{6.8}$$

The linear damping constant c_{cr} that critically damps the harmonic oscillator (*i.e.*, critical linear damping constant) can be determined by the damping ratio ζ:

$$\zeta = \frac{c}{2\sqrt{\kappa m}}. \tag{6.9}$$

The damped harmonic oscillator is under-damped when the damping ratio is $\zeta < 1$, over-damped when $\zeta > 1$ and critically damped when $\zeta = 1$ [79]. The critical damping factor is written as:

$$c_{\mathrm{cr}} = 2\sqrt{\kappa m}. \tag{6.10}$$

The particular solution $x_{\mathrm{p}}(t)$ is always harmonic, and has the same frequency as the external force. Only the amplitude and phase lag of the particular solution depend on the damping constant. The characteristic dynamic regime is thus determined by the homogeneous solution of the equation of motion [79]. Figure 6.2 is a sketch of the solutions of the characteristic dynamic regimes of the forced damped harmonic oscillator by a step-function with amplitude A_{h}.

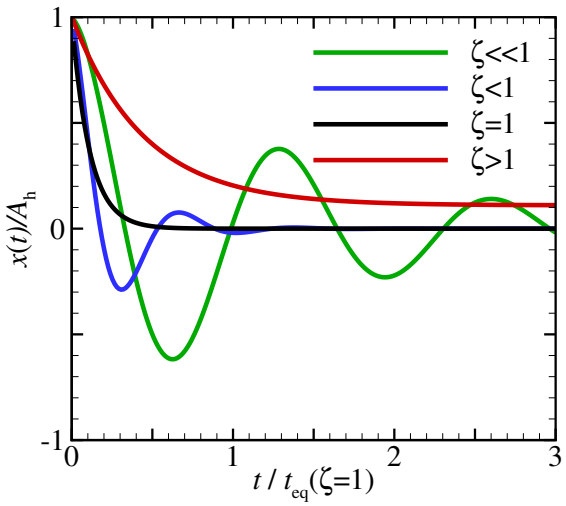

Figure 6.2: Sketch of the normalized displacement $x(t)/A_{\mathrm{h}}$ as a function of the normalized time $t/t_{\mathrm{eq}}(\zeta = 1)$ of the characteristic dynamic regimes of the damped harmonic oscillator forced by the step-function with $x(0) = A_{\mathrm{h}}$ and $\dot{x}(0) = 0$.

The critically damped harmonic oscillator returns to its equilibrium position in the shortest possible time [79]. When the system is under-damped $\zeta < 1$, the center of mass will overshoot its equilibrium position and oscillate around it. This causes an increase in equilibrium time. Equilibrium time t_{eq} is defined as the time necessary for the difference in the position of the center-of-mass between two subsequent time increments to fall below a certain value δ that we decide to tolerate. When the system is over-damped $\zeta > 1$, the center of mass will come to rest later and away from the equilibrium position of the critically damped oscillator. In this work we are interested in finding the correct equilibrium position.

6.2.1 Equilibrium time

The amplitude of the damped harmonic oscillator decays exponentially in time as [79]:

$$a_{\mathrm{h}}(t) = \sum_{i=1}^{2d} A_i e^{-(\frac{t}{\tau})}, \tag{6.11}$$

where $a(t)$ is the amplitude at time t of the homogeneous solution of the damped harmonic oscillator. The exponential time constant τ of the damped harmonic oscillator is defined as the inverse of the real part of the exponents of its homogeneous solution:

$$\frac{1}{\tau} = -\mathrm{Re}\{\lambda_{\pm}\}. \tag{6.12}$$

According to Ogata [44] the equilibrium time of an under-damped harmonic oscillator can be approximated as:

$$t_{\mathrm{eq}}(c < c_{\mathrm{cr}}) \approx C\tau, \tag{6.13}$$

with

$$C = -\ln \frac{\delta}{|a_{\mathrm{h}}(0)|}, \tag{6.14}$$

where C is a constant. According to Ramos [84] the equilibrium time estimated by Ogata [44] has an error up to 25% in the equilibrium time for the critically damped harmonic oscillator. The maximum error is observed for the critically damped harmonic oscillator [84]. The approximation by Ogata [44] for critically damped harmonic oscillator assumes that the initial conditions (*i.e.*, $x(0)$ and $\dot{x}(0)$) have no effect on the trajectory in the long time limit. This work shows in Sec. 6.5 that the approximation by Ogata [44] predicts the correct dependencies of the equilibrium time t_{eq} in GFMD simulations. This is could be explained by the large accumulated error in position and velocity for pSV. So, in this work, the equilibrium time of the critically damped harmonic oscillator becomes:

$$t_{\mathrm{eq}}(c = c_{\mathrm{cr}}) \propto \sqrt{\frac{m}{\kappa}}. \tag{6.15}$$

6.2.2 Position (Störmer-)Verlet method

The pSV method [16] is a numerical method used to integrate the equation of motion. The pSV method uses the first three terms of the Taylor expansion for the evaluation of the position of a particle with mass m at time t and coordinate $r(t)$ with velocity $v(t)$ and experiencing a force $f(r,t)$. The method introduces the discrete-time variables $r[n] = r(t[n])$, $v[n] = v(t[n])$ and $f[n] = f(r[n], t[n])$ and discrete time-step $\mathrm{d}t$. [80]. The original form of the pSV method is:

$$r[n+1] = 2r[n] - r[n-1] + \frac{\mathrm{d}t^2}{m} f[n], \tag{6.16}$$

with the associated velocity calculated by the central difference:

$$v[n] = \frac{r[n+1] - r[n-1]}{2\mathrm{d}t}. \tag{6.17}$$

This is also known as the implicit velocity. To determine the characteristic dynamic regimes and critical damping of the pSV method, a velocity explicit scheme is needed [80]. Following [81], the

velocity explicit scheme by Störmer is written as:

$$\ddot{r}[n] = \frac{v[n+1] - v[n]}{\mathrm{d}t} = \frac{\dfrac{r[n+1] - r[n]}{\mathrm{d}t} - \dfrac{r[n] - r[n-1]}{\mathrm{d}t}}{\mathrm{d}t} = \frac{r[n+1] - 2r[n] + r[n-1]}{(\mathrm{d}t)^2} = f[n]. \tag{6.18}$$

Equation (6.16) thus becomes:

$$r[n+1] = r[n] + v[n]\mathrm{d}t + \frac{\mathrm{d}t^2}{m} f[n], \tag{6.19}$$

where

$$v[n] = \frac{r[n] - r[n-1]}{\mathrm{d}t}. \tag{6.20}$$

Figure 6.3 is a schematic representation of pSV, as derived by Störmer [81]. According to Hairer *et al.* [81], this geometrically amounts to determining an interpolating parabola which, in the mid-point, assumes the second derivative prescribed by $m\ddot{r} = f(r)$.

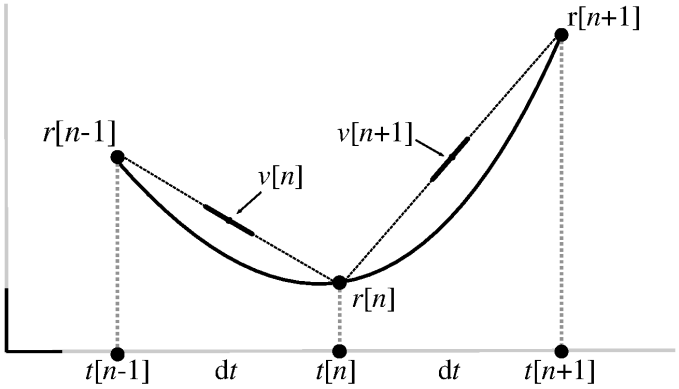

Figure 6.3: Schematic representation of the pSV method for the n^{th} iteration.

6.2.2.1 Characteristic dynamic regimes

Here, we determine the relationship between the linear damping coefficient c and the damping factor η for the damped harmonic oscillator. Moreover, we derive and study the characteristic dynamic regimes and critical damping coefficient in the limit $\mathrm{d}t \to 0^+$. In this limit, the analytical expression for pSV should be equal to the homogeneous solution of the differential equation of the damped harmonic oscillator Eq. (6.8). Following Eq. (6.2), the equation of motion is written as:

$$m\ddot{r} = f(r,t) - cv. \tag{6.21}$$

The mass m is unity. Eq. (6.21) is integrated over a time increment $\mathrm{d}t$ between two times $t[n]$ and $t[n+1] = t[n] + \mathrm{d}t$:

$$\int_{t[n]}^{t[n+1]} \ddot{r}\mathrm{d}t' = \int_{t[n]}^{t[n+1]} f(r,t)\,\mathrm{d}t' - c\int_{t[n]}^{t[n+1]} v\mathrm{d}t'. \tag{6.22}$$

The integral of the force f is approximated as:

$$v[n+1] - v[n] = \mathrm{d}t f[n] - c\int_{t[n]}^{t[n+1]} v\mathrm{d}t'. \tag{6.23}$$

Equation (6.23) is rewritten in terms of r as:

$$r[n+1] = 2r[n] - r[n-1] + \mathrm{d}t^2 f[n] - c\mathrm{d}t \int_{t[n]}^{t[n+1]} v\mathrm{d}t'. \tag{6.24}$$

The integral of the velocity v is approximated as $(\mathrm{d}t)v[n]$, because the velocity over $r(t[n+1]) - r([n])$ is determined by $v[n]\mathrm{d}t$ for $f(t[n]]) = 0$ in Eq. (6.19). Following Eqs. (6.3), (6.19) and (6.19), we rewrite Eq. (6.23) in the velocity explicit form as:

$$v[n+1] = \mathrm{d}t f[n] + (1 - c\mathrm{d}t)\, v[n], \tag{6.25}$$

and we determine η as:

$$\eta \equiv \frac{c}{\mathrm{d}t}. \tag{6.26}$$

In the limit $\mathrm{d}t \to 0^+$, the damping factor becomes infinity large. Note that this can be perceived as counterintuitive. However, substituting Eq. (6.26) in Eq. (6.3), we can rewrite $\tilde{\boldsymbol{F}}_{\mathrm{d}}[n]$ as:

$$\tilde{\boldsymbol{F}}_{\mathrm{d}}[n] = \tilde{\boldsymbol{F}}_{\mathrm{el}}[n] + \tilde{\boldsymbol{F}}_{\mathrm{ext}} + \boldsymbol{c}\left(\boldsymbol{v}[n]\right). \tag{6.27}$$

This is the velocity explicit pSV scheme of the damping force $\tilde{\boldsymbol{F}}_{\mathrm{d}}[n]$. Moreover, note that the critical damping coefficient c_{cr} for the pSV has a higher-order $\mathrm{d}t$ dependency that can not be correctly represented by writing (6.26) in terms of Eqs. (6.10) for a finite discrete time-step $\mathrm{d}t$. In this work, we derive this higher-order $\mathrm{d}t$ dependency, and to this end we write the velocity explicit pSV method (*i.e.*, Eqs. (6.24) and (6.25)) as a matrix difference equation:

$$\begin{bmatrix} r[n+1] \\ v[n+1] \end{bmatrix} = \mathcal{V} \begin{bmatrix} r[n] \\ v[n] \end{bmatrix}, \tag{6.28}$$

where $\mathcal{V}$ is the difference matrix. Following [81] and [80], the characteristic dynamic regimes of the velocity Verlet methods applied to the damped harmonic oscillator are determined by the eigenvalues $\Lambda_{\pm}$ of the matrix $\mathcal{V}$:

$$\begin{aligned} \Lambda_+ = \Lambda_- &\text{ if critically damped;} \\ \Lambda_{\pm} &\text{ is complex if under damped;} \\ \Lambda_{\pm} &\text{ is real and } \Lambda_{\pm} < 1 \text{ if over-damped;} \\ ||\Lambda_{\pm}|| \geq 1 &\text{ if unstable.} \end{aligned} \tag{6.29}$$

If the modulus of the eigenvalues is greater than one, repeated application of the linear transformation of the recursive scheme of a Verlet method will lead to exponential growth of the variations and the periodic solution is unstable [85]. Here, variations indicate the error in the linear approximation of the interpolation parabola and the original parabola (See Fig. 6.3). The corresponding formal Verlet stability limit determines the maximum discrete time-step $\mathrm{d}t$ for a given spring constant κ. The following derivation (Eqs. (6.30) to (6.33)) show how the characteristic regimes are derived. In Sec. 6.4 this derivation is used to approximate the equilibrium time t_{eq}. The characteristic dynamic regimes are determined by deriving the closed continuous expression $r(t)$.

The position $r[n]$ is written as:

$$r[n] = \sum_{i=1}^{2d} A_i \Lambda_i^n, \tag{6.30}$$

where A_i are real valued constants and $\Lambda_i = 1 + \dfrac{\xi_i}{2d}$ are the eigenvalues of $\mathcal{V}$. Equation (6.30) is written in a series expression with binomial coefficients:

$$r[n] = \sum_{i=1}^{2d} A_i \sum_{k=0}^{\infty} \binom{n}{k} \left(\frac{\xi_i}{2d}\right)^k, \qquad |\frac{\xi_i}{2d}| < 1. \tag{6.31}$$

The binomial $\binom{n}{k}$ is equal to the fraction $\dfrac{n^k}{k!}$ and the binomial series is evaluated as:

$$\sum_{k=0}^{\infty} \frac{\left(\dfrac{\xi_i}{2d}\right)^k n^k}{k!} = e^{\left(n\dfrac{\xi_i}{2d}\right)}. \tag{6.32}$$

By inserting $\dfrac{t}{\mathrm{d}t} = n$, the closed continuous expression in the limit $\mathrm{d}t \to 0^+$ of the trajectory $r(t)$ is written as:

$$r\left(t\right) = \lim_{\mathrm{d}t \to 0^+} \sum_{i=1}^{2d} A_i e^{\left(\dfrac{\xi_i}{2d}\dfrac{t}{\mathrm{d}t}\right)} = \sum_{i=1}^{2d} A_i e^{\lambda_i t}. \tag{6.33}$$

To determine the characteristic dynamic regimes and the critical linear damping coefficient of a damped harmonic oscillator solved by the pSV method, its geometric integration scheme is applied to the damped harmonic oscillator with mass m and spring constant κ. Here, $F_{\mathrm{el}}[n]\left(u[n]\right) = -\kappa u[n]$ represents a linear Hooke's spring with linear spring constant $\kappa > 0$. By inserting Eq. (6.19) in Eq. (6.28) matrix $\mathcal{V}$ becomes:

$$\mathcal{V} = \begin{bmatrix} 1 - \kappa\left(\mathrm{d}t\right)^2 & \mathrm{d}t - \eta\left(\mathrm{d}t\right)^3 \\ -\kappa\left(\mathrm{d}t\right) & 1 - \eta\left(\mathrm{d}t\right)^2 \end{bmatrix}. \tag{6.34}$$

The matrix $\mathcal{V}$ has the eigenvalues $\Lambda_\pm$:

$$\Lambda_\pm = \frac{2 - \mathrm{d}t^2\left(\eta + \kappa\right) \pm \sqrt{\mathrm{d}t^4\left(\eta + \kappa\right)^2 - 4\kappa\left(\mathrm{d}t\right)^2}}{2}. \tag{6.35}$$

The eigenvalues $\Lambda_\pm$ of the matrix $\mathcal{V}$ written in terms of κ and c thus become:

$$\Lambda_\pm = \frac{2 - \mathrm{d}t\left(c + \kappa\mathrm{d}t\right) \pm \sqrt{\mathrm{d}t^2\left(c + \kappa\mathrm{d}t\right)^2 - 4\kappa\left(\mathrm{d}t\right)^2}}{2}. \tag{6.36}$$

As expected, in the limit $\mathrm{d}t \to 0^+$ the eigenvalues λ_i (Eq. (6.33)) are equal to the eigenvalues of the homogeneous solution of a damped harmonic oscillator (Eq. (6.8)). The characteristic dynamic regimes of the pSV method are:

$$\begin{aligned} \xi_- = \xi_+ &\text{ if critically damped;} \\ \xi_\pm &\text{ is complex if under-damped;} \\ \xi_\pm \text{ is real and } \xi_\pm < 0 &\text{ if over-damped;} \\ \xi_\pm < -2 \text{ or } \xi_\pm \geq 0 &\text{ if unstable.} \end{aligned} \tag{6.37}$$

The dynamic regimes in Eq. (6.29) are equal to the dynamic regimes in Eq. (6.37). The formal stability limit can be rewritten as $\kappa \mathrm{d}t^2 \leq 4$ for the harmonic oscillator. This is done similarly in this work, because the stability of a geometric numerical integration method is traditionally evaluated with $c = 0$. The characteristic dynamic regime in this work are determined by the dependencies in Eq. (6.29).
The numerical critical damping factor η_{cr} is expected to deviate from the analytical expression $\zeta = 1$ for larger values of the discrete time-steps $\mathrm{d}t$. The calculated relationship between damping factor η and damping coefficient c (Eq. (6.26)) scales linearly with the discrete time-step $\mathrm{d}t$. Following [80], we write the Verlet-type method by Grønbech-Jensen as:

$$\begin{aligned} r[n+1] &= r[n] + b\mathrm{d}t v[n] + \frac{b\mathrm{d}t^2}{2m} f[n]; \\ v[n+1] &= av[n] + \frac{\mathrm{d}t}{2m}\left(af[n] + f[n+1]\right), \end{aligned} \tag{6.38}$$

where,

$$a \equiv \frac{1 - \dfrac{c\mathrm{d}t}{2m}}{1 + \dfrac{c\mathrm{d}t}{2m}}, \; b \equiv \frac{1}{1 + \dfrac{c\mathrm{d}t}{2m}}. \tag{6.39}$$

The characteristic dynamic regime of the Verlet-type method by Grønbech-Jensen should be better predicted by $\zeta = 1$ for large discrete time-steps $\mathrm{d}t$ then by pSV. The comparison with the Verlet-type method by Grønbech-Jensen [80] is made because of their derivation of the characteristic dynamic regimes of a damped harmonic oscillator with a Verlet-method comparable to the pSV method.
To evaluate the characteristic dynamic regimes of a damped harmonic oscillator solved by a Verlet-type method, the damping ratio ζ is written in terms of the two characteristic parameters, $\kappa \mathrm{d}t^2$ and $c\mathrm{d}t$. By multiplying the numerator and denominator of the damping ratio ζ with the dimensionless discretization time $\mathrm{d}t$, the damping ratio between the characteristic parameters can be determined as:

$$\zeta_{\mathrm{V}} = \frac{c\mathrm{d}t}{2\sqrt{\kappa \mathrm{d}t^2}} \tag{6.40}$$

When the ratio ζ_{V} is unity, it represents the ratio between the characteristic parameters $\kappa \mathrm{d}t^2$ and $c_{\mathrm{cr}}\mathrm{d}t$. The ratio ζ_{V} defines the characteristic dynamic regimes of a harmonic oscillator, which are independent of the dimensionless discretization time $\mathrm{d}t$, but this form allows for the comparison with the characteristic dynamic regimes of a damped harmonic oscillator solved by the Verlet-type methods.
Figure 6.4 displays the characteristic dynamic regimes, as a function of the two characteristic parameters $\kappa \mathrm{d}t^2$ and $c\mathrm{d}t$ for the pSV method and the Verlet-type method by Grønbech-Jensen [80].

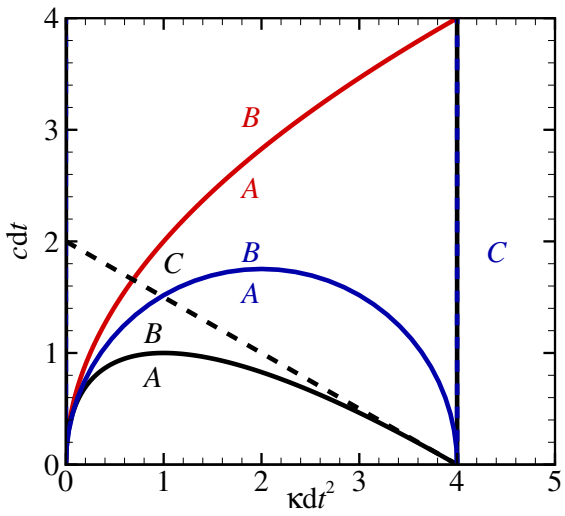

Figure 6.4: Sketch of the characteristic parameter $c\mathrm{d}t$ as a function of the characteristic parameter $\kappa \mathrm{d}t^2$ corresponding to the homogeneous solution of the differential equation of a damped harmonic oscillator (red line), the pSV method (black lines) and the Verlet-type method by Grønbech-Jensen [80] (blue lines). Solid line displays the boundary between characteristic dynamic regimes under-damped and over-damped regime represented by A and B, dashed lines display the boundaries between the characteristic dynamic over-damped and unstable regime represented by B and C. The vertical dashed black line and vertical dashed blue line represent the formal Verlet stability limit $\kappa \mathrm{d}t^2 = 4$.

The characteristic dynamic regimes obtained for $\kappa \mathrm{d}t^2 << 1$ are the same for all methods. The difference in accumulated error is the reason for the differences in characteristic dynamic regimes between the two Verlet-type methods (Fig. 6.4). The critical damping factor and the characteristic dynamic regimes of a harmonic oscillator solved by the pSV method is only approximated by the damping ratio $\zeta = 1$, for $\kappa \mathrm{d}t^2 << 1$. This is expected because of the scaling of the finite time error by $(\mathrm{d}t^2)$. Hence, the damped harmonic oscillator calculated with the pSV method is critically damped when the eigenvalues of the matrix $\mathcal{V}$ are real and equal (*i.e.*, $\Lambda_- = \Lambda_+$). The critical damping factor η_{cr} is determined by setting the part below the square root of the eigenvalues $\Lambda_\pm$ of the matrix $\mathcal{V}$ equal to zero. The critical damping factor of the pSV method:

$$\eta_{\mathrm{cr}} = 2\sqrt{\kappa}\frac{1}{\mathrm{d}t} - \kappa. \tag{6.41}$$

Using Eq. (6.26), equation (6.41) is rewritten in terms of the critical damping coefficient:

$$c_{\mathrm{cr}} = 2\sqrt{\kappa} - \kappa \mathrm{d}t. \tag{6.42}$$

As to be expected, in the limit $\Delta t \to 0^+$ Eq. (6.42) is equal to Eq. (6.10).

The critical damping coefficient c_{cr} and critical damping factor η_{cr} as a function of the discrete time-step $\mathrm{d}t$ and the linear constant κ are shown in Fig. 6.5.

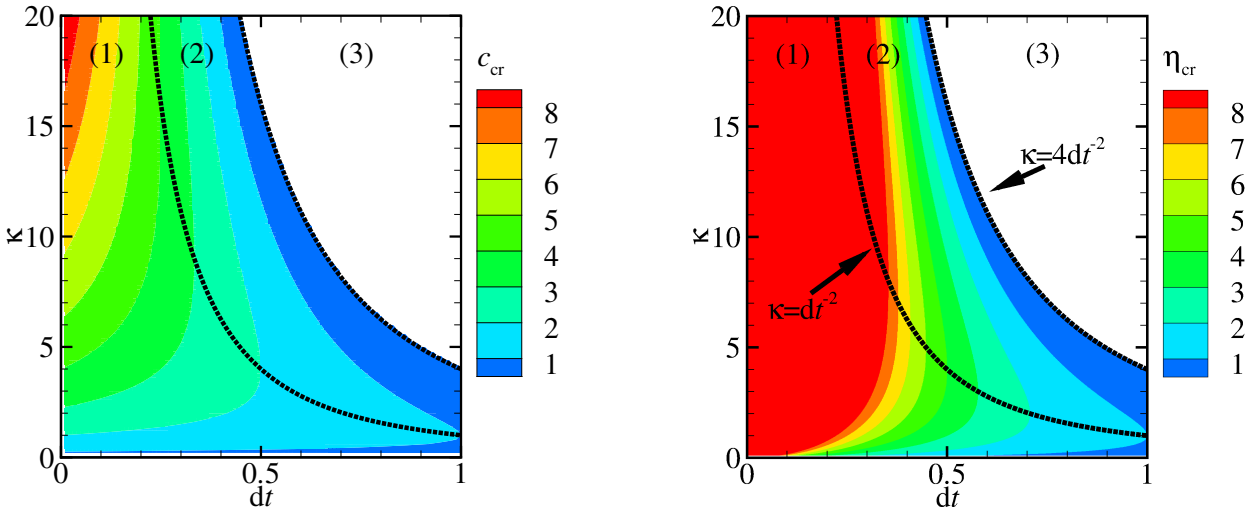

Figure 6.5: Contour plots of the critical damping (a) coefficient c_{cr} and (b) factor η_{cr} as a function of the discrete time-step $\mathrm{d}t$ and the linear constant κ for pSV with zones (1), (2) and (3).

In Fig. 6.5a, we observe three zones: (1) The critical damping coefficient c_{cr} increases with increasing linear constant κ for a given discrete time-step; (2) The critical damping coefficient c_{cr} in decreases with increasing linear constant κ for a given discrete time-step; And, (3) unstable solution. Therefore, we conclude that for a given discrete time-step $\mathrm{d}t$ damped harmonic oscillators with different linear constants κ have the same critical damping coefficient c_{cr} for pSV. Moreover, this again confirms that due to the dependency of the critical damping factor on $\mathrm{d}t$ in Eq. (6.41), the critical damping factor η_{cr} could not be known *a priori* from Eqs. (6.10) and (6.26), except for $\kappa \mathrm{d}t^2 << 1$. Considering Fig. 6.5b, we observe the same behavior. The ratio ϕ between the two linear force constants κ_{a} and κ_{b} for a constant critical damping factor η_{cr} is:

$$\phi = \frac{\kappa_{\mathrm{a}}}{\kappa_{\mathrm{b}}} = \frac{\mathrm{d}t^2\kappa_{\mathrm{a}} - 4\mathrm{d}t\sqrt{\kappa_{\mathrm{a}}} + 4}{\mathrm{d}t^2\kappa_{\mathrm{a}}}. \tag{6.43}$$

We observe in Fig. 6.5b also the three aforementioned zones. The border between zone (1) and zone (2) is determined by setting the ratio $\phi = 1$, *i.e.* $\kappa \leq \mathrm{d}t^{-2}$. The border between zone (2) and zone (3) is indicated by the formal Verlet stability limit, *i.e.* $\kappa \leq 4\mathrm{d}t^{-2}$. Note that for the remainder of this work, we assume that the discrete time-step is chosen such that $\mathrm{d}t \leq 1/\sqrt{\kappa}$.

6.2.2.2 Equilibrium time

The analytical expression to approximate the equilibrium time of the pSV method has not been derived or reported up till now. To determine the analytical expression of the equilibrium time dependency of the harmonic oscillator solved by the pSV-type method, the closed expression of the amplitude of the trajectory of the center-of-mass of the solved harmonic oscillator is used. Equation (6.30) is written as:

$$a_{\mathrm{h}}[t[n]] = \sum_{i=1}^{2d} A_i e^{\left(-\frac{\mathrm{Re}\{\xi_i\}}{2d}\frac{t[n]}{\mathrm{d}t}\right)}, \tag{6.44}$$

where $a_h[t]$ is the amplitude at time $t[n]$. The inverse of the real part of the closed expression of the eigenvalues of the damped harmonic oscillator with mass $m = 1$ is the exponential time constant:

$$\tau = \frac{1}{-\mathrm{Re}\{\frac{\xi}{2\mathrm{d}t}\}} = \frac{2}{\mathrm{d}t\,(\eta+\kappa)} = \frac{2}{c+(\mathrm{d}t)\,\kappa}. \tag{6.45}$$

Asymptotic analysis shows that the exponential time constant becomes proportional to the inverse of the linear damping constant, in the small discretization time limit ($\mathrm{d}t \rightarrow 0^+$). This proportionality is in correspondence with the results of the homogeneous solution of the differential equation of an under-damped harmonic oscillator (Sec. 6.2.1 and Eq. (6.15)). This is as expected and corresponds to the results for the characteristic dynamic regime studied in the limit ($\mathrm{d}t \rightarrow 0^+$) (Eq. (6.29)).
Similar to Sec. 6.2.1, the equilibrium time of the critically damped harmonic oscillator solved by the pSV method is written as:

$$t_{\mathrm{eq}}(c = c_{\mathrm{cr}}) \propto \frac{1}{\sqrt{\kappa}}. \tag{6.46}$$

The equilibrium time is independent of the discretization time $\mathrm{d}t$. This independence of the equilibrium time on the discretization time $\mathrm{d}t$ has not been reported before. The independence of the equilibrium time to the discrete time-step $\mathrm{d}t$ could be explained by the good conservation of oscillatory energy for a harmonic oscillator over long times even when $\kappa \mathrm{d}t^2 >> 0$ [81], but within the formal Verlet stability limit. The magnitude of the amplitude will be independent of the discrete time-step $\mathrm{d}t$. Hence, the equilibrium time will be independent of the discrete time-step $\mathrm{d}t$.

6.2.3 Coupling between multiple degrees of freedom

The number of DOF d of a system is the product of the number of masses in the system and the number of possible directions of motion of each mass [79]. The homogeneous solution can be extended to multi-DOF systems. The solution of the equation of motion of a d DOF system has d eigenvalue pairs, corresponding to d natural frequencies. Only during free vibration at one of these d natural frequencies, all centers of mass move sinusoidally with the same natural frequency. This sinusoidal motion is called a principal mode (*i.e.*, also known as normal mode, vibrational mode and natural mode) [79]. A mode is the standing wave state of excitation, where all centers-of-mass move sinusoidally with a fixed frequency.
The normal and tangential displacement of the surface in GFMD dynamics are coupled via the inverse Green's function. We treat the dynamics of the GFMD simulation as a system of independent damped harmonic oscillators with coupling of the normal and tangential displacement depending on the material's properties and geometry of the elastic body. The material's properties and elastic body geometry for which there is no dynamic coupling, are obtained by deriving the equation of motion of the elastic body. We assume that no body forces are exerted. The equilibrium condition $\partial_\alpha \sigma_{\alpha\beta}(r) = 0$, where $\sigma_{\alpha\beta}(\boldsymbol{r})$ is the stress at the point $\boldsymbol{r}$ inside the body and $\partial_\alpha \equiv \partial/\partial r_\alpha$. The equilibrium condition in Voigt notation is written as:

$$\begin{aligned} [C_{11}\partial_1^2 + C_{44}\partial_3^2]u_1 + (C_{44} + C_{12})\partial_1\partial_3 u_3 = 0; \\ [C_{11}\partial_3^2 + C_{44}\partial_1^2]u_3 + (C_{44} + C_{12})\partial_3\partial_1 u_1 = 0, \end{aligned} \tag{6.47}$$

where C_{ij} denote the coefficients of the elastic tensor:

$$\begin{aligned} C_{11} &= \frac{E\,(1-\nu)}{(1+\nu)\,(1-2\nu)}; \\ C_{12} &= \frac{E\nu}{(1+\nu)\,(1-2\nu)}; \\ C_{44} &= \frac{C_{11} - C_{12}}{2} = \frac{E}{2\,(1+\nu)}. \end{aligned} \tag{6.48}$$

The equation of motion is written as:

$$\partial_\alpha \sigma_{\alpha\beta} + \boldsymbol{F} = \rho \ddot{\boldsymbol{u}}, \tag{6.49}$$

where $\ddot{\boldsymbol{u}} = (\partial_{tt} u_1, \partial_{tt} u_3)$ is the acceleration, with time t and ρ is the material mass density. Using $s = C_{44}/C_{11}$, Eq. (6.49) is written in matrix notation as:

$$\begin{bmatrix} \ddot{u}_1 \\ \ddot{u}_3 \end{bmatrix} = \frac{C_{11}}{\rho} \begin{bmatrix} \partial_1^2 + s\partial_3^2 & (1-s)\partial_3\partial_1 \\ (1-s)\partial_1\partial_3 & \partial_3^2 + s\partial_1^2 \end{bmatrix} \begin{bmatrix} u_1 \\ u_3 \end{bmatrix}. \tag{6.50}$$

Using $s = C_{44}/C_{11}$, the relationship between the Poisson's ratio ν and s is written as:

$$s = \frac{1}{2(\nu - 1)} + 1, \tag{6.51}$$

The Born criterion [45] gives $0 \leq s \leq 1$ for plane strain conditions. In Fig. 6.6 s is plotted as a function of the Poisson's ratio ν.

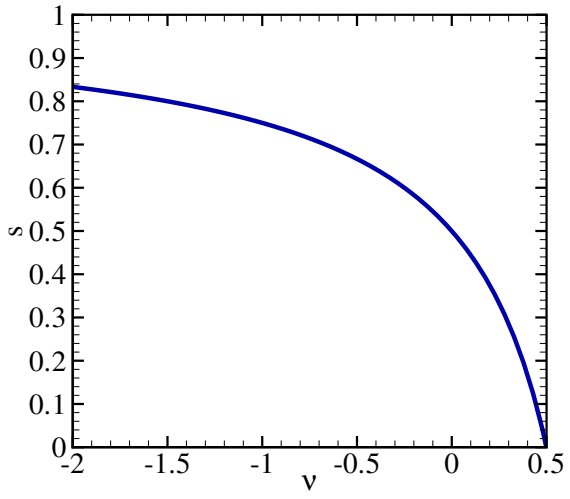

Figure 6.6: Plot of s as a function of the Poisson's ratio ν.

The Poisson's ratio ranges from -1 to 0.5 for engineering materials [41], and s approaches unity asymptotically as ν goes to $-\infty$. Meta-materials have a negative Poisson's ratio ν. In this work we are interested in metals. Metals have a Poisson's ratio $0.2 \leq \nu \leq 0.45$ [41]. However, for completeness, we show the dependency of η_{cr} on $s > 0.5$ to.
The mass matrix of a static coupled system is non-diagonal and the damping coefficient matrix and/or the spring coefficient matrix of a dynamically coupled system are non-diagonal. A multi-DOF system is weakly coupled when the off-diagonal elements of the afore-mentioned matrix are small compared with its diagonal elements. Equation (6.50) is dynamically uncoupled for two cases:

- $s = 1$;
- $\partial_3 \partial_1 u_3 = \partial_1 \partial_3 u_1 = 0$.

For $s = 0$ (i.e., $v = 0.5$) the off-diagonal elements of the matrix in Eq. (6.50) are non-zero. Hence, the equation of motion is dynamically coupled. When s increases the magnitude of the diagonal elements of the matrix in Eq. (6.50) increase while the magnitude of the off-diagonal elements decrease. Hence, for an increasing s the dynamic coupling becomes weaker.
Superposition of the homogeneous solutions of principal modes of the two directions is only valid if there is no static and dynamic coupling. However, the homogeneous solution of a weakly coupled multi-DOF system can be approximated by the superposition of the homogeneous solutions of the principal modes [86]. Moreover, since the high frequency modes die out faster than low frequency modes for an impulse response, the large time scale solution of a multi-DOF system can be approximated by its lowest frequency mode. The mode with the lowest natural frequency is mostly, but not necessarily, the center-of-mass mode. The error in the approximation increases as s decreases. Hence, the homogeneous solution of the surface displacements in GMFD-simulations cannot be known a-priori.

6.3 Damped dynamics in Green's function molecular dynamics

Derivation of the analytical expression for the critical damping factor $\boldsymbol{\eta}_{\mathrm{cr}}$ in GFMD simulations is based on the following concepts:
The equation of motion in real space can be solved by superposition of the independent solutions of the equation of motion in Fourier space corresponding to a wave number q. Every displacement mode $\tilde{\boldsymbol{u}}(q)$ of a system in Fourier space corresponds to a principal dynamic mode in real space [87]. Therefore, also in Fourier space coupling between the normal and tangential modes depends on the elastic properties of the substrate. In the following, modes in real-space will be referred to as dynamic modes. Modes in Fourier space will be called principal modes and the first principal mode is called the center-of-mass mode. The displacement of the center-of-mass modes correspond to the uniform displacement of the surface. The change in volume of the substrate is determined by the displacement of the center-of-mass mode in normal direction. A local displacement of the surface with zero volume change of the substrate can be viewed as a combination of the motion of the center-of-mass mode in tangential direction and all principal modes.
The Newton equation in GFMD dynamics is written as:

$$m\frac{\mathrm{d}^2\tilde{\boldsymbol{u}}\,(q,t)}{\mathrm{d}t^2}+\boldsymbol{c}\frac{\mathrm{d}\tilde{\boldsymbol{u}}\,(q,t)}{\mathrm{d}t}+\tilde{\boldsymbol{G}}\,(q)^{-1}\,\tilde{\boldsymbol{u}}\,(q,t)=-\tilde{\boldsymbol{F}}_{\mathrm{ext}}\,(q,t)-\tilde{\boldsymbol{F}}_{\mathrm{if}}\,(q,t)\,, \tag{6.52}$$

with homogeneous equation:

$$m\frac{\mathrm{d}^2\tilde{\boldsymbol{u}}\,(q,t)}{\mathrm{d}t^2}+\boldsymbol{c}\frac{\mathrm{d}\tilde{\boldsymbol{u}}\,(q,t)}{\mathrm{d}t}+\tilde{\boldsymbol{G}}\,(q)^{-1}\,\tilde{\boldsymbol{u}}\,(q,t)=0. \tag{6.53}$$

The critical damping factor $\boldsymbol{\eta}_{\mathrm{cr}}$ is chosen equal for all wave numbers q, such that for that particular damping factor all modes are critically damped and/or under-damped. we will see that the slowest mode is either the center-of-mass mode or the first principal mode.
The velocity explicit scheme of the damped pSV method for a traction prescribed GFMD simulation is now derived. The damped force of a single principal mode corresponding to a wave number q is:

$$\tilde{\boldsymbol{F}}_{\mathrm{d}}[n]=\tilde{\boldsymbol{F}}_{\mathrm{el}}[n]+\boldsymbol{\eta}\,(\tilde{\boldsymbol{u}}[n-1]-\tilde{\boldsymbol{u}}[n])\,. \tag{6.54}$$

Using Eq. (6.19), we give the explicit velocity scheme of a single principal mode corresponding to a wave number q as:

$$\tilde{\boldsymbol{u}}[n+1]=2\tilde{\boldsymbol{u}}[n]-\tilde{\boldsymbol{u}}[n-1]+\tilde{\boldsymbol{F}}_{\mathrm{el}}[n]\,(\Delta t)^2+\boldsymbol{\eta}\,(\Delta t)^2\,(\tilde{\boldsymbol{u}}[n-1]-\tilde{\boldsymbol{u}}[n])\,; \tag{6.55a}$$

$$\tilde{\boldsymbol{u}}[n+1]-\tilde{\boldsymbol{u}}[n]=\tilde{\boldsymbol{u}}[n]-\tilde{\boldsymbol{u}}[n-1]+\tilde{\boldsymbol{F}}_{\mathrm{el}}[n]\,(\Delta t)^2+\boldsymbol{\eta}\,(\Delta t)^2\,(\tilde{\boldsymbol{u}}[n-1]-\tilde{\boldsymbol{u}}[n])\,; \tag{6.55b}$$

$$(\Delta t)\,\tilde{\boldsymbol{v}}[n+1]=\tilde{\boldsymbol{v}}[n]\,(\Delta t)+\tilde{\boldsymbol{F}}_{\mathrm{el}}[n]\,(\Delta t)^2-\boldsymbol{\eta}\,(\Delta t)^3\,\tilde{\boldsymbol{v}}[n]; \tag{6.55c}$$

$$\tilde{\boldsymbol{v}}[n+1]=\tilde{\boldsymbol{F}}_{\mathrm{el}}[n]\,(\Delta t)+\tilde{\boldsymbol{v}}[n]\left(1-\boldsymbol{\eta}\,(\Delta t)^2\right), \tag{6.55d}$$

where $\tilde{\boldsymbol{v}}=(\tilde{v}_1,\tilde{v}_3)$ is the velocity of the surface displacement of a mode corresponding to wave number q. The explicit position scheme of a single principal mode corresponding to a wave number q is:

$$\tilde{\boldsymbol{u}}[n+1]=\tilde{\boldsymbol{u}}[n]+\tilde{\boldsymbol{F}}_{\mathrm{el}}[n]\,(\Delta t)^2+\tilde{\boldsymbol{v}}[n]\left((\Delta t)-\boldsymbol{\eta}\,(\Delta t)^3\right). \tag{6.56}$$

Following Venugopalan *et al.* [3], we write the areal elastic energy v_{el} as:

$$v_{\mathrm{el}}=\sum_{\boldsymbol{q}}\frac{q}{2}\left[\tilde{u}_1^*(q),\tilde{u}_3^*(q)\right]\begin{bmatrix}M_{11}(qz_{\mathrm{m}}) & -\mathrm{i}M_{13}(qz_{\mathrm{m}})\\ \mathrm{i}M_{13}(qz_{\mathrm{m}}) & M_{33}(qz_{\mathrm{m}})\end{bmatrix}\begin{bmatrix}\tilde{u}_1(q)\\ \tilde{u}_3(q)\end{bmatrix}, \tag{6.57}$$

with

$$
\begin{aligned}
M_{11}(q) &= (1-r)\frac{\cosh(qz_{\mathrm{m}})\sinh(qz_{\mathrm{m}}) - r(qz_{\mathrm{m}})}{\parallel f(z_{\mathrm{m}}) \parallel} C_{11};\\
M_{13}(q) &= \left(\frac{1-r}{1+r}\right)\frac{(1-r)\sinh^2(qz_{\mathrm{m}}) - 2r^2(qz_{\mathrm{m}})^2}{\parallel f(z_{\mathrm{m}}) \parallel} C_{11};\\
M_{33}(q) &= (1-r)\frac{\cosh(qz_{\mathrm{m}})\sinh(qz_{\mathrm{m}}) + r(qz_{\mathrm{m}})}{\parallel f(z_{\mathrm{m}}) \parallel} C_{11},
\end{aligned}
\tag{6.58}
$$

where

$$
r = \frac{1-s}{1+s}, \tag{6.59}
$$

and

$$
\parallel f(qz_{\mathrm{m}}) \parallel = \cosh^2(qz_{\mathrm{m}}) - (rqz_{\mathrm{m}})^2 - 1. \tag{6.60}
$$

The stiffness matrix is not diagonal (Eq. (6.57)), so there is coupling. Similar to Eq. (6.35), the matrix notation of the velocity explicit scheme for a single mode corresponding to wave number q is:

$$
\tilde{\boldsymbol{u}}[n+1] = \mathcal{V}\tilde{\boldsymbol{u}}[n] \tag{6.61}
$$

where

$$
\mathcal{V} = \begin{bmatrix}
1 - \dfrac{2\pi k M_{11}}{L_x}\Delta t^2 & -\dfrac{-\mathrm{i}2\pi k M_{13}}{L_x}\Delta t^2 & \Delta t - \eta_1 (\Delta t)^3 & 0 \\
-\dfrac{\mathrm{i}2\pi k M_{13}}{L_x}\Delta t^2 & 1 - \dfrac{2\pi k M_{33}}{L_x}\Delta t^2 & 0 & \Delta t - \eta_3 (\Delta t)^3 \\
-\dfrac{2\pi k M_{11}}{L_x}\Delta t & -\dfrac{-\mathrm{i}2\pi k M_{13}}{L_x}\Delta t & 1 - \eta_1 (\Delta t)^2 & 0 \\
-\dfrac{\mathrm{i}2\pi k M_{13}}{L_x}\Delta t & -\dfrac{2\pi k M_{33}}{L_x}\Delta t & 0 & 1 - \eta_3 (\Delta t)^2
\end{bmatrix}. \tag{6.62}
$$

Due to coupling the normal component and the tangential component of the displacement can no longer be independently determined, except for uniform displacement of a finite slab, a semi-infinite solid with the Poisson's ratio $\nu = 0.5$ and zero normal traction or frictionless contact. We present these limiting cases first.

6.3.1 Uniform displacement of a finite slab

The result of the asymptotic analysis of the $M_{ij}(qz_{\mathrm{m}})$ in the short wave vectors limit is:

$$
qM_{11}\left(z_{\mathrm{m}} << 1\right) = \frac{C_{44}}{z_{\mathrm{m}}}; \tag{6.63a}
$$

$$
qM_{13}\left(z_{\mathrm{m}} << 1\right) = 0; \tag{6.63b}
$$

$$
qM_{33}\left(z_{\mathrm{m}} << 1\right) = \frac{C_{11}}{z_{\mathrm{m}}}, \tag{6.63c}
$$

so the areal elastic energy related to the center-of-mass displacements is:

$$
v_{\mathrm{el}}\left(q=0\right) = \frac{C_{44}}{2z_{\mathrm{m}}}\tilde{u}_1^2\left(0\right) + \frac{C_{11}}{2z_{\mathrm{m}}}\tilde{u}_3^2\left(0\right). \tag{6.64}
$$

The matrix notation for the equation of motion for the center-of-mass modes are equal to the solution for the damped harmonic oscillator, *i.e.*, Eqs. (6.35) and (6.36). The critical damping factor for the center-of-mass displacement thus becomes:

$$\begin{aligned} \eta_{1,\mathrm{cr}} &= 2\sqrt{\kappa_1}\frac{1}{\Delta t} - \kappa_1; \\ \eta_{3,\mathrm{cr}} &= 2\sqrt{\kappa_3}\frac{1}{\Delta t} - \kappa_3, \end{aligned} \tag{6.65}$$

where

$$\begin{aligned} \kappa_1\left(q=0, z_{\mathrm{m}}\right) &= \frac{C_{44}}{z_{\mathrm{m}}} = \frac{E}{2aL_x\left(1+\nu\right)}; \\ \kappa_3\left(q=0, z_{\mathrm{m}}\right) &= \frac{C_{11}}{z_{\mathrm{m}}} = \frac{E(\nu-1)}{aL_x\left(2\nu^2+\nu-1\right)}. \end{aligned} \tag{6.66}$$

The linear force constant $\kappa_3(q=0, z_{\mathrm{m}})$ is always larger than or equal to $\kappa_1(q=0, z_{\mathrm{m}})$, because s ranges from 0 to 1. In the limit where s approaches zero, the linear force constant κ_3 goes to infinity which results in undamped oscillation of the corresponding center-of-mass mode in normal direction. The normalized linear force constants $\kappa(q=0, z_m)L_x/C_{44}$ as a function of s and the aspect ratio a is presented in Fig. 6.7. As reference the normalized linear force constants $\kappa(q=0, z_m)L_x/E$ as a function of the Poisson's ratio ν and the aspect ratio a is also plotted

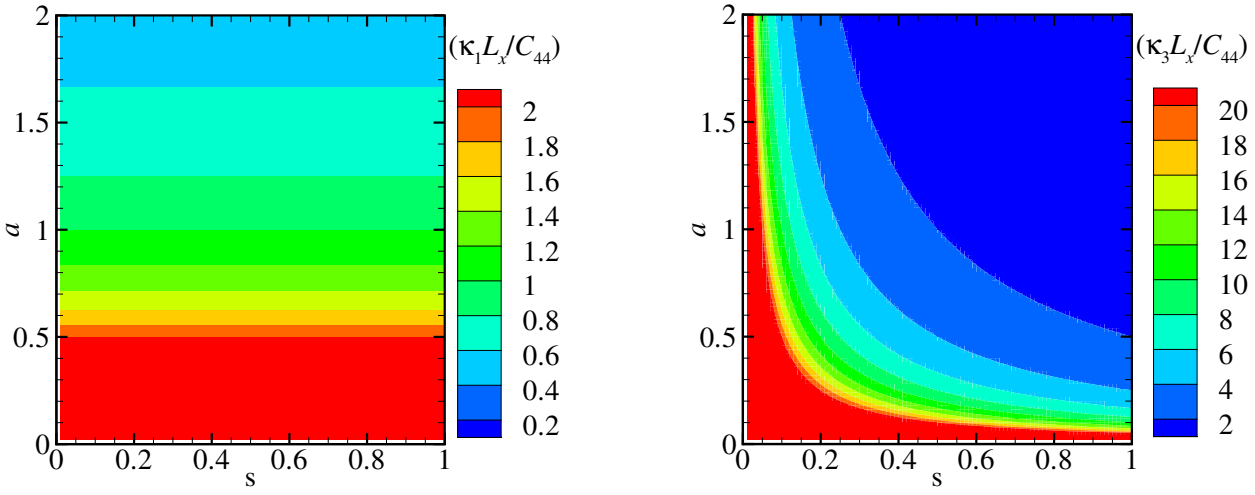

(a) (b)

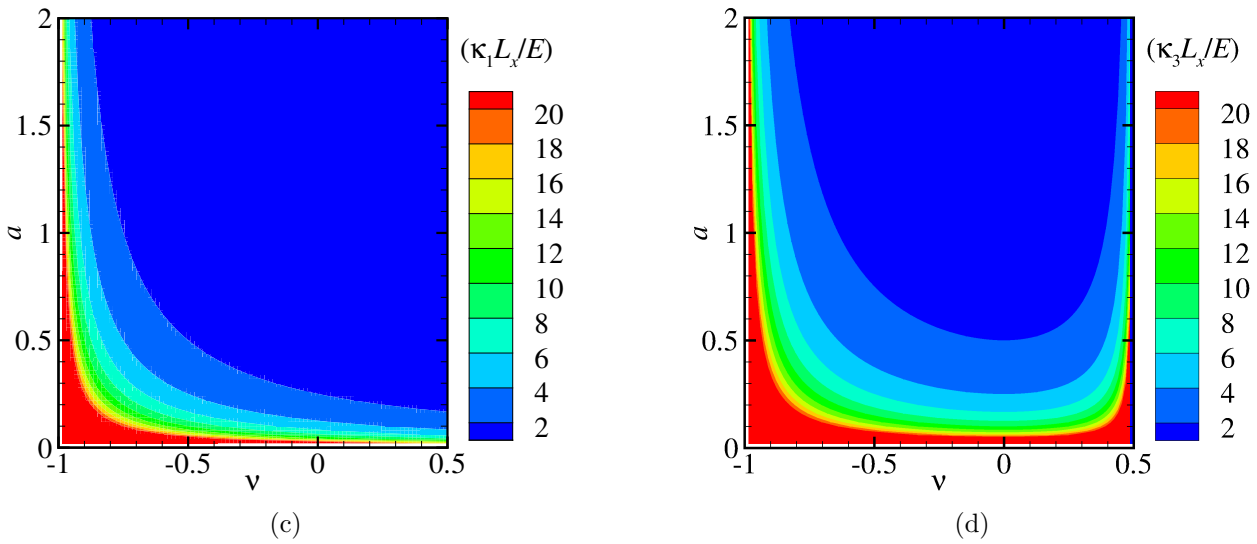

Figure 6.7: Contour plots of the normalized linear force constants (a) $\kappa_1 L_x/C_{44}$ and (b) $\kappa_3 L_x/C_{44}$ as a function of s and the aspect ratio a, and (c) $\kappa_1 L_x/E$ and (d) $\kappa_3 L_x/E$ as a function of the Poisson's ratio ν and the aspect ratio a for the center-of-mass mode, for uniform displacement in normal and tangential direction.

As to be expected, for all linear force constants we observe a dependency on the aspect ratio a. Note that only the linear force constant of the center-of-mass mode in tangential direction is independent of s, and the linear force constant κ in one of the two directions can be the smallest force constant depending only on s and the aspect ratio a. A change of the elastic modulus E and the periodicity L_x or the Voigt constant C_{44} and the periodicity L_x result in an out of plane shift of the linear force constant κ as depicted in Fig. 6.7. Therefore, the critical damping factor increases when the coefficient of the elastic modulus E increases, the width L_x decreases and the aspect ratio a decreases. In the limit $s \to 1$ the linear force constants are equal. In Fig. 6.7 it is seen that the linear force constant of the normal center-of-mass mode $\kappa_3(q = 0, z_\mathrm{m})$ increases for an increase in Poisson's ratio ν. It is well known that the only mode necessary to change the volume is the normal center-of-mass mode, *i.e.* $\tilde{u}_3(k = 0)$ and the change in volume decreases as the Poisson's ratio increases. Hence, for an increasing Poisson's ratio ν the elastic restoring force for a finite displacement of normal center-of-mass mode increases. The linear force constant is proportional to the elastic restoring force. It is also well known that for a decreasing Poisson's ratio ν the stress increases for a given elastic modulus and strain. Hence, both linear force constants increase for a decreasing Poisson's ratio ν. It is observed that $\kappa_1(0, z_\mathrm{m}, L_x, E, \nu) \leq \kappa_2(0, z_\mathrm{m}, L_x, E, \nu)$. Therefore, it can be concluded that the center-of-mass mode in tangential direction is the lowest frequency mode of both center-of-mass modes.

6.3.2 Normal displacement of an incompressible semi-infinite solid

Considering only the normal component of the displacement [5], the areal elastic energy is:

$$v_{\mathrm{el}} = \frac{\mathrm{E}^*}{4} \sum_{\mathbf{q}} q |\tilde{u}(\mathbf{q})|^2, \tag{6.67}$$

and the elastic force corresponding to the wave number q is:

$$\tilde{F}[n] = \nabla_{u[n]} v_{\mathrm{el}} = -q \frac{E^*}{2} \tilde{u}(n). \tag{6.68}$$

Following Eqs. (6.35) and (6.36), we give the critical damping factor as:

$$\eta_{\mathrm{cr}} = 2\sqrt{\kappa} \frac{1}{\Delta t} - \kappa, \tag{6.69}$$

with

$$\kappa\left(k, L_x, E^*\right) = \frac{\pi k E^*}{L_x}, \tag{6.70}$$

where κ is the linear force constant similar to the linear spring constant for the harmonic oscillator. The first principal mode (*i.e.* $k = 1$) has the smallest linear force constant compared to higher modes. Therefore, the critical damping factor for one DOF corresponds to the critical damping factor of the first principal mode. Figure 6.8 depicts the critical damping factor η_{cr} as a function of the effective modulus E^*, the width L_x and the discrete time-step Δt with $\Delta t = 1/4$ for (a) and (b) , $L_x = 10$ μm for (a) and (c), and $E^* = 70$ GPa for (b) and (c).

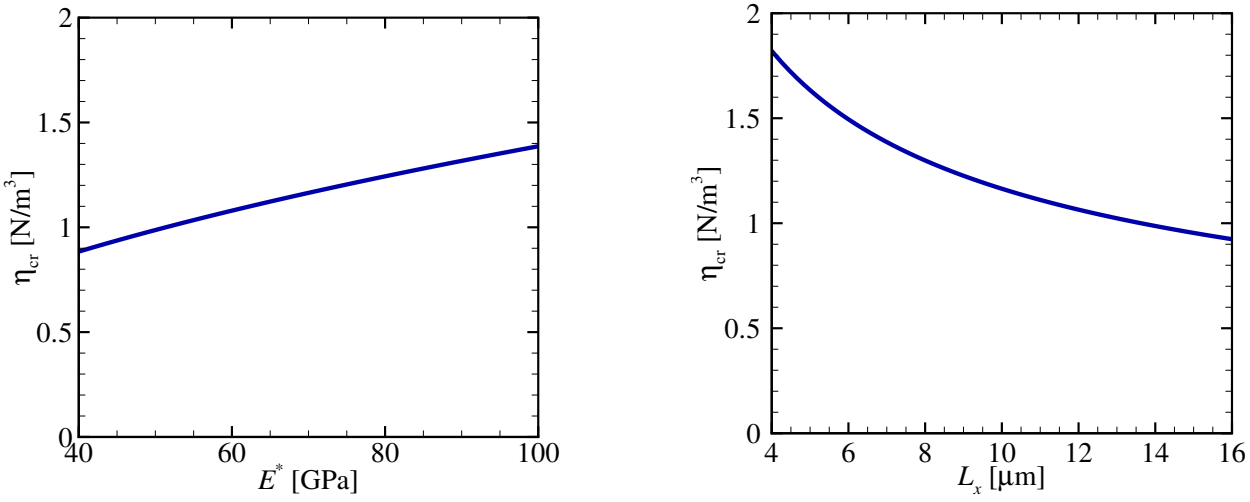

(a) (b)

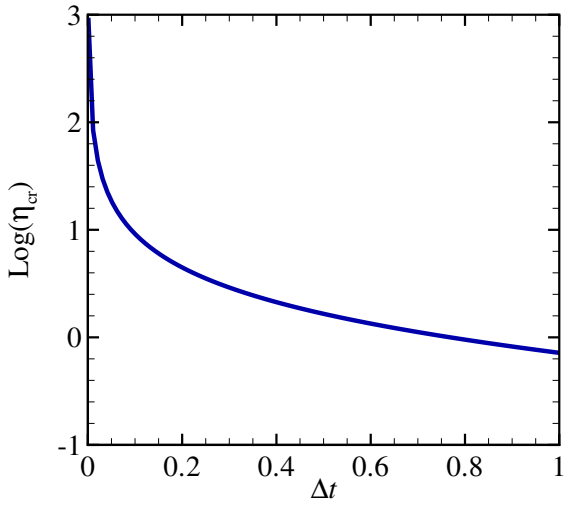

(c)

Figure 6.8: (a) Plot of the critical damping factor $\eta_{\rm cr}$ as a function of the effective modulus E^*. (b) Plot of the critical damping factor $\eta_{\rm cr}$ as a function of the width L_x. (c) Plot of the logarithm of the critical damping factor $\eta_{\rm cr}$ as a function of the discrete time-step Δt for normal displacement of incompressible semi-infinite solid.

As to be expected, the critical damping factor increases when the effective modulus E^* increases, and decreases with increasing width L_x. Note, that for the remainder of this section, we do not show plots of the dependency of the critical damping factor $\eta_{\rm cr}$ on the discrete time-step Δt. Instead, we show only the linear force constant κ, and with the aid of Fig. 6.5 and Eq. (6.41) the corresponding critical damping factor $\eta_{\rm cr}$ can be determined.

6.3.3 Normal displacement of an incompressible finite slab

Following [88], the elastic force for an incompressible slab of height $z_{\rm m}$ corresponding to the wave number q is:

$$\tilde{F}[n] = -q\frac{E^* f(qz_{\rm m})}{2}\tilde{u}(n), \tag{6.71}$$

with

$$f(qz_{\rm m}) = \frac{\cosh\left(2qz_{\rm m}\right) + 2\left(qz_{\rm m}\right)^2 + 1}{\sinh\left(2qz_{\rm m}\right) - 2qz_{\rm m}}, \tag{6.72}$$

where $f(qz_{\rm m})$ is the correction factor for an incompressible finite slab with $u_3(0,x) = 0$ and zero tangential traction. Contrary to the previously discussed case of the semi-infinite solid, the critical damping factor $\eta_{\rm cr}$ is expected to depend on the aspect ratio a. In the limit $q \to 0$, *i.e.*, short wave vectors, $f(q)$ approaches infinity. The limit $q \to 0$ corresponds to a uniform compression in normal direction of an incompressible solid. In the limit $q \to \infty$, *i.e.*, large wave vectors, the elastic force corresponding to wave number q is equal to that acting on the semi-infinite solid (Eq. (6.68)). Following Eqs. (6.35) and (6.36), we give the critical damping factor as:

$$\eta_{\rm cr} = 2\sqrt{\kappa}\frac{1}{\Delta t} - \kappa, \tag{6.73}$$

where

$$\kappa\left(k, a, L_x, E^*\right) = \frac{\pi k E^*\left(8\pi^2 a^2 k^2 + \cosh(4\pi a k) + 1\right)}{L_x(-4\pi a k + \sinh(4\pi a k))}. \tag{6.74}$$

For a given aspect ratio a, periodicity L_x and effective modulus E^* the first principal mode has the smallest linear force constant. The normalized linear force constants $\kappa(k=1)L_x/E^*$ as a function the aspect ratio a is plotted in Fig. 6.9.

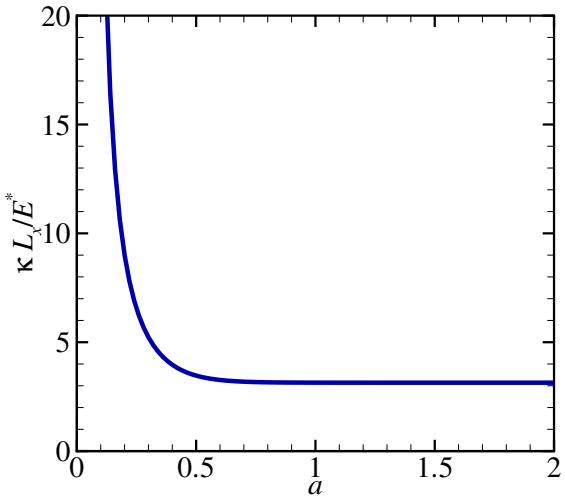

Figure 6.9: Plot of the normalized linear force constant $\kappa(1)L_x/E^*$ as a function of the aspect ratio a for normal displacement of an incompressible finite slab.

As to be expected, the linear force constant increases for a decrease in aspect ratio a. Therefore the critical damping factor η_{cr} increases. When $a >> 2$ the linear force constant becomes independent of the aspect ratio a. This is in agreement with the work by Carbone *et al.* [88] in which the effect of the thickness of the slab for $z_{\text{m}} >> 2\pi/q$ becomes negligible.

6.3.4 A finite slab with generic Poisson's ratio loaded in one direction

Following [3] for zero tangential (or normal) stress, the elastic energy (Eq. (6.57)) is minimized with respect to the lateral (or normal) displacement and is:

$$\begin{aligned} v_{\text{el}} &= \frac{q}{2}\left\{M_{11}\left(qz_{\text{m}}\right) - \frac{M_{13}^2\left(qz_{\text{m}}\right)}{M_{33}\left(qz_{\text{m}}\right)}\right\}|\tilde{u}_1(\boldsymbol{q})|^2 \qquad \text{(zero normal traction);} \\ v_{\text{el}} &= \frac{q}{2}\left\{M_{33}\left(qz_{\text{m}}\right) - \frac{M_{13}^2\left(qz_{\text{m}}\right)}{M_{11}\left(qz_{\text{m}}\right)}\right\}|\tilde{u}_3(\boldsymbol{q})|^2 \qquad \text{(frictionless contact).} \end{aligned} \tag{6.75}$$

The matrix notation of the velocity explicit scheme for a single principal mode with loading in normal or tangential direction collapses to the solution for one the damped harmonic oscillator *i.e.*, Eqs. (6.35) and (6.36). The critical damping factor is:

$$\begin{aligned} \eta_{1,\text{cr}} &= 2\sqrt{\kappa_1\left(qz_{\text{m}}\right)}\frac{1}{\Delta t} - \kappa_1\left(qz_{\text{m}}\right) \qquad \text{(zero normal traction);} \\ \eta_{3,\text{cr}} &= 2\sqrt{\kappa_3\left(qz_{\text{m}}\right)}\frac{1}{\Delta t} - \kappa_3\left(qz_{\text{m}}\right) \qquad \text{(frictionless contact),} \end{aligned} \tag{6.76}$$

where

$$\begin{aligned} \kappa_1\left(qz_{\text{m}}\right) &= \left\{M_{11}\left(qz_{\text{m}}\right) - \frac{M_{13}^2\left(qz_{\text{m}}\right)}{M_{33}\left(qz_{\text{m}}\right)}\right\}q; \\ \kappa_3\left(qz_{\text{m}}\right) &= \left\{M_{33}\left(qz_{\text{m}}\right) - \frac{M_{13}^2\left(qz_{\text{m}}\right)}{M_{11}\left(qz_{\text{m}}\right)}\right\}q. \end{aligned} \tag{6.77}$$

To evaluate the critical damping factor the linear force constants $\kappa_1(qz_{\rm m})$ and $\kappa_3(qz_{\rm m})$ in Eq. (6.77), we rewrite them as:

$$\begin{aligned}\kappa_1\left(k,a,L_x,C_{44},s\right) &= \frac{4\pi C_{44}k\left(8\pi^2a^2k^2(s-1)^2-\left(s^2-1\right)\cosh(4\pi ak)+s^2+1\right)}{L_x\left(-4\pi ak(s-1)+(s+1)\sinh(4\pi ak)\right)};\\ \kappa_3\left(k,a,L_x,C_{44},s\right) &= \frac{4\pi C_{44}k\left(8\pi^2a^2k^2(s-1)^2-\left(s^2-1\right)\cosh(4\pi ak)+s^2+1\right)}{L_x\left(4\pi ak(s-1)+(s+1)\sinh(4\pi ak)\right)}.\end{aligned} \tag{6.78}$$

For a given aspect ratio a, periodic substrate L_x, s and elastic modulus C_{44} the first principal mode has the smallest linear force constant compared to higher modes. As to be expected $\kappa_3\left(k,a,L_x,C_{44},s\right)$ is equal to the linear force constant for an incompressible normal displacement finite slab, in the limit $s\to 0$ (see Eq. (6.74)). The contour plots of the normalized $\kappa_1 L_x/C_{44}$ and $\kappa_3 L_x/C_{44}$ as a function of s and the aspect ratio a for wave index $k=1$ are shown in Fig. 6.10.

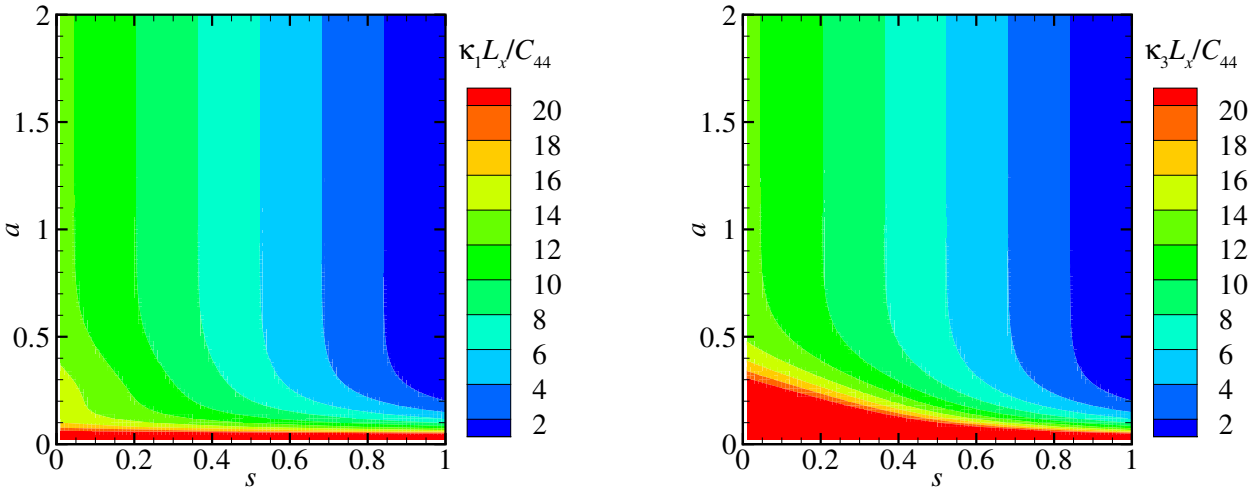

(a) (b)

Figure 6.10: Contour plots of the normalized linear force constant (a) $\kappa_1 L_x/C_{44}$ and (b) $\kappa_3 L_x/C_{44}$ as a function of s and the aspect ratio a with wave index $k=1$ for (a) zero normal traction and (b) frictionless contact.

The critical damping factor increases when the elastic modulus C_{44} increases, the Poisson's ratio ν increases and the aspect ratio a decreases. The ratio of the linear force constants of the center-of-mass mode and higher principal modes (*i.e.*, $\kappa(k)/\kappa(k=0)$) is evaluated over three limits: $s=\frac{1}{2}$ (*i.e.*, $\nu=0$), $s=0$ (*i.e.*, $\nu=\frac{1}{2}$) and $k=1$ (*i.e.*, first principal mode).
In the first limit, $s=\frac{1}{2}$:

$$\begin{aligned}\frac{\kappa_1\left(k,a\right)}{\kappa_1\left(k=0,a\right)} &= \frac{2\pi ka\left(5+8ka^2\pi^2+3\cosh\left(4\pi ka\right)\right)}{4\pi ka+3\sinh\left(4\pi ka\right)}; && \text{(zero normal traction)}\\ \frac{\kappa_3\left(k,a\right)}{\kappa_3\left(k=0,a\right)} &= \frac{\pi ka\left(5+8ka^2\pi^2+3\cosh\left(4\pi ka\right)\right)}{-4\pi ka+3\sinh\left(4\pi ka\right)}. && \text{(frictionless contact)}\end{aligned} \tag{6.79}$$

In the second limit, $s=0$:

$$\begin{aligned}\frac{\kappa_1\left(k,a\right)}{\kappa_1\left(k=0,a\right)} &= \frac{4\pi ka\left(1+8ka^2\pi^2+\cosh\left(4\pi ka\right)\right)}{\left(4\pi ka+\sinh\left(4\pi ka\right)\right)}; && \text{(zero normal traction)}\\ \frac{\kappa_3\left(k,a\right)}{\kappa_3\left(k=0,a\right)} &\to 0. && \text{(frictionless contact)}\end{aligned} \tag{6.80}$$

The results for all three limits combined (*i.e.*, third limit, $k = 1$) are plotted in Fig. 6.11.

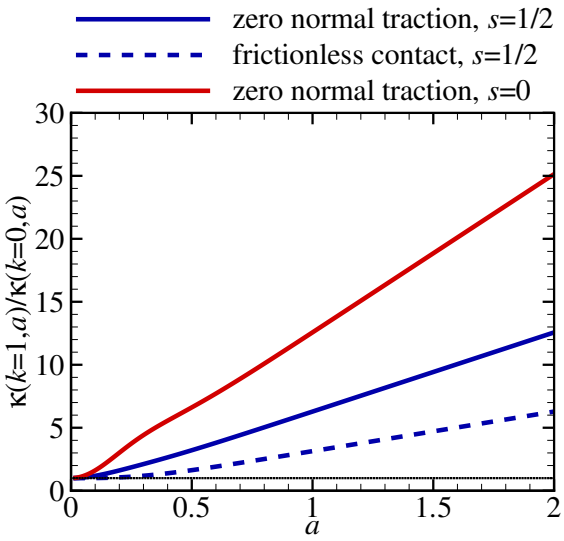

Figure 6.11: Plot of the ratio between the linear force constant of the first principal mode $\kappa\left(k=1,a\right)$ and the linear force constant of the center-of-mass mode $\kappa\left(k=0,a\right)$ as a function of the aspect ratio a, for the case of zero normal traction (frictionless contact) in two limits: $s=\frac{1}{2}$ (*i.e.*, $\nu=0$), $s=0$ (*i.e.*, $\nu=\frac{1}{2}$).

Asymptotic analysis, for the single loading direction, shows that the ratio of linear force constants of the center-of-mass mode and higher principal modes, in the first limit (*i.e.*, $s=\frac{1}{2}$) and the small aspect ratio limit (*i.e.* $a << 0.1$) becomes one. This corresponds to the short wave vector limit Eq. (6.63). In the second limit (*i.e.*, $s=0$) this is only true for zero normal traction. Considering frictionless contact, the smallest linear force constant depends on both the aspect ratio a and s. The linear force constant for frictionless contact and $s=0$ is:

$$\kappa_3\left(k,a,L_x,C_{44}\right)=\frac{4\pi C_{44}ka\left(1+8ka^2\pi^2+4\cosh\left(4\pi ka\right)\right)}{L_x\left(-4\pi ka+3\sinh\left(4\pi ka\right)\right)}. \tag{6.81}$$

The critical damping factor in GFMD simulations is the critical damping factor of the center-of-mass if the ratio of linear force constants is larger than one. If the ratio of linear force constants is smaller than one, the critical damping factor in GFMD simulations is the critical damping factor of the first principal mode.
To determine the aspect ratio a and s for which the ratio of linear force constants is one, the expression of the linear force constants of the center-of-mass mode and first principal mode are set equal to each other and a function $f(a,s)$ is derived. This function $f(a,s)$ is:

$$\begin{aligned} f_1(a,s)&=\frac{4\pi\left(8\pi^2a^2(s-1)^2-\left(s^2-1\right)\cosh(4\pi a)+s^2+1\right)}{(s+1)\sinh(4\pi a)-4\pi a(s-1)}-\frac{1}{a};\\ f_3(a,s)&=\frac{4\pi\left(8\pi^2a^2(s-1)^2-\left(s^2-1\right)\cosh(4\pi a)+s^2+1\right)}{4\pi a(s-1)+(s+1)\sinh(4\pi a)}-\frac{1}{as}. \end{aligned} \tag{6.82}$$

The values of aspect ratio a and s for which the ratio of linear force constants is one are obtained by setting $f(a,s)$ equal to zero.

The solid curve in Fig. 6.12 indicates the values of the aspect ratio a and s for which the critical damping factor of the GFMD simulation changes from the critical damping factor of the first principal mode to the critical damping factor of the center-of-mass mode, for an increase in s.

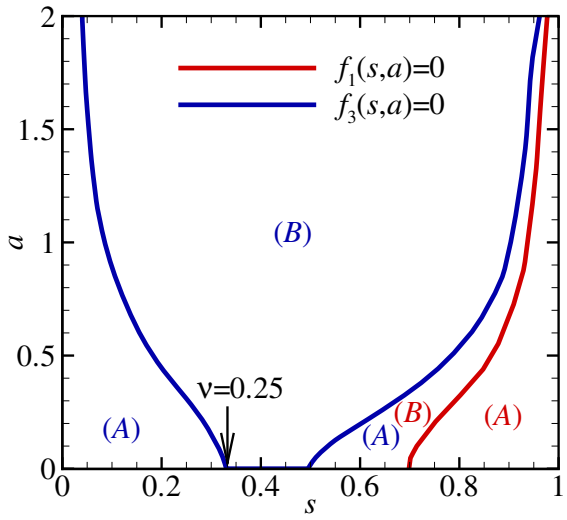

Figure 6.12: Regimes of smallest linear force constant as function of the aspect ratio a and s for a single loading direction for zero normal traction $f_1(s,a)$ and frictionless contact $f_3(s,a)$. Regime $\frac{\kappa_i(k=1,a,s)}{\kappa_i(k=0,a,s)} < 1$ (A). Regime $\frac{\kappa_i(k=1,a,s)}{\kappa_i(k=0,a,s)} > 1$ (B).

For an increasing s from $s = 0$ to $s = 0.5$ the smallest linear force constant for frictionless contact switches from the first principal mode to the center-of-mass mode, and it switches back to the first principal mode for $s \geq 0.5$. It is well known that when s decreases from 0.5 to 0 (*i.e.*, ν increases from 0 to 0.5) the substrate becomes incompressible. Therefore, the linear force constant of the center-of-mass mode in normal direction increases. In the limit $a \to 0^+$ for the Poisson's ratio $\nu = 0.25$ we find $f_3(s,a) = 0$. In this case, the resistance to compression equals the resistance to transverse contraction [41]. As the aspect ratio a increases and for the Poisson's ratio remains $\nu = 0.25$, the effective stiffness of the finite slab decreases, hence the center-of-mass mode becomes the lowest frequency mode. For the uniform displacement of the surface in normal direction when $s > 0.5$ the linear force constant of the center-of-mass mode becomes larger than the linear force constant of the first principal mode because of the constraint in x-direction. The smallest linear force constant for zero normal traction switches from the center-of-mass mode to the first principal mode, because of the decrease in Poisson's ratio (see Fig. 6.7c).

Figure 6.13 displays the contour plots of the smallest linear force constant κ_{cr} as a function of s and the aspect ratio a. Notice that which mode has the smallest linear force constant does not dependent on the periodicity L_x and C_{44}.

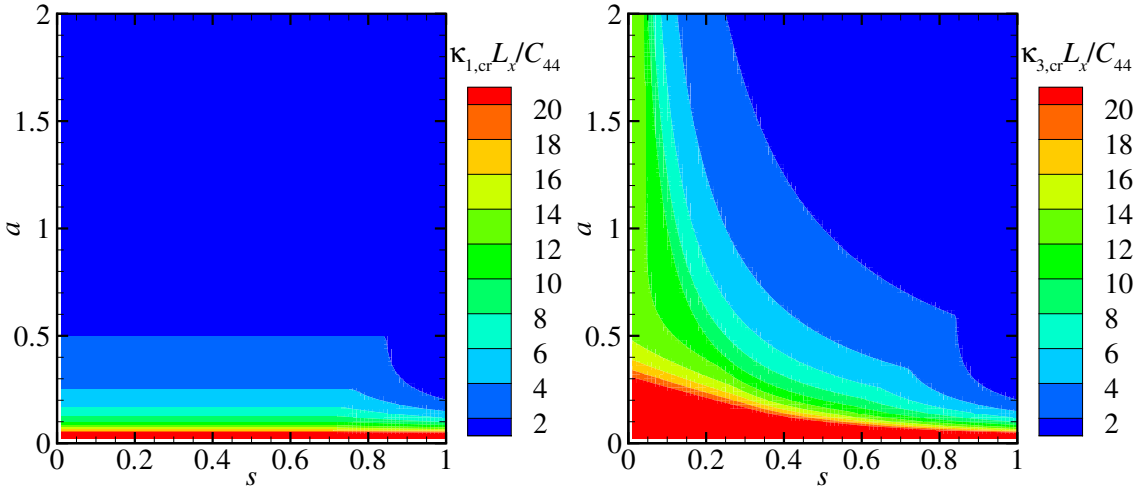

(a) (b)

Figure 6.13: Contour plot of the smallest normalized linear constant $\kappa_{\text{cr}}L_x/C_{44}$ as a function of s and aspect ratio a for (a) zero normal traction and (b) frictionless contact.

The critical damping factor increases when the elastic modulus C_{44} increases, the width L_x, s and the aspect ratio a decreases. It is observed that the critical damping factor for a single loading direction in GFMD simulations is the critical damping factor of the center-of-mass mode or the first principal mode for a given s and aspect ratio a. Therefore, it can be concluded that the lowest frequency mode depends on the Poisson's ratio ν and the aspect ratio a, but is independent of the elastic modulus E and periodicity L_x. We end the analyses of the limiting cases without dynamic coupling here, and the remainder of this section is dedicated to cases involving both normal and tangential displacement.

6.3.5 Normal and tangential displacement of a semi-infinite solid

Following [3], equation (6.58) for the semi-infinite solid is:

$$\begin{aligned} M_{11} &= \frac{2}{1+s}C_{44}; \\ M_{13} &= \frac{2s}{1+s}C_{44}; \\ M_{33} &= \frac{2}{1+s}C_{44}. \end{aligned} \tag{6.83}$$

The critical damping factor is independent of the aspect ratio a. Contrary to the previously discussed cases, the eigenvalues Λ_i of $\mathcal{V}$ are two sets of complex conjugates (*i.e.*, $\Lambda_{\pm,1}$ and $\Lambda_{\pm,3}$). The critical damping factor, which in previous sections was a scalar η_{cr}, now becomes a vector $\boldsymbol{\eta}_{\text{cr}}$ for the remainder of this section. The critical damping factor $\boldsymbol{\eta}_{\text{cr}}$ is determined by setting the roots of both sets of eigenvalues $\Lambda_{\pm,i}$ equal to zero. The resulting set of equations proved not to be readily simplified without prior assumptions. It is assumed that $\eta_1 = \eta_3$, *i.e.*, a directionally independent damping factor. For two sets of complex conjugates, this results in two possible critical damping

factors $\eta_{1',\mathrm{cr}}$ and $\eta_{3',\mathrm{cr}}$. The critical damping factor $\eta_{i',\mathrm{cr}}$ for which the root of one set of eigenvalues is zero and for the other set part below the root is negative. The critical damping factor is given by Eq. (6.69) with linear force constants $\kappa_{1'}(k, L_x, C_{44}, s)$ and $\kappa_{3'}(k, L_x, C_{44}, s)$. The linear force constants are written as:

$$\begin{aligned}\kappa_{1'}(k, s, C_{44}) &= \frac{4\pi k C_{44}}{L_x} = \frac{2\pi k E}{L_x(1+\nu)};\\ \kappa_{3'}(k, s, C_{44}) &= \frac{4\pi k C_{44}(1-s)}{L_x(s+1)} = \frac{2\pi k E}{L_x\left(-4\nu^2-\nu+3\right)}.\end{aligned} \tag{6.84}$$

For both linear force constants, the first principal mode has the smallest linear force constant compared to higher modes for a given s. The ratio between linear force constant $\kappa_{3'}$ and $\kappa_{1'}$ is written as:

$$\frac{\kappa_{1'}}{\kappa_{3'}} = \frac{1+s}{1-s}. \tag{6.85}$$

The ratio is larger or equal to one for $0 \leq s \leq 1$ and the logarithm of the ratio as a function of s is shown in Fig. 6.14.

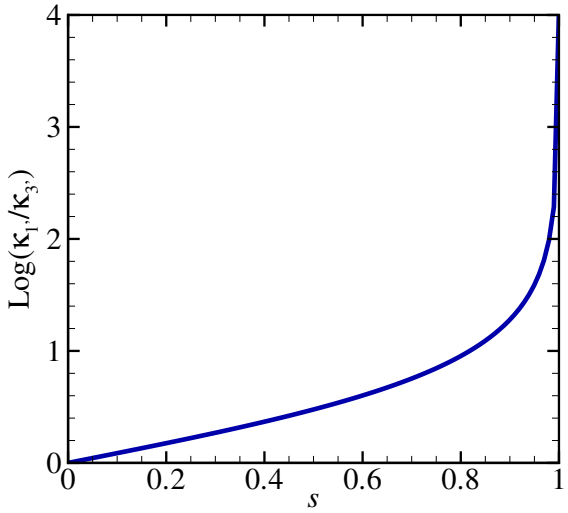

Figure 6.14: Plot of the logarithm of the ratio between linear force constants $\kappa_{3'}/\kappa_{1'}$ as a function of s for normal and tangential displacement of a semi-infinite solid.

Figure 6.15 displays the plot of the normalized linear constant $\kappa_{i'}(1)L_x/E$ as a function of the Poisson's ratio ν.

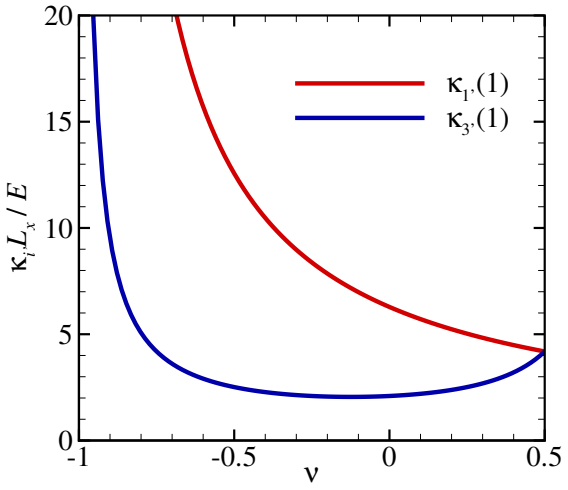

Figure 6.15: Plot of the normalized linear constant $\kappa_{i'}(1)L_x/E$ as a function of the Poisson's ratio ν for normal and tangential displacement of a semi-infinite solid.

The linear force constant $\kappa_{i'}(k)$ approaches infinity asymptotically as the Poisson's ratio ν goes to -1. The critical damping factor increases when the elastic modulus C_{44} increases, the width L_x decreases and the Poisson's ratio ν increases. It can be concluded that in GFMD simulations, considering both normal and tangential displacement for a semi-infinite solid, the critical damping factor scalar is $\eta_{3'}$ with $\kappa_{3'}$.

This section is concluded by making the link of the results in the previous paragraph to the effective modulus E^* introduced in Eq. (6.70). $\kappa_1(k, L_x, s, C_{44})$ and $\kappa_3(k, L_x, s, C_{44})$ for a single loading direction and semi-infinite solid (Eq. (6.78)) are written as:

$$\begin{aligned}\kappa_1(k, L_x, s, C_{44}) &= \frac{4\pi k C_{44}(1-s)}{L_x};\\ \kappa_3(k, L_x, s, C_{44}) &= \frac{4\pi k C_{44}(1-s)}{L_x}.\end{aligned} \tag{6.86}$$

For $s = 0$ (*i.e.*, $\nu = 0.5$), equation (6.84) is consistent with Eq. (6.86). The equation of motion in the limit of a semi-infinite solid with Poisson's ratio $\nu = 0.5$ (*i.e.*, rubber like material) is uncoupled. This as expected because $M_{13} = 0$ for $s = 0$ (Eq. (6.83)) and corresponds to $\partial_3\partial_1 u_3 = \partial_1\partial_3 u_1 = 0$ in Eq. (6.50). Following [3], equation (6.75) is consistent with Eq. (6.67) in the limit of a semi-infinite solid and frictionless contact. This corresponds to Eq. (6.70) being consistent with Eqs. (6.86) and (6.84) in the limit of a semi-infinite and Poisson's ratio $\nu = 0.5$. This is in agreement with the GFMD approach by C. Campáña [4] in which the normal and tangential displacement are treated independently for a semi-infinite solid with Poisson's ratio $\nu \approx 0.5$.

6.3.6 Normal and tangential displacement of a finite slab

The critical damping factor for a finite height solid depends on the aspect ratio a (see Eq. 2.12). The critical damping factor is determined similar to Sec. 6.3.5. The critical damping factor is given by Eq. (6.69) with linear force constants $\kappa_{1'}(k, L_x, a, C_{44}, s)$ and $\kappa_{3'}(k, L_x, a, C_{44}, s)$. For both linear force constants: The first principal mode has the smallest linear force constant compared to higher modes for a given periodic substrate L_x, aspect ratio a, s and elastic modulus C_{44}. The contour plots of the normalized linear force constants $\kappa_{1'}L_x/C_{44}$ and $\kappa_{3'}L_x/C_{44}$ as a function of s and the aspect ratio a for wave index $k = 1$ are shown in Fig. 6.16.

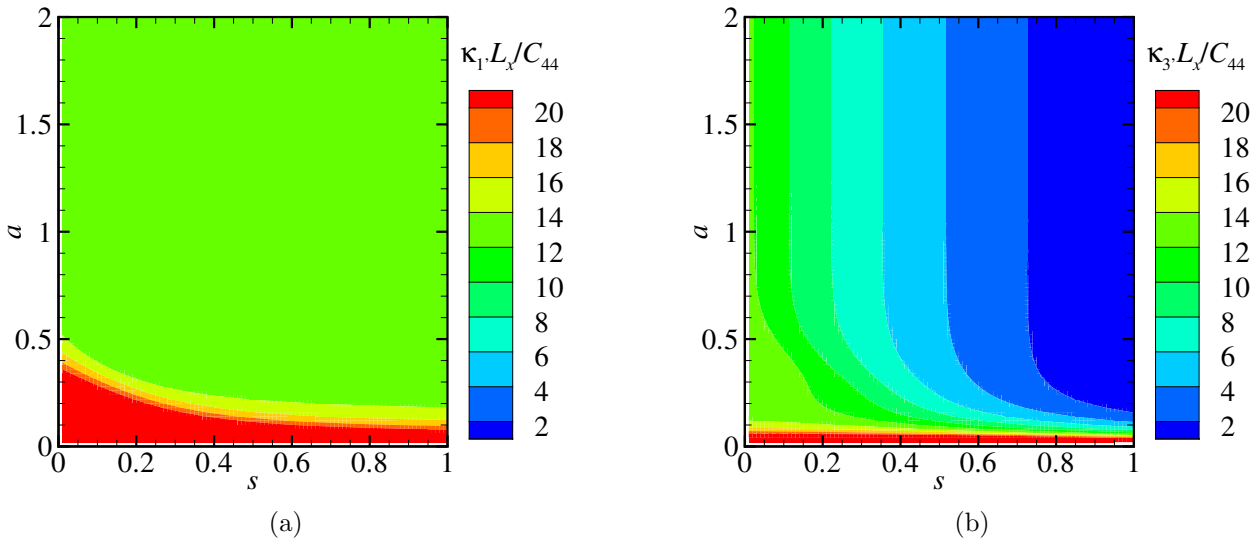

Figure 6.16: Contour plots of the normalized (a) $\kappa_{1'}L_x/C_{44}$ and (b) $\kappa_{3'}L_x/C_{44}$ as a function of s and the aspect ratio a for wave index $k = 1$ for normal and tangential displacement of a finite slab.

The ratio of the linear force constants of the center-of-mass mode and higher principal modes is evaluated over three limits: $s = \frac{1}{2}$ (*i.e.*, $\nu = 0$), $s = 0$ (*i.e.*, $\nu = \frac{1}{2}$) and $k = 1$ (*i.e.*, first principal mode). In the first limit, $s = \frac{1}{2}$:

$$\begin{aligned}
\frac{\kappa_{1'}(k,a)}{\kappa_1(k=0,a)} =& 8\pi ak\left(b_1(a,k) - \sqrt{b_2(a,k)}\right);\\
\frac{\kappa_{1'}(k,a)}{\kappa_3(k=0,a)} =& 4\pi ak\left(b_1(a,k - \sqrt{b_2(a,k)}\right);\\
\frac{\kappa_{3'}(k,a)}{\kappa_1(k=0,a)} =& 8\pi ak\left(b_1(a,k) + \sqrt{b_2(a,k)}\right);\\
\frac{\kappa_{3'}(k,a)}{\kappa_3(k=0,a)} =& 4\pi ak\left(b_1(a,k) + \sqrt{b_2(a,k)}\right),
\end{aligned} \tag{6.87}$$

where

$$\begin{aligned}
b_1(a,k) =& \frac{3\sinh(4\pi ak)}{-8\pi^2a^2k^2 + 9\cosh(4\pi ak) - 9};\\
b_2(a,k) =& \frac{-24\pi^2a^2k^2\sinh^2(2\pi ak) + 16\left(\pi^4a^4k^4 + \pi^2a^2k^2\right) + 9\sinh^4(2\pi ak)}{\left(8\pi^2a^2k^2 - 9\cosh(4\pi ak) + 9\right)^2}.
\end{aligned} \tag{6.88}$$

In the second limit, $s = 0$:

$$\begin{aligned}
\frac{\kappa_{1'}(k,a)}{\kappa_1(k=0,a)} =& 4\pi ak\left(\frac{\sinh(4\pi ak)}{-8\pi^2a^2k^2 + \cosh(4\pi ak) - 1} - 4\pi k\sqrt{\frac{4\pi^2a^4k^2 + a^2}{\left(-8\pi^2a^2k^2 + \cosh(4\pi ak) - 1\right)^2}}\right);\\
\frac{\kappa_{1'}(k,a)}{\kappa_3(k=0,a)} \to& 0;\\
\frac{\kappa_{3'}(k,a)}{\kappa_1(k=0,a)} =& 4\pi ak\left(\frac{\sinh(4\pi ak)}{-8\pi^2a^2k^2 + \cosh(4\pi ak) - 1} + 4\pi k\sqrt{\frac{4\pi^2a^4k^2 + a^2}{\left(-8\pi^2a^2k^2 + \cosh(4\pi ak) - 1\right)^2}}\right);\\
\frac{\kappa_{3'}(k,a)}{\kappa_3(k=0,a)} \to& 0.
\end{aligned} \tag{6.89}$$

The results for all three limits combined (*i.e.*, third limit, $k = 1$) are plotted in Fig. 6.17.

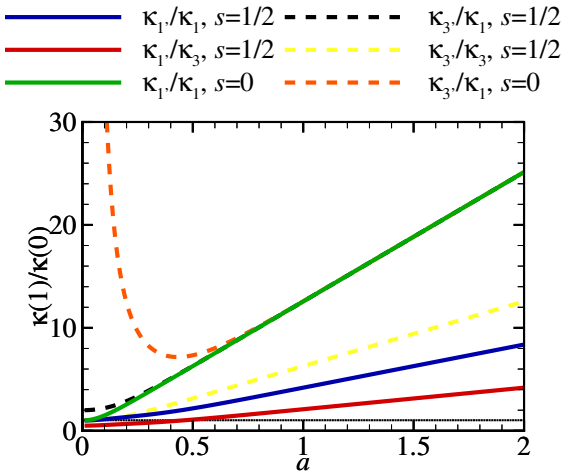

Figure 6.17: Plot of the ratio between the linear force constant of the first principal mode $\kappa\,(k = 1, a)$ and the linear force constant of the center-of-mass mode $\kappa\,(k = 0, a)$ as a function of the aspect ratio a, for both sets of conjugate eigenvalues Λ_i in two limits: $s = \frac{1}{2}$ (*i.e.*, $\nu = 0$), $s = 0$ (*i.e.*, $\nu = \frac{1}{2}$).

Because the linear force constant $\kappa_3\,(k = 0, a, s)$ is larger than or equal to $\kappa_1\,(k = 0, a, s)$, the critical damping factor in GFMD simulations with the single damping factor is determined by the ratio between the linear force constant of the principal mode $\kappa_1\,(k = 0, a, s)$ and the two linear force constants of the first principal mode (*i.e.*, $\kappa_{1'}\,(k = 1, a, s)$ and $\kappa_{3'}\,(k = 1, a, s)$). Analysis of the limits by Fig. 6.18, for a given aspect ratio a and $0 \leq s \leq 0.5$, yields:

a. $\dfrac{\kappa_{3'}\,(k = 1, a, s)}{\kappa_1\,(k = 0, a, s)} \leq \dfrac{\kappa_{1'}\,(k = 1, a, s)}{\kappa_1\,(k = 0, a, s)}$;

b. $\dfrac{\kappa_{3'}\,(k = 1, a, s)}{\kappa_1\,(k = 0, a, s)} \geq 1$.

So, the smallest critical damping factor for all modes is the critical damping factor of the center-of-mass mode $\eta_{1,\mathrm{cr}}$ (Eq. (6.65)).

To clarify the characteristic damping regimes of other principal modes: The curves in Fig. 6.18 indicate the values of the aspect ratio a and s for which the critical damping factor of the GFMD simulation changes from the critical damping factor of the first principal mode to the critical damping factor of the center-of-mass mode, for an increase in s.

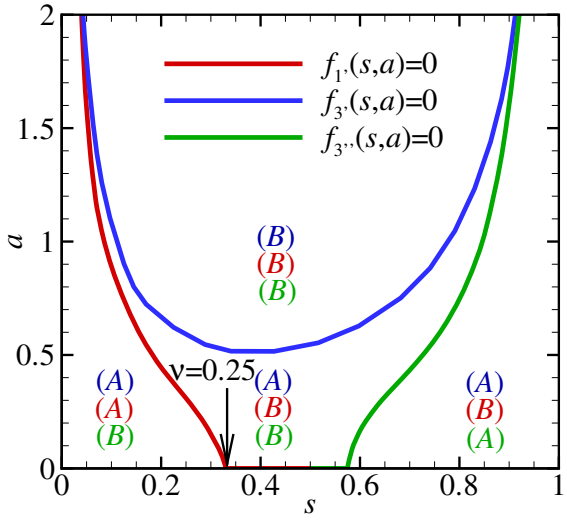

Figure 6.18: Regimes of smallest linear force constant for normal and tangential displacement of a finite slab as of function of the aspect ratio a and s. Regime $\dfrac{\kappa(k=1,a,s)}{\kappa_3(k=0,a,s)} < 1$ (A). Regime $\dfrac{\kappa(k=1,a,s)}{\kappa_3(k=0,a,s)} > 1$ (B). $f_{1'}(s,a)$ is for the ratio $\dfrac{\kappa_{1'}\,(k=1,a,s)}{\kappa_3\,(k=0,a,s)}$, $f_{3'}(s,a)$ for the ratio $\dfrac{\kappa_{3'}\,(k=1,a,s)}{\kappa_3\,(k=0,a,s)}$ and $f_{3''}(s,a)$ for the ratio $\dfrac{\kappa_{3'}\,(k=1,a,s)}{\kappa_1\,(k=0,a,s)}$.

As expected, the $f_{3'}(s,a)$ corresponds to the $f_3(s,a)$ in Fig. 6.12. As a result of coupling $f_3(s,a)$ is shifted upwards. This shift confirms that coupling has to be taken into account in determining the scalar critical damping factor $\eta_{\rm cr}$. Figure 6.13 displays the contour plot of the normalized smallest linear force constant $\kappa_{\rm cr}L_x/C_{44}$ as a function of s and the aspect ratio a.

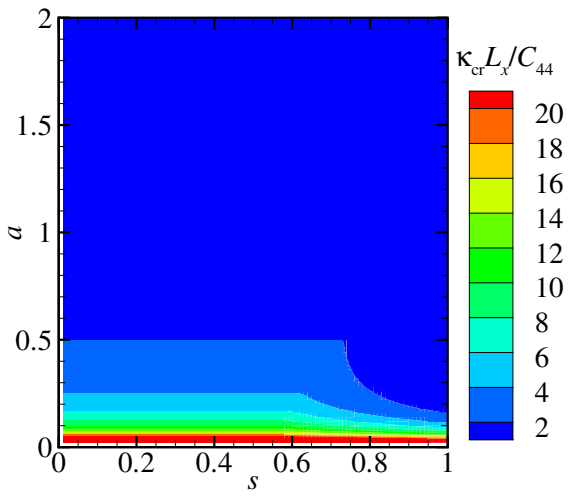

Figure 6.19: Contour plot of the smallest normalized linear constant $\kappa_{\mathrm{cr}} L_x / C_{44}$ as a function of s and aspect ratio a for normal and tangential displacement of a finite slab.

The smallest linear force constant is independent of s for $s \leq 0.5$. When $s > 0.5$ the smallest linear force constant depends on s. The smallest linear force constant decreases for an increasing s and a given width L_x, aspect ratio a and C_{44}. It is concluded that in GFMD simulations with both normal and tangential displacement (*i.e.*, two DOF) and a finite-height slab the critical damping factor is:

$$\boldsymbol{\eta}_{\mathrm{cr}} = \left(\eta_1(k=0, z_{\mathrm{m}}), \eta_1(k=0, z_{\mathrm{m}})\right), \qquad \text{if} \qquad 0 \leq \nu \leq 0.5. \tag{6.90}$$

As to be expected, the lowest frequency mode is one of the center-of-mass modes.
Note, that we assumed that the discrete time-step is chosen such that $\mathrm{d}t \leq 1/\sqrt{\kappa}$. This is done to simplify the presentation of the results in this work. Using Eq. (6.41) and the suitable expression of the linear force constant κ depending on the loading conditions and substrate geometry. It is, up to date, also possible to use a scalar critical damping factor η_{cr} so that each mode is critically damped. However, in this work, we do not use this mode dependent critical damping factor $\eta_{\mathrm{cr}}(q)$.

6.4 Equilibrium Time

6.4.1 Normal displacement of an incompressible semi-infinite solid

Similar to Sec. 6.2.2.2, the exponential time constant of a principal mode in a GFMD simulation, considering only the normal component of the displacement [64] is:

$$\tau = \frac{2L_x}{\Delta t\left(\eta L_x + E^*\pi k\right)}. \tag{6.91}$$

The exponential time constant τ is inversely proportional to the wave number index k for a constant damping factor η. The equilibrium time t_{eq} of successive principal modes is shorter for a constant damping factor η and a constant and/or diminishing C over successive modes. By inserting the proportionality of the critical damping factor into Eq. (6.91), the equilibrium time of a critically damped principal mode thus becomes:

$$t_{\mathrm{eq}}(\eta = \eta_{\mathrm{cr}}) \propto \frac{1}{\sqrt{\kappa}}, \tag{6.92}$$

with

$$\frac{1}{\sqrt{\kappa}} = \frac{\sqrt{L_x}}{\sqrt{2\pi E^* k}}. \tag{6.93}$$

6.4.2 Normal and tangential displacement of a finite slab

The proportionality of the equilibrium time in GFMD simulations, considering both the normal and shear component of displacement [3] (*i.e.*, two DOF), is derived. The closed expression of the amplitude of the trajectory of a principal mode for two DOF thus becomes:

$$a_{\mathrm{h}}[t[n]] = \sum_{i=1}^{2d} A_i e^{\left(-\frac{\mathrm{Re}\{\xi_i\}}{2d}\frac{t[n]}{\Delta t}\right)}. \tag{6.94}$$

Similar to Sec. 6.2.2.2, the exponential time constants of the center-of-mass modes for two DOF are:

$$\begin{aligned} \tau_1(q=0) =& \frac{2}{\Delta t\left(\eta + \kappa_1(q=0)\right)}; \\ \tau_3(q=0) =& \frac{2}{\Delta t\left(\eta + \kappa_3(q=0)\right)}. \end{aligned} \tag{6.95}$$

The equilibrium time of critically damped center of mass modes thus becomes:

$$\begin{aligned} t_{1,\mathrm{eq}}(q=0,\eta=\eta_{\mathrm{cr}}) \propto& \frac{1}{\sqrt{\kappa_1(q=0,z_{\mathrm{m}})}}; \\ t_{3,\mathrm{eq}}(q=0,\eta=\eta_{\mathrm{cr}}) \propto& \frac{1}{\sqrt{\kappa_3(q=0,z_{\mathrm{m}})}}. \end{aligned} \tag{6.96}$$

Because the linear force constant $\kappa_3\left(q=0,z_{\mathrm{m}}\right)$ is larger than or equal to $\kappa_1\left(k=0,z_{\mathrm{m}}\right)$, the equilibrium time in GFMD simulations, considering only the center-of-mass modes and $C_1 = C_3$, is the equilibrium time $t_{1,\mathrm{eq}}(q=0,\eta=\eta_{\mathrm{cr}})$.
Similar to Sec. 6.2.2.2, the exponential time constants of a principal mode for two DOF are:

$$\begin{aligned} \tau_{1'} =& \frac{2}{\Delta t\left(\eta + \kappa_{1'}\right)}; \\ \tau_{2'} =& \frac{2}{\Delta t\left(\eta + \kappa_{2'}\right)}. \end{aligned} \tag{6.97}$$

By comparing, Eqs. (6.95) and (6.97), the equilibrium time is determined by the center-of-mass mode or higher principal mode with the smallest linear force constant κ. The analysis in Sec. 6.3.6 shows: The linear force constant of the principal mode $\kappa_1(q = 0, z_\mathrm{m})$ is the smallest linear force constant. Therefore, the proportionality of the equilibrium time, for a constant and/or diminishing $C_i(q)$ over successive modes, is determined by $t_{1,\mathrm{eq}}(q = 0, \eta = \eta_\mathrm{cr})$.

6.5 Numerical results

6.5.1 Methodology

The analytical expression for the critical damping factor and equilibrium time are compared to numerical results in this section. This is done to determine whether the characteristic dynamic regimes and equilibrium time obtained by numerical calculations correspond to the derived analytical expressions. The numerical results are obtained without any prior knowledge or use of their respective analytical expressions. A small difference in results is expected because of the machine precision and the way equilibrium time is numerically calculated.
The variables of the GFMD simulation are normalized with respect to L_x. The width will be presented by the discretization nx for the remainder of this section. This is done in order to present values for the critical damping factor $\boldsymbol{\eta}_\mathrm{cr}$ in the order of magnitude of those used in GFMD simulations.
The characteristic dynamic regimes and critical damping of a system are determined for no external force $\tilde{\boldsymbol{F}}_\mathrm{ext}(q) = 0$ and no interfacial force $\tilde{\boldsymbol{F}}_\mathrm{if}(q) = 0$ at simulation time $t \geq 0$ in GFMD simulations. The principal mode that comes to equilibrium the slowest depends on the initial conditions and dynamic (or static) coupling of the system. To determine the critical damping coefficients, a step function is imposed on all modes (*i.e.*, equivalent to Fig. 6.2). The step function is:

$$\begin{aligned} \tilde{u}_1(k) &= \frac{A_\mathrm{h}}{1+k} \text{ for } t \leq 0; \\ \tilde{u}_3(k) &= \frac{A_\mathrm{h}}{1+k} \text{ for } t \leq 0. \end{aligned} \tag{6.98}$$

The center-of-mass, the first principal mode or even higher principal mode that comes slowest to equilibrium depends on the initial condition. We choose this particular step function to minimize the computational time, because we predict the center-of-mass mode or first principal mode to be the lowest frequency mode, but we want be save and sample all modes. The equilibrium position is known, therefore we can reject the damping factors that result in over-damped dynamics. The numerical GFMD simulations are performed without the assumption $\eta_1 = \eta_3$, *i.e.*, a damping factor vector. This method is chosen to show the drawbacks of assuming a damping factor scalar.
The equilibrium position of all principal modes is known beforehand as $\tilde{\boldsymbol{u}}(q) = 0$. The fast Fourier transform library (FFTW3) used in the GFMD simulation has machine precision error $\mathcal{O}^{-16}$ in the transformations from real to Fourier space values and vice versa [68], *i.e.* $\delta = 10^{-16}$. Therefore, the equilibrium condition is written as:

$$|\tilde{\boldsymbol{u}}(q)|^2 \;\leq\; |\delta|^2 \text{ for } t \geq t_\mathrm{eq}. \tag{6.99}$$

Figure 6.20 shows the equilibrium times as a function of the critical damping factor for two Poisson's ratios $\nu = 0.3$ and $\nu = 0.49$, with $nx = 2048$, $E = 70$ GPa and $a = 1$.

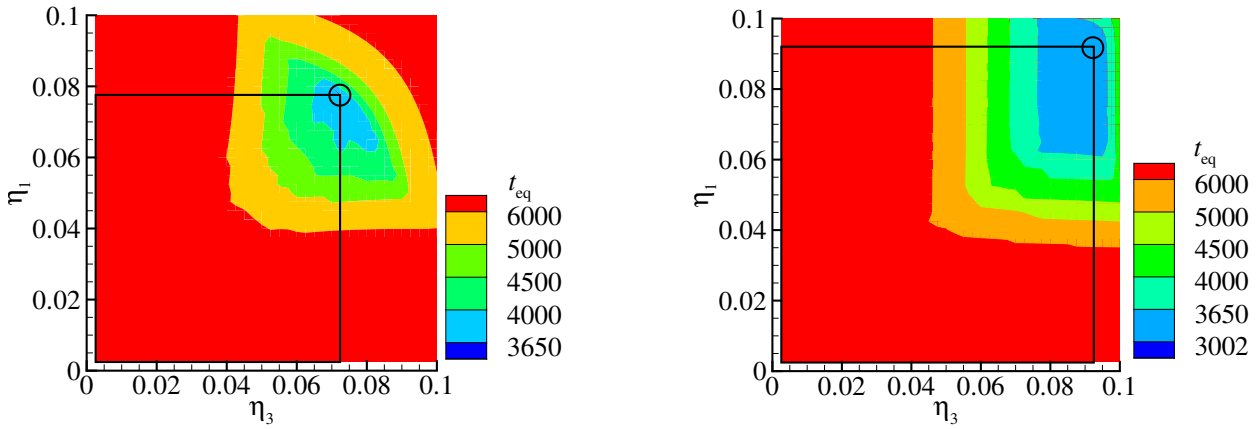

(a) (b)

Figure 6.20: Equilibrium time t_{eq} as a function of the damping factors $\boldsymbol{\eta}$ for an elastic substrate with Poisson's ratio (a) $\nu = 0.3$ and (b) $\nu = 0.49$. The region enclosed by the solid black line represents the under-damped characteristic dynamic regime. The position of the shortest equilibrium time is indicated with the black circle.

Figure 6.20 is a graphic representation of the method to determine the vector critical damping factor $\boldsymbol{\eta}_{\text{cr}}$. The equilibrium time for the critically damped GFMD simulation is the shortest equilibrium time measured, 3650 in Fig. 6.20a and 3002 in Fig. 6.20b respectively. The corresponding critical damping factors are the values on the two axis, *i.e.*, η_1 and η_3.
Assuming:

$$\boldsymbol{\eta}_{\text{cr}} = \text{f}\left(nx, E, \Delta t, \nu, a\right), \tag{6.100}$$

the critical damping factors can be expressed in terms of other independent parameters as:

$$\log \boldsymbol{\eta}_{\text{cr}} = \boldsymbol{\alpha} \log nx + \boldsymbol{\beta} \log E + \boldsymbol{\gamma} \log \Delta t + \boldsymbol{\xi} \log \nu + \boldsymbol{\chi} \log a + \boldsymbol{K}, \tag{6.101}$$

where $\boldsymbol{\alpha}$, $\boldsymbol{\beta}$, $\boldsymbol{\gamma}$, $\boldsymbol{\xi}$, and $\boldsymbol{\chi}$ are the exponents to the independent variables and $\boldsymbol{K}$ is an independent constant. To determine the exponents, the critical damping factor is determined as a function of a single independent variable, while the remaining independent variables are kept constant. Assuming:

$$t_{\text{eq}} \propto \text{f}\left(nx, E, \nu, a\right), \tag{6.102}$$

the equilibrium time can be expressed in terms of the other independent parameters as:

$$\log t_{\text{eq}} \propto \alpha_{\text{t}} \log nx + \beta_{\text{t}} \log E + \xi_{\text{t}} \log \nu + \chi_{\text{t}} \log a + K, \tag{6.103}$$

where α_{t}, β_{t}, ξ_{t}, and χ_{t} are the exponents to the independent variables and K is an independent constant.
The expression for the number of iterations to equilibrium n_{eq} is written as:

$$n_{\text{eq}} = \frac{t_{\text{eq}}}{\Delta t}. \tag{6.104}$$

6.5.2 Normal displacement of an incompressible semi-infinite solid

In this section, the critical damping factor obtained using GFMD simulations studying only the normal component of the displacement [64] are compared to the analytical expression for the critical damping factor η_{cr} in Eq. (6.69) (see Fig. 6.21). The following parameters are chosen for the simulations: $nx = 2048$, $E^* = 70$ GPa, $\Delta t = 0.25$, and $A = 0.01 L_x$.

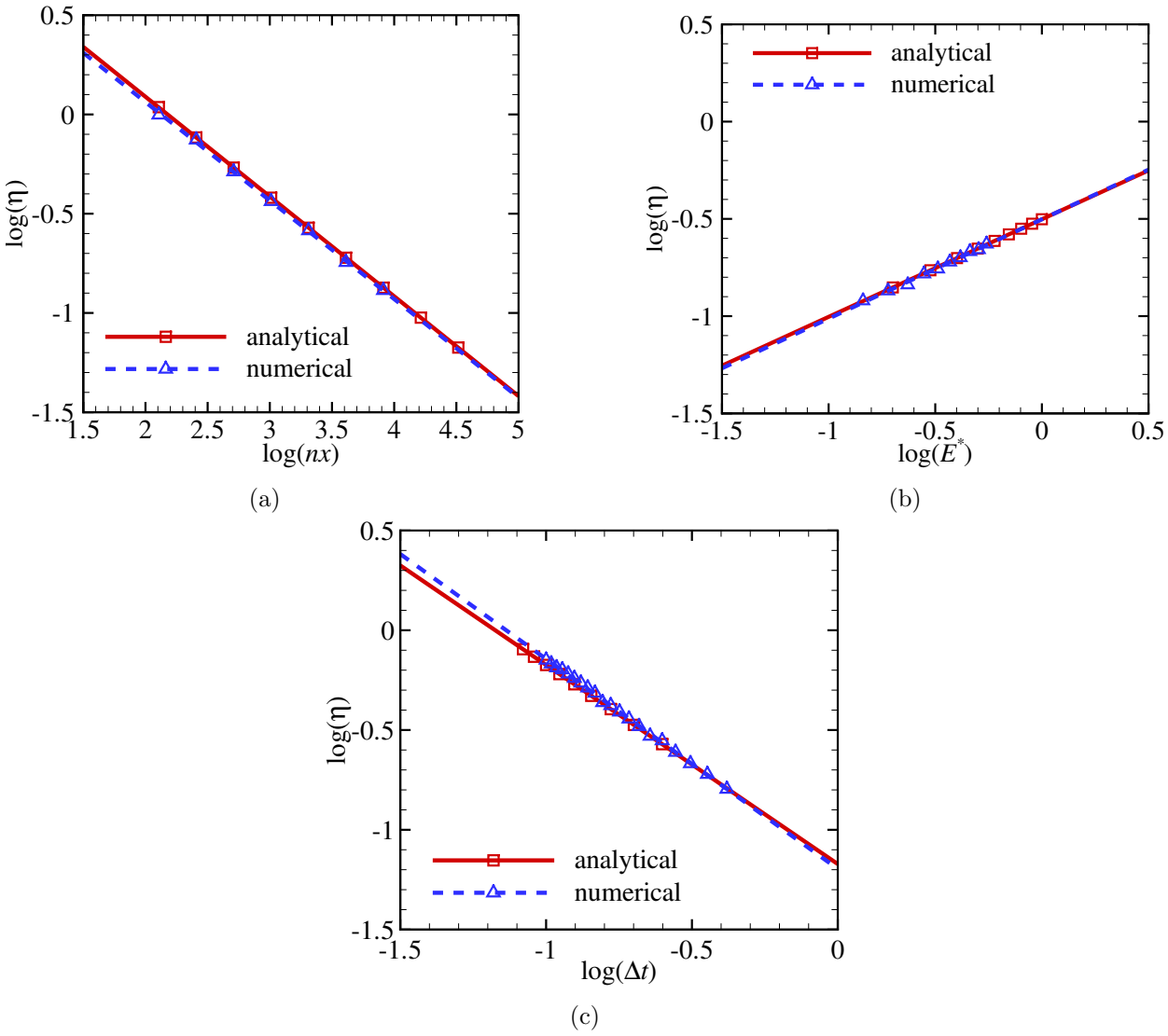

Figure 6.21: Log-log plots of critical damping factor η as a function of (a) the discretization nx, (b) the effective modulus E^*, (c) the dimensionless discretization time Δt.

The numerical critical damping factor is in good accordance with the analytical critical damping factors. It is found that the critical damping factor is:

$$\eta_{\text{cr}} \propto (nx)^{-0.50} (E^*)^{0.50} (\Delta t)^{-1.0}. \tag{6.105}$$

As to be expected, this result corresponds to the analytical expression for the critical damping factor η_{cr} in Eq. (6.69).

In Tab. 6.1, the numerical exponents obtained using GFMD simulations are compared with those obtained from the analytical expression.

	numerical	analytical
α_t	0.501	0.500
β_t	-0.513	-0.500

Table 6.1: The numerical exponents α_t and β_t to the independent variables of the equilibrium time compared to the analytically derived exponents of the equilibrium time.

The numerical exponents to the independent variables of the equilibrium time differ slightly from the analytical exponents. A possible explanation is the assumption of no effect of initial conditions on the equilibrium time made in Sec. 6.4. It is found that the equilibrium time is:

$$t_{eq} \propto (nx)^{0.50}(E^*)^{-0.51}. \tag{6.106}$$

As expected, this result is comparable to the analytical expression for the equilibrium time t_{eq} in Eq. (6.92).
In Fig. 6.22, the numerical number of iterations to equilibrium n_{eq} is plotted as a function of the dimensionless discretization time Δt.

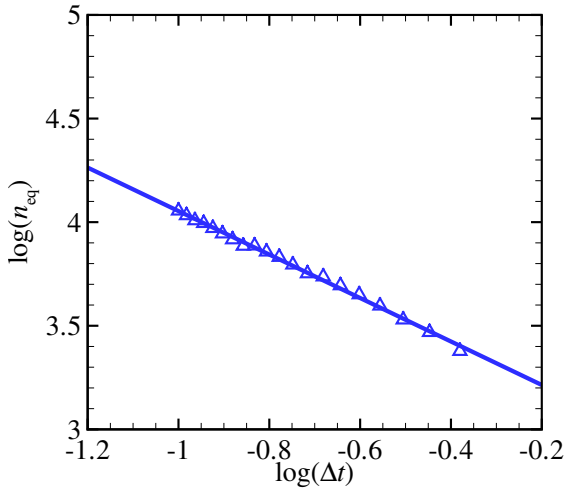

Figure 6.22: Log-log plot of the number of iterations to equilibrium n_{eq} as a function of the dimensionless discretization time Δt. The gradient of the linear fit line is -1.049.

It is found that the equilibrium time t_{eq} of a GFMD simulation is independent of the discretization time Δt. As to be expected, this result is in accordance with the analytical expression for approximating the equilibrium time t_{eq} in Eq. (6.46).

6.5.3 Normal and tangential displacement of a finite slab

In this section, the vector damping factor in GFMD simulations studying both normal and tangential displacement and a finite-height slab are compared to the analytical expression for the scalar critical damping factor η_{cr} in Eq. (6.65) (see Fig. 6.23). The following parameters are chosen for the simulations: $\mathrm{d}t = 0.25,\ \nu = 0.20,\ a = 1,\ L_x = 20\ \mu\mathrm{m},\ nx = 2048,\ A = 0.01 L_x$ and $E = 70$ GPa.

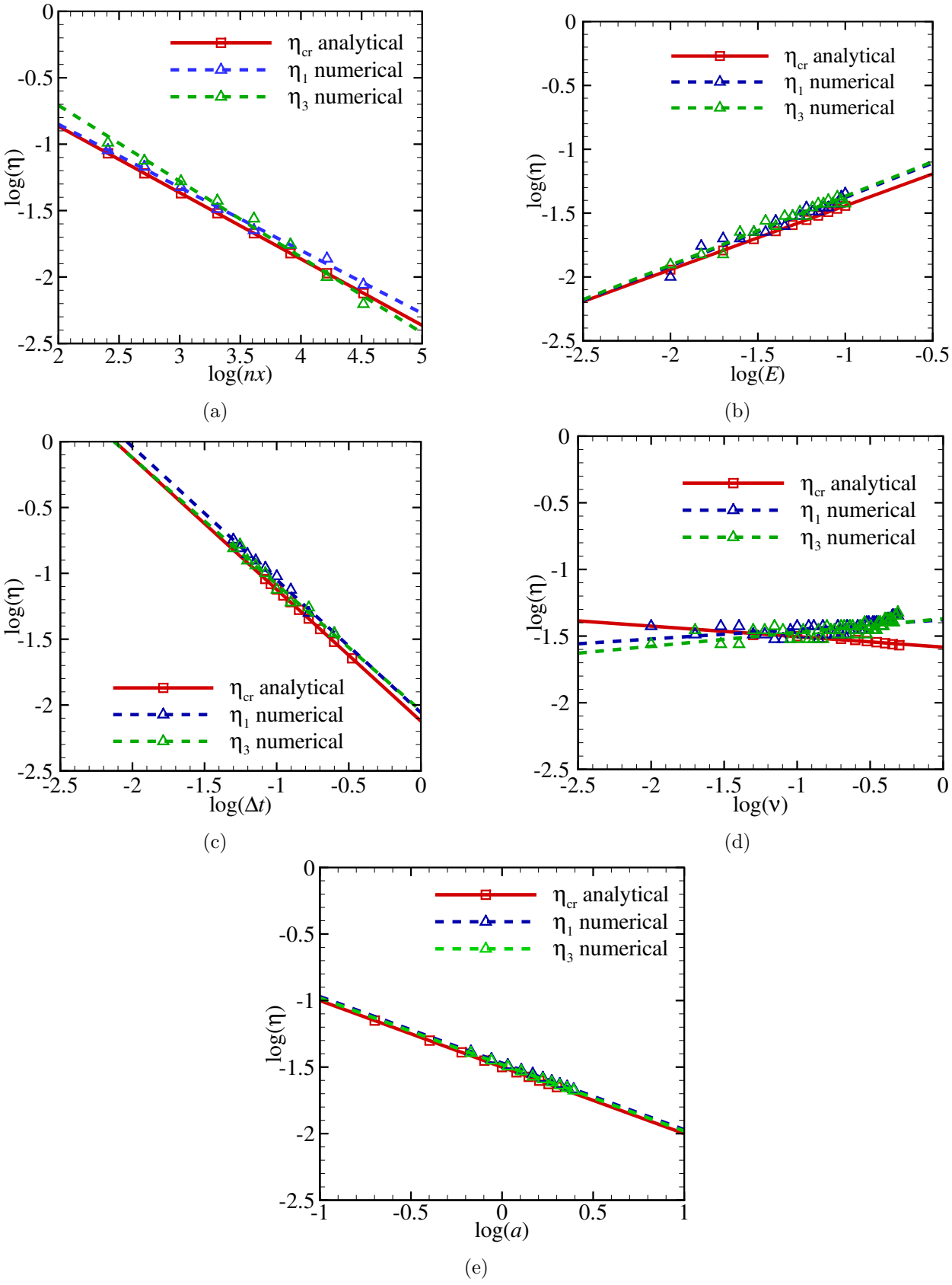

Figure 6.23: Log-log plots of the critical damping factor $\boldsymbol{\eta}$ a function of (a) discretization nx, (b) elastic modulus E, (c) discretization time dt, (d) Poisson's ratio ν and (e) aspect ratio a.

The numerical vector critical damping factor is in good accordance with the analytical scalar critical damping factors, except its dependency on the Poisson's ratio ν (*i.e.*, see Fig. 6.23d). The difference in critical damping factors for $\nu > 0.35$ are due to the difference between the numerical result for the vector damping factor and analytical results for the scalar damping factor. However, the change in magnitude of the critical damping factor is only minor compared to the results for the remaining four independent parameters. It is found that the vector critical damping factor is:

$$\begin{aligned} \eta_1 &\propto (nx)^{-0.47}(E)^{0.53}(\nu)^{0.07}(a)^{-0.50}(\Delta t)^{-1.0}; \\ \eta_3 &\propto (nx)^{-0.56}(E)^{0.54}(\nu)^{0.1}(a)^{-0.50}(\Delta t)^{-0.97}. \end{aligned} \tag{6.107}$$

As expected, this result is comparable to the analytical expression for the scalar critical damping factor η_{cr} in Eq. (6.65).
In Tab. 6.2, the numerical exponents obtained using GFMD simulations are compared with those obtained from the analytical expression.

	numerical	analytical
α_{t}	0.556	0.500
β_{t}	-0.526	-0.500
ξ_{t}	-0.012	0.081
χ_{t}	0.501	0.500

Table 6.2: The numerical exponents α_{t}, β_{t}, ξ_{t} and χ_{t} to the independent variables of the equilibrium time (Eq. (6.92)), compared to the analytically derived exponents of the equilibrium time (Eq. (6.96)).

The numerical exponents to the independent variables of the equilibrium time differ from the analytical exponents. A possible explanation is the assumption of no effect of initial conditions on the equilibrium time made in Sec. 6.4. The calculated and analytical exponent ξ_{t} differ in sign due to the afore-mentioned reasons for a difference in dependency of the damping factor on the Poisson's ratio ν (see Fig. 6.23d). It is found that the equilibrium time is:

$$t_{\mathrm{eq}} \propto (nx)^{0.56}(E)^{-0.53}(\nu)^{-0.01}(a)^{0.50}. \tag{6.108}$$

As to be expected, this result is comparable to the analytical expression for the equilibrium time t_{eq} in Eq. (6.97).

6.6 Effect of interfacial interactions on the critical damping coefficient

The conversion of kinetic energy to potential energy at the interface influences the damped dynamics [79]. The adhesive or repulsive character of the interfacial interactions influences the characteristic dynamic regimes of the GFMD damped dynamic energy minimization. The interface can also be modeled by means of a hard-disk interaction [78] with a coefficient of restitution e which specifies the amount of kinetic energy conserved during the collision.

6.6.1 Finite-Range interaction

A finite-range interactions $\boldsymbol{V}_{\mathrm{fr}}$ [83], which only depend on the local gap, can be written as:

$$\boldsymbol{V}_{\mathrm{fr}}(t) = -\Delta\gamma \int \mathrm{d}x^2 e\left(\frac{-\left(\boldsymbol{u}_{\mathrm{punch}}(x) - \boldsymbol{u}(x,t)\right)}{z_{\mathrm{r}}}\right), \tag{6.109}$$

where $\Delta\gamma$ is the work of adhesion and z_{r} is the interaction length. The force in normal direction on the surface as a function of the gap $g(x,t) = z_{\mathrm{punch}}(x,t) - u_3(x,t)$ is:

$$f_3(r) = -\frac{\Delta\gamma}{z_{\mathrm{r}}}\gamma e\left(\frac{-\left(g(x,t)\right)}{z_{\mathrm{r}}}\right). \tag{6.110}$$

In this section, Equation (6.110) is used to study the influence of finite-range interaction on the damping factor. Following [89], the equation of motion without the driving terms in Eq. (6.53) can be written in real-space as a general wave equation:

$$\frac{\mathrm{d}^2 r}{\mathrm{d}t^2} + c\frac{\mathrm{d}r}{\mathrm{d}t} + \kappa r = a_0 + a_1\frac{\mathrm{d}r}{\mathrm{d}x} + a_2\frac{\mathrm{d}^2 r}{\mathrm{d}x^2}, \tag{6.111}$$

where a_i are constants with units N/m. The force $F(r)$ acts on a line segment $r \pm \delta r$. The force $f(r)$ at the point r on the surface is derived as:

$$\lim_{\delta r \to 0} f(r - \delta r) + f(r + \delta r) = F(r)2\delta r = 2f(r). \tag{6.112}$$

The Fourier transform of Eq. (6.112) is:

$$\tilde{f}\,(q) = \frac{\tilde{F}(q)}{q}. \tag{6.113}$$

Equation (6.2) is rewritten as:

$$\frac{\mathrm{d}^2\boldsymbol{u}(x,t)}{\mathrm{d}t^2} + c\frac{\mathrm{d}\boldsymbol{u}(x,t)}{\mathrm{d}t} + \mathcal{F}^{-1}\{\frac{\boldsymbol{G}^{-1}(q)}{q}\}\boldsymbol{u}(x,t) = \boldsymbol{f}_{\mathrm{ext}}(x,t), \tag{6.114}$$

where $\mathcal{F}^{-1}\{\tilde{x}\}$ is the inverse Fourier transform. Equations (6.110) and (6.114) are combined. The equation of motion in GFMD damped dynamic energy minimization, with the external force on a grid-point described by a finite-range exponential interaction, can be written as:

$$\frac{\mathrm{d}^2\boldsymbol{u}(x,t)}{\mathrm{d}t^2} + c\frac{\mathrm{d}\boldsymbol{u}(x,t)}{\mathrm{d}t} + \mathcal{F}^{-1}\{\frac{\boldsymbol{G}^{-1}(q)}{q}\}\boldsymbol{u}(x,t) = -\frac{\Delta\gamma}{z_{\mathrm{r}}}\gamma e\left(\frac{-\left(g(x,t)\right)}{z_{\mathrm{r}}}\right). \tag{6.115}$$

For frictionless contact, $|\boldsymbol{u}| << z_{\mathrm{r}}$ and $z_{\mathrm{punch}}(x,t) = 0$, the first and second term of the series expansion of Eq. (6.110) form the driving terms. The equation of motion of the normal displacement is written as:

$$\frac{\mathrm{d}^2 u_3(x,t)}{\mathrm{d}t^2} + c\frac{\mathrm{d}u_3(x,t)}{\mathrm{d}t} + \left(\mathcal{F}^{-1}\{\frac{G^{-1}(q)}{q}\} + \frac{\Delta\gamma}{z_{\mathrm{r}}^2}\right)u_3(x,t) + \frac{\Delta\gamma}{z_{\mathrm{r}}} = 0. \tag{6.116}$$

In Fourier space the homogeneous equation of motion for $q \geq 1$ is:

$$\frac{\mathrm{d}^2\tilde{u}_3\left(q,t\right)}{\mathrm{d}t^2} + c_3\frac{\mathrm{d}\tilde{u}_3\left(q,t\right)}{\mathrm{d}t} + \left(\tilde{G}\left(q\right)^{-1} + q\frac{\Delta\gamma}{z_\mathrm{r}^2}\right)\tilde{u}_3\left(q,t\right) = 0. \tag{6.117}$$

Two regimes can be identified depending on the sign of the work of adhesion: Squeeze-out for finite-range repulsion where $\Delta\gamma < 0$ and pull-off for finite-range attraction where $\Delta\gamma > 0$. As to be expected, interfacial b.c. do influence the characteristic dynamic regimes of the GFMD-simulations. Note that the coefficient of the third term in Eq. (6.117) is the linear force constant $\kappa_3(q)$ for the principal mode with wavenumber q in the normal direction. The influence of the work of adhesion in the case of frictionless contact for a sufficiently large interaction length z_r is:

- When the work of adhesion is $\Delta\gamma < 0$, the critical damping factor η_cr decreases;
- When the work of adhesion is $\Delta\gamma > 0$, the critical damping factor η_cr increases.

We observe that for the finite-range adhesive potential the critical damping factor η_cr increases for a generic punch shape. Therefore, we conclude that the analytical expression of the critical damping factor, as derived in Sec. 6.3, is also applicable with the finite-range adhesive interfacial interactions at the surface. However, the energy minimization dynamics for the finite-range adhesive interfacial interactions will be under-damped. Vice versa, the finite-range repulsive potential decreases the critical damping factor η_cr. Which mode is the slowest frequency mode depends on the punch shape, therefore the center-of-mass or the first principal mode is not per definition the lowest frequency mode anymore. For a cohesive zone model [76], we can not draw any conclusion as it has both an adhesive and a repulsive zone. Note that for a constant traction prescribed $\boldsymbol{\tau}(x)$ at the surface, the analytical expression for the critical damping factor derived in this work still holds true (see Sec. 6.2). Alternatively, one can formally introduce a short-range interaction, hard-wall repulsion [83]:

$$\boldsymbol{V}_\mathrm{sr}(t) = \lim_{z_\mathrm{r}\to 0}\int \mathrm{d}x^2\left(F_\mathrm{r}z_\mathrm{r}\right)e^{\left(\frac{-\left(\boldsymbol{u}_\mathrm{punch}(x)-\boldsymbol{u}(x,t)\right)}{z_\mathrm{r}}\right)}, \tag{6.118}$$

where F_r is an arbitrary positive constant of unit force per area. The series expansion of Eq. (6.110) is not valid for hard-wall interaction, in the limit $z_\mathrm{r} \to 0$. Therefore, the influence of hard-wall interaction on the GFMD damped dynamic energy minimization can not be derived in a similar fashion as for finite-range interaction.

6.6.2 Hard-wall interaction

We observe from the simulations performed in Chapter 4 with hard-wall interaction, that the critical damping factor η_cr derived in this work ensures the energy minimization is under-damped. Moreover, we use 'safety coefficient' was used to ensure under-damped dynamic. We found no analytical expression for the critical damping factor η_cr which included the hard-wall interaction, because the hard-wall interaction is a non-linear velocity boundary condition on a non-integrable boundary, *i.e.*, a non-holonomic boundary condition according to Prodanov *et al.* [5]. However, we want to present the considerations we made to come to this conclusion in this section.
For an impulse based contact model in real space, a reaction force $f_\mathrm{r}(t)$ acting on a body with a constant mass m for a time interval t to $t + \mathrm{d}t$ generates a change in the body's momentum. The effect of the reaction force over the interval of collision is represented by a collision impulse J_r.

The equations of motion for a two-body collision yields the relation between pre- and post-collision velocities:

$$\begin{aligned}\dot{\boldsymbol{r}}_1' =& \dot{\boldsymbol{r}}_1 - \frac{J_r}{m_1}\hat{\boldsymbol{n}};\\ \dot{\boldsymbol{r}}_2' =& \dot{\boldsymbol{r}}_2 + \frac{J_r}{m_2}\hat{\boldsymbol{n}},\end{aligned} \tag{6.119}$$

where $\dot{\boldsymbol{r}}_1$ and $\dot{\boldsymbol{r}}_2$ are the pre-collision velocities, $\dot{\boldsymbol{r}}_1'$ and $\dot{\boldsymbol{r}}_2'$ are the post-collision velocities of bodies with mass m_1 and m_2 and $\hat{\boldsymbol{n}}$ is the contact normal. When both bodies have no angular momentum the coefficient of restitution e relates the pre-collision relative velocity $\dot{\boldsymbol{r}}_\mathrm{r} = \dot{\boldsymbol{r}}_1 - \dot{\boldsymbol{r}}_2$ to the post-collision relative velocity $\dot{\boldsymbol{r}}_\mathrm{r}' = \dot{\boldsymbol{r}}_1' - \dot{\boldsymbol{r}}_2'$. This is written as:

$$\dot{\boldsymbol{r}}_\mathrm{r}'\boldsymbol{n} = -e\dot{\boldsymbol{r}}_\mathrm{r}\hat{\boldsymbol{n}}. \tag{6.120}$$

Substituting Eq. (6.119) into Eq. (6.120), we give the reaction impulse:

$$J_\mathrm{r} = \frac{-(1+e)\,\dot{\boldsymbol{r}}_\mathrm{r}\hat{\boldsymbol{n}}}{m_1^{-1} + m_2^{-1}}. \tag{6.121}$$

The coefficient of restitution for hard-wall interaction is $e = 0$. In GFMD, body one can be represented by the substrate modeled with nx grid-points and body two is represented by the rigid punch. The punch is modeled as a body with an infinite mass m_2 and zero velocity $\dot{r}_2 = 0$. Hence, the velocity of the grid-points post-collision is $\dot{r}_1' = 0$.
The non-holonomic b.c. at the interface described by Eq. (6.5) can be written as:

$$\dot{\boldsymbol{u}}(x,t) = 0, \qquad \text{for} \qquad \boldsymbol{u}(x,t) = z_\mathrm{punch}(x). \tag{6.122}$$

The velocity of the surface displacement at the location of the punch $\boldsymbol{u}_\mathrm{punch}(x)$ will be non-linear. The pSV method models the non-linearity in velocity by a virtual impulse J_v. This virtual impulse depends on the velocity $\dot{r}_1$ and the discrete time-step Δt. For this specific case there is no analytical expression for the critical damping factor currently known by the author.
An other approach is to model the GFMD simulations with one DOF and the hard-wall b.c. as follows. A grid-point hitting the punch can be represented by the mass of the damped harmonic oscillator elastically colliding with a wall with a coefficient of restitution $e = 0$ at $t = t_\mathrm{cl}$, where t_cl is the time at collision. The velocity and position after collision are then the initial conditions for its equation of motion for $t > t_\mathrm{cl}$. As long as the wall is placed at position $x_\mathrm{w} > x_\mathrm{eq}$, where x_eq is the position at equilibrium of the mass of the damped harmonic oscillator, the characteristic dynamic regime depends on the damping coefficient. When the wall position is $x_\mathrm{w} \leq x_\mathrm{eq}$, the damped harmonic oscillator is infinitely over-damped. The analogy with a 1 DOF damped harmonic oscillator elastically colliding with a wall is not further pursued, because the equilibrium position of a single grid-point depends on the position of the punch (*i.e.*, position of the elastic wall) and the position of all other $nx - 1$ grid-points. No qualitative nor quantitative expression for the critical damping factor in GFMD simulations with hard-wall interaction is available at the moment.

6.7 Conclusions and discussion

For the first time the pSV method used in the GFMD simulations is rewritten in its velocity explicit scheme to analytically derive the characteristic dynamic regimes of the damped harmonic oscillator. The newly presented analytical expression for the critical damping coefficient and characteristic dynamic regimes are valid for an arbitrary finite discrete time-step $\mathrm{d}t$. The analytical expression for the critical damping coefficient of the damped harmonic oscillator and the numerical critical damping coefficient of the damped harmonic oscillator for pSV differ significantly for a finite discrete time-step $\mathrm{d}t$. For the first time, it is shown that the equilibrium time of the damped harmonic oscillator for pSV is independent of the discrete time-step $\mathrm{d}t$. For a given equilibrium time t_{eq}, the number of iterations till equilibrium n_{eq} depends only on the discrete time-step Δt. The maximum value of the discrete time-step is determined by the relation $\kappa \Delta t^2 \leq 4$. The equilibrium time t_{eq} can be correctly approximated prior to the simulation. Note that for this work we assume $\mathrm{d}t \leq \sqrt{\kappa}$, in order to ensure the magnitude of the critical damping factor η_{cr} increases for a generic increase of the magnitude of the linear force constant κ. However, when the discrete time-step is increased from $\mathrm{d}t \leq \sqrt{\kappa}$ up to $\mathrm{d}t \leq 2/\sqrt{\kappa}$, we can further reduce the computational time. Note also, that it is now possible to use a scalar critical damping factor η_{cr} so that each mode is critically damped.
As predicted, the critical damping factor η_{cr} depends on the aspect ratio a, the material properties, the loading directions, the interfacial conditions and the dimensionless discrete time-step Δt. The presence of coupling of the normal and tangential displacement depends solely on the Poisson's ratio ν, the aspect ratio a and the loading conditions. The normal and tangential displacement are decoupled for a semi-infinite body with Poisson's ratio $\nu = 0.5$, zero normal traction, frictionless contact and in the limit $\nu \to -\infty$. Except for these special cases, it is shown that coupling can not be neglected. The equilibrium time t_{eq} depends on the lowest frequency mode, which is the mode of the scalar critical damping factor η_{cr}.
From the numerical calculations in Sec. 6.5, we conclude that the critical damping factor η_{cr} is proportional to the elastic modulus E and inversely proportional to the width L_x, aspect ratio a and discrete time-step Δt. Moreover, we find a weak dependency of the value of the critical damping factor on the Poisson's ratio for $\nu > 0.35$. We conclude that for the value of the critical damping factor η_{cr} with $\nu \approx 0.5$ for a given elastic modulus E, width L_x, aspect ratio a and discrete time-step Δt, the dynamics are always under damped. We conclude that the equilibrium time t_{eq} for GFMD simulations is also independent of the discrete time-step Δt.
For the first time the effect of the interfacial conditions on the critical damping factor η_{cr} is determined by taking the Fourier transform of the first two terms of the series expansion of the exponential interaction potential. When the work of adhesion is negative, the critical damping factor η_{cr} decreases. When the work of adhesion is positive, the critical damping factor η_{cr} increases. For hard-wall interaction we find no analytical expression for the critical damping factor η_{cr}. However, we conclude that with a carefully chosen scaling of the critical damping factor η_{cr} the dynamic energy minimization is assured to be under-damped. To perform the simulations with a hard-wall potential a 'safety coefficient' was used;
The computational time in GFMD simulations is minimized by using the analytical expression for the scalar critical damping factor η_{cr}. This scalar critical damping factor η_{cr} can be determined prior to the simulation. However, the analytical expression for the vector critical damping factor $\boldsymbol{\eta}_{\mathrm{cr}}$ will further reduce the computational time for the Poisson's ratio $\nu > 0.35$.

Chapter 7

Concluding remarks

7.1 Conclusions

The ultimate objective of this work is to obtain a better understanding of the contact mechanics of deformable bodies with self-affine roughness. To this end, we take three steps: First, a computational study is performed, focusing on proportionality between load and contact area for low nominal pressures; Second, we present an extended GFMD approach for deformable bodies with a simple surface topography; And, third, we derive here the analytical expression for the critical damping coefficient in the damped dynamic energy minimization used in GFMD. In the following, the main conclusion of each chapter is presented.
Chapter 3, is devoted to finding an appropriate numerical description for rough fractal surfaces. This study leads to the following conclusions:

- Power spectral density method (PSDM) is capable of numerically generating surface topographies highly comparable to experimentally measured topographies for a given Hurst's exponent H, roll-off wavelength λ_r and root mean square height w (RMSH). Moreover, in this work, PSDM is the most suitable method to generate surface topographies to be used in GFMD simulations to determine the proportionality between load and contact area;

- The minimum ratio L_x/ξ of a numerically generated topography with a Gaussian height distribution $p(h)$ increases for an increase in Hurst's exponent H. The rate of convergence in the mean-square to the Gaussian distribution depends on the Hurst's exponent H. Moreover, there is a minimum ratio, $1 \leq L_x/\xi < 400$, depending on the Hurst's exponent $H < 0.8$ for which the height distribution $p(h)$ resembles a Gaussian distribution;

- $\zeta/\lambda \leq 0.1$ is the maximum ratio for which a mounded structure can be modeled as self-affine roughness.

In Chapter 4, the determination of the proportionality constant κ for an elastic slab with the Poisson's ratio ν and aspect ratio a that can be arbitrarily chosen is presented. We assume a small nominal pressure $\bar{p}$ and a nominally flat surface topography, and use the commonly presumed expression for the relation between the contact area fraction a_r and low nominal pressure $\bar{p}$: $a_\mathrm{r} = \kappa\bar{p}/\bar{g}E^*$, where $\bar{g}$ is the root mean square gradient (RMSG) and E^* the effective modulus. This leads to the following conclusions:

For the semi-infinite solid;

- The proportionality coefficient κ is independent of the Hurst's exponent H. There is no higher-order dependency of the value of the proportionality coefficient on the Poisson's ratio in the range studied $0.2 \leq \nu \leq 0.5$;
- The proportionality coefficient has the value $\kappa \approx 1.45$. This value of κ is closer to the prediction of Persson's theory [12], *i.e.*, $\kappa = \sqrt{8/\pi} \approx 1.59$, than previously reported values of κ;
- Previously reported values of the proportionality coefficient κ studied using GFMD [4, 5] are between 1.5 and 2 times larger than our prediction. The reason for this difference is using twice the areal elastic energy in the previous studies due to omission of the scaling of displacements in the FFTW3 library [49].

For the finite-height slab;

  - The proportionality coefficient with the value $\kappa \approx 1.5$, can be used as a good approximation for a generic Poisson's ratio $0.2 < \nu \leq 0.5$ and aspect ratio $0.5 \leq a \leq \infty$;
  - We do not observe the higher-order dependency of the proportionality coefficient κ on the Poisson's ratio ν for linear-elastic slabs as observed in the previous study [40]. We conclude that the most likely reason this higher-order dependency is observed, because of the choice of insufficiently small fractal- and continuum discretizations.

- The predicted continuum mechanical value of κ suffers a large error for a large Hurst's exponent, *i.e.*, $H > 0.5$, when one choses the ratio L_x/ξ too small, *i.e.*, large thermodynamic discretization. This is the result of the strictly non-Gaussian height distribution $p(h)$ of the numerically generated surface topography by PSDM.

In Chapter 5, we extend GFMD to study the contact mechanics of deformable bodies with a simple surface topography. This extended GFMD method is called two-step GFMD. This GFMD approach allows one to study frictional interfaces. We study the limiting case of an array of rectangular asperities flattened by a rigid body, and determine the maximum allowable RMSG $\bar{g}$. Moreover, we make the following observations:

- Two-step GFMD is capable of approximating the displacement of the surface to $\mathcal{O}^{-6}L_x$ precision, and the traction to within $\mathcal{O}^{-4}E$ precision;

- The analytical expression in [3] corrected with the expected error in uniform strain leads to a precision $\mathcal{O}^{-3}E$ in the stress fields;

- The maximum allowable RMSG for performing two-step GFMD is found to be $\bar{g} \leq 0.030$, tolerating the aforementioned precisions.

Chapter 6, the focus is on finding *a priori* the critical damping coefficient for fast convergence of the simulations. To this end, the position (Störmer-)Verlet (pSV) method used in the GFMD simulations is rewritten in its velocity explicit scheme to analytically derive the characteristic dynamic regimes of the damped dynamic energy minimization. This leads to the following conclusions:

- The critical damping factor η_{cr} is proportional to the elastic modulus E and inversely proportional to the width L_x, aspect ratio a and discrete time-step Δt. Moreover, we find a weak dependency of the value of the critical damping factor η_{cr} on the Poisson's ratio for $\nu > 0.35$;

- We use a scalar damping factor η_{cr} corresponding to critical damping factor of the slowest mode (*i.e.*, center-of mass mode in tangential direction) to damp all other modes. This choice is purely for simplicity, and results in the center-of-mass mode in tangential direction being critically damped, while all other modes are under-damped. It is now possible to use a scalar critical damping factor η_{cr} so that each mode is critically damped.

- The principal mode that is the lowest frequency mode depends on the aspect ratio a, the material properties, the loading directions, the interfacial conditions and the dimensionless discrete time-step Δt. When we ensure $\kappa \Delta t^2 \leq 1$ for all modes, the slowest frequency mode is always the center-of-mass mode or the first principal mode;

- When the work of adhesion is negative, the critical damping factor η_{cr} decreases. When the work of adhesion is positive, the critical damping factor η_{cr} increases. To perform the simulations with a hard-wall potential a 'safety coefficient' was used;

– The equilibrium time of the damped harmonic oscillator for pSV is independent of the discrete time-step dt. The equilibrium time t_{eq} depends on the lowest frequency mode, which is the mode of the critical damping factor η_{cr}.

7.2 Outlook

The motivation to this work is to get a better understanding of rough metallic surfaces in contact. Recent work by Venugopalan *et al.* [47] is already as step in the right direction to study plasticity through discrete dislocation dynamics in combination with the GFMD approach. However, the small-slope assumption limits the gradients $g(x)$ and root mean square heights w (RMSH) one can study. The gradients and RMSH experimentally observed can be orders of magnitude bigger than we can accurately numerically calculate up to date [24, 2]. Therefore, one of the recommendations is to relax the small-slope assumption in GFMD.
While the contact area fraction a_{r} can only be rigorously and non-arbitrarily determined in continuum mechanics, an in depth analysis of the proportionality between the contact area and the pressure might help discern the validity and applicability of various statistical models. Due to the scatter in experimental results and the difficulty in reproducibility [27], brute-force methods are expected to be one of the ways to validate statistical models. Therefore, a recommendation is to extend the thermodynamic, fractal and continuum corrections presented in this work to a larger range of discretization values, 2-dimensional surfaces with different RMSH w and vary the Hurst's exponent H, Poisson's ratio ν in their limiting values of $H = [0, 1]$ and $\nu = [0, 0.5]$ for various aspect ratio's, while ensuring the ratio L_x/ξ is large enough to numerically generate a topography with the Gaussian height distribution $p(h)$. Note that, up to date, the classical GFMD method by Venugopalan *et al.* [3] is extended to $(2+1)-$dimensional compressible bodies. Therefore, another one of the recommendations is to research possible (empirical) relationships between contact mechanical properties of $(1+1)$- and $(2+1)$-dimensional bodies with (an)isotropic fractal roughness, as introduced by Scaraggi *et al.* [73].
Two-step GFMD is capable of numerically calculating contact mechanical properties of a deformable elastic layer with self-affine surface roughness. It is straightforward to extend this method for a generic interaction potential at the surface, *i.e.*, finite range adhesive/repulsive potential [74]. Also, two-step GFMD can be used to numerically calculate the displacement of the surfaces for two deformable elastic slabs contact with generic aspect ratios, Poisson's ratios and surface topographies. Two-step GFMD allows a non-deterministic description of the surface topography otherwise commonly found in models including adhesion and friction. For example, simulate multi-body contacts, where the more realistic interaction between metallic asperities can be effectively studied using an exponential potential like Xu-Needleman [75] or the cohesive zone model according to McGarry *et al.* [76], also allowing the study of interplay between adhesion and friction at the interface.
In this work, we numerically calculate contact mechanical properties independent of length scale, and do not give an answer to the interplay of different mechanisms over different length scales. Two-step GFMD is also a suitable candidate to build a multi-scale model as introduced by
Pastewka *et al.* [48] in which the surface had an atomistic description and the flat linear-elastic substrate was treated with harmonic approximations [47]. Two-step GFMD can be used to give large length scale roughness on the surface of the substrate, while an atomistic description could be used for smaller length scale roughness. Note that this would reduce the areas needing an atomistic description compared to a flat linear-elastic substrate, and in turn reduce the computational complexity.

Bibliography

[1] B. B. Mandelbrot, D. E. Passoja, and A. J. Paullay, *Fractal character of fracture surfaces of metals*. Nature Publishing Group, 1984.

[2] F. Plouraboué and M. Boehm, "Multi-scale roughness transfer in cold metal rolling," *Tribology International*, vol. 32, no. 1, pp. 45–57, 1999.

[3] S. P. Venugopalan, L. Nicola, and M. H. Müser, "Green's function molecular dynamics: Including finite heights, shear, and body fields," *Modelling and Simulation in Materials Science and Engineering*, vol. 25, no. 3, p. 034001, 2017.

[4] C. Campañá and M. H. Müser, "Contact mechanics of real vs. randomly rough surfaces: A Green's function molecular dynamics study," *EPL (Europhysics Letters)*, vol. 77, no. 3, p. 38005, 2007.

[5] N. Prodanov, W. B. Dapp, and M. H. Müser, "On the contact area and mean gap of rough, elastic contacts: Dimensional analysis, numerical corrections, and reference data," *Tribology Letters*, vol. 53, no. 2, pp. 433–448, 2014.

[6] W. B. Dapp, N. Prodanov, and M. H. Müser, "Systematic analysis of Perssons contact mechanics theory of randomly rough elastic surfaces," *Journal of Physics: Condensed Matter*, vol. 26, no. 35, p. 355002, 2014.

[7] F. P. Bowden and D. Tabor, *The friction and lubrication of solids*, vol. 1. Oxford university press, 2001.

[8] K. Komvopoulos and D. Choi, "Elastic finite element analysis of multi-asperity contacts," *Transactions-Aamerican society of mechanical engineers journal of tribology*, vol. 114, pp. 823–823, 1992.

[9] S. Hyun and M. O. Robbins, "Elastic contact between rough surfaces: Effect of roughness at large and small wavelengths," *Tribology International*, vol. 40, no. 10, pp. 1413–1422, 2007.

[10] J. Greenwood and J. Williamson, "Contact of nominally flat surfaces," *Proceedings of the Royal Society of London A: Mathematical, Physical and Engineering Sciences*, vol. 295, no. 1442, pp. 300–319, 1966.

[11] A. Bush, R. Gibson, and T. Thomas, "The elastic contact of a rough surface," *Wear*, vol. 35, no. 1, pp. 87–111, 1975.

[12] B. N. Persson, "Theory of rubber friction and contact mechanics," *The Journal of Chemical Physics*, vol. 115, no. 8, pp. 3840–3861, 2001.

[13] M. Ciavarella, J. Greenwood, and M. Paggi, "Inclusion of interaction in the Greenwood and Williamson contact theory," *Wear*, vol. 265, no. 5, pp. 729–734, 2008.

[14] G. Carbone, "A slightly corrected Greenwood and Williamson model predicts asymptotic linearity between contact area and load," *Journal of the Mechanics and Physics of Solids*, vol. 57, no. 7, pp. 1093–1102, 2009.

[15] K. L. Johnson, *Contact mechanics*. Cambridge university press, 1987.

[16] L. Verlet, "Computer experiment of classical fluids. i. thermodynamical properties of Lennard-Jones molecules," *Physical Review 159,* ***98***, 1967.

[17] K. Gillingham, M. J. Kotchen, D. S. Rapson, and G. Wagner, "Energy policy: The rebound effect is overplayed," *Nature*, vol. 493, no. 7433, pp. 475–476, 2013.

[18] J. Gao, W. Luedtke, D. Gourdon, M. Ruths, J. Israelachvili, and U. Landman, *Frictional forces and Amontons' law: from the molecular to the macroscopic scale*. ACS Publications, 2004.

[19] E. Gnecco and E. Meyer, *Fundamentals of Friction and Wear on the Nanoscale*. Springer, 2007.

[20] H. Hertz, "Uber die Beruhrung fester elastischer Korper," *Journal fur die reine und angewandte Mathematik*, vol. 92, pp. 156–171, 1882.

[21] J. Greenwood and J. Tripp, "The contact of two nominally flat rough surfaces," *Proceedings of the institution of mechanical engineers*, vol. 185, no. 1, pp. 625–633, 1970.

[22] M. Ciavarella, V. Delfine, and G. Demelio, "A re-vitalized Greenwood and Williamson model of elastic contact between fractal surfaces," *Journal of the Mechanics and Physics of Solids*, vol. 54, no. 12, pp. 2569–2591, 2006.

[23] J. Archard, "Contact and rubbing of flat surfaces," *Journal of applied physics*, vol. 24, no. 8, pp. 981–988, 1953.

[24] A. Majumdar and C. Tien, "Fractal characterization and simulation of rough surfaces," *Wear*, vol. 136, no. 2, pp. 313–327, 1990.

[25] B. Persson, O. Albohr, U. Tartaglino, A. Volokitin, and E. Tosatti, "On the nature of surface roughness with application to contact mechanics, sealing, rubber friction and adhesion," *Journal of Physics: Condensed Matter*, vol. 17, no. 1, p. R1, 2004.

[26] R. L. Jackson and J. L. Streator, "A multi-scale model for contact between rough surfaces," *Wear*, vol. 261, no. 11, pp. 1337–1347, 2006.

[27] M. H. Müser and W. B. Dapp, "The contact mechanics challenge: Problem definition," *arXiv preprint arXiv:1512.02403*, 2015.

[28] B. Bhushan, "Contact mechanics of rough surfaces in tribology: Multiple asperity contact," *Tribology letters*, vol. 4, no. 1, pp. 1–35, 1998.

[29] J. Williamson, "Paper 17: Microtopography of surfaces," in *Proceedings of the Institution of Mechanical Engineers, Conference Proceedings*, vol. 182, pp. 21–30, SAGE Publications Sage UK: London, England, 1967.

[30] P. Gupta and N. Cook, "Junction deformation models for asperities in sliding interaction," *Wear*, vol. 20, no. 1, pp. 73–87, 1972.

[31] B. Bhushan and N. Cook, "On the correlation between friction-coefficients and adhesion stresses," *Journal of Engineering Materials and Technology*, vol. 97, no. 3, pp. 285–287, 1975.

[32] V. A. Yastrebov, J. Durand, H. Proudhon, and G. Cailletaud, "Rough surface contact analysis by means of the finite element method and of a new reduced model," *Comptes Rendus Mécanique*, vol. 339, no. 7-8, pp. 473–490, 2011.

[33] K. Komvopoulos and Z.-Q. Gong, "Stress analysis of a layered elastic solid in contact with a rough surface exhibiting fractal behavior," *International Journal of Solids and Structures*, vol. 44, no. 7, pp. 2109–2129, 2007.

[34] H. Stanley and T. Kato, "An FFT-based method for rough surface contact," *Transactions-American society of mechanical engineers journal of tribology*, vol. 119, pp. 481–485, 1997.

[35] I. Polonsky and L. Keer, "Fast methods for solving rough contact problems: A comparative study," *ASME J. Tribol*, vol. 122, no. 1, pp. 36–41, 2000.

[36] J.-J. Wu, "Numerical analyses on elliptical adhesive contact," *Journal of Physics D: Applied Physics*, vol. 39, no. 9, p. 1899, 2006.

[37] S. Ilincic, G. Vorlaufer, P. Fotiu, A. Vernes, and F. Franek, "Combined finite element-boundary element method modelling of elastic multi-asperity contacts," *Proceedings of the Institution of Mechanical Engineers, Part J: Journal of Engineering Tribology*, vol. 223, no. 5, pp. 767–776, 2009.

[38] S. Medina and D. Dini, "A numerical model for the deterministic analysis of adhesive rough contacts down to the nano-scale," *International Journal of Solids and Structures*, vol. 51, no. 14, pp. 2620–2632, 2014.

[39] C. Campaná and M. H. Müser, "Practical Green's function approach to the simulation of elastic semi-infinite solids," *Physical Review B*, vol. 74, no. 7, p. 075420, 2006.

[40] S. Hyun, L. Pei, J.-F. Molinari, and M. O. Robbins, "Finite-element analysis of contact between elastic self-affine surfaces," *Physical Review E*, vol. 70, no. 2, p. 026117, 2004.

[41] Ashby, F. Michael, and D. Cebon, "Materials selection in mechanical design," *Le Journal de Physique IV*, vol. 3, no. C7, pp. C7–1, 1993.

[42] R. F. Voss, "Random fractal forgeries," pp. 805–835, 1985.

[43] S. B. Ramisetti, C. Campañá, G. Anciaux, J.-F. Molinari, M. H. Müser, and M. O. Robbins, "The autocorrelation function for island areas on self-affine surfaces," *Journal of Physics: Condensed Matter*, vol. 23, no. 21, p. 215004, 2011.

[44] K. Ogata, *Modern Control Engineering*. AEEIZH, 2002.

[45] M. Born, "On the stability of crystal lattices. I," in *Mathematical Proceedings of the Cambridge Philosophical Society*, vol. 36, pp. 160–172, Cambridge Univ Press, 1940.

[46] K. Marguerre, "Druckverteilung durch eine elastische schicht auf starrer rauher unterlage," *Ingenieur-Archiv*, vol. 2, no. 1, pp. 108–117, 1931.

[47] S. Venugopalan, M. Müser, and L. Nicola, "Green's function molecular dynamics meets discrete dislocation plasticity," Modell. Simul. Mater. Sci. Eng., submitted(2017).

[48] L. Pastewka and M. O. Robbins, "Contact between rough surfaces and a criterion for macroscopic adhesion," *Proceedings of the National Academy of Sciences*, vol. 111, no. 9, pp. 3298–3303, 2014.

[49] M. Frigo and S. G. Johnson, "The design and implementation of FFTW3," *Proceedings of the IEEE*, vol. 93, no. 2, pp. 216–231, 2005.

[50] Y. Zhao, G.-C. Wang, and T.-M. Lu, *Characterization of Amorphous and Crystalline Rough Surface–Principles and Applications*, vol. 37. Academic press, 2000.

[51] L. T.-M. M. Pelliccione, *Evolution of thin Film Morphology: Modeling and Simulations*. Springer, 2007.

[52] M. S. Longuet-Higgins, "Statistical properties of an isotropic random surface," *Philosophical Transactions of the Royal Society of London A: Mathematical, Physical and Engineering Sciences*, vol. 250, no. 975, pp. 157–174, 1957.

[53] P. R. Nayak, "Random process model of rough surfaces," ASME, 1971.

[54] F. M. Borodich, A. Pepelyshev, and O. Savencu, "Statistical approaches to description of rough engineering surfaces at nano and microscales," *Tribology International*, vol. 103, pp. 197–207, 2016.

[55] W. Dong, E. Mainsah, and K. Stout, "Reference planes for the assessment of surface roughness in three dimensions," *International Journal of Machine Tools and Manufacture*, vol. 35, no. 2, pp. 263–271, 1995.

[56] N. A. Feidenhans, P.-E. Hansen, L. Pilný, M. H. Madsen, G. Bissacco, J. C. Petersen, and R. Taboryski, "Comparison of optical methods for surface roughness characterization," *Measurement Science and Technology*, vol. 26, no. 8, p. 085208, 2015.

[57] M. Pelliccione, T. Karabacak, C. Gaire, G.-C. Wang, and T.-M. Lu, "Mound formation in surface growth under shadowing," *Physical Review B*, vol. 74, no. 12, p. 125420, 2006.

[58] G. Dalakos, J. Plawsky, and P. Persans, "Topographic evolution during deposition of plasma-deposited hydrogenated silicon on glass," *Physical Review B*, vol. 72, no. 20, p. 205305, 2005.

[59] G. Palasantzas and J. Krim, "Effect of the form of the height-height correlation function on diffuse X-ray scattering from a self-affine surface," *Physical Review B*, vol. 48, no. 5, p. 2873, 1993.

[60] G. Palasantzas, "Self-affine fractals and the limit $H \to 0$," *Physical Review E*, vol. 49, no. 2, p. 1740, 1994.

[61] S. K. Sinha, E. B. Sirota, S. Garoff, and H. B. Stanley, "X-ray and neutron scattering from rough surfaces," *Phys. Rev. B*, vol. 38, pp. 2297–2311, Aug 1988.

[62] G. Palasantzas, "Roughness spectrum and surface width of self-affine fractal surfaces via the K-correlation model," *Physical Review B*, vol. 48, no. 19, p. 14472, 1993.

[63] J. A. Goff and T. H. Jordan, "Stochastic modeling of seafloor morphology: Inversion of sea beam data for second-order statistics," *Journal of Geophysical Research: Solid Earth*, vol. 93, no. B11, pp. 13589–13608, 1988.

[64] C. Campaña, M. Müser, "Practical Green's function approach to the simulation of elastic, semi-infinite solids," *Physical Review B* ***74****, 075420*, 2006.

[65] A. Maystrenko, S. Melnik, G. Pritula, and O. Usatenko, "Bunches of random cross-correlated sequences," *Journal of Physics A: Mathematical and Theoretical*, vol. 46, no. 39, p. 395002, 2013.

[66] N. Garcia and E. Stoll, "Monte-Carlo calculation for electromagnetic-wave scattering from random rough surfaces," *Physical review letters*, vol. 52, no. 20, p. 1798, 1984.

[67] B. Osgood, "The Fourier Transform and its Applications," 1995.

[68] url: http://www.fftw.org/accuracy/ [Accessed: 01-01-17].

[69] G. E. Box, M. E. Muller, *et al.*, "A note on the generation of random normal deviates," *The annals of mathematical statistics*, vol. 29, no. 2, pp. 610–611, 1958.

[70] A. K. Chakraborty and M. Chatterjee, "On multivariate folded normal distribution," *Sankhya B*, vol. 75, no. 1, pp. 1–15, 2013.

[71] A. Papoulis and S. U. Pillai, *Probability, random variables, and stochastic processes*. Tata McGraw-Hill Education, 2002.

[72] R. J. Adler and J. E. Taylor, *Random fields and geometry*. Springer Science & Business Media, 2009.

[73] M. Scaraggi, C. Putignano, and G. Carbone, "Elastic contact of rough surfaces: A simple criterion to make 2d isotropic roughness equivalent to 1d one," *Wear*, vol. 297, no. 1, pp. 811–817, 2013.

[74] G. Carbone, L. Mangialardi, and B. Persson, "Adhesion between a thin elastic plate and a hard randomly rough substrate," *Physical Review B*, vol. 70, no. 12, p. 125407, 2004.

[75] X.-P. Xu and A. Needleman, "Void nucleation by inclusion debonding in a crystal matrix," *Modelling and Simulation in Materials Science and Engineering*, vol. 1, no. 2, p. 111, 1993.

[76] J. P. McGarry, É. Ó. Máirtín, G. Parry, and G. E. Beltz, "Potential-based and non-potential-based cohesive zone formulations under mixed-mode separation and over-closure. Part I: Theoretical analysis," *Journal of the Mechanics and Physics of Solids*, vol. 63, pp. 336–362, 2014.

[77] B. Persson, "Elastoplastic contact between randomly rough surfaces," *Physical Review Letters*, vol. 87, no. 11, p. 116101, 2001.

[78] M. Allen and D. Tildesly, *Computer Simulation of Liquids*. Oxford University Press, Oxford, 1987.

[79] S. Rao, *Mechanical vibrations*. Addison-Wesley PC, 2000.

[80] O. Grönbech-Jensen, N. Farago, "A simple and effective Verlet-type algorithm for simulating Langevin dynamics," *Molecular Physics Vol.111, p.983*, 2013.

[81] E. Hairer, C. Lubich, and G. Wanner, "Geometric numerical integration illustrated by the Störmer-Verlet method," *Acta Numerica, pp. 399-450*, 2003.

[82] A. W. Sandvik, "Numerical Solutions of the Schrödinger equation," *Department of Physics, Boston University*, 2013.

[83] M. H. Müser, "Single-asperity contact mechanics with positive and negative work of adhesion: Influence of finite-range interactions and a continuum description for the squeeze-out of wetting fluids," *Beilstein journal of nanotechnology*, vol. 5, p. 419, 2014.

[84] C. Ramos-Paja, S. González, and D. Montes, "Accurate calculation of settling time in second order systems: a photovoltaic application," *Rev.fac.ing.univ. Antioquia no.**66***, 2013.

[85] J. MacKay, R.S. Meiss, *Hamiltonian Dynamical Systems.* Adam Hilger, 1987.

[86] J. X. A. Bower, P. Vlahovska, *Introduction to Dynamics and Vibrations.* School of Engineering Brown University, 2016. [Accessed: 01-01-17].

[87] F. Major, *The Quantum Beat: Principles and Applications of Atomic Clocks.* Sprinter, 2007.

[88] G. Carbone and L. Mangialardi, "Analysis of the adhesive contact of confined layers by using a Green's function approach," *Journal of the Mechanics and Physics of Solids*, vol. 56, no. 2, pp. 684–706, 2008.

[89] R. Boyce, W.E. DiPrima, *Elementary Differential Equations and Boundary Value Problems.* Wiley, 2010.